INDIUM GALLIUM ZINC OXIDE: PHASE FORMATION AND CRYSTALLIZATION KINETICS DURING MILLISECOND LASER SPIKE ANNEALING

A Dissertation

Presented to the Faculty of the Graduate School

of Cornell University

in Partial Fulfillment of the Requirements for the Degree of

Doctor of Philosophy

by

David Michael Lynch

December 2017

INDIUM GALLIUM ZINC OXIDE: PHASE FORMATION AND CRYSTALLIZATION KINETICS DURING MILLISECOND LASER SPIKE ANNEALING

David Michael Lynch, Ph.D.

Cornell University 2017

Flat panel displays have become ubiquitous, enabling products from high-resolution cell phones to ultra-large television panels. Amorphous silicon (a-Si) has been the industry workhorse as the active semiconductor in pixel-addressing transistors due to its uniformity and low production costs. However, a-Si can no longer support larger and higher-resolution displays, and new materials with higher electron mobilities are required. Amorphous indium gallium zinc oxide (a-IGZO), which retains the uniformity and low cost of amorphous films, has emerged as a viable candidate due to its enhanced transport properties. However, a-IGZO devices suffer from long-term instabilities—the origins of which are not yet fully understood—causing a drift in switching characteristics over time and affecting product lifetime. More recently, devices fabricated from textured nanocrystalline IGZO, termed c-axis aligned crystalline (CAAC), have demonstrated superior stability. Unfortunately, little is known regarding the phase formation and crystallization kinetics of either the CAAC structure or in the broader ternary IGZO system.

Crystallinity and texture of CAAC IGZO films deposited by RF reactive sputtering were studied and characterized over a wide range of deposition conditions. The characteristic CAAC (0 0 9) peak at $2\theta = 30^\circ$ was observed by X-ray diffraction, and nanocrystalline domain texture was determined using a general

area detector diffraction system (GADDS). Highly ordered CAAC films were obtained near the $InGaZnO_4$ composition at a substrate temperature of 310°C and in a 10% O_2/90% Ar sputtering ambient. High-resolution transmission electron microscopy (HRTEM) confirmed the formation of CAAC and identified 2–3 nm domains coherently aligned over large ranges extending beyond the field of view (15 nm × 15 nm). Cross-section HRTEM of the CAAC/substrate interface shows formation of an initially disordered IGZO layer prior to CAAC formation, suggesting a nucleation mechanism similar to ZnO thin films. A classical nucleation and growth model is proposed and compared to alternative models proposed in literature.

Extending this study of CAAC IGZO, the formation and growth of crystalline IGZO over a wide composition range and processing conditions were explored. IGZO itself is one composition of a class of homologous structures in the pseudo-binary $InGaO_3(ZnO)_m$ system. For integer m, the equilibrium structure is known and well-characterized; however, for non-integer m, disorder must exist and the kinetics of the structural development remain almost completely unknown. A high-throughput (combinatorial) approach utilizing co-sputter deposition, millisecond timescale thermal gradient laser annealing, and spatially-resolved characterization using microbeam wide-angle X-ray scattering was used to probe the structural evolution as a function of temperature, time, and composition. As-deposited films were amorphous in the $InGaO_3$-rich composition range, becoming crystalline (wurtzite) with increasing ZnO content. Under millisecond heating, films evolved toward the equilibrium layered structure consisting of nearly pure In_2O_3 layers with $(Ga, Zn)O_x$ interlayers. Composition deviations (non-integer m) are discussed within a model of cationic disorder in both the In_2O_3 layers and the $(Ga, Zn)O_x$ layers. Crystal-to-

crystal transformations in the high-ZnO region are discussed within the context of a new growth model for these homologous structures. This deeper understanding of the nature of crystalline IGZO will help to enable the successful implementation of CAAC IGZO for high-performance display applications.

BIOGRAPHICAL SKETCH

David Lynch was born in Fairfax, Virginia on June 10, 1990. Always interested in the sciences—mainly from an early suggestion from his loving parents (both accountants) to avoid accounting—David pursued studies at the University of Virginia in Charlottesville, Virginia, where he earned the degrees of Bachelor of Science in Chemical Engineering and Bachelor of Arts in Physics in 2012. What began with taking a few courses for a minor led to undergraduate research in Materials Science and Engineering under the direction of Professor James Fitz-Gerald and Matthew Steiner, which led David to conclude that he might have picked the wrong major.

David continued into graduate studies in Materials Science and Engineering at Cornell University in Ithaca, New York working with Professor Michael Thompson. David is forever grateful for and indebted to Professor Thompson for all of the opportunities made available (and taken liberties overlooked) during his graduate school career. As a second-year student, David created the one-man LynchPin Consulting LLC in 2014 to engage in industrial consulting projects on the side with Surmet Corporation and Applied Materials, Inc. After earning the degree of Master of Science in 2015, David took a year-long leave of absence to intern at Corning Incorporated in Painted Post, New York and Apple, Inc. in Cupertino, California, where he gained invaluable perspective into a career in industry. David decided to pursue a career in process development, joining Intel Corporation following his graduation in 2017.

May the bird of paradise fly up your nose.

ACKNOWLEDGEMENTS

It takes a village to raise an idiot.

—Misquoted African Proverb

I would not be where I am today without a little bit of luck and a massive amount of support from family, friends, and colleagues. I will do my best to acknowledge them here, and I apologize if I left out a few names by accident (fact of the matter is, they'll probably never notice anyway).

It would be egregiously remiss of me not to first thank my family, who made me the man I am today. My parents Michael and Thuy have been there every step of the way, providing everything from life advice to phenomenal home-cooked meals. I know there is unspoken sadness (right?) that I will be moving to the wrong coast, but in response: hurry up and retire already, and I can fly you out to visit! My younger sister Lynne has been there for almost as long as somone to talk to during hard times, and I've watched her grow up into an intelligent and resilient young woman that I am immensely proud of.

As hinted slightly in my biographical sketch, I am extremely grateful to Professor Michael Thompson for accidentally letting me into his group. He has been a wonderful mentor and has made the experience I had at Cornell truly unique. I have also had the pleasure of TAing for him four (yes, 4) times, from which I learned and now understand his joy of teaching. It is absolutely infectious. Aside from being the best teacher I have ever had in the sciences, I had the opportunity of learning more auxiliary things from him that I probably could not have learned elsewhere (i.e., children should climb more trees, the full range of use of industrial gases, what a deadline really means, and that I was doing Pink Floyd's The Dark Side of the Moon injustice by not listening to it all at once).

My entire committee has been extremely supportive. I especially want to thank Professor Emeritus Dieter Ast, without whom I may have never become so interested in semiconductor processing, and without whom I certainly would never have become involved with the Applied Materials project. I cannot thank you enough for your mentorship. I also want to thank Ray Greene at Corning Incorporated, who I have had the pleasure to work with on both the CAAC IGZO project and on my internship project. In particular, his support early in my graduate school career when I lacked direction was truly pivotal, and I am eternally grateful for it. I would also like to thank Dick Shealy for some of the best courses that I've taken at Cornell and for his incredible sense of humor (and for passing me on my minor courses).

I probably wouldn't have passed the qualifying exam if not for the A Team: Joseph Carloni, Benjamin Revard, and Benjamin Richards. Their friendship and support both on and off the clock (writing, of course) has been incredible, and I look forward to reuniting with two-thirds of them in Portland at Intel (don't worry guys, Richards just doesn't know he's applying yet).

The Thompson Zoo has been like a work family to me. I am grateful to my Thompson group mentor Byungki Jung for taking me under his wing and for his invaluable graduate school advice (like where the best fried chicken is), and I look forward to seeing him again out in Portland. Alan Jacobs and Bob Bell have been a blast to work with all five years, and it was their gregarious personalities that got me interested in the group in the first place. I could not have asked for a better team in our IGZO subgroup: Chenyang Chung (poring over papers over a pitcher of beer every Monday made Mondays even bearable), Bin Zhu, and especially Kate Roach—who was forced to put up with me both as an undergraduate and as a Masters student. I thank Victoria Sorg for decid-

ing to move over from the Clancy group office, putting up with my bad jokes, and being an awesome friend. I also wish the best of luck to the future of the Thompson group: Steve Huang, Emily Cheng, and Katherine Quinn—you have all been incredible and your futures are bright ones! I'd also like to thank my UTA armada Matti Thurston, Divya Srinivasan, and Andres Larraza for their help in helping me survive TAing my last semester.

I've had many wonderful collaborators. I would like to thank my friend Barnaby Levin for is wonderful help with HRTEM imaging and analysis, as well as for getting me into the Marvel movies. I would also like to thank Peter Beaucage, who let me barge in these WAXS samples at CHESS on his time.

I would also like to thank the Applied Materials project team for their support: Kevin Papke and Mats Larsson at Applied for keeping the project running behind the scenes; Professor Dieter Ast, Joe Carloni, and Tasnuva Tabassum, who made up the core team when we were knee-deep in the beginning; and Professor Bruce van Dover, Rui Zeng, and Lewis Haber, the future of the project! It has been a particular pleasure working with Tas, who will no doubt be successful in her career at Applied, and Bruce—I spent nearly four years looking for an excuse to work with this legend and I finally got my wish.

Cornell is blessed with an armada of superior staff members, and I need to single-out a few for a good, sound thanking. In CNF, I want to thank Aaron Windsor for his help and advice on deposition and ICP, Mike Skvarla for his advice when I was starting LynchPin, and Tom Pennell—who I can't imagine a CNF without—for his support in depositions and for his friendship. In CCMR, I want to thank John Grazul for personally embodying what makes learning and working in the lab fun and Don Werder for his patience when I kept crashing the microprobe and for the incredible Bell Labs stories. There have been several

others who have helped me in times of great need—often without any thought of the inconvenience. I especially want to thank Rick Brown for his assistance on evaporation, electrical characterization, getting that big pump installed on the etcher in the teaching lab, and for helping me find Dick Shealy. The CNF contractors Chris Martin and Stephen Jones have provided invaluable processing advice, and Gregg McElwee helped me out tremendously by squeezing us in on the ICP-OES schedule on such short notice.

A big thank you to both of my industrial mentors Rakiba Chowdhury (Corning) and Amir Dindar (Apple) for their patience, friendship, and advice. I would also like to acknowledge industrial sponsorship from Corning Incorporated and Kionix, Inc. that supported me through graduate school.

Lastly, I would like to give a big thank you to my fiancée Teresa Kao for putting up with my insanity for four years—there are many years more of this yet to come! I would never have survived graduate school without her love and support (and, when necessary, keeping my ballooning ego in check). I am thrilled that she will be joining me at Intel in Portland, where we somehow simultaneously figured out a solution to the dreaded two-body problem and a wedding venue.

TABLE OF CONTENTS

LIST OF TABLES

LIST OF FIGURES

CHAPTER 1

INTRODUCTION

1.1 Motivation For This Work

The last decade has seen a tremendous jump in the prominence of flat panel displays, with a clear market trend toward increased size, higher resolution, and improved efficiency. The liquid crystal display (LCD) is one of the most commercially successful flat panel display platforms, reaching a value of $133.5 billion in 2016 and expected to increase by another 50% by 2022 [18, 19]. Even more recently, organic light-emitting diode (OLED) displays have emerged as a competing technology that offers higher contrast ratios and are promising for thin or flexible display applications.

At the heart of these display pixel are transistors that control the output of the pixel. The design requirements for the semiconductor material used in these devices are very different from those used other electronic applications and are typically dictated by the size and temperature limitations of the substrates (usually glass). Typical deposition areas span several square meters, compared to the 300 mm substrate size used in CMOS applications, and deposited films must be uniform across this entire area. Furthermore, typical display glass substrates densify and compact at high temperatures, restricting processing temperatures to a critical value. This effect will be further exacerbated in the future with the use of polymeric substrates for flexible applications. Hydrogenated amorphous silicon (a-Si:H) has been the workhorse of the display industry for many years as the active semiconductor material, providing adequate electronic performance within these design criteria.

As high-peformance displays move to 4K and higher resolutions, and as pixels become increasingly dense, the display industry has reached a critical materials problem: the incumbent and mature amorphous silicon-based technology is no longer adequate to meet the requirements of these new applications. The need for smaller transistors and, in the case of OLEDs higher drive currents, translates to a critical need for higher carrier mobilities with uniformities at least equivalent to a-Si:H. Of the materials systems proposed and investigated, amorphous indium gallium zinc oxide (a-IGZO) has emerged as a promising system, providing a ten-fold increase in carrier mobility while maintaining a low processing temperature and uniform properties over extremely large areas.

Introducing a new material platform introduces a plethora of issues. Beyond the obvious infrastructural changes and investment risks associated with a new material, optimizing a material system often leads to a trade-off between desirable traits, such as carrier mobility, ease of defect engineering, uniformity variations, and unforeseen long-term instabilities. Even with the implementation of a-IGZO in commercial products, challenges associated with long-term instabilities have remained due, in part, to the extreme complexity of this amorphous ternary oxide semiconductor.

Much of the current effort in IGZO research is based on the need to understand and eliminate the origin of these long-term instability effects. Of the many proposed solutions, one of the most promising is the reduction of defect states by crystallization. This pathway has two immediate benefits: (1) a reduction of the defect states caused by structural disorder inherent in an amorphous material and (2) reversion to an simplified system in which the defect chemistry can be quantitatively studied.

1.2 Organization of This Dissertation

The goal of this work is to develop an understanding of the structural formation characteristics of crystalline IGZO. While the vast majority of previous IGZO studies have focused on a-IGZO, relatively little is known or understood regarding the crystalline form. This work is deviced here in two general sections: (1) the investigation of crystalline microstructures formed during deposition (CAAC) and (2) a comprehensive study of crystallization kinetics based on a high-throughput approach coupled with short timescale thermal (laser) annealing.

Chapter 2 contains a general overview of the body of a-IGZO research within the context of display applications. It is intended to provide a basic understanding of the state of the field and the challenges associated with this complex material system. The chapter ends with a brief summary of the potential pathways to address these challenges, with a particular focus on crystalline IGZO.

Chapter 3 gives a detailed description of the methods used to fabricate and characterize IGZO films and devices in this work. This dissertation is focused primarily on sputter deposition techniques, a developed composition characterization technique, and structural characterization using X-ray diffraction.

Chapter 4 discusses experimental work on textured IGZO microstructure (CAAC IGZO) demonstrated in the literature to exhibit improved electronic characteristics. Formation regimes and characteristics are discussed, and a model for growth is proposed. This model is compared and contrasted with other proposed models for growth in this system.

Chapter 5 examines the effect of the film microstructure and composition on extracted device parameters from TFTs fabricated in CAAC IGZO, expanding upon the published work in Chapter 4.

Chapter 6 presents a high-throughput study of IGZO crystallization kinetics as a function of composition (Zn cation fraction), temperature, and time accessed by millisecond timescale laser annealing. The impact of the observed metastable structures are discussed in terms of defect chemistry energetics.

Chapter 7 condenses the key results of these studies and provides recommendations for future study.

Supplementary work is contained within the appendices. Appendix A discusses the physics and current-voltage (IV) characteristics of a MOSFET device and models for thin film transistors. Appendix B contains a review of amorphous semiconductor theory that provides critical insight into amorphous semiconductor device operation. Appendix C discusses the deposition of SiN_x films by plasma-enhanced chemical vapor deposition (PECVD) and is an adaptation of a report done for a collaborator on a side project. Appendix D contains information on etch rates used in this work and in other side work.

CHAPTER 2

BACKGROUND

2.1 Display Transistor Technology

Virtually all research and development of semiconducting indium gallium zinc oxide (IGZO) over the past decade has been driven by needs of the flat panel display industry. Pixels in flat panel displays are driven by arrays of thin film transistors (TFTs) fabricated from an active layer of some semiconducting material. Indeed, the growth of the flat panel display industry is tied closely to advances in the manufacturability of these TFTs and their associated addressing circuitry. While the display market has historically been dominated by liquid crystal displays (LCDs) utilizing hydrogenated amorphous silicon (a-Si:H), the current trend is toward more efficient and higher-resolution displays requiring development of semiconductor materials that can support the demand of these applications.

2.1.1 Pixel Operation

Liquid Crystal Displays

LCDs rely on liquid crystals composed of molecules which can structurally organize into a semi-crystalline arrangement, while retaining the viscosity of a liquid. The anisotropic nature of molecules in this crystalline network gives rise to birefringence and dielectric anisotropy, allowing optical properties of a liquid crystal to be controlled by an electric field. The low viscosity of a liquid crystal

allows rapid response to an external electric field stimulus, enabling the liquid crystal to act as an optical shutter for polarized light.

Figure 2.1 schematically shows operation of a liquid crystal cell. Liquid crystal molecules are set between two glass plates, internally coated with transparent conducting electrodes such as indium tin oxide (ITO). A textured liquid crystal alignment layer is used to anchor the liquid crystal molecules near the glass plates. Outside of the glass plates are crossed linear polarizers, back-lit on one side with some light source.

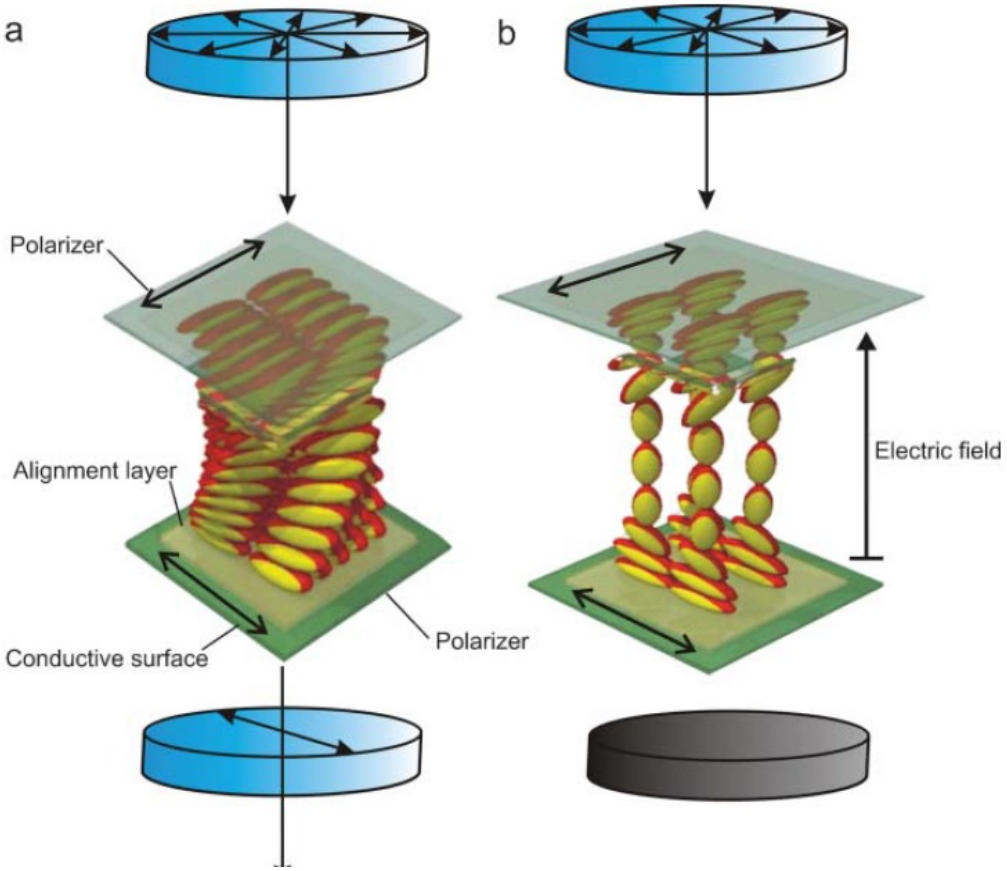

Figure 2.1: Schematic diagram of a twisted-nematic LCD indicating (a) the on-state and (b) the off-state. Reproduced with permission from Ref. [1]. Copyright 2006 The Royal Society of Chemistry.

In the absense of an applied bias, the molecules self-align to the anchoring alignment coatings on the glass plates, creating the twisted nematic structure shown in Figure 2.1a. This twisted structure induces a 90° rotation in the polarization of the light entering the cell, such that the light entering one end of the cell is transmitted through the other side to create an on-state cell. With a bias applied to the ITO electrodes, liquid crystal molecules align themselves along the lines of the electric field as shown in Figure 2.1b, removing the 90° twist. Light can no longer transmit through the cell, and the cell is switched off. Removing the electric field allows the structure to relax back into the twisted nematic orientation.

Thus each liquid crystal cell can be viewed as a voltage-controlled monochromatic light valve, and controlling the cell voltage between fully-on and fully-off states allow for fractional transmission of the light. Colored displays are achieved by passing the light through a color filter (typically red, green, and blue), with each set of three subpixel cells composing a single display pixel.

The driving voltage of each sub-pixel is controlled using a thin film transistor (TFT), the operation of which will be discussed in greater detail in the next section. At the most basic level, a TFT is a voltage controlled three-terminal device that allows current flow between two electrodes (source and drain) by changing the bias on the third electrode (gate). Modern LCDs utilize matrix addressing in which each subpixel is cyclically addressed through orthogonally arranged source and gate lines shown in Figure 2.2.

An important consequence of these circuit arrays is the so-called "aperture effect." As can be seen in Figure 2.2, addressing lines and transistors form

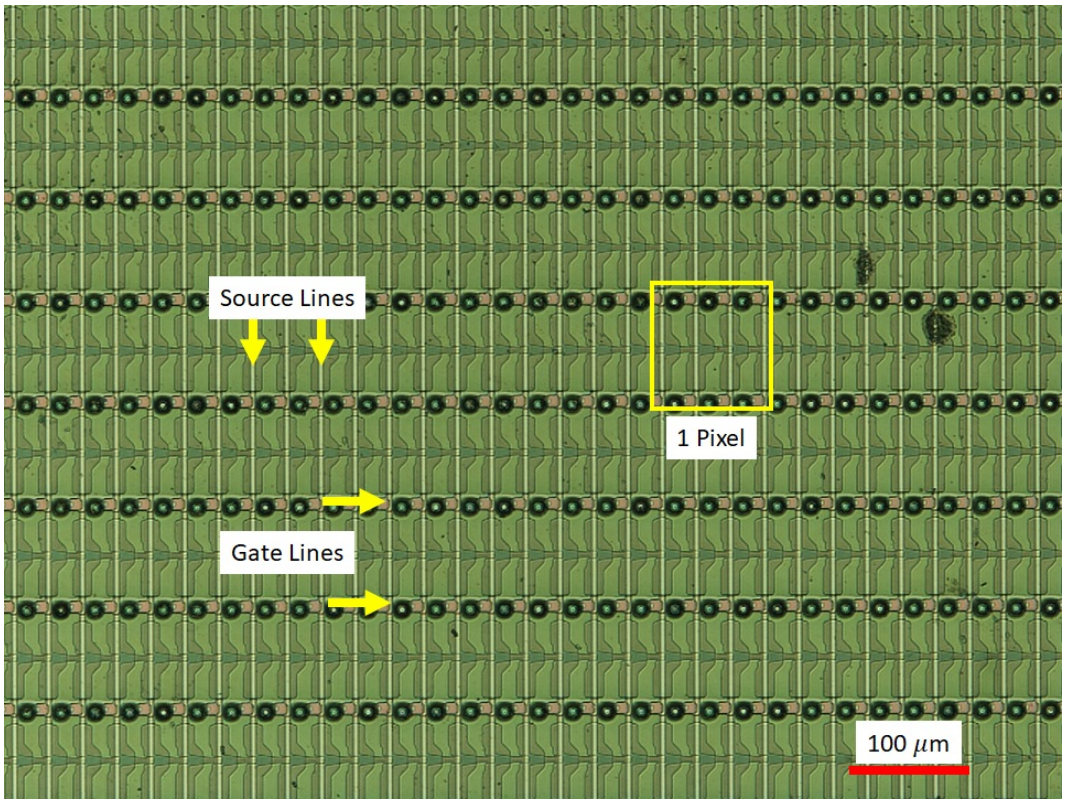

Figure 2.2: A typical active-matrix LCD pixel circuit layout (color filter removed). Denoted are the size of a single pixel and the orthogonally arranged source and gate lines.

opaque regions with each pixel reducing the "aperture" through which light can be transmitted. While inconsequential for low-resolution displays, high-resolution displays with high pixel densities now require size reduction of these devices to prevent a loss in brightness. Implementation of a TFT semiconductor material with a higher carrier mobility allows the reduction of the transistor size and—as a result—an improved aperture ratio. This is one of the key driving factors toward new material platforms for LCD applications.

Organic Light Emitting Diodes

As an alternative display technology, organic light emitting diode (OLED) displays exploit electron-hole recombination between electronic states in an organic molecule to emit light, eliminating the need for both the LCD and the associated backlight [18]. In addition, various emitted colors can be achieved by the selection of the organic material, potentially eliminating the need for a color filter.

As an emissive device, a top-emitting OLED display does not suffer from the same aperture effect as in the case of an LCD. However, to support the current required to drive an OLED device, the semiconductor material used in the TFT must support stable high-current operation. In addition, any non-uniformities in the semiconductor film can lead to brightness variations across the display area. As transistors remain in the on-state for a substantial fraction of the time, shifts in switching characteristics over time plays a critical role, and additional compensating mechanisms are commonly required in the circuit design. Control of these three features must be considered in moving to a new semiconductor material platform.

2.1.2 Thin Film Transistors

The thin film transistor (TFT) is the key operating device in flat panel display. Put most simply, a TFT can be considered as a basic switch or a flow-controlled valve. Whether it is used as a voltage switch in an optical shutter of an LCD or as a current source for an OLED, understanding the basic operation principles leading to the switching of TFT operation is critical.

TFT Basic Design

One of the simplest and most commonly used TFT architectures is shown in Figure 2.3: the bottom-gate inverted staggered structure. Core to function of the device is the semiconductor channel layer (typically Si or IGZO in display applications). The channel layer is contacted by two conductive electrodes (typically metal) referred to as the source and drain. In many cases, the device is symmetric with no distinciton between the source and the drain. For most purposes, the source is typically held common (grounded) as a reference point, and the voltage bias between the drain and the source (V_{DS}) describes the driving force for current flow through the channel.

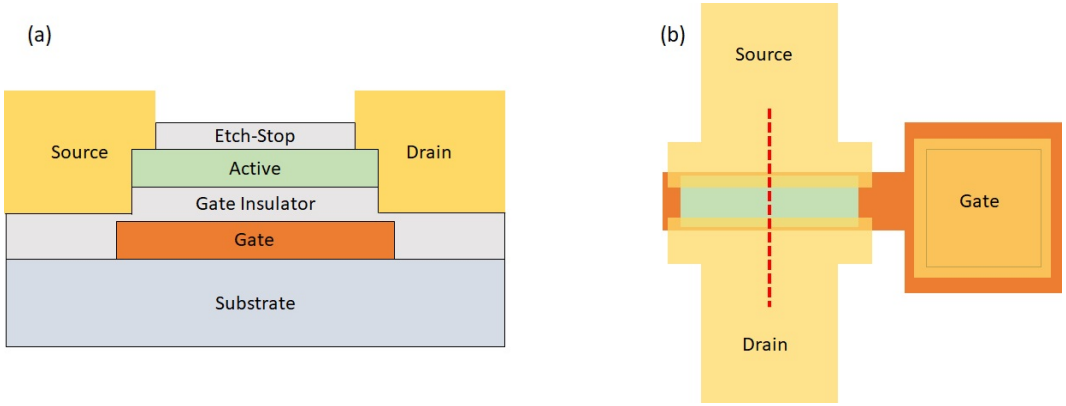

Figure 2.3: Typical bottom-gate inverted staggered TFT layout used in many commerical and lab-scale applications. (a) Cross-section showing the thin film stack composing the TFT with an etch-stop layer to protect the active layer backchannel. (b) Plan-view of the same structure, showing the spatial layout and indicating by dashed line the section shown in (a).

The carrier density in the semiconducting channel layer is modulated by the introduction of an electric field in the channel. This is achieved by biasing an adjacent conductive layer (gate) separated by an insulating material (gate insulator, typically SiO_2 or SiN_x); due to this gate oxide, there is negligible current flow through the gate. In a TFT, the applied electric field (gate bias V_{GS}) is used

to accumulate or deplete carriers in the active channel, hence modulating the conductance of the channel.

The selection of source/drain electrodes is determined primarily by the metal work function to optimize contact resistance with many industrial applications using Ti/Cu or Ti/Al metal stacks. In contrast, the gate material used is nearly independent of TFT operation, and gate materials in industrial uses vary from Cu to W. In lab-scale research devices, where a functional pixel is not required, test devices can be fabricated directly onto an oxidized Si wafer, using the Si as the gate material and the oxide as the gate dielectric.

TFT device operation bears great resemblance to that of the metal-oxide-semiconductor field effect transistor (MOSFET), and the extraction of key device parameters such as carrier mobility, turn-on voltage, and subthreshold slope relies on methods developed for the MOSFET. A more detailed description of the *IV* characteristics of a MOSFET, and the extraction methods used in this work, are discussed in Appendix A.

TFT Architectures

For display applications, the staggered bottom-gate top-contact geometry is the most common architecture. This geometry is easily optimized, with a balance between ease of fabrication at reasonable temperatures for glass substrates, a good interface between gate insulator and semiconductor, and easily controlled contact resistance.

The most common of these staggered layout used for oxide TFTs is the etch-stop layer (ES) architecture, shown in Figure 2.3. In this layout, a protective

"etch-stop" layer, such as SiN_x or SiO_2, is deposited directly on top of the channel layer prior to metal electrode deposition. When the metal electrodes are deposited and patterned, the etch-stop layer halts the etching without damage to the active channel. Post-fabrication, the etch-stop layer also serves as a passivation layer to protect the channel from environmental factors that could affect long-term stability.

Many more mature technologies, especially with optimzied a-Si:H, utilize a backchannel etch (BCE) architecture, which is identical to the ES layout without the etch-stop layer. The backchannel (the semiconductor interface opposite the gate insulator-semiconductor interface) is exposed to the metal etchant during the processing of a BCE structure, introducing defects in the backchannel. However, processing with this architecture requires one fewer photolithography step and photomask, which significantly reduces manufacturing costs. While typically used for a-Si:H, for which backchannel defects can be easily controlled by hydrogenation, use of this layout for IGZO devices is hampered by current understanding of the backchannel defects introduced during the metal etch process [20]. Indeed, understanding the fundamental nature and passivation methods for these defects is critical before oxide BCE TFTs can be successfully implemented.

Desirable Active Channel Material Traits

The properties of the active channel layer material are key in realizing higher-resolution, higher-efficiency displays. For these applications, the critical material metrics can be summarized into five key elements:

1. High carrier mobility. In both major applications (LCD and OLED), a high carrier (typically electron) mobility is paramount to achieving high-resolution, high-efficiency displays. High-mobility materials enable the reduction of transistor size and supporting circuitry, thus increasing the aperture ratio of a display. Further, higher mobilities enable higher on-state driving current I_{on} for OLED applications.

2. Low leakage current. A low off-state (leakage) current I_{off} is desirable from the perspective of power consumption. While I_{on} is typically several orders of magnitude higher than I_{off}, a finite I_{off} translates to constant power draw of the transistor, even when the device is turned "off."

3. Large-area film uniformity. As-deposited thin films of the channel material must be uniform across the entire substrate. Substrate size scales in production are on the order of several m^2 (Gen 10 substrates, which went into production in 2009, are 2.9 m $\times$ 3.1 m [21]). Non-uniformities, which can manifest in several different ways (thickness, composition, microstructure, defect structure, etc.), must be minimized to control final display image quality.

4. Low processing temperature. Many potential materials for TFT applications require either high-temperature deposition or post-deposition annealing. However the glass substrates used for display applications limit the maximum processing temperature to values that are far below those used in silicon VLSI technology. At temperatures above the annealing point of the glass (722 °C for Corning® Eagle XG® glass [22]), glass compaction (densification) can affect pitch variation between processing steps. Additionally, the prospect of using flexible polymeric substrates for roll-to-roll processing limits this temperature even further.

5. Threshold stability. Most of the suitable materials that meet previous criteria are amorphous semiconductors. However, amorphous semiconductors intrinsically possess a high density of electronic defect states that may act as carrier traps. As a result, electronic performance (characterized primarily by a device "turn-on" threshold) may shift over time, limiting product lifetime. There are a variety of potential mechanisms in each material system, which in many systems are poorly understood. This consequently is a major area for continued research and development of these materials.

2.1.3 Active Channel Material Platforms

The following is a brief overview of the characteristics of each semiconductor material considered for use in display transistors. All materials are compared to amorphous silicon (the incumbent technology), identifying specific advantages and disadvantages.

Amorphous Silicon

Amorphous silicon (a-Si), which is usually hydrogenated to reduce dangling bonds as a-Si:H, has been the workhorse of the display industry for decades. As an amorphous material, one of the major benefits of using a-Si:H is its inherent film uniformity over large deposited areas and a low required processing temperature (<350°C) [18]. However, a-Si:H suffers from a low carrier mobility (~1 cm^2/Vs), especially compared to high-quality crystalline Si used in CMOS applications (~1000 cm^2/Vs) [23]. In addition, the defect structure of a-Si:H give

rise to a relatively high leakage current and turn-on voltage/threshold instabilities [24, 25], limiting the use of a-Si:H for next-generation display applications. Indeed, this is the driving force for finding new materials for use as an active channel material in TFTs.

Polycrystalline Silicon

One potential solution involves crystallizing a-Si:H to yield higher mobility materials. Low-temperature polycrystalline silicon (LTPS) TFTs can be fabricated by furnace or excimer laser annealing (ELA) prior to patterning and electrode deposition [26]. While ELA allows fabrication of polycrystalline films with an ~100x higher carrier mobility and minimal effects on glass substrates [23], key issues remain that limit large-scale LTPS production, such as grain boundary scattering [27, 28]. The grain size distribution within the active device area (~10 μm x 10 μm) must be tightly controlled over the entire substrate since non-uniformities can cause vastly different device properties and, as a result, poor image quality [18]. Secondly, grain boundaries also provide pathways for leakage current, contributing to power draw even in the off-state [25].

Oxide Semiconductors

Oxides are frequently used in the microelectronics industry, and are generally compatible with low temperature deposition and large area uniformity using modern techniques. Historically however, the most common use of oxides is as an insulator. For instance, SiO_2 is often used as a passivating layer to protect microcircuitry from environmental effects (a planarization layer for subsequent

layer circuit patterning) or as the gate dielectric for metal-oxide-semiconductor field-effect transistors (MOSFETs) and for thin film transistors (TFTs).

Conductive oxides, such as SnO_2, In_2O_3, indium tin oxide (ITO), and indium zinc oxide (IZO), are also used in the place of metal contacts and circuits. These materials are ideal for transparent electronics applications due to their wide bandgap energies (>3 eV). These oxides can also exhibit large carrier mobilities (up to ~200 cm^2/Vs), providing a useful electronic structure template from which to design oxide-based semiconductors [29].

ZnO has been extensively studied as a TFT semiconductor material due to its device switching capabilities and its relatively high field-effect mobilities of up to 40 cm^2/Vs [30]. However, structural control of ZnO remains an issue, and achieving uniform ZnO films over large areas is difficult, as uniform amorphous ZnO films are difficult to obtain; deposited ZnO readily crystallizes at any reasonable deposition or processing temperatures [31]. Because of this, other oxide systems have been explored for potential TFT applications.

Indium Gallium Zinc Oxide

The promising semiconducting behavior of ZnO has encouraged its use as a model system for material development. Alloying ZnO with other oxides has been shown to suppress crystallization. Combining ZnO, with a hexagonal wurtzite structure [32], and In_2O_3, a known oxide conductor with a high electron mobility and a cubic bixbyite structure [33], leads to typically amorphous films of IZO [34]. While high-mobility IZO can be deposited uniformly, carrier densities are typically too high to be controlled by an electric field in a TFT.

Ga_2O_3, added to IZO to form indium gallium zinc oxide (IGZO), helps to stabilize carrier-contributing point defects and generates a material suitable for a TFT channel layer [8].

IGZO satisfies many of the material needs for application in display TFTs. IGZO devices have demonstrated electron mobilities greater than 10 cm^2/Vs (an order of magnitude greater than a-Si:H) and very low leakage current due to fewer defect states in the sub-gap [26]. As an amorphous film deposited at temperatures as low as room temperature, IGZO is compatible with display glass substrates and can be formed uniformly over large areas. Indeed, IGZO serves as an ideal choice due to its low toxicity and a demonstrated balance between high mobility and large area uniformity attributed to its structural stability in the amorphous state [35]. However, devices fabricated from IGZO still exhibit long-term stability issues, and much of the research effort has focused on understanding the nature of defects in IGZO and the vast complexity of this amorphous quaternary system.

2.2 Indium Gallium Zinc Oxide Fundamentals

Unlike most crystalline semiconductors, characterization of the electronic properties of indium gallium zinc oxide (IGZO) has been a slow and circuitous process. Understanding of a-Si:H evolved from characterization of the single crystal Si system. However, much of the body of IGZO literature focuses only on the complex amorphous structure, complicating experimental analysis and interpretation. Indeed, characterizing an amorphous semiconductor is challenging, as the traditional approach to semiconductor theory based on crystalline solids

breaks down for amorphous materials. A review of the basic considerations of amorphous semiconductor theory is included in Appendix B.

The understanding of the electronic structure of IGZO has come instead from a variety of indirect techniques. First-principles calculations, using density functional theory (DFT)[1], have been used to investigate the nature of the native band structure and the effect of point defects on the positioning of the Fermi level and to determine the effects of doping [6, 38–41]. The density of states within the bandgap has been further characterized using various electronic and optical techniques [5, 42–48]. The comprehensive results of these different techniques has led to the current, though incomplete, understanding of the structure and challenges of the IGZO system.

2.2.1 Crystal Structure of IGZO

Crystalline IGZO (c-IGZO) was first reported in 1985 by Kimizuka and Mohri [49] as exhibiting a spinel-type $InGaZnO_4$ structure, but was later found to belong to a larger class of homologous structures, with the chemical formula $InGaO_3(ZnO)_m$ (where m is an integer) [50–52]. The $InGaO_3(ZnO)_m$ structure is composed of In_2O_3 sheets composed of octahedrally-coordinated In cations sandwiching $(m + 1)$ $(GaZn_m)O_x$ layers composed of a mixture of 4-fold and 5-fold coordinated cations, as shown in Figure 2.4. The cations within the $(GaZn_m)O_x$ layer maintain a hexagonal arrangement, and the overall crystal symmetry is determined by the number of planes between each In_2O_3 sheet: rhombohedral symmetry for odd m and hexagonal symmetry for even m.

[1] An introduction to DFT can be found in references [36, 37].

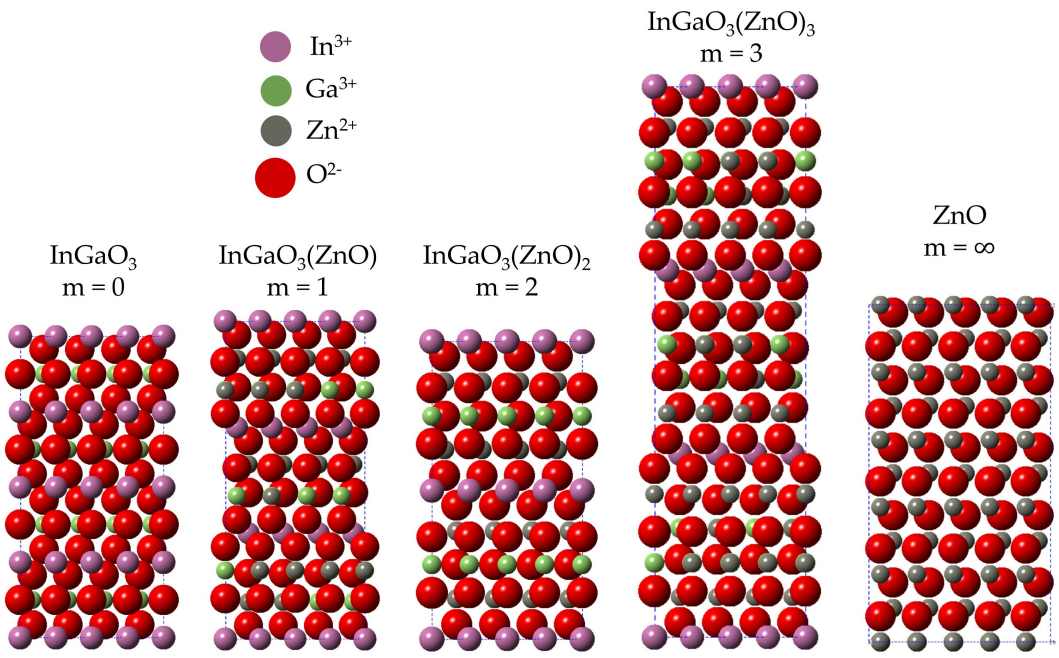

Figure 2.4: Selected structures from the $InGaO_3(ZnO)_m$ homologous structure series: $InGaO_3$ ($m = 0$), $InGaO_3(ZnO)$ ($m = 1$), $InGaO_3(ZnO)_2$ ($m = 2$), $InGaO_3(ZnO)_3$ ($m = 3$), and ZnO ($m = \infty$). Structural data from Refs. [2–4].

There has been some dispute in literature pertaining to the coordination geometries and arrangement of Ga and Zn atoms within the $(GaZn_m)O_x$ layers. Isobe *et al.* [53] concluded from their structural analysis that Ga and Zn are randomly arranged throughout the $(GaZn_m)O_x$ layers (a hypothesis later supported by Nomura *et al.* in 2004 [54]) with 5-fold coordination on average. Nakamura *et al.* [50] noted that the structures of high-m $InGaO_3(ZnO)_m$ compounds were indistinguishable from a disordered wurtzite structure, suggesting that the $(GaZn_m)O_x$ layers are simply a solid solution of Ga_2O_3 and ZnO in a wurtzite arrangement. Later computational work by Orita *et al.* [55] and Omura *et al.* [6] suggested that, while the X-ray data accurately reflects the average atomic positions, Zn will adopt 4-fold coordination (as in pure ZnO wurtzite) and Ga will adopt 5-fold coordination in a relaxed structure allowing local deviations.

The cation arrangement within the $(GaZn_m)O_x$ layers has been debated to a greater extent. While the occupation of the cation sites is often believed to be random [6, 16, 50, 55, 56], researchers such as Narendranath *et al.* [3] have suggested ordering of the Ga polyhedra into a sheet at the center of the $(GaZn_m)O_x$ layer. From first-principles calculations, Da Silva *et al.* [57] predicted that the Ga polyhedra would preferrentially form zigzag structures within the $(GaZn_m)O_x$ layer to minimize lattice strain, supported by high-resolution TEM studies of $InGaO_3(ZnO)_m$ and other isostructural compounds [58–62]. Overall, the atomic structure of $InGaO_3(ZnO)_m$ is complex, compounding the challenges of understanding the formation characteristics of these structures.

Figure 2.5b shows the structure of c-IGZO represented in units of In_2O_3 octahedra (compared also to the pure In_2O_3 structure, shown in Figure 2.5a) and Ga/Zn-O polyhedra. It is generally believed that the extent of the In_2O_3 edge-sharing polyhedra network is predominantly responsible for the high carrier mobility and the relative insensitivity to perturbations by structural disorder [5]. The zinc and gallium are thought to be randomly distributed among the remaining cation sites between the In_2O_3 layers, with the random distribution creating an electronic potential barrier distribution that affects conduction [54].

Moriga *et al.* [42] first demonstrated the use of IGZO as a transparent conductor in pressed pellets, showing a wide range of compositions, conductivities ranging from 10^{-1} to 10^2 S/cm, and band absorption edges ranging from 320 to 440 nm (corresponding to a band gap between 2.8 and 3.9 eV). TFTs fabricated from c-IGZO have been reported to exhibit mobilities as high as ~80 cm^2/Vs [63].

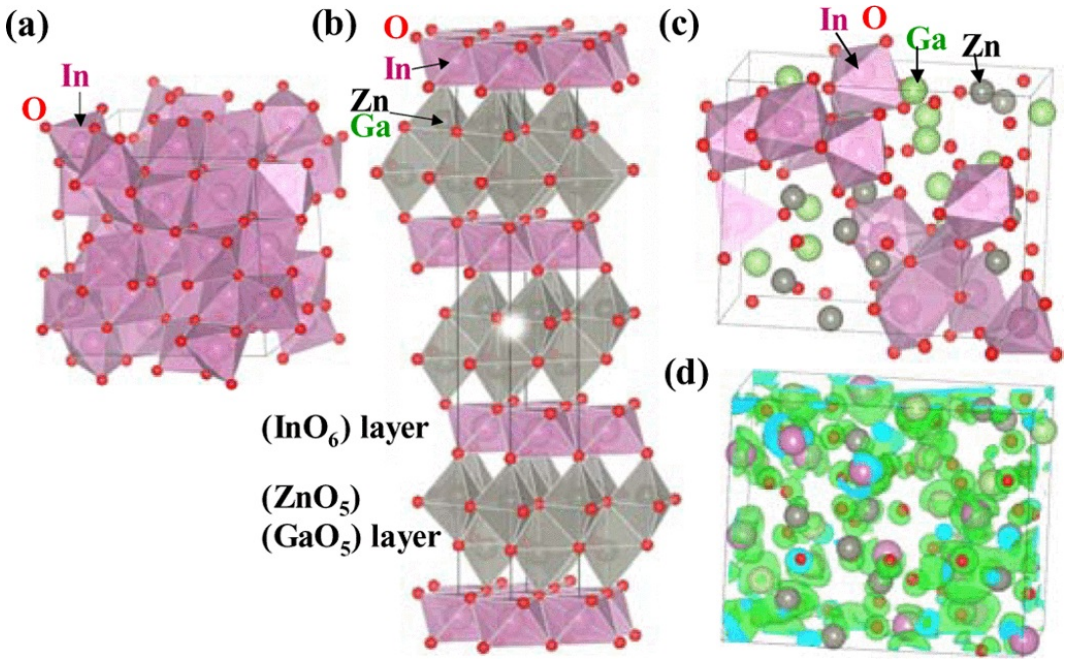

Figure 2.5: A polyhedral view of (a) In_2O_3, (b) $InGaZnO_4$, and (c) a-IGZO. (d) Isosurface of the conduction band minimum wavefunction in a-IGZO, showing spatial extent of the conduction band minimum in a-IGZO. Reproduced with permission from Ref. [5]. Copyright 2009 IEEE.

2.2.2 Amorphous IGZO

Most of the limited work on c-IGZO, including c-IGZO TFTs [63], was published before the first demonstration of a-IGZO TFTs [7]. Since then, interest in c-IGZO has declined owing mainly to the ease of fabrication of the amorphous phase and its attractiveness for use in the display industry. The 1:1:1 (In:Ga:Zn) cation ratio composition ($InGaZnO_4$) is the most typical composition investigated in IGZO literature. This composition exhibits an experimental crystalline band gap of ~3.6 eV [42], which is supported by first-principles calculations [38].

The complex structure of IGZO gives a much deeper perspective of the challenges faced in characterizing and improving its electronic properties. As in classical semiconductor systems, the atomic structure dictates the resulting elec-

tronic characteristics. The electronic structure of the amorphous phase often resembles the corresponding crystalline form, but with greatly deteriorated properties due to the structural disorder.

In amorphous materials, the introduction of structural disorder has profound impact on the electronic structure (see Appendix B). One of these effects is the smearing of near-band edge electronic states into the bandgap. In IGZO, this results in a reduction of the band gap, as is predicted theoretically [38] and observed experimentally [40]. However, whereas a-Si exhibits a carrier mobility reduction to ~0.1% of its crystalline value [64], a-IGZO does not with devices routinely demonstrating field-effect mobilities of ~10 cm^2/Vs (>10% of the crystalline value) [7]. Further, metastable states accessed by millisecond timescale laser annealing have demonstrated ultra-high mobilities in a-IGZO TFTs that approach the crystalline value [65].

When considering high mobility materials, amorphous structures do not often come to mind. Indeed, the low mobility exhibited by a-Si:H would seem to indicate other amorphous semiconductor platforms would lead only to incremental improvements. However, whereas a-Si exhibits a 3 order of magnitude reduction in carrier mobility compared to c-Si, IGZO only suffers a 1 order of magnitude reduction. This contrast originates from the differing bonding structures between a covalently-bonded semiconductor like silicon and the ionic metal oxide structure of semiconductors such as IGZO.

2.2.3 Electronic Structure of IGZO and the Origin of High Mobility

The disorder in an amorphous material gives rise to several electronic effects not present in a crystalline phase. Because of the added complexities of non-periodicity, carrier transport properties cannot be directly calculated by an E-k dispersion relationship (as is the case for a crystalline material), but instead must be inferred from the electron orbital structure and first-principles calculations.

The conduction and valence bands in a semiconductor fundamentally originate from the energy splitting of bonding atomic orbitals due to the Pauli exclusion principle. In a Si-Si covalent bond between two equivalent sp^3 bonding orbitals, shown in Figure 2.6a, the energy is split into a bonding (σ) orbital and and an antibonding (σ^*) orbital. In a 3D network, the bonding and antibonding states form the valence band maximum (VBM) and the conduction band maximum (CBM) respectively. Electrons are normally bound to the valence band and can access the conduction band by thermal excitation from the valence band or from dopant states. As sp^3 hybridized orbitals, both the valence band and conduction band exhibit strong orientational assymmetry—which ultimately is the root cause of the low mobility in a-Si.

In a metal oxide such as IGZO, the bonding is much more ionic in character. In this case, the ionization effectively lowers the energy level of the oxygen $2p$-orbital and increases the energy of the metal cation s-orbital, shown in Figure 2.6c. As a result, the valence band is predominantly p-orbital-like in character (directional bonding), and the conduction band is predominantly s-

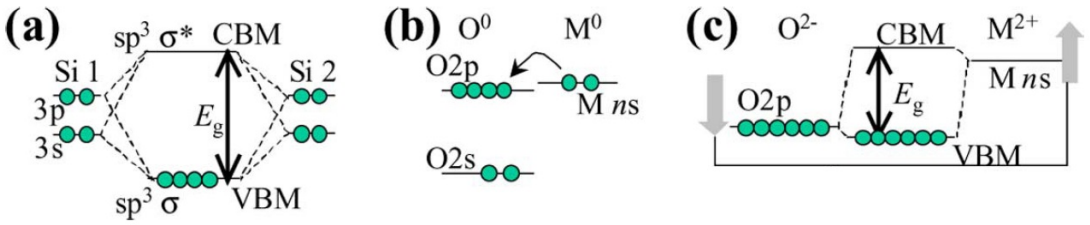

Figure 2.6: Schematic of the bandgap formation mechanisms in different semiconductor systems. (a) The VBM and CBM states in a covalently-bonded semiconductor originate from the sp^3 bonding and antibonding orbitals. In an ionic metal oxide, (b) the metal and oxygen atoms are ionized, and (c) the VBM and CBM exhibit predominantly O $2p$ and M ns character respectively. Reprinted with permission from Ref. [5]. Copyright 2009 IEEE.

orbital-like in character (spherically symmetric). This has been supported by first-principles calculations of the partial density of states [6], describing the partial contribution to states from each orbital type (s, p, d) and from each atom, shown in Figure 2.7. The relatively high electron mobilities observed in a-IGZO is derived from the nature of the conduction band.

Figure 2.8 shows the effect of disorder on the overlap of the bonding orbitals in different semiconductor systems. In covalent systems such as silicon (Figure 2.8a), which has directional bonding due to sp^3-orbital hybridization, amorphization creates strained, weak, and dangling bonds in the bond network. These defects contribute to localized and defect states and the degradation of carrier mobility relative to the crystalline phase. However in a post-transition-metal oxide semiconductor system such as IGZO (Figure 2.8b), the conduction band is composed mostly of the spherical metal cation s-orbitals. Because the overlap of these symmetric orbitals is not nearly as perturbed as in the covalent case, amorphous oxide semiconductors exhibit carrier mobilities much closer to those observed in the crystalline phase.

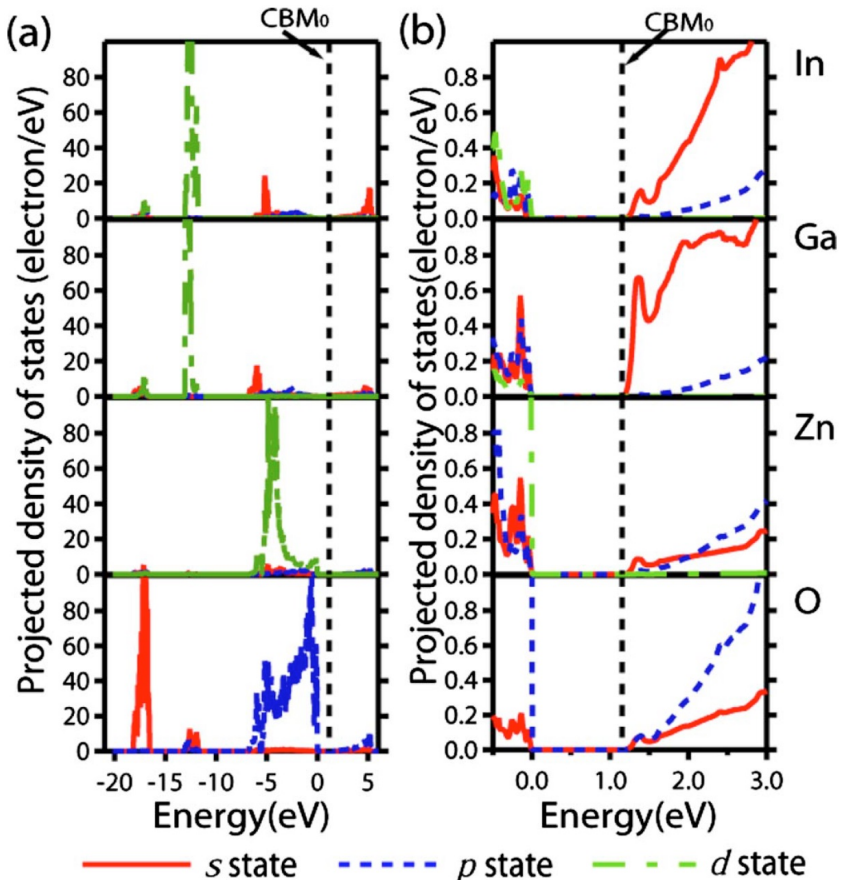

Figure 2.7: Partial density of states calculation for c-IGZO showing (a) the contribution from each orbital type (s, p, d) from each atom in the structure and (b) an enlarged view near the CBM. Reprinted with permission from [6]. Copyright 2009 AIP Publishing.

Nomura *et al.* [54] first investigated carrier transport in c-IGZO films in 2004, the same year they also demonstrated a-IGZO TFTs [7]. They observed two phenomenon in c-IGZO: (1) in films with low carrier concentrations ($<10^{17}$ cm^{-3}), Hall signals were not measurable, and the conductivity exhibited a $T^{-1/4}$-dependency; and (2) above carrier concentrations of $\sim 10^{17}$ cm^{-3}, Hall voltages became detectable and plots of conductivity vs. $T^{-1/4}$ exhibited a different slope, indicating a different carrier transport mechanism. This mechanism was consistent with variable-range hopping (VRH) transport due to localized states, observed typically in amorphous or degenerately-doped semiconductors [66].

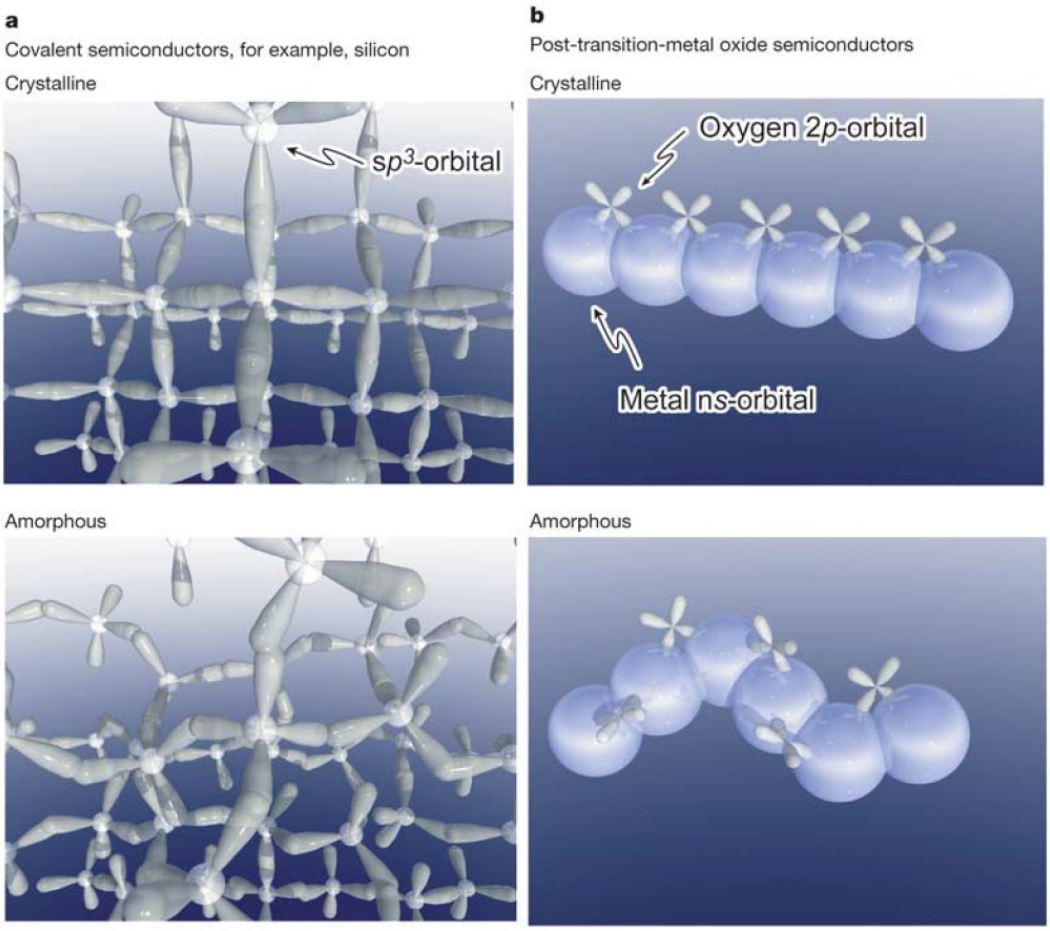

Figure 2.8: The effect of amorphization on the orbital overlap in (a) covalent systems such as silicon and (b) post-transition-metal oxides such as IGZO. Reprinted with permission from [7]. Copyright 2004 Nature Publishing Group.

They suggested a percolation conduction model in which the disorder due to the random arrangement of Ga and Zn cations in the c-IGZO lattice creates localized states—manifesting as tail states in the band gap normally attributed to an amorphous structure. When the Fermi level E_F lies below a critical threshold (either due to doping or to an applied electric field), conduction takes place via hopping between localized tail states and c-IGZO behaves essentially like an amorphous semiconductor. Above the threshold, c-IGZO behaves like a degenerately-doped conductor.

Thus, it is hypothesized that c-IGZO possesses localized tail states typical of an amorphous semiconductor. The introduction of further structural disorder by amorphization effectively increases the density of these tail states. The result is the density of states versus energy shown schematically in Figure 2.9. Even with the induced disorder and increase in localized tail states, the conduction band states near the mobility edge (denoted henceforth by the crystalline anolog CBM) exhibit a high degree of spatial percolation. This is observed in Figure 2.5d which shows the isosurface of the CBM wavefunction superimposed on the structure from Fig. 2.5c. The large spatial extent of the CBM wavefunction suggests the lessened perturbation caused by disordering in contrast with what is observed in, and expected from, covalently-bonded systems.

2.2.4 Point Defect States

As a wide band gap material requiring ~3 eV for the thermal excitation of intrinsic carriers, IGZO-based device operation must rely on the modulation of extrinsic carriers introduced by point defects (including dopants). Oxygen vacancies and hydrogen dopants are believed to be the two most commonly formed defects in a-IGZO during the deposition process, and are therefore the most frequently studied. The states created by these defects remain debated, with the majority of conclusions drawn from first-principles calculations.

Oxygen Vacancies

Oxygen vacancies are the primary native point defect studied in IGZO literature. They are readily formed during the sputter deposition process, and can be

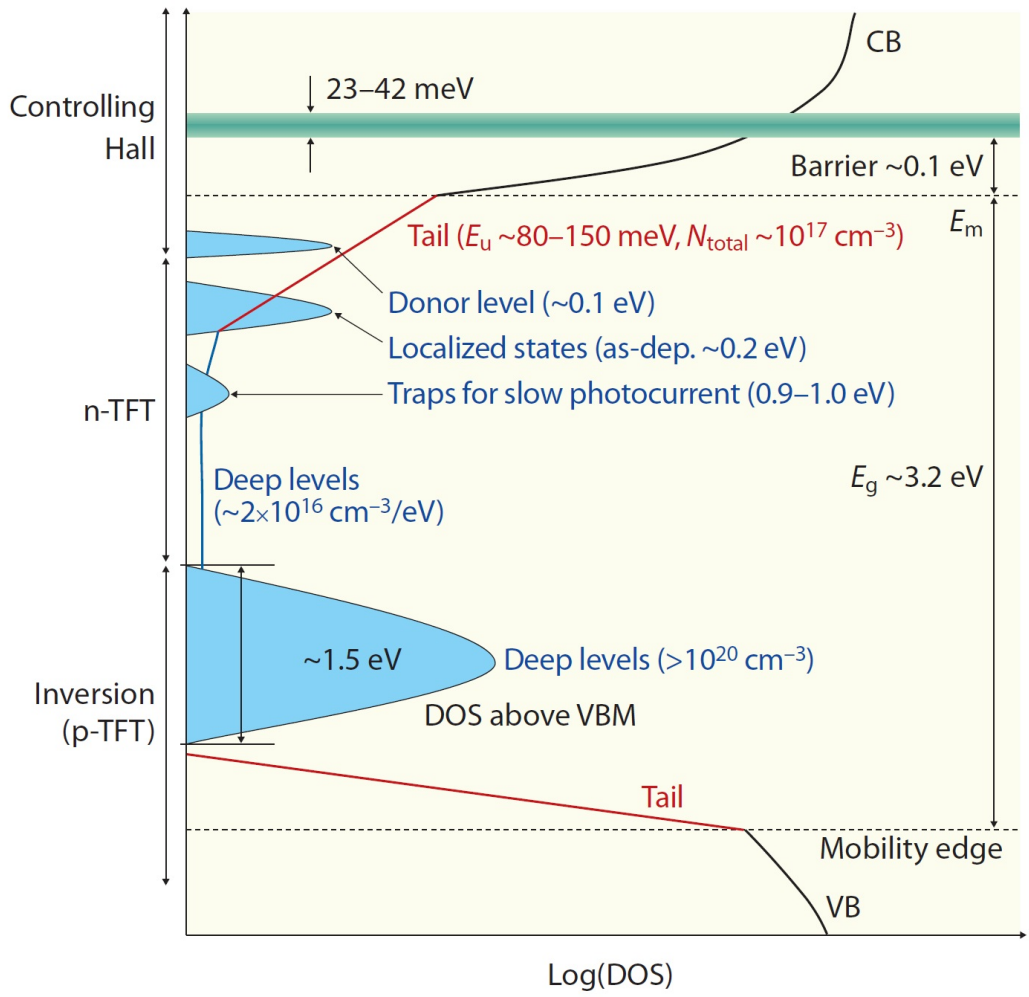

Figure 2.9: Schematic diagram of the density of states in IGZO, indicating the tail states due to structural disorder, donor level states near the conduction band minimum, a high density of deep level states near the valence band maximum, and various deep level states that act as carrier traps. Reprinted with permission from [8]. Copyright 2010 Nature Publishing Group.

controlled by fixing the oxygen partial pressure in the deposition environment or during post-deposition annealing. The formation of oxygen vacancies can be best understood by the defect formation reaction [67]:

$$O_O^x \rightleftharpoons V_O^{\cdot\cdot} + 2e'' + \frac{1}{2}\mathrm{O}_2(\mathrm{g}) \tag{2.1}$$

where O_O^x denotes the neutral state of an oxygen atom on an oxygen site, and $V_O^{\cdot\cdot}$ is a vacancy on an oxygen site with a net 2+ charge. Two electrons must be included for charge balance, and devolved oxygen gas is included for species balance. Thus, decreasing the concentration of oxygen in the deposition or annealing environment drives the reaction toward a higher concentration of oxygen vacancies.

From the simple relationship in equation 2.1, it would then follow that increasing the number of oxygen vacancies should increase the number of free electrons by a 2:1 ratio. However, this is not strictly the case, as it is also possible to form charge-defect complexes in which the electrons are essentially bound to the charged vacancy:

$$O_O^x \rightleftharpoons (V_O^{\cdot\cdot} + 2e')^x + \frac{1}{2}\mathrm{O_2(g)} \tag{2.2}$$

Thus, while the oxygen ambient during deposition or post-deposition annealing can be used to control the oxygen vacancy concentration, not all electrons associated with this reaction are "free" for conduction.

Whether an electron is free as in equation 2.1, or bound as in equation 2.2, is determined by the energetics of a particular defect. In either case, for metal oxides, the oxygen vacancy defect forms a defect state within the band gap. The location of the defect energy level relative to the CBM and VBM have been investigated using DFT. Most DFT studies concerning crystalline metal oxides (IGZO, ZnO, and Ga_2O_3) describe an oxygen vacancy as forming a deep state [6, 68–70], in which the defect state exists near the VBM and electrons are bound according to equation 2.2. However other sources on similar crystalline materials (IGZO, ZnO, and In_2O_3) report the same defects forming shallow donor states [71, 72], creating defects near the CBM and nearly free electrons accord-

ing to equation 2.1. Indeed, there is still considerable debate over the nature of these defects in c-IGZO [6, 68–72].

While the energy calculations for oxygen vacancies in crystalline IGZO are still debated, the role of oxygen vacancies have been extensively investigated in a-IGZO. In the case of a-IGZO, oxygen vacancies have been calculated to exhibit either shallow or deep characterstics depending on the local bonding structure [38, 39, 41]. While this was first reported for a-IGZO from DFT calculations, it was supported later by experimental work [43–45, 73–75]. By altering the oxygen partial during deposition or annealing, the conductivity of a-IGZO has been noted to change according to equation 2.1. This supports the case of oxygen vacancies as shallow donors: processing in an oxygen-deficient environment increases the carrier density, while processing in an oxygen-rich environment reduces the carrier density [73–75], suggesting shallow donor defects. In contrast, studies using hard X-ray photoelectron spectroscopy (HAXPES), to obtain direct measurements of deep states near the VBM, have shown a large density of electron-filled defect states within ~1 eV of the VBM several orders of magnitude higher than typical measured carrier densities. Further, annealing in an oxygen-rich environment reduces the density of these deep defects [43–45]. As such, it is believed that these states are due to oxygen vacancies that follow equation 2.2.

Based on these observations, it is generally believed that oxygen vacancies in a-IGZO can form one of two types of states: a lower concentration of shallow donor states near the CBM contributing to the conduction electron concentration and a higher concentration of deep states near the VBM containing bound electrons that do not normally contribute to conduction.

Hydrogen Doping

Hydrogen impurities have been linked to the formation of donor defect states in several oxide systems, including SnO_2 [76, 77], Ga_2O_3 [77, 78], In_2O_3 [33, 77], and ZnO [77, 79, 80]. Hydrogen is also believed to form donor states in IGZO based both on computational [6, 41, 81, 82] and experimental [81, 83, 84] evidence. Unlike other semiconductor dopant species, hydrogen concentrations are typically very difficult to control as hydrogen is always present in the background ambient of a deposition system due to poor pumping efficiencies [85] and in deposition gases as an impurity [86]. Special care is often needed to control hydrogen, including use of ultra high vacuum (UHV) systems [86] and ultra-pure gas sources [87].

Like the other defects in IGZO, the exact nature of hydrogen is not well understood. While it is considered a donor impurity, it has been noted that not all hydrogen atoms contribute carriers to conduction [81, 84], with hydrogen believed by several researchers to passivate defect states [38, 77, 81, 88–93]. However, unlike in the case of a-Si:H in which H passivates covalent dangling bonds, an analogous mechanism in this ionic solid is not clear. Hydrogen has also been linked by others to trap states [94] and long-term instability effects [83, 86, 94, 95]—effects also observed in a-Si:H.

Needless to say, the full effect of hydrogen is not fully known. It is difficult to control or track, and it is frequently invoked in the literature as the origin of any inexplicable characteristics [94, 96–99]. However, the link between hydrogen and carrier density and the defect chemistry makes it one of the most critical elements in determining the properties of IGZO transistors.

Other Deep Defect States

Whereas the absolute effect of oxygen vacancies and hydrogen impurities are still debated, their general effects have been widely accepted. In addition to these defects, which may give rise either to shallow donors contributing to conduction or deep donors that do not affect conduction, a number of other defect states have been observed or hypothesized to exist in the mid-gap. The nature of these mid-gap states remain poorly understood. Because of the inherent complexity of an amorphous quaternary system, a wide number of defect types may possibly contribute to these states, such as oxygen miscoordination [38, 100, 101], metal cation miscoordination [38], oxygen interstitials [102], zinc interstitials [103], or alternate oxygen vacancy configurations [103, 104]. Regardless of the origin of these defects, the effects of these states are felt, as they have profound impact on the long-term stability of IGZO-based devices.

2.2.5 Origin of Long-Term Instabilities

The key limitation of IGZO technology in production has been the long-term instability exhibited by IGZO-based devices. These instabilities manifest as a shift in the device turn-on voltage over time, causing a shift in switching characteristics, pixel brightness, and overall product lifetime. The effects fundamentally originate from unstable or metastable sub-gap defect states, but are exacerbated by three external stresses present during transistor operation in a display:

1. Electric Field. The electric field induced by gate bias (either positive or negative bias) provides an electrical driving force for defect relaxation.

The direction of the applied electric field determines the fundamental mechanism involved in the instability.

2. Temperature. Any elevated temperature (typically up to ~100°C in a display) gives added thermal energy to allow defect relaxation; temperature is typically regarded as an accelerant rather than a driving factor.

3. Illumination. Photons from an LCD backlight or an OLED can be absorbed by sub-gap defects to either eject electrons into the conduction band or to provide additional energy for relaxation. Illumination typically plays a much larger role in the case of negative bias than in the case of positive bias, as transistors are typically held in an off-state (negative bias) for longer than in an on-state (positive bias): ~17 ms vs. ~20 μs in TFT displays [9].

In the literature, many researchers have studied different variations and subsets of these stress effects. However, most mechanisms fall under two general categories: positive-bias temperature illumination stress (PBTIS) and negative-bias temperature illumination stress (NBTIS), shown in Figure 2.10. Other studies usually cover subsets of these two categories (i.e., NBS, NBIS, PBTS, etc.). While many mechanisms have been proposed, only the predominant ones for PBTIS and NBTIS will be discussed.

In the case of PBTIS, while the *n*-type IGZO TFT is in the on-state, majority carriers are attracted to the insulator-semiconductor interface (Fig. 2.10c). Figure 2.10a shows a schematic of the gate-insulator-semiconductor band diagram. For extended periods of positive gate bias, the electrons held at the insulator-semiconductor interface can diffuse or be injected into the gate insulator material, becoming trapped [68, 105, 106]. A trapped negative charge in the gate

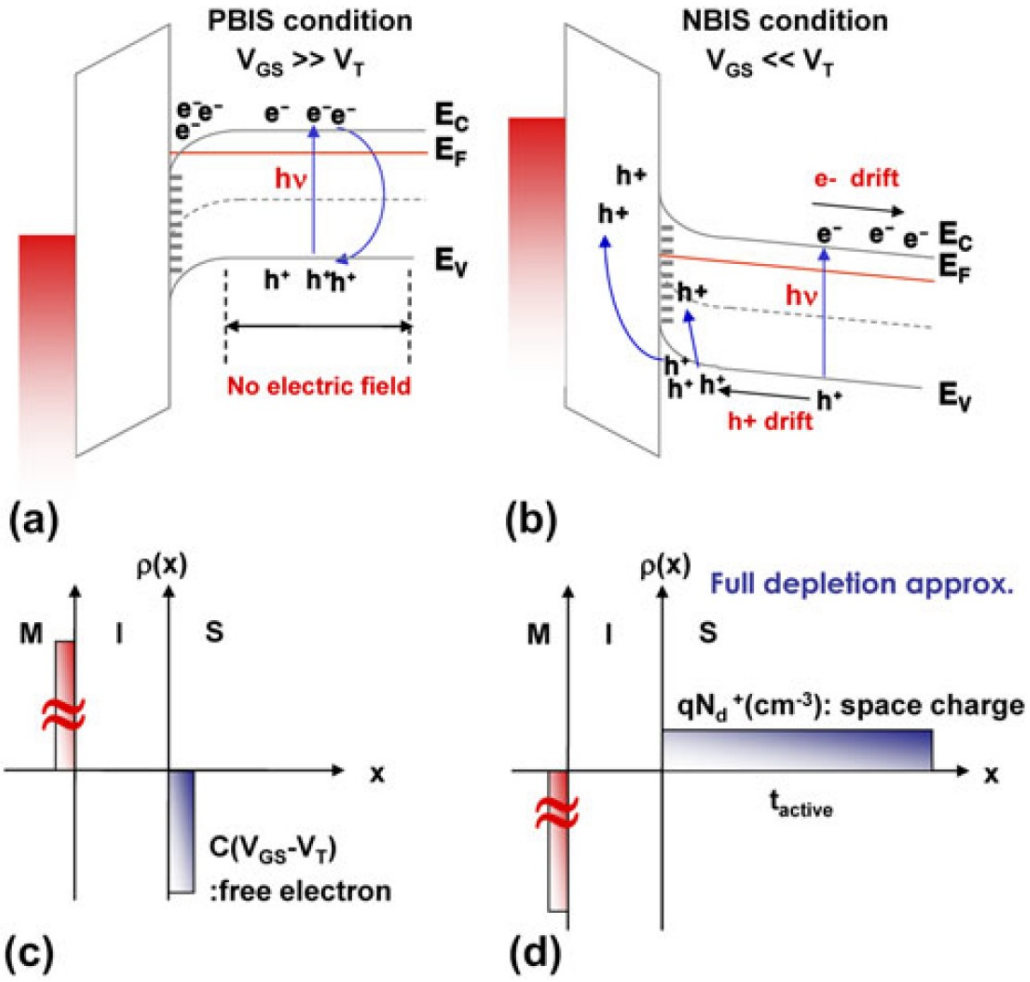

Figure 2.10: Schematic of the metal-insulator-semiconductor band structure in (a) the PBTIS case of an on-state device ($V_{GS} > V_{\text{on}}$) under positive gate bias and (b) the NBTIS case of an off-state device ($V_{GS} < V_{\text{on}}$) under negative gate bias. The associated schematic charge densities in the (c) on-state case and the (d) off-state case. Reprinted with permission from [9]. Copyright 2013 Cambridge University Press.

insulator increases the turn-on voltage of the device (an increasingly positive V_{GS} is required to induce the same negative charge density in the channel). This mechanism has been also observed in a-Si:H-based TFTs [107–109]. Electrons can also become trapped in sub-gap defect states in the IGZO films [110–112]. Further, it has been shown that illumination of the IGZO TFT during bias testing

can actually reduce the threshold shift, attributed to optically-enhanced detrapping of these carriers [68, 113–116].

The NBTIS mechanism is much more complex and is shown in Figure 2.10b. NBTIS leads to a negative shift of the turn-on voltage, and is believed to be a combination of several different mechanisms. In this case, because of the *n*-type characteristics of IGZO TFTs, a negative bias induces the formation of a positively-charged space charge region extending into the IGZO bulk (Fig. 2.10d). Any photo-generated electron-hole pairs that are created in this space charge region can separate and drift apart.

Figure 2.11 shows a schematic diagram of the three main mechanisms believed responsible for the NBTIS characteristics of an IGZO TFT. In Fig. 2.11i, photo-induced holes can become trapped in interface states or are injected into the gate insulator [116–119], decreasing the turn-on voltage (i.e., requiring a lower value of V_{GS} to induce the same negative charge density in the channel at turn-on—the opposite of the PBTIS mechanism). However, given the short expected lifetime of holes in IGZO [120] and that NBTIS effects have been observed to depend on oxygen vacancy defects, others have proposed an alternate mechanism (Fig. 2.11ii). The defect relaxation of the local coordination around oxygen vacancies (accelerated by thermal or optical effects) may energetically shift these defects from a deep-gap state to a shallow donor state, inducing a higher free electron density and a negative shift in the V_{on} [99, 121–123]. Lastly, in the case of unpassivated devices, oxygen vacancies located at the backchannel (the free IGZO surface) can provide active chemisorption sites for oxygen ions or molecules (Fig. 2.11iii). Some researchers have proposed a mechanism in which optical desorption of these species leave behind free electrons for con-

duction, thereby reducing V_{on} [20, 124, 125].

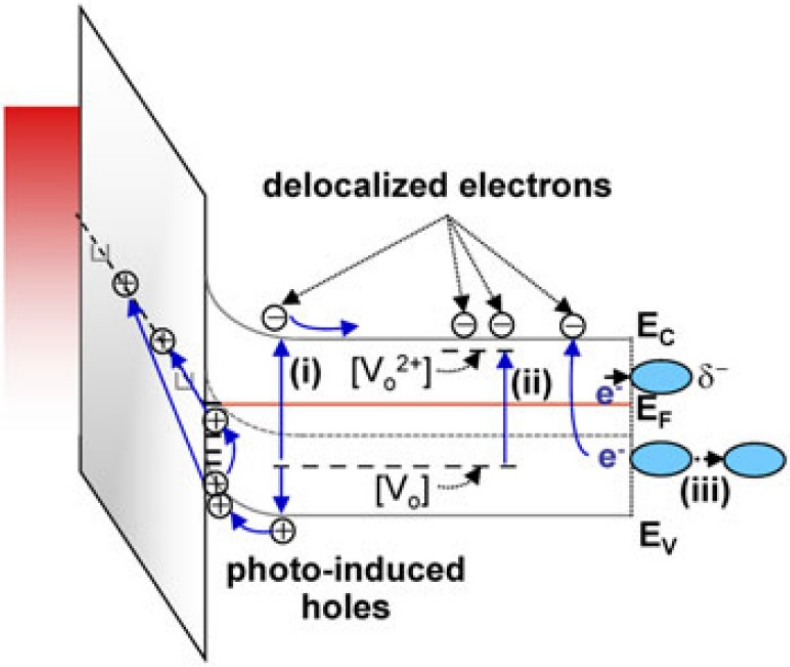

Figure 2.11: Proposed mechanisms for NBTIS degradation: (i) the trapping of photo-generated holes in interface and gate insulator states, (ii) the relaxation of deep oxygen vacancy defects into shallow defects that contribute free carriers to the conduction band, and (iii) the desorption of oxygen species from backchannel states. Reprinted with permission from [9]. Copyright 2013 Cambridge University Press.

2.2.6 Methods for Improving Stability

A wide variety of techniques have been investigated to reduce the issue of bias stability in IGZO TFTs. While some have focused on device geometry and processing techniques [126–129], or the use of dual active layer structures [120, 130–133], to circumvent the effects of bias instability, most have focused on addressing the fundamental source of the instability: the IGZO sub-gap defect states.

A variety of different doping schemes have been attempted to reduce the

electronic defect density, including the use of hydrogen [89], fluorine [134], magnesium [135], nitrogen [136], and aluminum [137] among many other species. However, these studies remain an empirical endeavor as the doping and defect compensation mechanisms of these impurities are poorly understood. Since the majority of the sub-gap states in a-IGZO linked to threshold instability originate from the disorder of the amorphous structure, other efforts have focused on the reduction of these states by crystallization and microstructure manipulation [138–141].

While full or partial crystallization of IGZO is an attractive solution, several challenges must be addressed before large-scale commercial implementation can be achieved. Most studies on crystalline IGZO involve the annealing of a-IGZO films at temperatures >600°C [138–140], too high for commercial processing on glass substrates. More recently, a textured nanocrystalline microstructure formed during the deposition process, known as c-axis aligned crystalline (CAAC) IGZO, has been demonstrated at typical deposition temperatures of ~300°C [13, 141, 142] and as low as room temperature [143].

2.3 Crystalline IGZO Films

As was the case with the advent of LTPS, after almost a decade of limited work on crystalline IGZO, attention has now shifted back toward the potential use of the crystalline phase in display applications. However, unlike LTPS, the major impetus for this work has been the reduction of defect states and not the incremental improvement of carrier mobility. This section discusses several breakthroughs in crystalline IGZO, the challenges that remain, and paths forward to

understanding and successful implementation of crystalline IGZO in these applications. Understanding this crystalline variation of IGZO forms the central thesis of the current work.

2.3.1 CAAC IGZO

In 2012, Shunpei Yamazaki at the Semiconductor Energy Laboratory (SEL) in Japan demonstrated a thin film microstructure of IGZO not previously reported in IGZO literature [142]. This material, termed c-axis aligned crystalline (CAAC) IGZO, is essentially a nanocrystalline (~2–5 nm domain size) film that is textured such that the crystallographic c axis is preferrentially oriented perpendicular to the substrate, as shown from initial reports in Figure 2.12. While novel in the IGZO community, this microstructure has also been observed in other oxide systems such as ZnO sputter deposited under similar conditions [32, 144, 145]. Regardless, this material holds great potential as an active channel layer material for high-performance display TFTs.

TFTs fabricated from CAAC IGZO have exhibited many improved electronic characteristics [146]. Most importantly, devices were reported to have an enhanced stability against threshold voltage shifts attributed to the sharp reduction of the density of sub-gap defect states by 3–4 orders of magnitude (Figure 2.13). CAAC IGZO devices also exhibit extremely low leakage currents, estimated to be below 10^{-24} A/μm at room temperature [87]. While CAAC IGZO TFTs exhibit carrier mobilities similar to a-IGZO TFTs (5–10 cm^2/Vs), they do not seem to suffer from grain boundary effects and exhibit large-area uniformity atypical for a crystalline film [142].

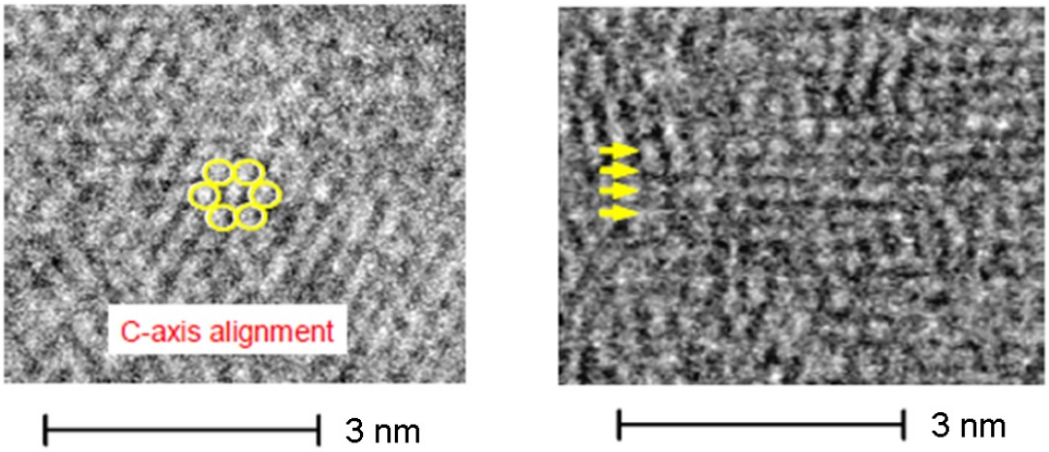

Figure 2.12: Plan-view (left) and cross-section (right) HRTEM images of CAAC IGZO first reported by SEL identifying apparent 6-fold symmetry and lattice plane formation. Reprinted with permission from Ref. [10]. Copyright 2013 IEEE.

Still, CAAC IGZO remains a somewhat controversial topic. The first CAAC IGZO reports did not explicity describe deposition conditions, leaving some to doubt its existence with reports considered merely a marketing ploy [147]. These suspicions were later alleviated by indepenently published reports from Cornell University [13]. While its existence is now widely accepted, the formation and growth mechanism of CAAC IGZO films is still debated. While the work at Cornell supports a classical nucleation and growth model moderated by the sputter deposition environment, Yamazaki holds that CAAC IGZO is a novel crystalline morphology formed via non-classical mechanisms enabled by a sputter deposition process. Other hypotheses for CAAC formation have also been suggested [148], which are discussed in greater detail in Chapter 4.

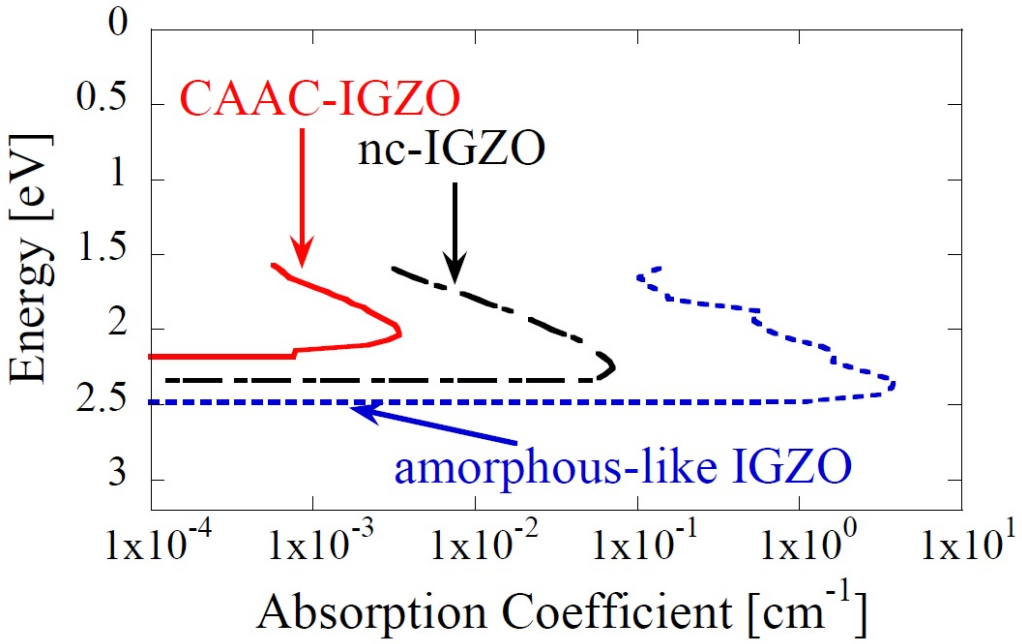

Figure 2.13: A comparison of measured absoption coefficient (linked to density of states) in a-IGZO, nanocrystalline (nc) IGZO, and CAAC IGZO. Reprinted with permission from Ref. [11]. Copyright 2013 John Wiley and Sons.

2.3.2 Polycrystalline IGZO

Though the novelty of CAAC IGZO is linked to strong texturing and small grain size, CAAC can been seen as an individual point in thin film microstructure space.[2] It is, in some sense, more useful to consider CAAC IGZO as a specific class of polycrystalline IGZO. Zhu *et al.* [150–152] have demonstrated access to a spectrum of RF sputter-deposited IGZO microstructures spanning a-IGZO, CAAC IGZO, and randomly-oriented polycrystalline IGZO by tuning deposition conditions. This seems to suggest more universal formation characteristics governing the formation of these structures.

While the formation mechanism of CAAC IGZO is not currently well-

[2]Thornton [149] gives an excellent overview of the microstructure space accessible using sputter deposition.

understood, it is prudent to note that none of the crystalline IGZO phases are well understood. Studies on the equilibrium IGZO structure as a function of composition and—to some extent—temperature exist, but very little is known regarding the crystallization kinetics and energetics. However, nearly all of these phases have been formed on time and temperature scales far exceeding those compatible with display substrates.

Millisecond timescale laser annealing opens a brand new avenue for annealing of IGZO. Although temperatures can far exceed those typically acceptable (>1000 °C), the short timescales limit potential glass compaction in display substrates. The potential for annealing on this timescale was first noted by Chung *et al.* [65] who demonstrated metastable behavior in a-IGZO devices using this method. Further, Bell *et al.* have demonstrated the use of laser annealing to access a wide range of the temperature and time phase space to explore a variety of material properties [12], including the formation of metastable phases. In addition to easier access to crystalline film morphologes in TFTs, this technique also provides pathways for studying crystallization kinetics and metastable phase formation in IGZO, as will be discussed in Chapter 6.

CHAPTER 3

EXPERIMENTAL METHODS

3.1 Sputter Deposition of IGZO Films

Sputter deposition is a physical vapor deposition process that has several benefits over other techniques, including both simple source material requirements and resulting film uniformity and conformity. Unlike evaporative processes, it is not necessary to reach the melting or sublimation temperature of the material enabling deposition of refractory films. Other techniques, such as chemical vapor deposition, require exotic and potentially hazardous precursors along with typically elevated substrate temperatures. In contrast, sputter deposition uses the desired compound (or a pressed mixture of compounds) as the source material and films can be readily deposited on room temperature substrates.

An additional key advantage of sputtering is that the resulting film stoichiometry can be easily controlled. For an alloy or a compound, the resulting film stoichiometry is nearly the same as the target stoichiometry after an initial transient period. Fine control of the stoichiometry of compound films (typically oxides and nitrides) can also be achived by the flow of reactive gases into the sputter deposition environment.

This section presents a description of the sputter technique used to deposit IGZO films used in this study. An overview of the sputtering process is first reviewed. Next, the key deposition parameters used to control film properties are identified, and the parameter space explored in this work is presented. Lastly, co-sputtering from two targets simultaneously to create composition gradients

in deposited films is discussed.

3.1.1 Sputtering Process

In this study, IGZO films were deposited using reactive RF magnetron sputtering. This section provides an overview of several variations of sputtering processes, from basic DC sputering to the additional effects of magnetron, RF, and reactive sputtering environments.

DC Sputtering

The simplest picture of sputter deposition is shown schematically in Figure 3.1, depicting the controlled removal of material from source material (the target) and deposition onto a substrate. A vacuum chamber is filled with a low pressure (typically a few mTorr to a few Torr) sputtering gas ambient (typically Ar) and a bias is applied between the target (cathode) and the substrate (anode).[1]

The sputtering process can be summarized into three general steps:

1. The applied electric field ionizes Ar atoms to create a plasma.
2. Ar^+ ions are accelerated onto the negatively-biased target, ejecting (sputtering) atoms from the target.
3. Ejected neutral atoms (and some ions) transit the gap and are collected on the substrate.

[1] In the simple schematic shown in Figure 3.1, the substrate is the anode. However, in the deposition system used in this study, the grounded chamber walls are constructed as the anode, and the substrate is electrically floating.

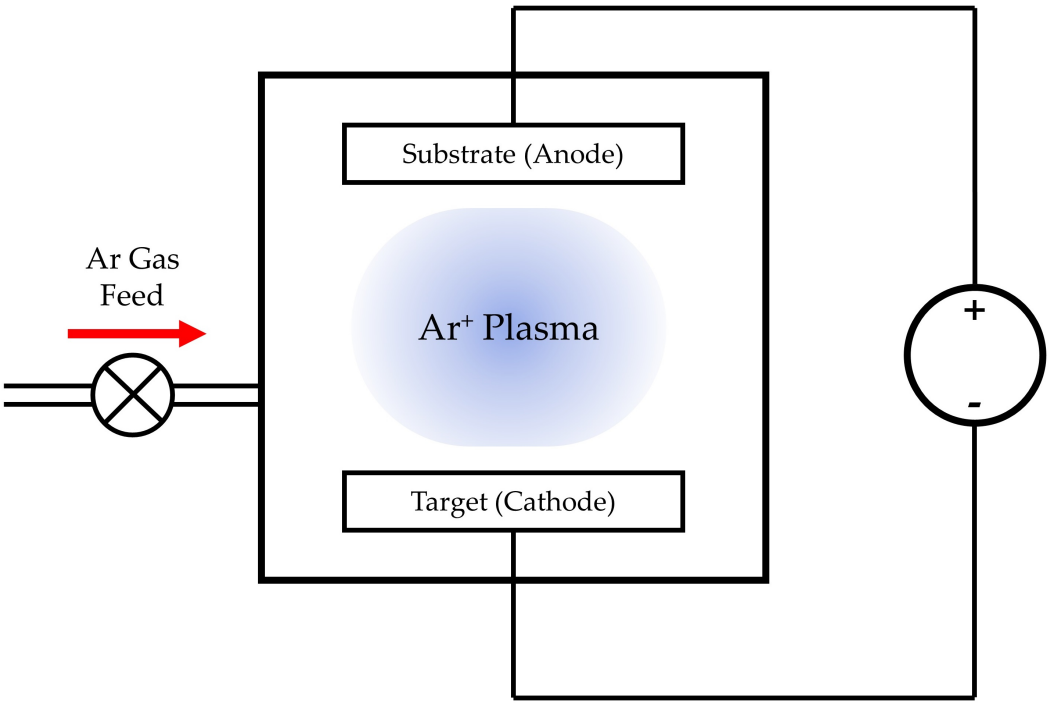

Figure 3.1: A schematic of a basic DC sputter system. The electric field ionizes the Ar gas to create a plasma. These positive Ar^+ ions are accelerated into the target, resulting in the ejection of atoms from the target material. These ejected atoms condense on the substrate.

Ionization of the Ar gas in the sputter chamber creates Ar^+ ions and free electrons, with both species accelerated by the electric field: the Ar^+ ions toward the negatively-biased target and the electrons toward the anode. Accelerated electrons can collide with neutral gas species, either creating additional ion-electron pairs or neutralizing other ionized gas species; this recombination will emit light ("glow discharge").

Atoms are ejected from the target by momentum transfer from the Ar^+ to the atoms in the target through a collision-recoil process [153, 154], as shown in Figure 3.2. A distribution of species are ejected from the surface, with the vast majority being single neutral atoms from the target. While ejection of large clusters (2 or more atoms) is possible, the probability decreases exponentially

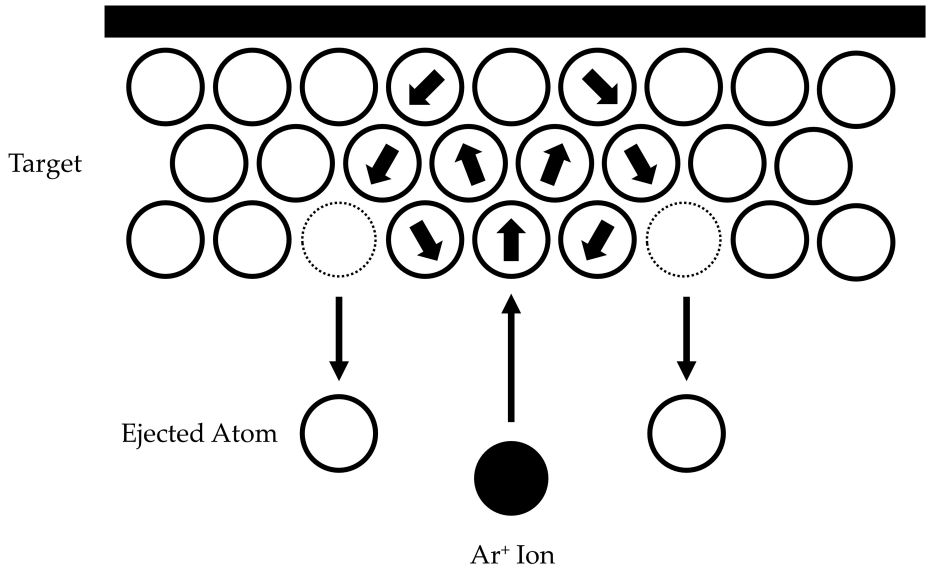

Figure 3.2: Momentum transfer model of the sputtering process.

with size [155]. Thus, single-atom ejection is typically assumed and accepted.

Magnetron Sputtering

In addition to the electric field applied between the anode and the cathode, an applied magnetic field can also be used to improve the efficiency of the deposition system. This is usually achieved by the placement of magnets behind the sputter target. This construction with superimposed fields has two benefits: an increased ionization efficiency and the confinement of plasma electrons near the surface of the target. This confinement results in the characteristic formation of grooves, or "racetracks" in magnetron-sputtered targets [154].

RF Sputtering

Upon collision with the target, an Ar^+ atom is normally neutralized by electron transfer from the target electrode. Thus, the DC sputter technique generally requires a conductive target material. In the case of an insulating target, in which the depleted electron density near the target surface cannot be replenished, a net positive charge would accumulate near the target surface, resulting in an increasing repulsion of Ar^+ ions and a decreasing sputter yield.

RF sputtering compensates for this effect by superimposing an AC bias (typically 13.56 MHz) with a relatively small DC bias. While the applied voltage is negative, sputtering proceeds as in the DC case, and a positive charge is built up on the surface of the target. After each deposition cycle, the applied voltage polarity is reversed, accelerating electrons from the plasma into the target to neutralize the surface. While this results in an overall reduction in deposition rate compared to DC sputtering for a conductive target, it enables the sputter deposition of insulating materials that would be otherwise incompatible with DC sputtering.

Reactive Sputtering

In some cases, it may be desirable to deposit various compounds, such as nitrides or oxides. Reactive sputtering involves sputtering a chemically reactive target material in the presence of a N_2 or O_2 ambient, resulting in such a compound film. This is typically used to fabricate oxide and nitride films from metal targets, and can be preferrable to sputtering from a compound target for several reasons. Metal targets are typically less expensive, easier to obtain in high pu-

rity, easier to work with, and the resulting film stoichiometry can be precisely controlled by the partial pressure of reactive gas. Reactive sputtering can be performed with either DC or RF sputtering. However, as reaction products can form and accumulate on the surface of the target, RF sputtering is often preferred [154].

In some cases, even sputtering from a compound target can benefit from a reactive gas environment. For example, sputtering from a stoichiometric oxide target in pure Ar can result in an oxygen-deficient (or oxygen vacancy-rich) film. Tuning the partial pressure of O_2 gas in the reactive sputtering environment then provides control over the resulting concentration of oxygen vacancies in the deposited film.

3.1.2 Deposition Parameter Space

Several key parameters are used to control the resulting film composition, microstructure, electronic properties, and deposition rate during the sputter deposition of IGZO films. These factors are controlled primarily by target composition, substrate temperature, oxygen partial pressure, and target RF power.[2] However, in addition to these primary effects, several non-intuitive secondary effects of these deposition parameters are also present. This section provides an overview of each of these parameters and potential sources of secondary effects, with a much more detailed discussion in Chapter 4. Lastly, a description of the parameter space explored in this work is discussed.

[2]Deposition pressure and, to a lesser extent, gas flow rate can also impact these film properties. To eliminate variation due to these effects, the pressure and total gas flow were maintained at 5 mTorr and 10 sccm in this work.

Deposition System Overview

Figure 3.3 schematically shows the sputter system used in this study. The system is a load-locked chamber with a base pressure of 10^{-7} Torr (turbomolecular pumped). Base pressure gas species are monitored using a residual gas analyzer (RGA) (Figure 3.4a). This system is also equipped with a liquid nitrogen cold trap, which can further reduce the partial pressure of H_2O (which dominates the pressure at high vacuum) by one order of magnitude (not used in this work).

Substrates are loaded face-down on an electrically floating holder that is typically rotated during deposition. The substrate holder can be radiatively heated (between room temperature and 400°C using halogen lamps located behind a quartz window above the substrate. The substrate temperature is actively monitored *in situ* using a calibrated pyrometer located below the chamber and viewing the substrate through a ZnSe viewport (Figure 3.4b).

Target Composition

The composition of a deposited film is impacted most strongly by the composition of the target and, to first-order, the deposited film composition is the same as the target composition. However, atoms ejected from the target can be scattered in the deposition gas, reducing the effective flux of individual atomic species to the substrate. This scattering effect is greater for lighter elements. As a result, an IGZO film is typically indium-rich and oxygen-deficient relative to the composition of the target in the absence of additional oxygen in the sputter gas.[3]

[3]Approximating the deposition gas as pure Ar at room temperature, for a deposition pressure of 5 mTorr, the mean free path is ~100 cm. Given the throw distance (target-to-substrate

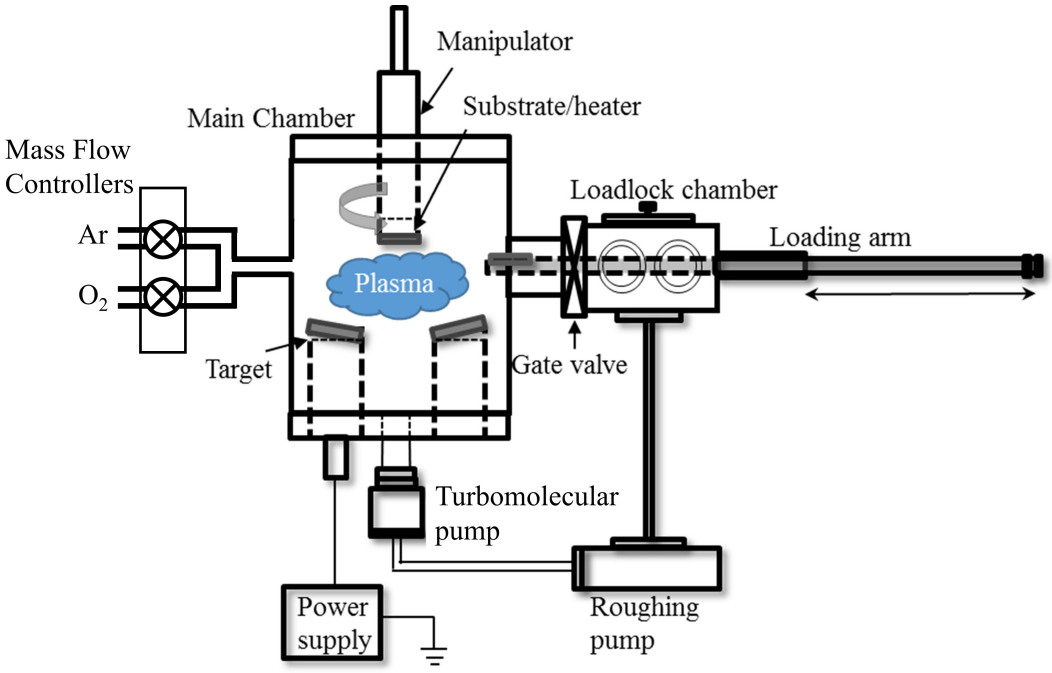

Figure 3.3: A schematic diagram of the sputter deposition chamber used in this study.

This study used IGZO targets with 1:1:1 (Kurt J. Lesker Company) and 2:2:1 (AJA International) In:Ga:Zn cation ratios.[4] In general, films deposited with high-In (low-Zn) exhibit higher carrier mobility, while films deposited with high-Zn (low-In) more readily formed textured crystalline as-deposited films.

Substrate Temperature

Substrate heating during deposition can be used to control the film microstructure. *In situ* heating of IGZO films with compositions that normally form amorphous as-deposited structures at room temperature can lead to densification

distance) of ~15 cm for the deposition system used in this study, this effect is minimal, but observable.

[4]It is common in IGZO literature to refer to either the In:Ga:Zn cation ratios (1:1:1 and 2:2:1) or the In_2O_3:Ga_2O_3:ZnO oxide ratios (1:1:2 and 1:1:1). To avoid confusion, only cation ratios will be used here.

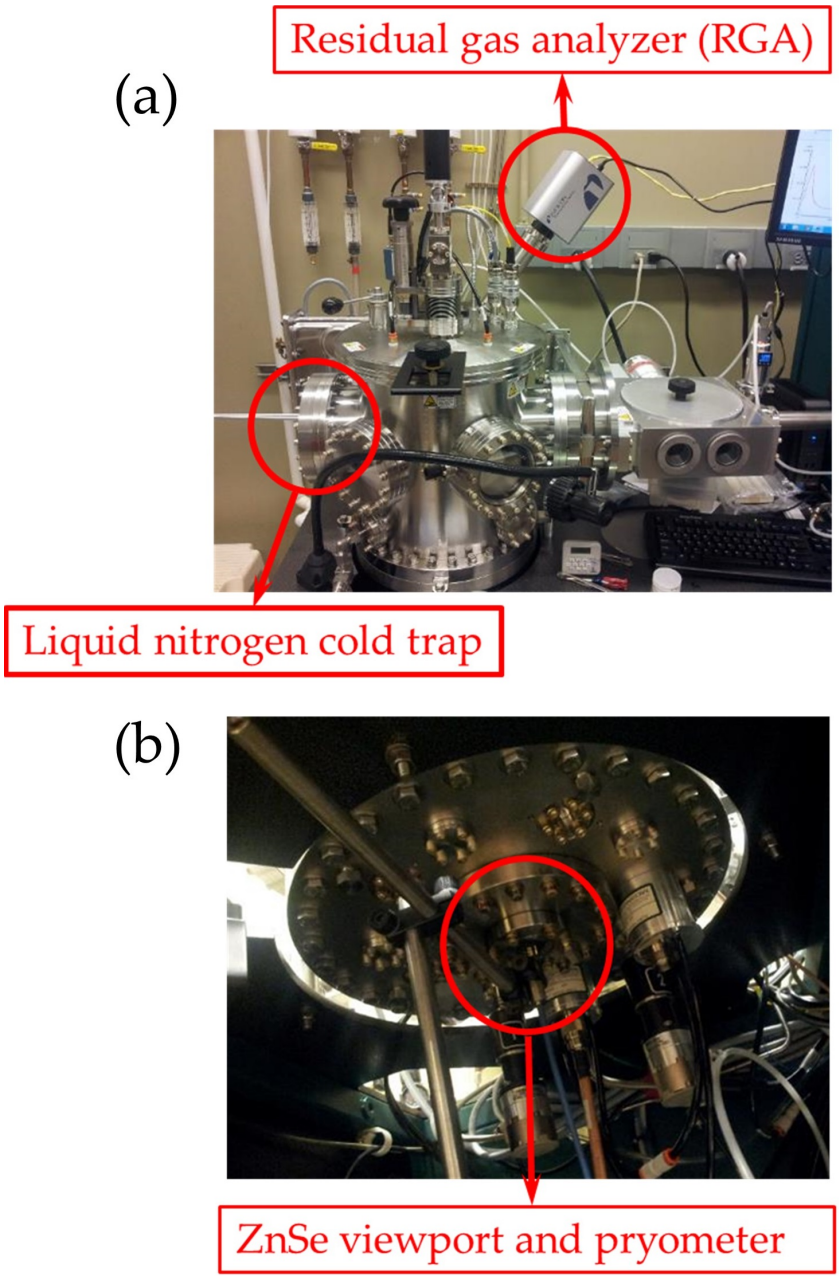

Figure 3.4: (a) The sputter system, indicating the residual gas analyzer (RGA) and the liquid nitrogen cold trap (not used in this study). (b) The bottom of the sputter system, showing the orientation of the substrate pyrometer through a ZnSe viewport.

and, in some cases, crystallization. However, elevated temperatures can also lead to the preferrential desorption of low-vapor pressure materials and stoichiometry shifts in the as-deposited films, as shown in Figure 3.5. IGZO films heated during deposition are often Zn-deficient, with the magnitude of the deficiency increasing with substrate temperature. In contrast, Ga and In, with low vapor pressures, are relatively unaffected by substrate temperatures.

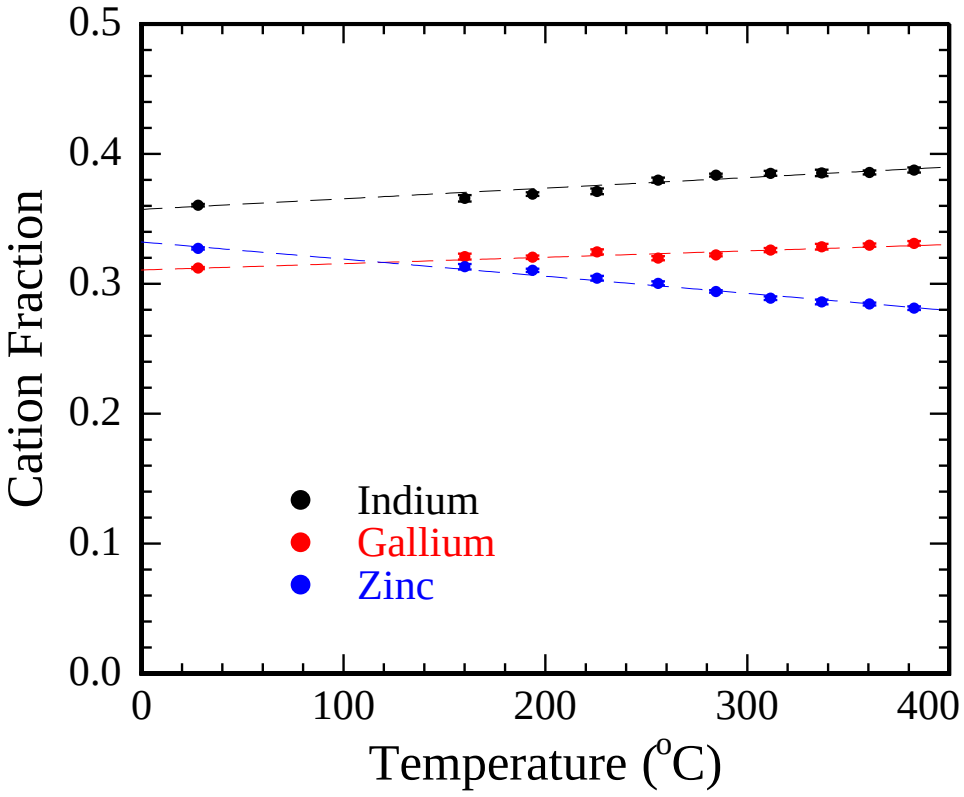

Figure 3.5: Measured cation fractions in IGZO films as a function of substrate temperature. Films were sputtered from a 1:1:1 In:Ga:Zn IGZO target using 190 W RF in 10% O_2. With increasing substrate temperature, films become increasingly deficient in Zn (higher vapor pressure) relative to In and Ga.

In this work, substrate heating was achieved using radiative heating from halogen lamps through a quartz window behind a rotating substrate holder. Lamp intensity, and hence the substrate temperature, were controlled via a

thermocouple feedback loop. Because the substrate is rotated during deposition, the controller thermocouple contacts and measures the temperature of the quartz window located between the halogen bulbs and the substrate holder. As a result, while the heater provides consistent and uniform substrate heating for a given substrate material, the thermocouple reading for the heater controller (the "set point" temperature) does not correspond to the actual temperature of the substrate. In addition, due to the nature of the radiative heating process and differences in thermal contact beween different substrate materials, the final substrate temperature was found to be material sensitive.

To ensure quantitative temperature control, substrate temperature calibrations were completed for three substrate materials: silicon, Corning® Lotus™ glass, and Corning® Eagle XG® glass. In addition, each calibration was conducted both with and without a "dummy" spacer Si wafer (placed between the substrate and the substrate holder, as shown in Figure 3.6 to emulate the set-up used for wafer experiments). Actual surface temperatures as a function of set point temperature were measured (following temperature stabilization) by a K-type thermocouple attached to each sample surface. Six calibration curves (Figure 3.7) were used to calibrate a secondary pyrometer for *in situ* measurements of actual rotating substrates. We believe these calibrations provide temperature accuracies of ±10 K.

Oxygen Partial Pressure

As discussed in the context of reactive sputtering, the partial pressure of oxygen in the ambient sputter gas plays a significant role on oxygen stoichiometry in as-deposited films. Since films deposited in this work were sputtered from oxide

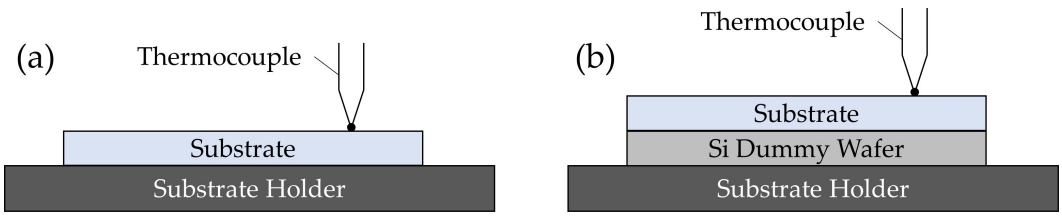

Figure 3.6: Substrate configurations for calibration: (a) without a dummy wafer, with the substrate fixed directly to the substrate holder; (b) with a dummy wafer spacer between the substrate holder and the substrate.

targets, off-stoichometry is manifested as oxygen vacancies, which yield films with high conductivity. For a fixed total gas flow rate of 10 sccm, changing the O_2 fraction (O_2/(Ar+O_2)) provides control of the oxygen vacancy concentration and consequently the as-deposited conductivity of the IGZO films.

Increasing the O_2 fraction also causes several secondary effects. Increasing O_2 fraction decreases the deposition rate, in part due to the decreasing average mass of bombarding ions and reactions of O_2 with the surface of the oxide target [156, 157]. However, changing the O_2 fraction can also alter the composition and the microstructure of as-deposited films. Figure 3.8 shows this effect on film composition over a wide range of O_2 fractions in the sputter ambient. These effects will be discussed in greater detail in Chapter 4.

Target RF Power

RF power applied to the sputter target is the primary control for the film deposition rate, with the rate approximately proportional to the RF power. The maximum power used in this study was 200 W, corresponding to a deposition rate of ~3 nm/min, with lower deposition power used for TFT fabrication and composition gradients (discussed in the next section). For comparison between

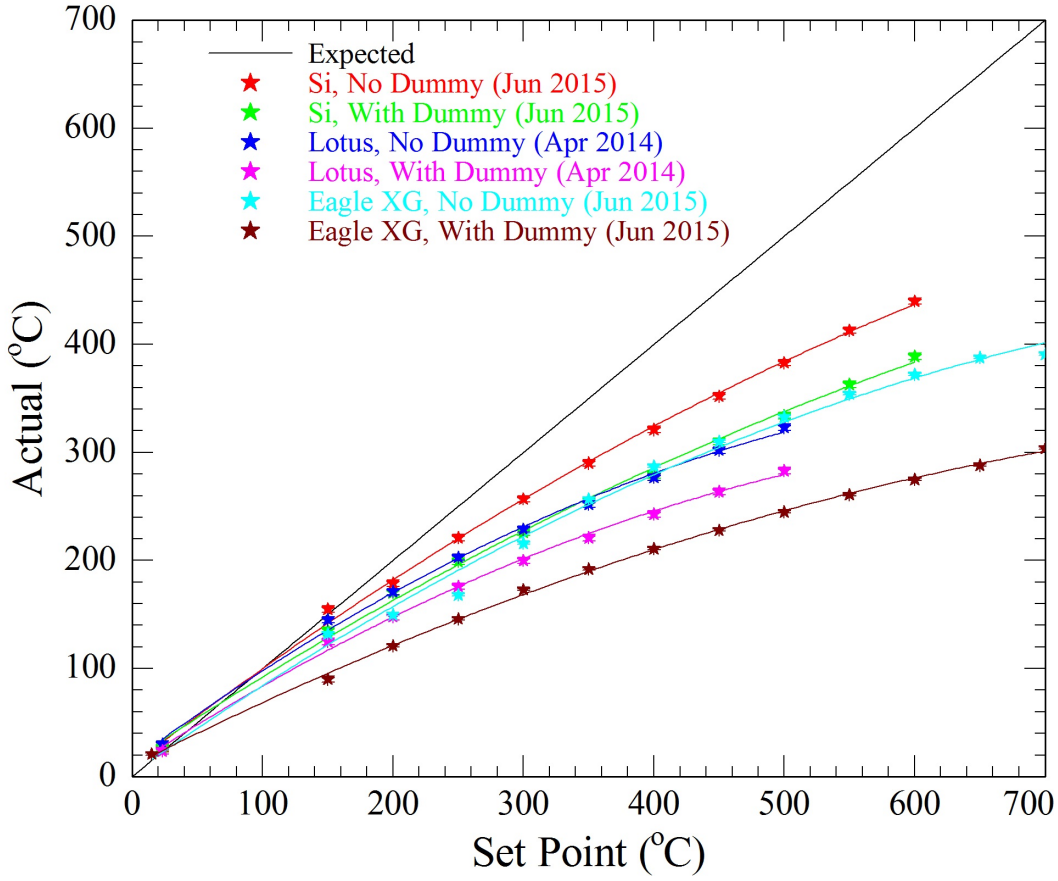

Figure 3.7: Calibration curves for six substrate configurations, showing the actual substrate temperature for each configuration as a function of the set point temperature. Each dataset was fit with a simple parabolic function, both as a guide to the eye and as a method of interpolation for processing. The solid black "Expected" line indicates a hypothetical 1-to-1 correspondence between the actual temperature and the set point temperature.

deposition systems, it is typical to compare the power density (W/cm^2) on the exposed target area. For a 200 W RF power applied to the 2 in. diameter (20 cm^2 area) targets used in this work, this corresponds to a power density of about 10 W/cm^2.

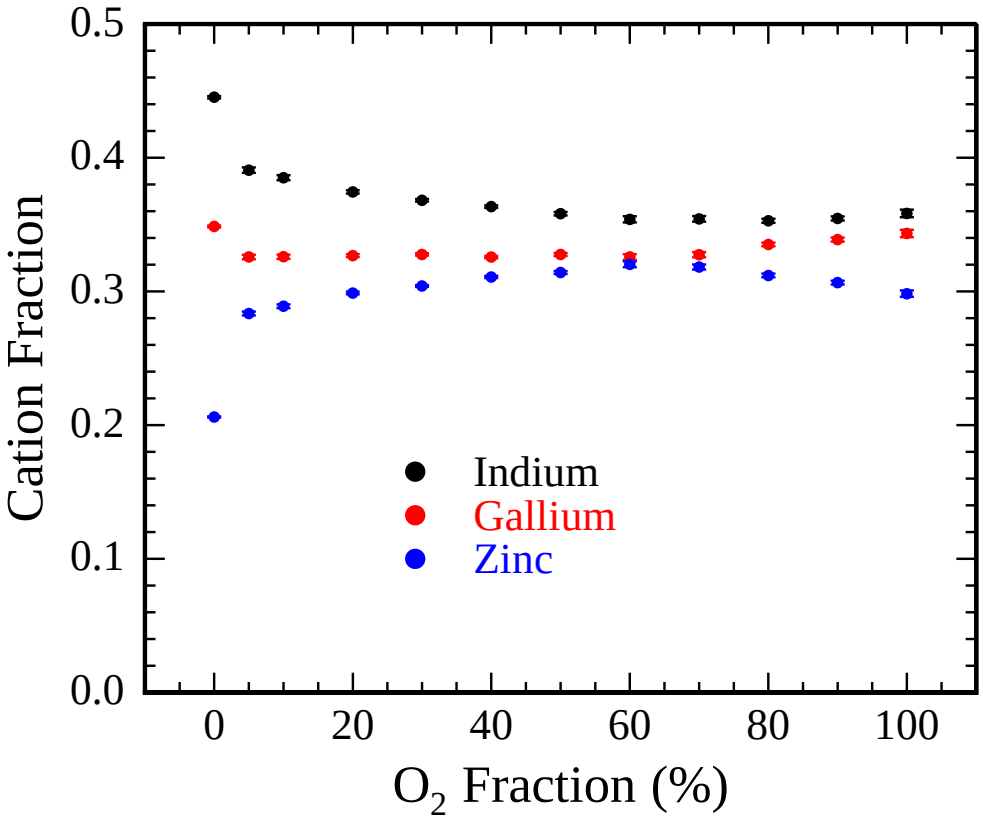

Figure 3.8: Measured cation fractions in IGZO films as a function of O_2 fraction. Films were sputtered from a 1:1:1 In:Ga:Zn IGZO target using 190 W RF with a substrate temperature of 310°C.

3.1.3 Deposition of Films with Composition Gradients

Films can be sputtered from multiple targets simultaneously (co-sputtering) to create an alloy of two or more alloy materials. The total atomic flux during deposition is, to a good approximation, the weighted atomic flux from each target. Thus, both the deposition rate and the resulting film stoichiometry are controlled by the relative power applied to each target, and homogeneous films can be achieved by rotating the sample during deposition. Composition gradients (or "combinatorial spreads") in as-deposited films can be achieved by

co-sputtering without sample rotation.

3.1.4 Parameters Used in This Work

General Parameters

In this work, all film samples were deposited on p^{++} Si (100) wafers (100 mm diameter, 0.01–0.02 Ω-cm) thermally oxidized at 1000°C for ~30 minutes in dry O_2 and 3% HCl to from ~100 nm thermal SiO_2. IGZO films were reactively sputtered using the load-locked RF magnetron system in a 5 mTorr environment containing Ar (99.999% purity, 0.211 ppm water) and O_2 (99.944% purity, 0.165 ppm water).

CAAC IGZO Formation

The following parameters are specific to Chapters 4 and 5 for CAAC IGZO films and devices. O_2 fractions were varied between 0% and 100%. Targets of sintered polycrystalline 1:1:1 In:Ga:Zn IGZO (Kurt J. Lesker, 99.999% purity) and 2:2:1 In:Ga:Zn IGZO (AJA International, 99.99% purity) were sputtered with up to 200 W of RF power to achieve a deposition rate of up to 3 nm/min to give approximately 100 nm films. The substrates, electrically floating, were heated radiatively with temperatures measured *in situ* using a calibrated pyrometer. These studies examined elevated substrate temperatures ranging from 160°C to 380°C in approximately 25°C increments, and were compared to amorphous films deposited at nominally room temperature. All substrates were rotated during deposition to ensure film uniformity at 40 RPM. Measured uniformity

was typically <5% over a 100 mm wafer.

Device Study

In addition to the parameters used for CAAC IGZO formation listed above, substrates used for device fabrication were cleaned prior to IGZO deposition. After cleaning with solvents, the substrates were then cleaned using an O_2 plasma (5 minutes, 40 W RF, ~4.5 inch diameter substrate holder) to remove any residual organics from the surface of the substrates. Following O_2 plasma cleaning, the O_2 gas was pumped out over a 5 minute period at high vacuum. Approximately 50 nm of IGZO was deposited over a 19 minute period (~2.63 nm/min) using 120 W of RF power.

Laser Annealing of Samples with Composition Gradients

The following parameters are specific to Chapter 6 for laser annealed samples with composition gradients. Substrate temperatures were maintained at nominally room temperature, and the O_2 fraction in the sputter gas was fixed at 10% by volume. Targets of sintered polycrystalline ZnO (Kurt J. Lesker Company) and 2:2:1 In:Ga:Zn IGZO (AJA International) were co-sputtered with 60–200 W RF power without sample rotation to achieve various composition gradients.

3.2 IGZO Thin Film Composition Characterization

The electronic properties of the IGZO films are, to a large extent, determined by the composition of the films. To a fair approximation, the composition of the

sputtered IGZO films can be estimated by the composition of the sputter targets. However, due to several secondary effects (Figures 3.5 and 3.8), deviation can be significant. Accurate composition characterization is essential to quantitatively study of IGZO thin films, as properties such as mobility are strong functions of the composition.

Energy dispersive X-ray spectroscopy (EDS), using a scanning electron microscope (SEM), is an attractive characterization technique to determine cation ratios due to its speed, simplicity, and non-destructive nature. An average measurement takes only a few minutes and can be performed directly on a thin film sample. However, most EDS characterization packages are calibrated for bulk samples (several μm in thickness) to account for the effects of electron-matter interactions that do not apply to thin film samples, leading to systematic measurement errors.

In contrast, other powerful techniques to determine composition, such as inductively-coupled plasma optical emission spectroscopy (ICP-OES). ICP-OES can provide absolute and precise measurements of cation concentrations in oxide films, but has its own drawbacks. For example, sample preparation and analysis can take several hours with film samples that must be dissolved in HCl and diluted to enable measurement.

This section discusses a technique to remove the systematic error from EDS measurements of IGZO films using calibrations based on ICP-OES measurements. By characterizing a relatively small number of IGZO samples using ICP-OES, a calibration curve was developed to extract cation ratios from EDS measurements with atomic percent level precision and accuracy. First, the underlying thin film assumptions will be reviewed in the context of EDS theory.

Then, a more detailed description of the ICP-OES measurements is provided. Lastly, the development and application of calibration curves is discussed.

3.2.1 Energy Dispersive X-ray Spectroscopy (EDS) of Thin Films

The bombardment of materials with an electron beam (for example, in a scanning electron microscope environment), causes the emission of X-rays from two sources: *Bremsstrahlung* radiation and characteristic radiation. *Bremsstrahlung* (or braking) radiation is caused by the deceleration of the primary electron inside the sample material, which produces a continuous background X-ray signal. This background signal must be accounted for when performing composition analysis using EDS, often by a simple background subtraction method.

Characteristic radiation originates from the decay of outer-shell electrons into inner-shell vacancies created by the incident electron beam, as shown schematically in Figure 3.9. This relaxation of an outer-shell electron to the core shell produces electromagnetic radiation in the form of an X-ray. It is this characteristic signal which can be used to identify the atomic species in the sample. Table 3.1 lists the characteristic X-ray lines of the cation species in IGZO. These peaks are observed in the EDS spectrum shown in Figure 3.10.

It is critical to calibrate the EDS technique to obtain accurate values of composition. The X-ray yield Y of atom X at a given depth t in a material is given by [159, 160]:

$$Y_X(t) = N_X \, \Delta t \, \sigma_X(t) \, \omega_X \, \exp\left[-\frac{\mu t}{\cos\theta}\right] I(t) \, \epsilon \, \frac{d\Omega}{4\pi} \tag{3.1}$$

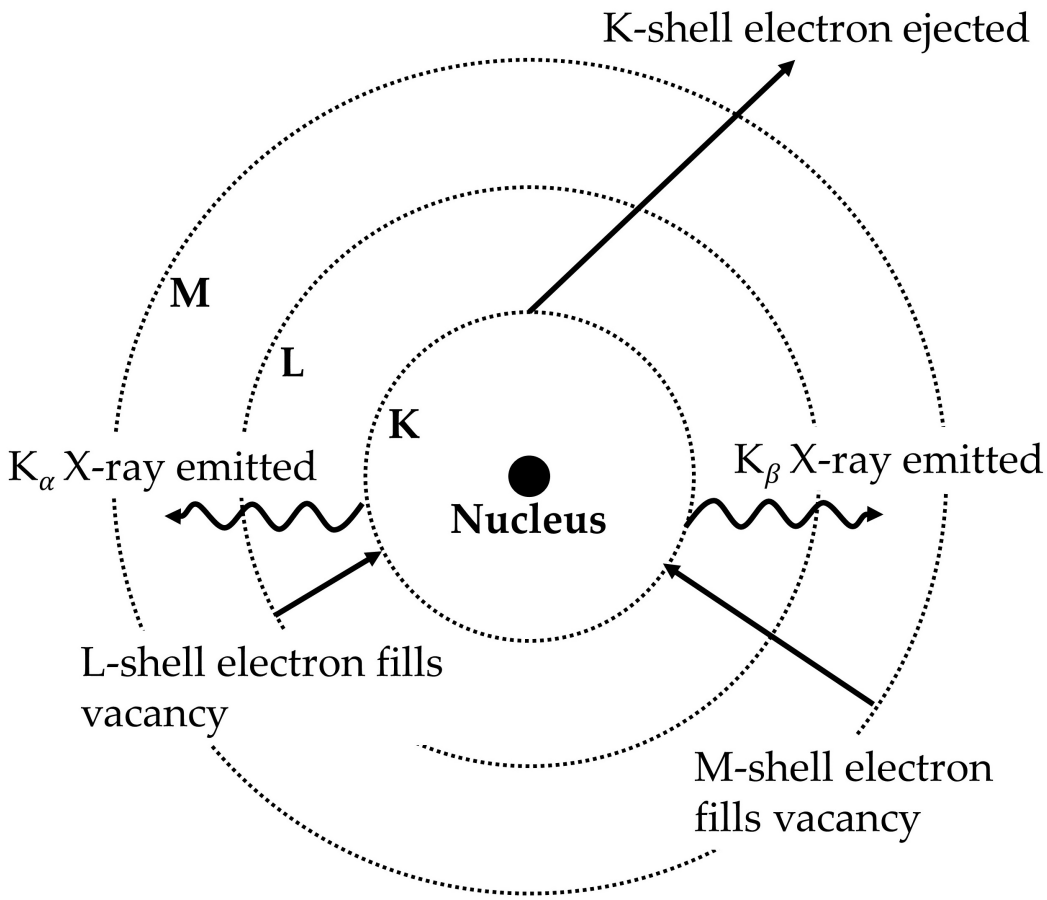

Figure 3.9: K X-ray production using the Bohr model of the atom.

where N_X is the atomic density of species X, Δt is the width of the layer under question, $\sigma_X(t)$ is the ionization cross section of species X at depth t, μ is the average X-ray absorption coefficient of the sample material, ω_X is the fluorescence yield of species X, θ is the angle between the incident electron beam and the X-ray detector axis, $I(t)$ is the electron beam intensity at depth t, ϵ is the detector efficiency, and $d\Omega$ is the solid angle subtended by the detector.

The yield of X-rays consequently depends on several factors, including the point of origin of the X-rays relative to the sample surface. These matrix effects, due to atomic size effects, sample absorption, and secondary X-ray fluorescence,

Table 3.1: Selected characteristic X-ray emission energies. Emission lines with omissions in the subscript labels are superpositions of X-ray lines not typically resolvable in EDS. Data from Ref. [158].

Element	Emission Line	Energy (keV)
Zn	K_α	8.63
	K_β	9.57
	L	1.01
Ga	K_α	9.25
	K_β	10.26
	L	1.10
In	K_α	24.21
	K_β	27.28
	L_α	3.28
	$L_{\beta 1}$	3.49
	$L_{\beta 2}$	3.71
	L_γ	3.92
Si	K_α	1.74

must typically be accounted for in a thick sample [161]. However, in the case of thin films, several approximations and simplifications can be made.

For thin films less than ~100 nm thick, the film thickness is negligible compared to the interaction volume of the electron beam in the sample (typically on the order of several μm) and all values in Eq. 3.1 can be approximated as thickness-independent. For a given measurement, the thin film thickness Δt, the exponential term accounting for X-ray absorption, the incident beam intensity I, the detector efficiency ϵ, and the detector orientation θ and solid angle $d\Omega$ are all constant. Thus, for *relative* measurements of yield (i.e., Y_{X1}/Y_{X2}), these terms cancel. The relative yield between two different atomic species $X1$ and $X2$ is then:

$$\frac{Y_{X1}}{Y_{X2}} = \frac{N_{X1}\,\sigma_{X1}\,\omega_{X1}}{N_{X2}\,\sigma_{X2}\,\omega_{X2}} \tag{3.2}$$

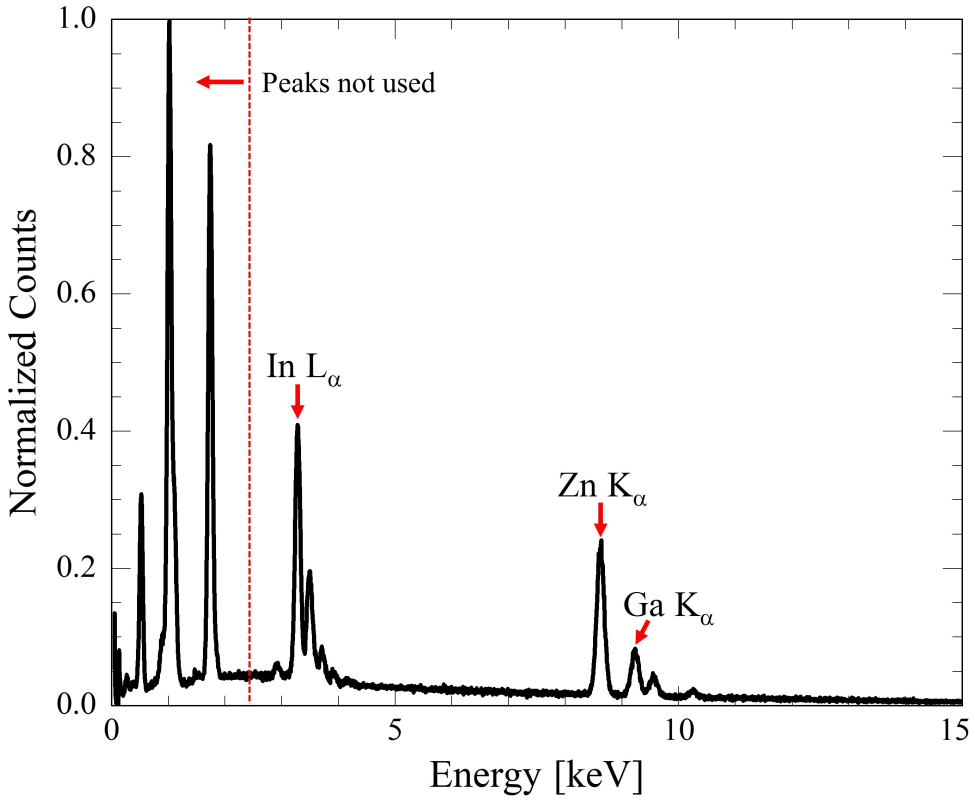

Figure 3.10: An example of a normalized EDS spectrum (20 keV incident beam energy) of an IGZO film on a Si substrate with ~100 nm thermal SiO_2 prior to background subtration. The three peaks used to characterize film composition are identified.

Rearranging to solve for the relative atomic fractions, this becomes

$$\frac{N_{X1}}{N_{X2}} = \frac{Y_{X1}/\sigma_{X1}\,\omega_{X1}}{Y_{X2}/\sigma_{X2}\,\omega_{X2}} = A_{X1/X2}\,\frac{Y_{X1}}{Y_{X2}} \tag{3.3}$$

where $A_{X1/X2}$ is a constant of proportionality determined by the identity of $X1$ and $X2$ and by the selected characteristic peaks. Using Eq. 3.3, EDS can be used for the measurement of relative atomic fractions once the proportionality constant $A_{X1/X2}$ is known. This factor can be determined for each component pair by the development of a calibration curve between EDS data (Y_{X1}/Y_{X2}) and an independently-determined measure of the atomic ratios (N_{X1}/N_{X2}), in this case using the absolute technique ICP-OES.

Using this method, the cation fractions can be accurately determined. The accurate determination of oxygen content in IGZO films, however, remains challenging using EDS. From a practical standpoint, EDS measurements of IGZO films that are deposited on a SiO_2 layer (either a native oxide or a grown oxide) are limited by the oxygen background signal from the SiO_2. In addition, ICP-OES cannot accurately determine oxygen concentrations due to background signals, as will be discussed in the next section.

3.2.2 Inductively-Coupled Plasma Optical Emission Spectroscopy (ICP-OES) Measurements of IGZO

For ICP-OES measurements, IGZO films were dissolved in an HCl solution (a typical wet etchant for IGZO films). These solutions were diluted and passed through an inductively-coupled Ar plasma to generate an optical emission spectrum of excited electronic states of the component atoms of the film. Each atom produces characteristic visible radiation that is dispersed by a spectrometer and measured by a charge-coupled device (CCD) array. As the emission intensity is proportional to concentration of excited atomic species in the plasma, the relative intensity of these characteristic lines can be used to identify the absolute concentration of the atomic species present in the sample.

To determine absolute atomic concentrations from measured atomic emission intensities, calibration curves were developed using standard calibration solutions of In, Ga, and Zn in dilute HNO_3. From these curves, the concentration of In, Ga, and Zn atoms in an unknown solution could be determined to an absolute accuracy better than 1%. From this technique, the relative concen-

trations of In, Ga, and Zn were determined and converted to relative concentrations in the form of the N_{X1}/N_{X2} term in Eq. 3.3 and compared to EDS measurements of the same samples. The relative concentration of anionic O species in the IGZO film is not reported due to the large oxygen background signal from H_2O, HNO_3, and air, making the measurement of O concentration impractical.

3.2.3 Calibration of EDS to ICP-OES

The three specific peaks chosen for composition quantification (In L_α, Zn K_α, and Ga K_α) are identified and labeled in Figure 3.10. The Zn and Ga K_α lines (8.63 keV and 9.25 keV, respectively) were selected based on their high intensities relative to the K_β lines and because the Zn and Ga L lines are not easily deconvoluted.

While the In L_α line (3.28 keV) was selected for the similar reasons, in some cases the In $L_{\beta 1}$ (3.49 keV) signal was measured to be anomalously more intense—typically with thinner IGZO films. This anomaly has been attributed to pulse pile-up from the Si K_α peak (1.74 keV), which occurs when two Si K_α photons reach the lithium-drifted silicon X-ray detector simultaneously and are binned as a single "double-energy" photon. The result is a Si sum peak at 3.48 keV. While sum peaks are typically small for any reasonable count rate [162], the measurement of thin IGZO films (~100 nm) on a thick Si substrate results in a much stronger Si signal relative to the other elements. Use of the In L_α line avoids this issue altogether.

To extract composition information, the background was first fit to a cubic function and subtracted. The area under each of the selected peaks in Figure 3.10

Table 3.2: Proportionality constants determined by calibrating EDS measurements with ICP-OES measurements, corresponding to the $A_{X1/X2}$ term in Eq. 3.3.

Calibration Constant	Value
$A_{\mathrm{In/Ga}}$	0.611 ± 0.001
$A_{\mathrm{Zn/Ga}}$	1.121 ± 0.003

was then integrated, allowing calculation of the Y_{X1}/Y_{X2} ratios (see Eq. 3.3). Selected samples were measured using both EDS and ICP-OES. For these samples, the N_{X1}/N_{X2} and Y_{X1}/Y_{X2} terms for In:Ga and Zn:Ga ratios were determined, shown plotted in Figure 3.11. Each of these curves were fit with a proportionality constant to determine $A_{X1/X2}$, listed in Table 3.2.

This calibration enabled rapid characterization of the composition of IGZO thin films. Rather than depending on ICP-OES, which requires the majority of a day to perform, calibrated EDS characterization of films achieve reliable composition measurements with an absolute uncertainty below ±5%. All reported IGZO thin film compositions reported in this work were measured using this technique.

3.3 TFT Fabrication and Characterization

IGZO TFTs were used to investigate the effect of deposition temperature on the electronic properties of IGZO films (Chapter 5). Devices were fabricated and tested in the Cornell NanoScale Science & Technology Facility (CNF).[5] This section will provide an overview of the process flow for IGZO TFT fabrication

[5]With the exception of the IGZO sputter deposition and the post-deposition anneal, which were conducted in the Thompson Lab in 331 Duffield Hall.

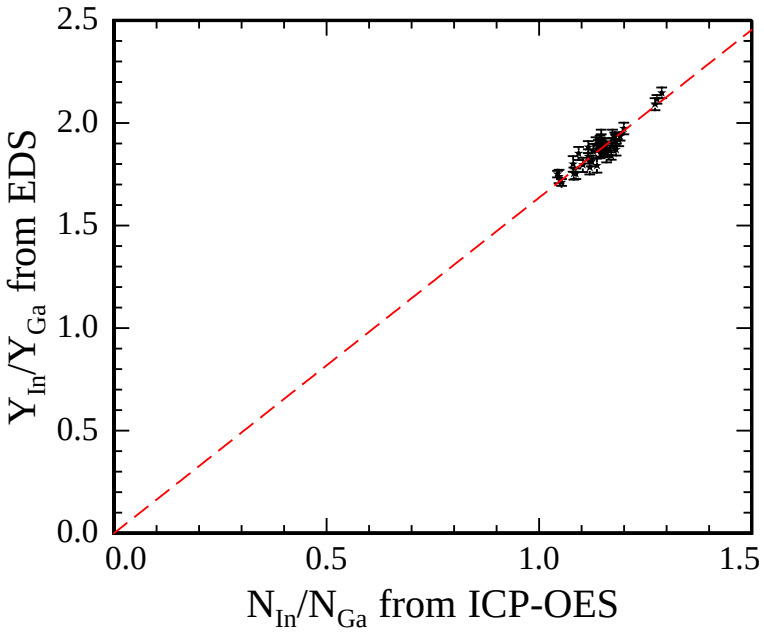

(a) In:Ga ratio calibration

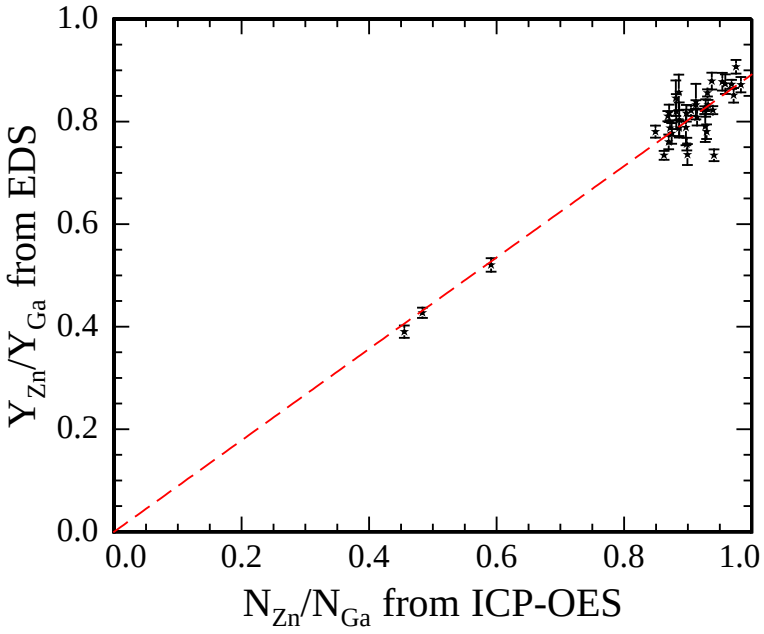

(b) Zn:Ga ratio calibration

Figure 3.11: EDS calibration curves for (a) In:Ga ratio and (b) Zn:Ga ratio.

to achieve an inverted-staggered bottom-gate TFT device. An overview of the electrical measurements are provided here, with a detailed description of the parameter extraction techqniues discussed in Appendix A.

3.3.1 TFT Layout

Figure 3.12 shows a schematic diagram of the structure of the TFTs fabricated for this study. The three terminals of the device are shown in Fig. 3.12a, with the source and the drain electrodes directly contacting either end of the active channel layer and the gate electrode contacting the degenerately doped p^{++} Si substrate through a gate via etched through the thermal oxide dielectric. Long active channels ($W/L = 50\,\mu\text{m}/550\,\mu\text{m}$) were used to reduce the effect of any contact resistance in the IV measurements. Fig. 3.12b shows the resulting inverted-staggered bottom-gate structure using the Si substrate as the TFT gate.

3.3.2 Process Flow

The device study in Chapter 5 investigates the effect of varying IGZO (active channel layer) deposition conditions on device characteristics. As such, the following process flow is common to the entire fabrication process; only processing conditions for the active channel layer were varied in the experiments.

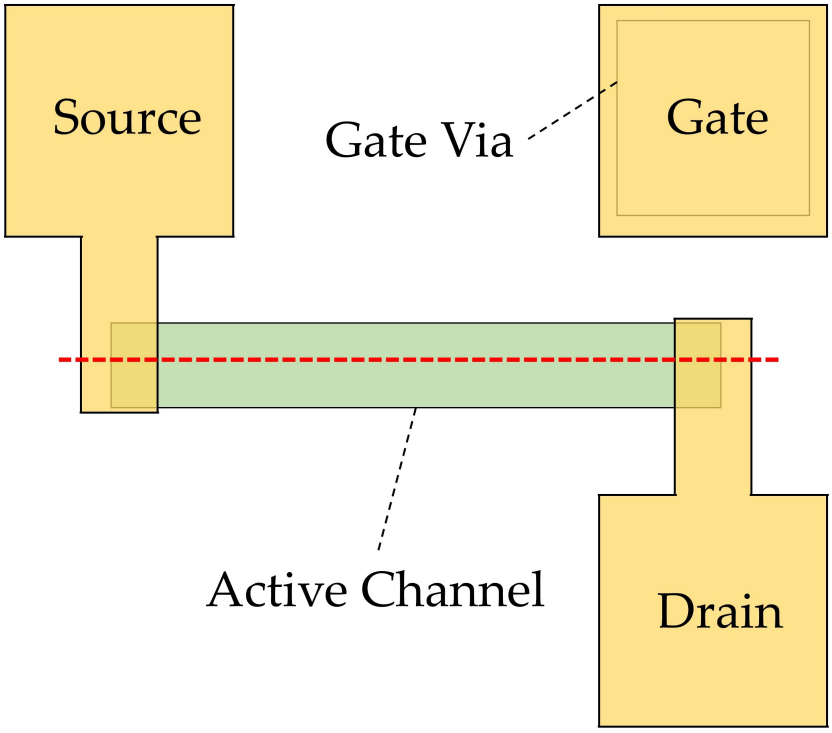

(a) Plan-view layout

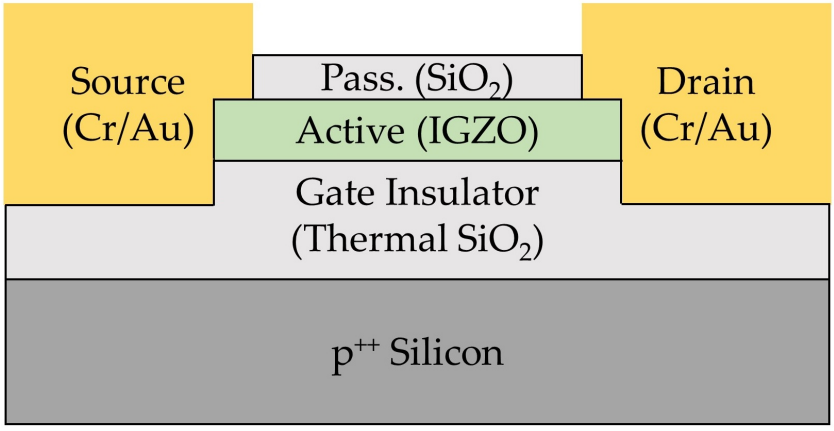

(b) Device cross-section

Figure 3.12: Schematic layout of TFT device structure used in this work. Dashed line in (a) along the channel length denotes the region represented in the cross-section (b). Device cross-section not drawn to scale.

Substrates and Gate Electrode

All devices discussed here were fabricated on 100 mm (100) p^{++} Si wafers that were heavily doped with boron to achieve a resistivity of 0.01–0.02 Ω-cm. These degenerately doped substrates were used as the gate electrode for fabricated TFTs.

Gate Dielectric

Thermally-grown SiO_2 was used as the TFT gate dielectric. Prior to furnace oxidation, all substrates were cleaned using a modified (no HF oxide strip) RCA clean process [163]. Substrates were cleaned of organics using a heated NH_4OH/H_2O_2 bath, cleaned of ionics using a heated HCl/H_2O_2 bath, then rinsed with deionized water. Wafers were then thermally oxidized in a tube furnace at 1000 °C for ~30 minutes in dry O_2 and 3% HCl, forming ~100 nm of high-quality SiO_2.

Active Channel Material

IGZO thin films were typically deposited onto one quarter of a thermally oxidized Si wafer using the reactive RF magnetron sputter deposition system described previously. Prior to deposition, substrates were cleaned by rinsing with acetone, isopropyl alcohol, and deionized water. After loading the substrates into the deposition system, the substrates were further cleaned using an O_2 plasma by biasing the substrate with 40 W of RF power for 5 minutes (30 mTorr pressure, 10 sccm O_2 flow). IGZO films were all deposited using similar deposition conditions (120 W, 10% O_2 in Ar, 10 sccm total gas flow rate,

5 mTorr pressure, 19 minute deposition), varying only the target source material (1:1:1 In:Ga:Zn IGZO from Kurt J. Lesker Company or 2:2:1 In:Ga:Zn IGZO from AJA International) and the substrate temperature (ranging from nominally room temperature to 385°C), producing approximately 50 nm-thick films with varying microstructures and properties.

Passivation Layer

To protect the exposed backchannel surface of the active channel material and to help eliminate existing backchannel defect states, ~30 nm of surface-passivating SiO_2 was deposited by PECVD using an Oxford 100 PECVD System (1800 mTorr, 50 W RF, 20 sccm SiH_4, 2500 sccm N_2O). A deposition temperature of 200°C was used to minimize thermal effects on the IGZO film.

Active/Passivation Patterning

The passivation and active layers were patterned using standard photolithographic and etching techniques. Shipley Microposit S1813 photoresist (nominally 1.3 μm thick) was selectively exposed to UV light (280–350 nm) using a Karl Suss MA6-BA6 Contact Aligner and developed to form 50 μm × 550 μm islands. The passivating SiO_2 was first dry etched with in a CF_4/O_2 environment using a load-locked Plasma-Therm 700 Series Reactive Ion Etcher (40 mTorr, 150 W RF, 30 sccm CF_4, 2 sccm O_2, 19 nm/min). IGZO films were wet etched in dilute (5 vol%) HCl for 3 minutes.[6] The remaining photoresist was then stripped by rinsing with acetone, isopropyl alcohol, and deionized water.

[6]Mixture of 20 parts deionized water and 1 part electronics-grade HCl stock solution.

Gate Via Patterning

Gate vias were patterned using an identical photolithographic technique to produce etched areas in the gate dielectric for electrical contact to the gate electrode (Si wafer). The exposed thermal SiO_2 areas were wet etched in 6:1 BOE[7] for 2 minutes.

Metallization

The metal electrodes were pattered by a liftoff technique using a bilayer resist structure. A stacked film structure of MicroChem NANO LOR 5A resist (nominally 5 μm thick) and S1813 was selectively UV-exposed to create a lipped resist profile compatible with solvent liftoff. Prior to metal deposition, exposed areas were dry etched (see Active/Passivation Patterning) to remove passivation SiO_2 and expose areas of the IGZO film for contact. Metal contacts were deposited by thermally evaporating 100 nm of Cr and 50 nm of Au to protect the Cr from oxidation during post-fabrication annealing. The final contact structure was formed by dissolving the resist in Shipley Microposit Remover 1165 and subsequently rinsed in acetone, isopropyl alcohol, and deionized water.

Post-Fabrication Annealing

As-deposited TFTs typically exhibit conductive "metal-like" behavior, characterized by a large positive gate bias (V_{GS}) required to turn off the device, consistent with the excess carriers associated with a high concentration of oxygen vacancies in the IGZO film. To reduce the carrier density and achieve

[7] Buffered oxide etch: mixture of 6 parts 40% NH_4F in water and 1 part 49% HF in water.

"semiconductor-like" behavior, TFTs were annealed in a 3-zone quartz tube furnace at 350°C in dry air (nominally dry air further dried to <10 ppb H_2O for 30 minutes.

IV Measurements

TFT *IV* characteristics were measured using an Everbeing EB-6 DC probe station and high-precision Keithley source measurement units. Two types of 3-terminal measurements were conducted: I_{DS}-V_{GS} sweeps at fixed V_{DS} (transfer characteristics, indicating transistor turn-on operation) and I_{DS}-V_{DS} sweeps at stepped V_{GS} (output characteristics, indicating transistor output and saturation in the on-state). A detailed discussion of device parameter extraction can be found in Appendix A.

3.4 Lateral Gradient Laser Spike Annealing (lgLSA)

All samples with composition gradients were annealed post-deposition using the lateral gradient laser spike annealing (lgLSA) technique with a continuous wave CO_2 laser (λ = 10.6 μm). This technique, developed by Bell *et al.* [12] and shown schematically in Figure 3.13, anneals stripes of film material by scanning the sample on a moving stage under a fixed laser beam (Fig. 3.13a). This spikes the temperature of the film up to a peak temperature for a characteristic period of time (dwell time) determined by the stage velocity and the focus of the laser. Fig. 3.13c shows the temperature of an annealed area on the sample as a function of time. The laser is focused such that a Gaussian thermal profile (FWHM ~600 μm) is achieved transverse to the scanning direction (Fig. 3.13b).

The resulting samples contain regions annealed up to a maximum peak temperature T_{peak} (center of laser stripe) and unannealed regions maintained near room temperature (far away from the center of the laser-annealed stripe).

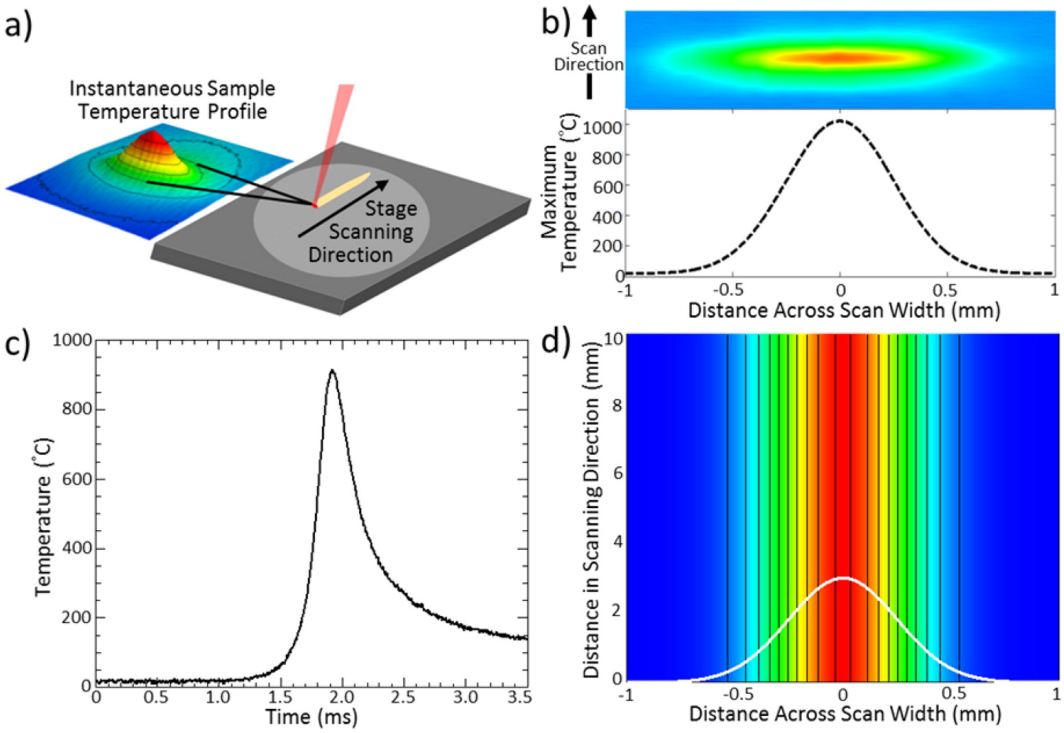

Figure 3.13: Overview of the lgLSA technique. (a) Schematic of a sample scanning through a line-focused laser beam. (b) Intensity profile of the line-focused beam (top) and lateral temperature profile orthogonal to the scanning direction (bottom). (c) Measured temporal temperature profile for 150 μs anneal with a peak temperature of 900 °C. (d) Schematic contour map of peak annealing temperatures along an lgLSA scan with the lateral temperature profile overlaid. Reprinted with permission from [12]. Copyright 2016 American Chemical Society.

Samples in this study were annealed to a peak temperature T_{peak} = 1200 °C. Each laser-annealed stripe intrinsically contains information as a function of annealing temperature (Fig. 3.13d). Measurements at the center of the laser-annealed stripe yielded film structures annealed at T_{peak} = 1200 °C, while measuring between each laser stripe center yielded the unannealed, as-deposited structure. The laser-annealed stripes were separated by 1.5 mm to eliminate any

effect of thermal history between scans and to ensure the film areas between scans remained nominally unannealed. To investigate the effect of annealing time, dwell time was varied between laser stripes from 250 μs to 10 ms. These anneals were each conducted in iso-composition regions, allowing each subsequent laser-annealed stripe to sample a different point in composition space. Using this lgLSA technique, the post-annealed structure of IGZO films was investigated as a function of composition, temperature, and processing time.

3.5 X-Ray Diffraction Characterization

Film crystal structure, degree of crystallinity, and crystallographic texturing of IGZO films were primarily assessed using X-ray diffraction (XRD) techniques. Standard lab-scale measurements were conducted in the facilities of the Cornell Center for Materials Research (CCMR). Standard θ-2θ XRD measurements provided a quick measure of as-deposited film structure and crystallinity. To quantify crystallographic alignment in these films, a 2D diffraction system was used, providing a faster-throughput technique than the traditional rocking curve technique. While these characterization tools are fairly ubiquitous, they provide relatively poor spatial resolution (~mm to cm scales). To probe the narrower length scales required across an lgLSA thermal profile, laser-annealed film samples were characterised using a focused synchrotron radiation source at the Cornell High Energy Synchrotron Source (CHESS). The synchrotron allowed high-flux X-ray diffraction measurements with 25 μm lateral spatial resolution.

3.5.1 θ-2θ X-ray Diffraction (XRD)

Crystallographic quality and basic phase identification of IGZO thin films were determined using θ-2θ XRD. θ-2θ scans discussed in Chapter 4 were measured using a Rigaku SmartLab X-ray diffractometer with a monochromated Cu K_α X-ray source and a scintillation counter detector. Scans were conducted with a 3° offset in ω to eliminate diffraction peaks associated with the single-crystal Si substrates.[8] All of these measurements were conducted using the same source, slit, and detector parameters, and the measured counts were normalized by film thickness. This results in a self-consistent measure of relative crystallinity between samples. However, since the intensity of the Cu X-ray source can drift over time, this measurement method does not allow reliable comparisons between measurements over long periods of time.

In later work (Chapter 5), $\theta - 2\theta$ scans were measured using a Bruker D8 ECO Powder Diffractometer with a Ni-filtered (0.2 μm thick filter) Cu K_α X-ray source and a silicon drift detector (SDD) array, which subtends a maximum of 2.5° about the set detector angle. All peak intensity values reported in the later work have been normalized using a corundrum (Al_2O_3) powder sample standard.[9]

The Scherrer formula is often used to estimate the grain size and is given by [164–166]:

$$t = \frac{K\lambda}{B\cos\theta_B} \tag{3.4}$$

where t is the estimated grain size, K is a geometric factor (the Scherrer con-

[8] The angle ω is in the same plane as θ, however ω typically refers to sample orientation and θ typically refers to the source and detector orientations.

[9] All measured intensities are normalized by the factor $(10^4/I)$, where I is the maximum peak intensity of the corundrum $(01\bar{4})$ peak.

stant) accounting for the shape of the grain, λ is the X-ray wavelength, B is the broadness of the diffraction peak in radians, and θ_B is the Bragg angle. In the absense of grain shape information, a Scherrer constant of $K = 0.9$ is typically used. It must be emphasized that this is only an estimate, as additional peak broadening may also arise from strain or equipment artifacts.

3.5.2 2D Diffraction Characterization Using a General Area Detector Diffraction System (GADDS)

Quantification of crystal texture and alignment in Chapter 4 was achieved using a Bruker AXS general area detector diffraction system (GADDS) with a monochromated Cu K_α X-ray source and a 2D detector array. For these measurements, the source and detector angles were fixed such that $2\theta = 30^\circ$. This technique enables the simultaneous measurement of X-rays scattered in the incidence plane (normal to sample surface) with an angle of 2θ and scattered out of the incidence plane with an angle of χ. The resulting 2D diffraction pattern contains information on X-ray scattering in 2θ (radial direction) and in χ (azimuthal direction). Integrating one of these diffraction rings in 2θ (between 28° and 34°) yields a intensity as a function of χ, a direct measure of crystallographic alignment analogous to a rocking curve on a 1D diffractometer.

In later work (Chapter 5), these 2D scans were measured using a Bruker-AXS D8 Discover Diffractometer using a 2D Vantec detector and a Ni-filtered (12 μm thick filter) Cu K_α X-ray source. The source-detector 2θ was set to a fixed 30° for these measurements also; however, to eliminate substrate artifacts due to the imperfectly monochromated source, the source and detector angles were each

offset by 3° (θ_{source} = 12° and $\theta_{detector}$ = 18°).

3.5.3 High-Resolution Diffraction Using Microbeam Wide Angle X-Ray Scattering (μ-WAXS)

For laser-annealed films, film structures were characterized using microbeam wide angle X-ray scattering (μ-WAXS) at CHESS along the thermal profile of each laser stripe, giving effectively the film structure as a function of the peak annealing temperature between room temperature and T_{max} = 1200°C (within a single laser stripe), annealing time (between laser stripes annealed at different dwell times), and composition gradient (along the length of the film sample).

X-ray focusing optics (9.93 keV photons) were used to achieve an incident X-ray beam focused down to a ~12 μm spot, enabling spatially-resolved probing (25 μm steps) across the lateral thermal gradient with a significant signal-to-noise ratio due to the large X-ray flux of the synchrotron source. Scattered X-rays were detected using a 2D Eiger 1M detector (1 Megapixel, 75 μm pixel size). Thus, the μ-WAXS techniques provided structural information analogous to a spatially-resolved GADDS scan and is better suited for the identification of textured films than typical θ-2θ X-ray diffraction (XRD), as measurements are not limited to only out-of-plane scattering.

3.6 High-Resolution Transmission Electron Microscopy (HRTEM)

In addition to X-ray characterization, selected samples were imaged by high-resolution transmission electron microscopy (HRTEM) using a 200 kV FEI Tecnai F-20 field emission electron microscope in CCMR. Film samples were prepared by tripod polishing with a 1° nominal bevel, with cross-section samples further thinned using a Fischione Instruments Model 1010 Ar ion mill at acceleration potentials of 3.0 to 0.5 keV. Film samples were imaged in two orientations: in cross-section aligned on the Si substrate [0 1 0] zone axis (perpendicular to the IGZO [0 0 1] axis) and in plan-view aligned on the Si [0 0 1] zone axis.

CHAPTER 4

CHARACTERIZATION OF REACTIVELY SPUTTERED c-AXIS ALIGNED NANOCRYSTALLINE $InGaZnO_4$

Portions of this chapter are adapted from D. Lynch *et al.* in *Applied Physics Letters* (reprinted from [13], with the permission of AIP Publishing) and from D. Lynch *et al.* in *Society for Information Display International Symposium Digest of Technical Papers* (reprinted from [14], with the permission of John Wiley and Sons).

4.1 Introduction

In 2012, Shunpei Yamazaki at the Semiconductor Energy Laboratory in Japan demonstrated c-axis aligned crystal (CAAC) IGZO, a nanocrystalline microstructure in IGZO showing strong crystallographic texture [142]. When used as the active channel material in TFTs, this material retains the excellent uniformity of the amorphous phase while exhibiting improved stability and extremely low leakage currents [87]. These characteristics make CAAC IGZO an ideal candidate for applications beyond traditional displays, including low-power displays, non-volatile RAM, and sensors [10, 167].

However, until this work [13, 14], little was known about CAAC formation conditions. Yamazaki's initial reports did not identify specific deposition or annealing conditions. Matsubayashi *et al.* [167] more recently reported CAAC formation after annealing DC sputtered films at 400°C. In this work, CAAC IGZO films were directly formed by reactive RF magnetron sputtering at elevated temperatures over a range of processing conditions. Film deposition under optimal

conditions showed a high degree of crystallinity and strong c-axis alignment. Highly oriented films were obtained directly by sputtering at an optimal substrate temperature of 300°C with a transition from CAAC to randomly oriented nanocrystalline material at higher temperatures.

In this chapter, the structure and formation regimes of CAAC IGZO films were investigated using X-ray diffraction (XRD) and high-resolution transmission electron microscopy (HRTEM). Structural analysis of films sputtered over a wide range of deposition conditions gives insight into the film growth process during deposition and identifies subtle secondary effects of the sputtering process. A nucleation and growth model is discussed in the context of these results and compared to other proposed formation mechanisms from literature.

4.2 X-ray Characterization

Figures 4.1a and 4.1b compare 2θ XRD patterns of amorphous (scaled 5x) and crystalline films deposited with an O_2 sputter gas fraction of 10%. With substrate temperatures below 190°C, as-deposited films exhibited only weak scattering at ~32° (Fig. 4.1a), which is characteristic of local bond ordering in the amorphous structure. By 190°C, a crystalline IGZO peak develops at 30^o corresponding to (009) planes (shown schematically in Fig. 4.1d), with the peak intensity increasing with substrate temperature up to 310°C. By 310°C, the full-width at half-maximum (FWHM) decreases to 4° and highly aligned CAAC is formed (Fig. 4.1b). Assuming a typical geometric factor of $K = 0.9$, the estimated grain size is greater than 2.1 nm. The peak intensity decreases slightly as temperatures increase above 310°C while the FWHM continues to decrease.

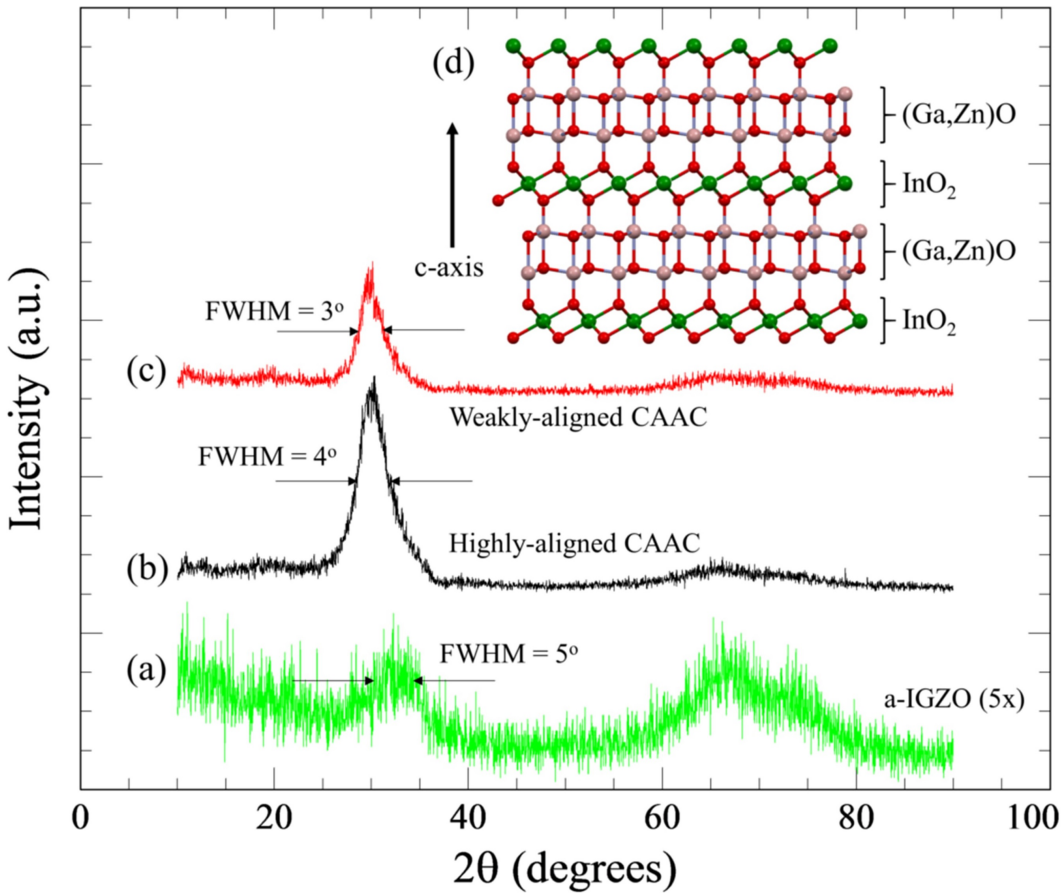

Figure 4.1: XRD of the (a) a-IGZO (5x), (b) highly aligned (310°C, 10% O_2) CAAC IGZO, and (c) weakly aligned (310°C, 100% O_2) CAAC IGZO films. Inset (d) is a schematic diagram of theatomic arrangement within the CAAC crystalline structure. Reprinted with permission from [13]. Copyright 2014 AIP Publishing.

This decrease in XRD intensity suggests a loss of c-axis alignment as the film becomes increasingly polycrystalline and fewer domains satisfy the Bragg condition. The GADDS measurements below confirm this hypothesis.

Figure 4.1c shows an XRD scan for a film deposited with an O_2 fraction of 100% at 310°C. At fixed temperature, the XRD peak intensity initially increases with increasing O_2 fraction, reaching a maximum at 50% O_2. In general, the impact of increasing the O_2 fraction beyond 50% at a constant deposition tem-

perature is equivalent to increasing the deposition temperature above 310°C at a fixed O_2 fraction. Above 70% O_2, the XRD intensity decreases, which again suggests a loss of the c-axis alignment and the development of a randomly oriented nanocrystalline morphology. The FWHM decreases slowly with O_2 fraction, reaching 3° at 100% O_2 with an estimated grain size of at least 2.8 nm.

The crystal orientation texture was determined using GADDS area scans (Fig. 4.2), which represent diffracted X-ray intensity as function of both 2θ (radial direction) and azimuthal angle χ (angular direction). XRD 2θ scans are equivalent to the radial slice along $\chi = 90°$, and the arc near the center of the GADDS scan corresponds to the (009) IGZO peak. Figures 4.2a and 4.2b show scans for films deposited at 310°C in 10% and 100% O_2, respectively, with the 10% O_2 film (Fig. 4.2a) exhibiting much stronger c-axis texture. Radially integrating the intensity of a GADDS scan gives the intensity distribution as a function of χ (Fig. 4.2c), analogous to an XRD rocking curve. The full width at half-maximum (FWHM) of these intensity distributions provides a quantitative measure of the film texture. Thus, films deposited at 310°C with 10% O_2 exhibit a FWHM of 20°, indicating strong c-axis alignment. In contrast, the FWHM of films deposited in 100% O_2 is 35°, indicating much weaker alignment.

At temperatures below 190°C, as-deposited films are amorphous and exhibit no texturing. At 190°C, texture develops and increases up to a maximum near 310°C (see: highly aligned film in Fig. 4.2c). In addition to substrate temperature, the O_2 fraction during deposition plays a key role in CAAC alignment. Non-reactive sputtering in pure Ar yields amorphous films, even with substrate temperatures of 310°C. However, 5% O_2 is sufficient to induce growth of CAAC. The effect of O_2 fraction is approximately constant up to ~50% O_2. Film c-axis

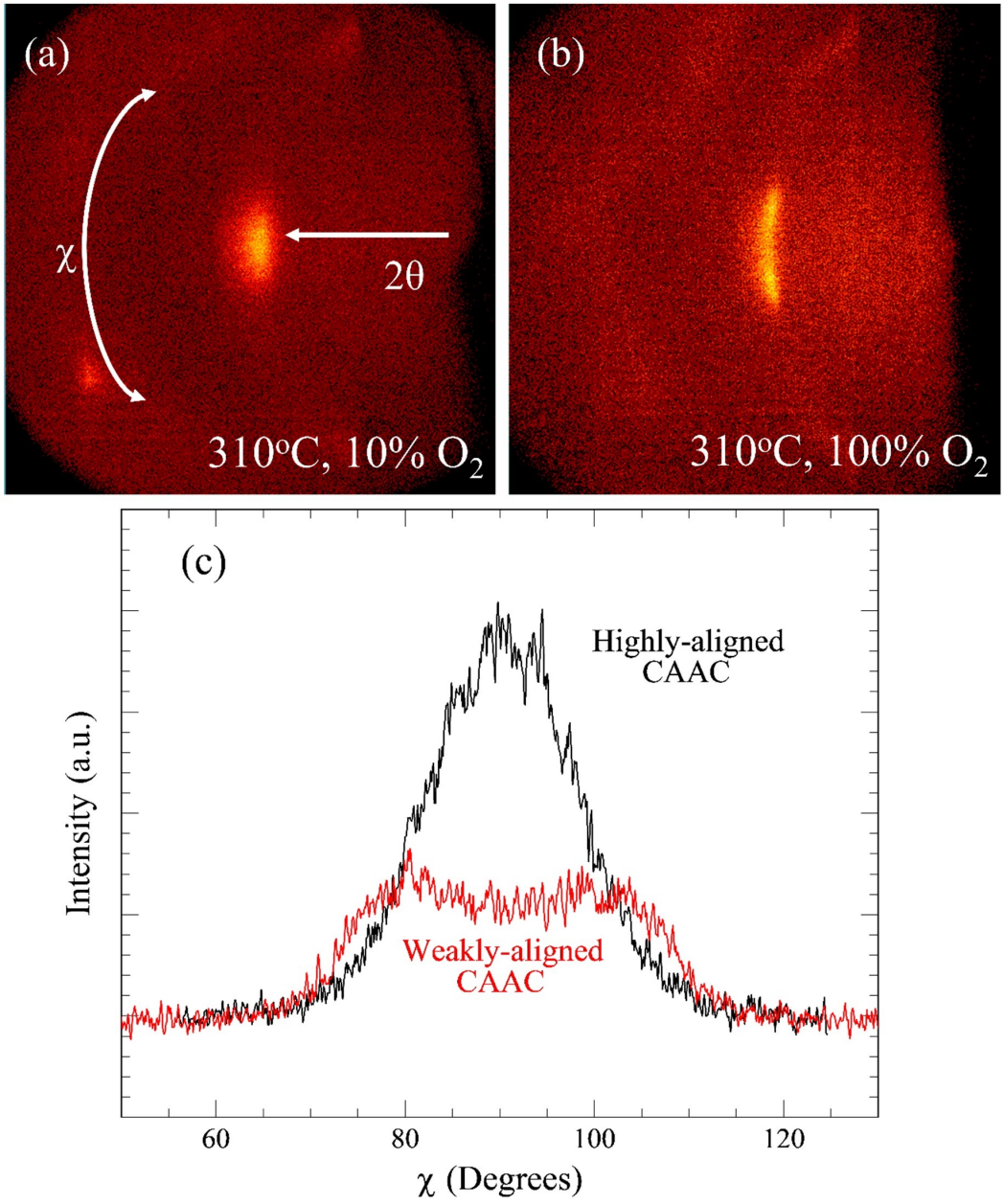

Figure 4.2: (a) GADDS area scan of the highly aligned CAAC IGZO film indicating X-ray intensity as a function of 2θ (radially) and χ (angularly). (b) GADDS scan of the weakly aligned IGZO. (c) The radially-integrated intensity distributions as a function of χ directly corresponding to c-axis alignment. Reprinted with permission from [13]. Copyright 2014 AIP Publishing.

alignment decreases at O_2 fractions above 50% and sharply falls above 70% (see weakly aligned film in Fig. 4.2c). A summary of these X-ray results are shown graphically in Figure 4.3.

4.3 HRTEM Characterization

To distinguish the microstructure of the highly aligned CAAC IGZO structure from the more randomly-oriented structures, select IGZO films were further characterized using HRTEM in both cross-section and plan-view orientations, shown in Figure 4.4. A highly aligned CAAC IGZO film deposited under optimal conditions (310 °C/10% O_2), shown in Fig. 4.4a and Fig. 4.4b, was compared to an IGZO film deposited under conditions yielding a weakly aligned structure (310 °C/100% O_2), shown in Fig. 4.4c and Fig. 4.4d.

4.3.1 Highly Aligned CAAC IGZO Film

The HRTEM cross-section image of the highly aligned CAAC film (310 °C/10% O_2) in Figure 4.4a shows alignment of crystal planes (shown schematically in Fig. 4.1d) approximately perpendicular to the substrate interface with an interplanar spacing of ~0.3 nm, agreeing well with the expected 0.29 nm from (0 0 9) reflections estimated from a lattice parameter of $c = 2.60$ nm [168]. Individual crystalline domains 2-3 nm in size are separated by regions unresolved by HRTEM, consistent with initial reports by Yamazaki [142]. Strong alignment to the substrate (oriented horizontally) is observed across the entire 15 nm × 15 nm field of view of Figure 4.4a, characteristic of the entire film. Figure 4.5a

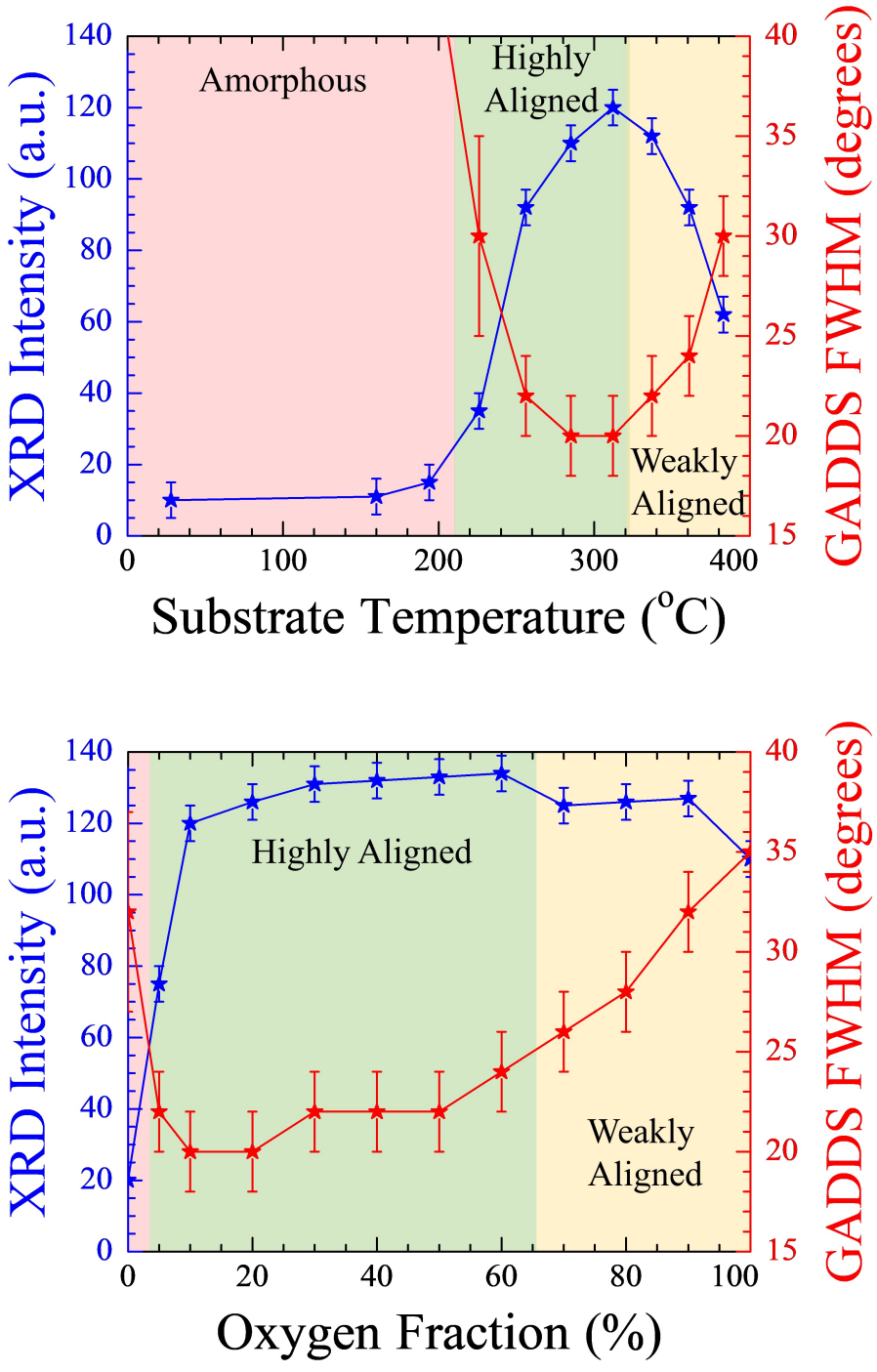

Figure 4.3: Summary of X-ray diffraction data.

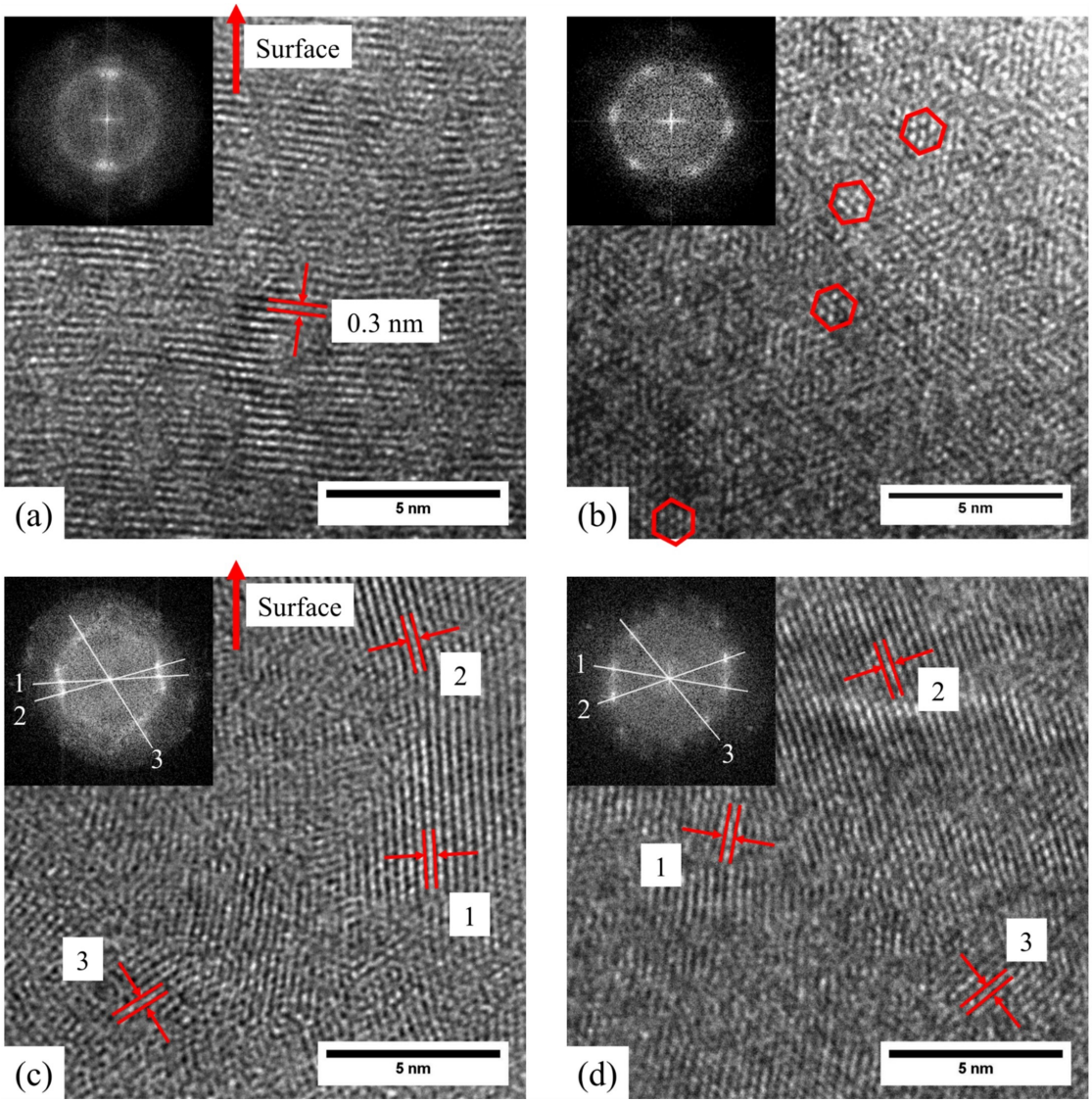

Figure 4.4: (a) Cross-section and (b) plan-view HRTEM images of the highly aligned CAAC IGZO (310 °C/10% O_2) film and (c) cross-section and (d) plan-view HRTEM images of the weakly aligned CAAC IGZO (310 °C/100% O_2) film. Image FFTs are inset, and key regions of interest are identified in red. Reprinted with permission from [13]. Copyright 2014 AIP Publishing.

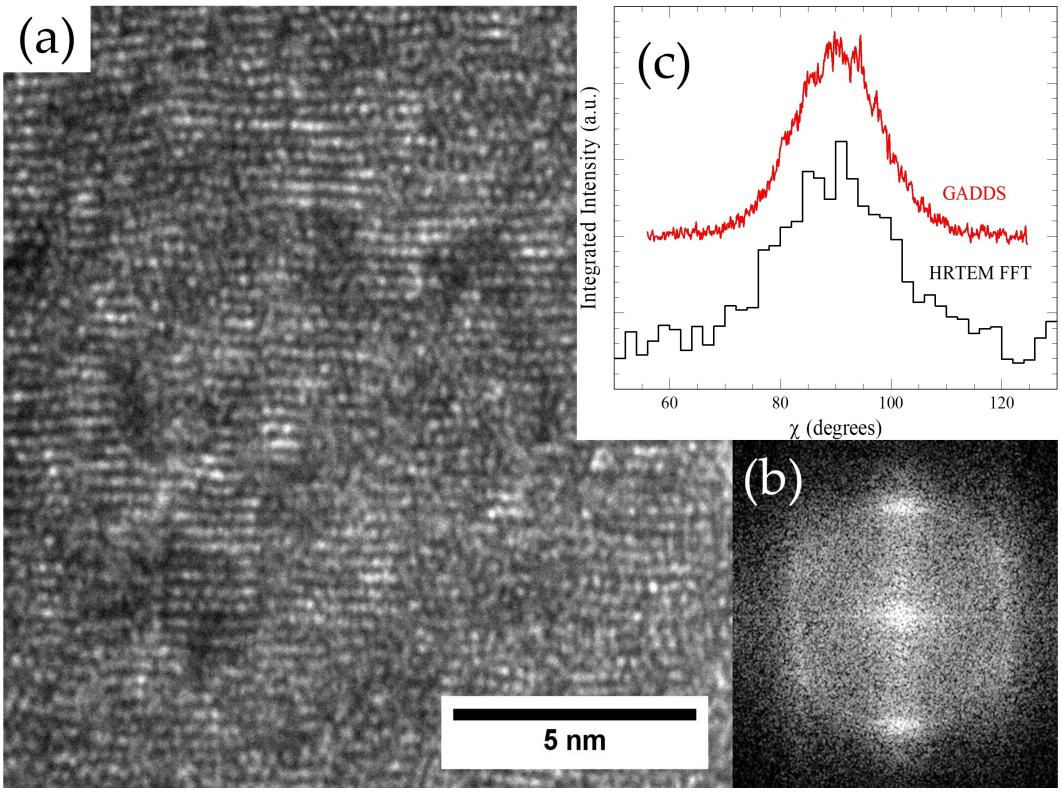

Figure 4.5: (a) Cross-section HRTEM image of the highly aligned CAAC IGZO film in a different region than shown in Figure 4.4a. (b) Image FFT showing bright arcs due to the (0 0 9) planes. (c) Intensity distribution histogram showing similar alignment observed in GADDS data. Reprinted with permission from [14]. Copyright 2015 John Wiley and Sons.

demonstrates the extent of this alignment in a different area of the same highly aligned CAAC sample. This high degree of crystallinity and strong texturing is consistent with XRD and GADDS measurements.

The Fast Fourier Transform (FFT) diffractogram of the HRTEM image, shown in the Fig. 4.4a inset and in Fig. 4.5b provides an indication of the plane tilt distribution over the this field of view. Tilt of the planes relative to the average was quantitatively determined by radially integrating the FFT (equivalent to a radial integration in GADDS analysis) and displaying this integrated intensity as a function of angle (equivalent to χ in GADDS analysis). The resulting

angular distribution of FFT intensity, shown in Figure 4.5c, is analogous to the intensity distribution of the GADDS scan plotted on the same graph. The extracted FWHM of the FFT tilt distribution is 23°, which is consistent with the GADDS FWHM of 20° measured from the same sample. The correspondance of the tilt distribution width indicates that essentially all of the plane deviations occur on sub-15 nm length scales and are not due to significant misalignments over large scales.

Both X-ray diffraction and cross-section HRTEM primarily probe structural features parallel to the film surface. To characterize the in-plane mosaic spread, plan-view HRTEM images of the CAAC films were obtained. For the highly aligned CAAC film shown in Fig. 4.4(b), hexagonal domains are apparent throughout the 15 nm × 15 nm field of view. These individual domains average 2-3 nm in size, consistent with observation from cross-section HRTEM. The inset FFT diffractogram shows the hexagonal pattern characteristic of this projection with the expected 0.28 nm spacing [169]. The sharp peaks suggest a single orientation with near-single crystal-like character and only minor distortions across this field of view. As with the alignment observed in cross-section, this high degree of alignment is characteristic of the entire film. Figure 4.6a shows the extent of this alignment in a different area of the same sample. A radial integration of the FFT in Fig. 4.6b gives the intensity distribution in Fig. 4.6c, confirming the 6-fold symmetry in the image and indicates an angular variation of ±10° (FWHM).

Given the 20° spread in c-axis alignment observed in HRTEM, only a fraction of the IGZO atomic columns are aligned with sufficient precision to the incident electron beam to be resolved in plan-view. A rough estimate, assuming a

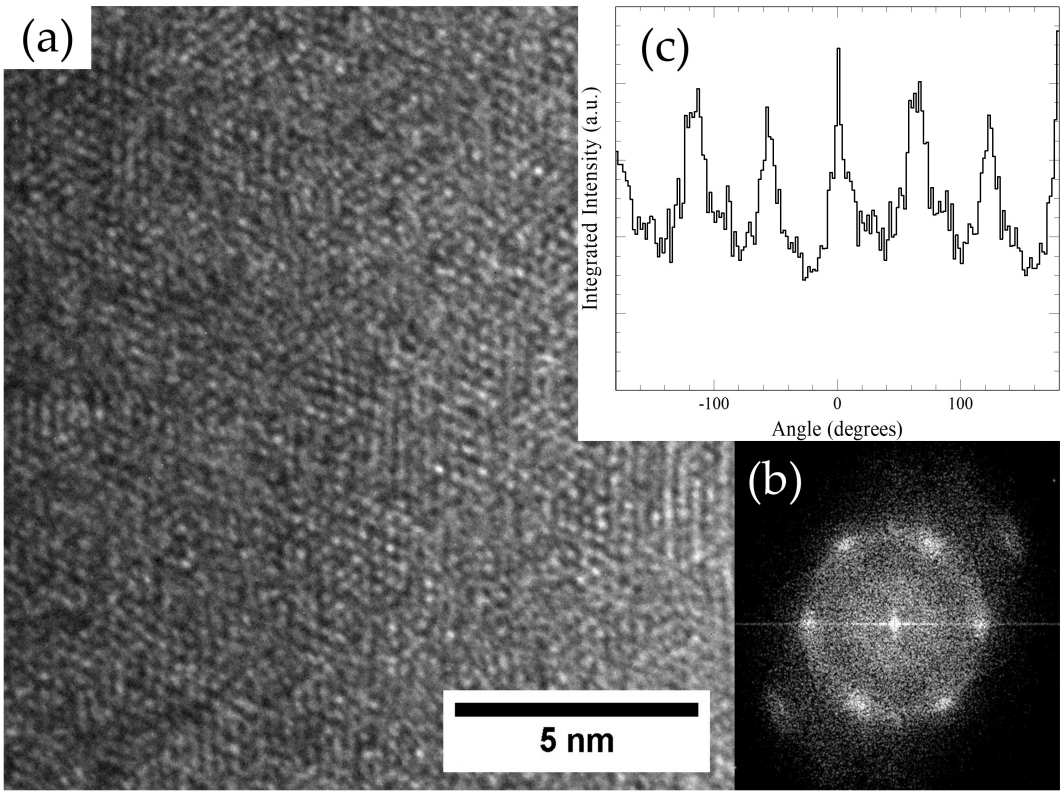

Figure 4.6: (a) Plan-view HRTEM image of the highly aligned CAAC IGZO film in a different region than shown in Figure 4.4b. (b) Image FFT suggesting little alignment variation in the a-b plane. (c) Intensity distribution histogram, confirming the 6-fold symmetry and indicates an angular variation of ±10°. Reprinted with permission from [14]. Copyright 2015 John Wiley and Sons.

plan-view sample thickness of 3 nm, indicates that approximately 40% of atomic columns in the material will be fully visible at a given orientation with respect to the electron beam. This suggests that the areas between HRTEM-resolved crystalline domains may still be crystalline but tilted to a degree that they do not show an atomic image in projection. This model accounts for the common rotational orientation of CAAC domains observed in the diffractogram. In essence, while distorted and strained, the film exhibits structure consistent with near-single grains extending over distances >15 nm.

4.3.2 Weakly Aligned CAAC IGZO Film

HRTEM images of weakly aligned films (310°C/100% O_2) were also obtained for comparison. In cross-section (Fig. 4.4c), long-range order is no longer observed and the film exhibits very weak alignment relative to the substrate interface. The FFT (Fig. 4.4c inset) similarly shows much weaker alignment with the strongest (0 0 9) reflections almost parallel to the substrate interface. This is consistent with the broad GADDS distribution observed under these deposition conditions.

The plan-view image in Figure 4.4d shows a similar loss of the a-b plane hexagonal structure. Indeed, several regions within this field of view show in-plane c-axis alignment. The FFT (Fig. 4.4d inset) similarly shows weak 6-fold symmetry, as well as the 2-fold symmetry corresponding to the (0 0 9) planes. Overall, GADDS and HRTEM indicate a randomly oriented nanocrystalline morphology under these deposition conditions.

More detailed structural interpretation is achieved by FFT integration analysis. Figure 4.7a shows a cross-section image of another region within the same film. Overlaid on the image FFT (Fig. 4.7b) are dotted rings corresponding with the expected radii corresponding to c-plane reflections (0.29 nm) and a-b plane reflections (0.28 nm). Intensity distributions as a function of azimutha angle are shown in Fig. 4.7c (c-axis) and Fig. 4.7d (a-b plane). Fig. 4.7c shows 2-fold symmetry excpected for c-axis alignment perpendicular to the substrate, while Fig. 4.7d shows the 6-fold symmetry for c-axis alignment in the plane of the substrate. Similar to the highly aligned film in plan-view, the hexagonal ordering in this region exists with little angular variation across the field of view. Indeed, the orientation of the two domain structures are correlated. Fig. 4.7c

and Fig. 4.7d both exhibit maxima at -100° and 80°, suggesting some form of templating between the two structures, possibly a result of the very similar interplanar spacings.

4.3.3 Nucleation Layer

These HRTEM images confirm the strong alignment of CAAC films. However, the mechanism for nucleation of the nanocrystalline phase is poorly understood. Figure 4.8 shows a cross-section HRTEM of the interface between the highly aligned CAAC IGZO film and the amorphous SiO_2 substrate. Area FFTs of selected regions are shown on the left. Region (a) is the thermally grown SiO_2 substrate surface. Region (b) represents the first few nanometers of deposited IGZO film, with no immediately apparent ordering, which is confirmed by the local area FFT. After ~4 nm of IGZO deposition, CAAC domains (c) appear to nucleate and grow with subsequent deposition. As depositions were conducted with well-stabilized parameters prior to the target shutter opening, this effect is not believed to be due to changes in extrinsic growth conditions. Films deposited under other conditions also exhibited this initally disordered zone of similar thickness, both in the weakly aligned IGZO films of this work and in work by others. HRTEM images of CAAC IGZO films deposited from targets of varying compositions (1:1:1 vs. 4:2:3 In:Ga:Zn cation ratio) both formed this disordered IGZO layer in work done by Yamazaki and colleagues [16].

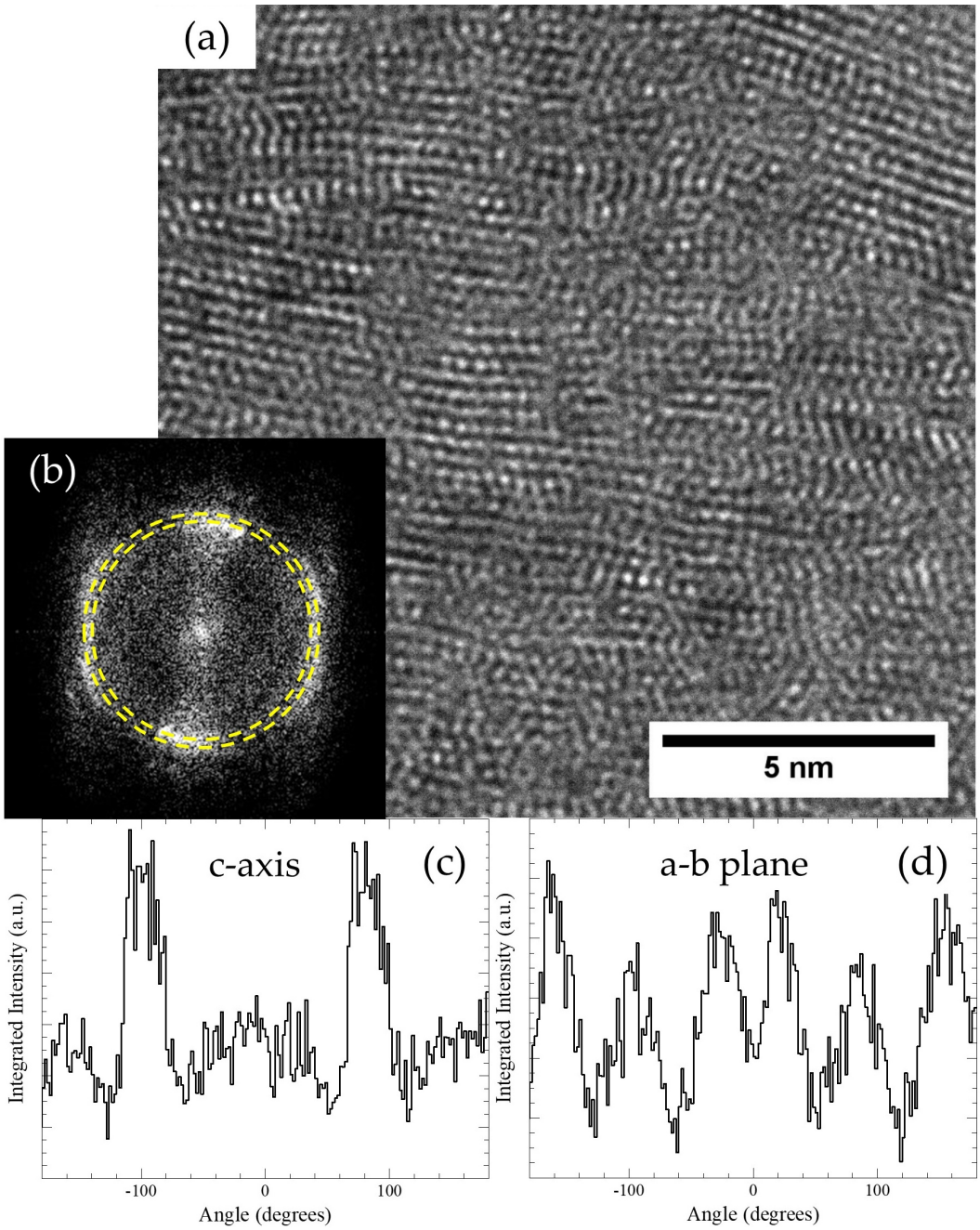

Figure 4.7: (a) Cross-section HRTEM of a weakly aligned CAAC IGZO film. (b) FFT shows multiple alignment orientations. Dotted rings correspond to inter-planar spacing for c-axis (0.29 nm) and a-b plane (0.28 nm) alignments. Intensity distribution plots identify (c) 2-fold symmetry along the inner ring (c-axis) and (d) 6-fold symmetry along the outer ring (a-b plane). Reprinted with permission from [14]. Copyright 2015 John Wiley and Sons.

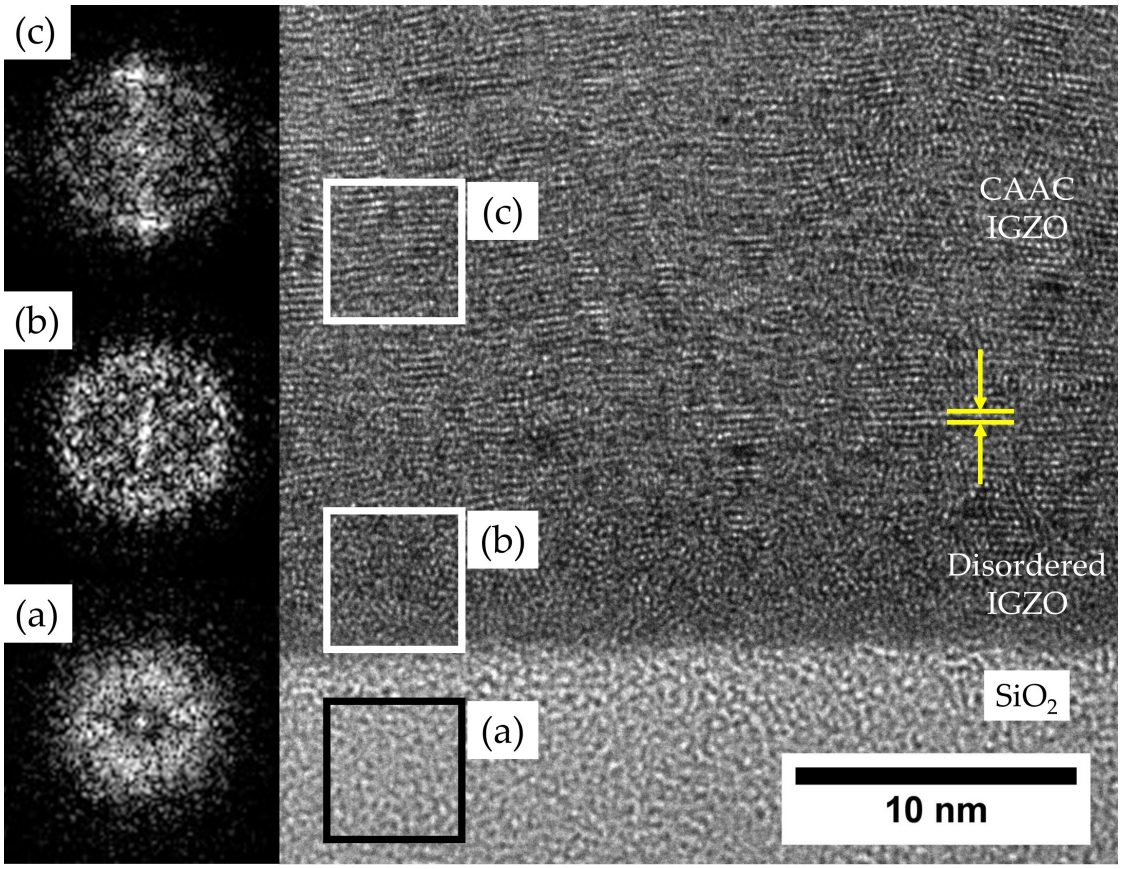

Figure 4.8: Cross-section HRTEM image of highly aligned CAAC at the substrate interface with FFTs of indicated regions: (a) the thermally grown amorphous SiO_2 substrate surface, (b) the first few nanometers of deposited IGZO film, and (c) the bulk film. Reprinted with permission from [14]. Copyright 2015 John Wiley and Sons.

4.4 Discussion: The Growth Mechanism of CAAC IGZO

The observed c-axis texturing of CAAC IGZO films is not uncommon in thin film growth. Other oxide systems, such as ZnO, also form textured films at elevated temperatures on amorphous substrates [170, 171]. Textured film growth on amorphous substrates has also been observed in deposited films of Cu_3N [172], ITO [173], NiAl and Ni-Al-N [174], and several III-V semiconductors [175].

The initial growth of a thin disordered layer prior to crystal nucleation has also been previously observed. The mechanism for growth of textured ZnO by sputtering involves the nucleation of crystallites on an initially disordered (~5 nm) layer; subsequent ordered growth occurs if the substrate temperature is high enough to induce coalescence [32, 176].

It is not immediately clear how the textured crystalline IGZO microstructure forms at 310 °C. The amorphous SiO_2 substrate prohibits epitaxy, and crystallization of IGZO is difficult with post-deposition processing. As-deposited a-IGZO is relatively stable with crystallization requiring temperatures above 700°C [177, 178]. Heating during the deposition process reduces the kinetic limitations of structural formation during growth. At low temperatures, the atomic mobility is insufficient to either form these nuclei or to grow laterally with sufficient speed to coalesce into an aligned film, and amorphous structures are formed. Above 190 °C, the film increasingly adopts the ordered growth as the enhanced atomic mobility near the surface of the growing film enables the coalescence of crystalline domains. At high temperatures, above 310°C, nucleation occurs more readily even on the surface of existing IGZO material, resulting in reduced CAAC alignment. In addition, compositional analysis of the films, measured using energy-dispersive X-ray spectroscopy (EDS) and inductively-coupled plasma optical emission spectroscopy (ICP-OES), shows steadily decreasing Zn concentration with increasing deposition temperatures (see Fig. 3.5). This suggests a potential coupling between temperature and Zn concentration effects on grain nucleation.

The influence of the oxygen fraction during deposition is more subtle. Film composition measurements show the Zn concentration increasing sharply be-

tween 0% and 10% O_2 fractions, with a subsequent small decrease above 70%. The initial sharp increase corresponds to the alignment seen in GADDS measurements as more oxygen is incorporated into the film. The subsequent preferential loss of Zn correlates with the decreasing film texturing (increasing GADDS FWHM) above 70% O_2 (see Fig. 3.8) and is attributed to the effects of substrate resputtering due to the increasing concentration of ionized oxygen. This effect has been studied and demonstrated in other sputtered mixed oxide systems, as with the preferential removal of Cu from $YBa_2Cu_3O_x$ films with oxygen resputtering [179]. While it is apparent that the nucleation of grains appears much easier at high O_2 fractions, the direct link between oxygen resputtering, Zn concentration, and alignment remains unclear.

Deposition rate also fell steadily with increasing O_2 fraction, decreasing by a factor of 3 from 10% O_2 to 100% O_2; this is attributed to the reduced average mass of ions bombarding the sputter target. To determine the impact of deposition rate, films were deposited with varying RF power between 100 W and 200 W (310°C/10% O_2) to achieve deposition rates of 2–5 nm/min. Films exhibited no change in XRD or GADDS scans, and it is concluded that the deposition rate has no effect on film morphology over this range.

Under conditions examined in this study, HRTEM shows nucleation of CAAC only after ~5 nm of disordered IGZO growth. Understanding this intermediate layer is crucial to understanding the CAAC nucleation. Stresses developed during deposition in this initially disordered IGZO layer may provide sufficient driving force at elevated temperature to induce crystal nucleation. Such behavior would suggest a critical stress above which it becomes thermodynamically favorable to form crystalline domains.

Others have offered alternative explanations for this region of disordered growth. Kawata *et al.* [180] attributed this effect to interdiffusion between the IGZO film and the SiO_2-coated substrate with justification from time-of-flight secondary ion mass spectroscopy (ToF-SIMS). However, significant interdiffusion (~5 nm) with a high-quality SiO_2 at a low temperature of only 300°C is unlikely, and those measurements were performed near the depth resolution limit for SIMS [181]. The source of the SiO_2 layer is also unclear; the 3 nm thick SiO_2 layer [16] is too thick to be a native oxide layer (~1 nm) [182], and poorer-quality SiO_2 films (such as from plasma oxidation or low-temperature PECVD) may lead to the effects observed. Further, their HRTEM images clearly show that the thickness of the disordered IGZO region depends upon sputter geometry, supporting a growth mechanism moderated by the deposition environment.

While the mechanism is not fully understood, modern theories of glass formation may address the interesting microstructures observed [183]. Ast [148] has proposed an interesting hypothesis on the formation of CAAC IGZO as the result of a Boolchand-Phillips-Thorpe glass phase transformation in the context of topological constraint theory [184] that is consistent with these results. Further study is necessary to understand the complex nature of the transition between disordered and CAAC IGZO.

Yamazaki [16, 141, 146, 185] also proposed an alternative growth mechanism for CAAC IGZO in which crystalline domains are not formed by the classical nucleation method, but rather originate from 1–3 nm "pellets" (~84 atoms per cluster) cleaved directly from the target during sputter deposition. This hypothesis is based on three central concepts. First, the final microstructure of a CAAC IGZO film exhibits a high degree of a-b plane alignment over relative long dis-

tances (>10 nm). Second, IGZO crystalline domains tend to grow more rapidly within the a-b plane rather than in the c-axis direction, also supported by other studies [168]. Third, cleavage along the IGZO (0 0 1) plane requires much less energy than cleavage along any other crystallographic plane [16].

However, no firm justification for the assumption of the production of a nano-sized pellet is given, and well-established sputter theory and existing sputter literature support the contrary. The most widely accepted mechanism for the sputtering process, described theoretically by Sigmund [153] (see also: Chapter 3), is an entirely atomic collision-recoil process. The primary species ejected from the target would therefore be atomic species. While it is possible that some species ejected are multi-atomic clusters of ≥2 atoms, Gnaser and Hofer found that the yield of clusters decays exponentially with cluster size [155]. While even larger clusters have been experimentally demonstrated using mass spectroscopy at high ionic energies (using Xe as the bombardment gas with an acceleration potential of 10 keV, compared to ~1 keV Ar typically used in laboratory sputter systems), the yields of these larger clusters are several orders of magnitude lower than for atoms and small clusters [186]. It is therefore much more likely that the predominant species deposited on the substrate are atomic (or very small cluster) species. Even if large pellets were formed, they would be quickly buried by the orders-of-magnitude higher rates of atomic species being deposited.

This initial disordered structure has also potentially significant device implications. As TFT properties are strongly influenced by the structure of the channel/gate dielectric interface, bottom-gate TFTs fabricated from CAAC IGZO may exhibit inferior transport properties despite the nanocrystalline struc-

ture in the bulk of the film. Essentially all CAAC IGZO literature presents electrical characteristics, such as extremely low leakage currents, low threshold instabilities, and mobilities of ~10–20 cm^2/Vs, measured using top-gate TFTs [16, 87, 167]. These results hint that access to novel electronic properties offered by CAAC IGZO may require carrier transport in the nanocrystallized bulk far from the substrate interface.

4.5 Conclusions

This study of the deposition conditions of textured nanocrystalline IGZO by reactive RF magnetron sputtering has identified optimal growth conditions for highly aligned CAAC IGZO and the formation regimes of various microstructures in IGZO thin films. Deposited at low substrate temperatures and O_2 fractions, films exhibit amorphous characteristics. Above 190°C and 5% O_2 fraction, CAAC begins to form with increasing alginment as the temperature is increased. At optimal conditions of 310°C and 10% O_2, films exhibit long-range ordering and alignment with local distortions. These films more closely resemble a single crystals in HRTEM images than previously reported. At higher temperatures or in higher O_2 fractions, above 310°C or 70% O_2, film texturing decreases as c-axis alignment is lost and films adopt a more random microstructure.

We propose a nucleation and growth model similar to that of ZnO on amorphous substrates. During the initial stages of deposition, disordered material forms before nuclei are able to coalesce. Film stresses in this disordered intermediate layer may provide the driving force required for CAAC nucleation

with elevated temperatures required to achieve strong texture. Continuous nucleation events at high temperatures, however, leads to a reduction in c-axis alignment and more random microstructure. Oxygen also plays a critical role in the formation of CAAC films, but extremely high O_2 fractions leads to the degradation of the texture. This is attributed to increased oxygen resputtering coupled with a decrease in the Zn concentration of the resultant film. These results indicate that grain nucleation occurs more readily at high O_2 fractions.

CHAPTER 5

EFFECT OF FILM MORPHOLOGY ON IGZO TFT ELECTRICAL CHARACTERISTICS

5.1 Introduction

The observed microstructure of CAAC IGZO presentes several materials research challenges. With regard to the fundamental structure, the nature of the boundary between crystalline domains remains poorly understood [16, 141, 146, 185]. Diffraction data exhibits the characteristic $InGaZnO_4$ (0 0 9) peak, but expected (0 0 3) and (0 0 6) peaks corresponding to the superlattice of InO planes are apparently missing. Further, published mobility values are typically closer to a-IGZO values than values for single crystal films [7, 16, 63]. Indeed, the advantage of CAAC IGZO TFTs seems to be largely driven by the added threshold stability and low-leakage currents, demonstrated in the initial reports, and are attributed to the improved crystallinity of the film. However, very little is known regarding the effect of film morphology on the device properties.

Most studies on CAAC IGZO have been performed on films sputtered from a 1:1:1 In:Ga:Zn (stoichiometrically balanced for $InGaZnO_4$) [16, 141, 146, 185], and TFTs fabricated from these films exhibit mobilities of ~10 cm^2/Vs. However, the vast majority of IGZO device studies have focused on the Zn-deficient composition of 2:2:1 In:Ga:Zn, presumably due to the higher relative In_2O_3 fraction leading to high carrier mobilities, typically higher than those reported for CAAC IGZO films. ($\geq$10 cm^2/Vs). More recently, CAAC IGZO films of other compositions have also been reported, such as 4:2:3 In:Ga:Zn [16], which retain the average 1/3 Zn cation concentration, but increase the relative In fraction to

achieve higher mobilities of ~20 cm^2/Vs.

Over the many studies in literature, there is considerable variation in the TFT geometry, deposition conditions, and device parameter extraction techniques used, and there are no systematic studies on the effect of substrate temperature and composition performed under identical, reproducible conditions. This study investigates the effect of substrate temperature during IGZO deposition on the film microstructure and device characteristics for both a high-Zn (1:1:1 In:Ga:Zn cation ratio) and a low-Zn (2:2:1 In:Ga:Zn) target. In total, 18 conditions were investigated for these two target compositions at nine different temperatures, as shown in Table 5.1. For each condition, film samples that underwent X-ray characterization were deposited on the same substrate as the films used for device fabrication. Upon removal from the deposition system, substrates were sectioned into two pieces: one piece for film characterization (XRD, GADDS, and EDS) and one piece for device fabrication and characterization. In an attempt to further minimize systemic errors, all devices were fabricated simultaneously over a period of several days. As an extention of the structure study discussed in Chapter 4, this chapter provides a detailed comparison of the structural differences arising from the different compositions from X-ray diffraction studies as a function of substrate temperature. These results are correlated with the changes observed in electron mobility, extracted from DC *IV* measurements of IGZO TFTs.

Table 5.1: Temperatures investigated in this work.

Temperature Set Point (°C)	Actual Temperature (°C)
Off	25
250	195
300	230
350	260
400	285
450	315
500	340
550	360
600	385

5.2 Results

For films sputtered from each target, film crystallinity and crystallographic texturing were determined as a function of deposition temperature using θ-2θ XRD and GADDS, respectively. A summary of these results are shown in Figure 5.1.

The data shown for films sputtered from the Zn-rich target in Fig. 5.1a is consistent with the findings discussed in Chapter 4. Crystalline domains begin to coalesce at 195°C and form at elevated temperatures up to a maximum near 315°C, manifesting as an increase in the normalized XRD intensity. However, above 315°C, the XRD signal decreases due to loss of crystallographic alignment, observed as an increase in the characteristic width (FWHM) of the GADDS distribution.

In contrast, while films sputtered from the Zn-deficient target in Fig. 5.1b exhibited the onset of crystalline formation near the same temperature (195°C) and increasing crystallinity under higher-temperature conditions, the maximum peak intensity is far smaller for Zn-deficient films than for Zn-rich films

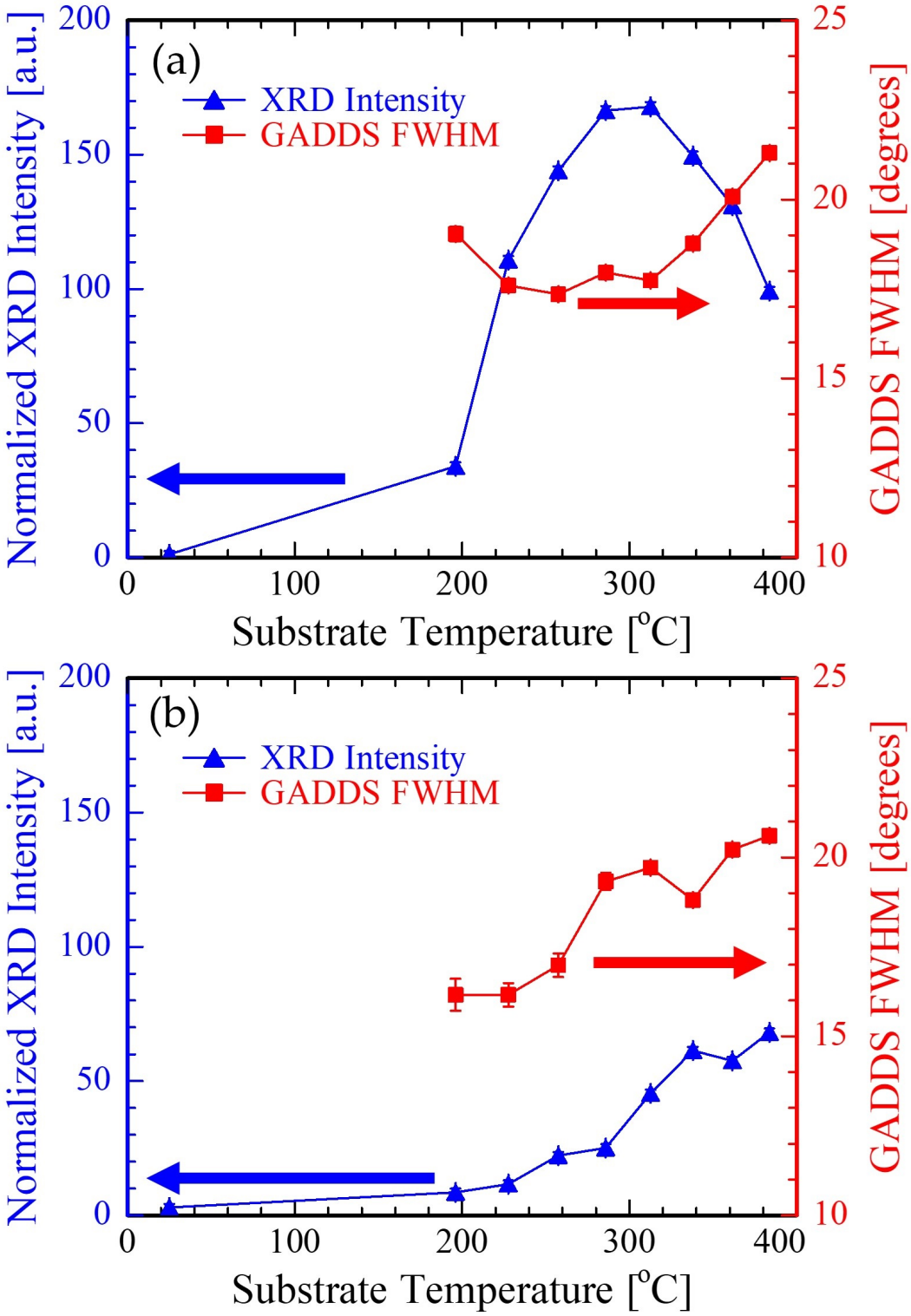

Figure 5.1: Summary of X-ray diffraction measurements of (a) Zn-rich IGZO films deposited from a 1:1:1 In:Ga:Zn IGZO target and (b) Zn-deficient IGZO films deposited from a 2:2:1 In:Ga:Zn IGZO target.

(roughly half). This indicates the inhibition of crystalline growth in Zn-deficient systems, supporting the hypothesis [13, 14] that the growth mechanism in CAAC IGZO films requires a critical Zn fraction to drive crystallization.

The Scherrer Equation (eq. 3.4) provides a simple estimate of the average crystalline domain size in samples measured by XRD. Figure 5.2 shows the minimum estimated grain size as a function of deposition temperature for films deposited from both targets. For Zn-rich films, roughly 2 nm crystalline domains form at the lowest substrate temperatures 195°C. Grain size increases slowly as a function of temperature up to a maximum of ~3 nm around 360°C, consistent with the trends observed in Chapter 4. In Zn-deficient films, although there is increased noise in the data (due to a lower crystalline signal), grain sizes are estimated to be ~2 nm and roughly temperature-independent. The correlation of crystallinity and grain size in each film is more clearly seen in Figure 5.3, which displays the estimated grain size as a function of crystallinity (XRD intensity) for both film sets. It is clear from this data that, while grain size in Zn-rich films generally increase with improved crystallinity, Zn-deficient films remain relatively amorphous, and the low scattering intensities in these films result in the large noise in the data.

Figure 5.4 shows the electron mobility extracted from IGZO TFTs fabricated from Zn-rich and Zn-deficient IGZO films as a function of deposition substrate temperature. Devices fabricated from low-Zn films generally exhibit a higher carrier mobility than those fabricated from high-Zn films, consistent with the general findings from literature data. In low-Zn devices, for active layer depositions performed at room temperature, devices yield a low mobility of about 3 cm^2/Vs. With the introduction of heating during deposition, carrier mobility

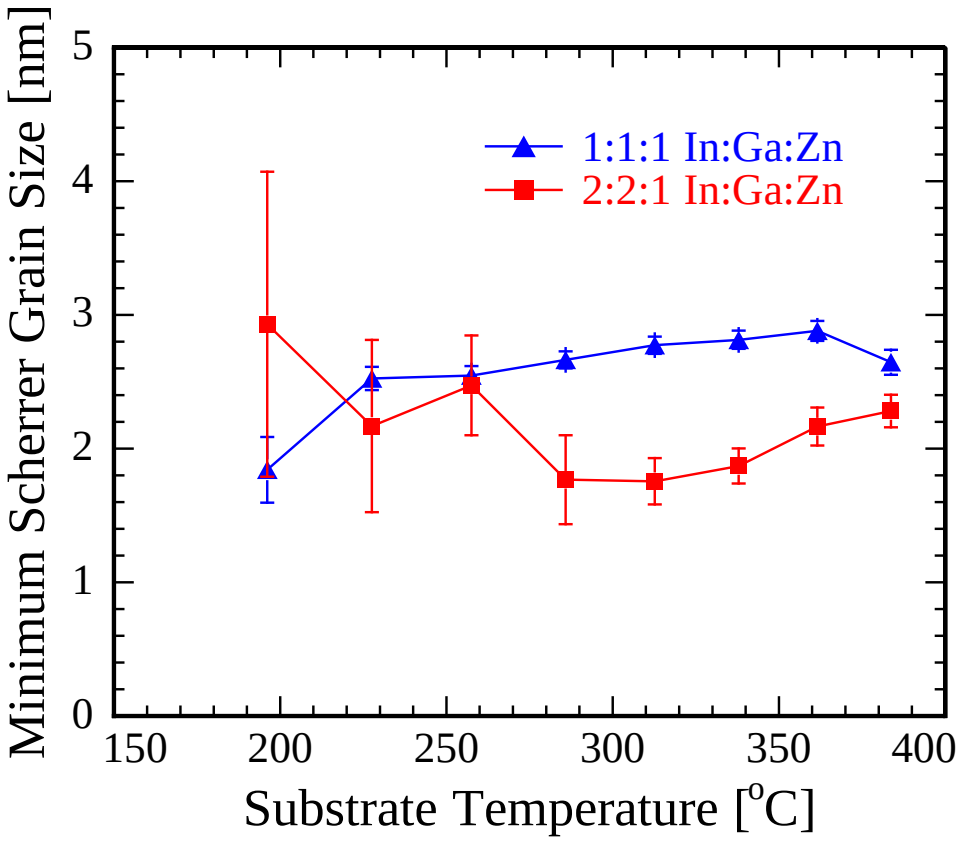

Figure 5.2: Minimum grain size estimated using the Scherrer equation (K = 0.9, λ = 0.154 nm) for films deposited from the Zn-rich target (blue) and the Zn-deficient target (red).

increases to 7–9 cm^2/Vs. In the high-Zn devices, active layers deposited at room temperature have mobilities near zero, but with the introduction of heating increases to about 2 cm^2/Vs. The mobility saturates at this value until higher substrate temperatures: the mobility increases to about 3 cm^2/Vs at 360°C and increases nearly five-fold to 9 cm^2/Vs at 385°C.

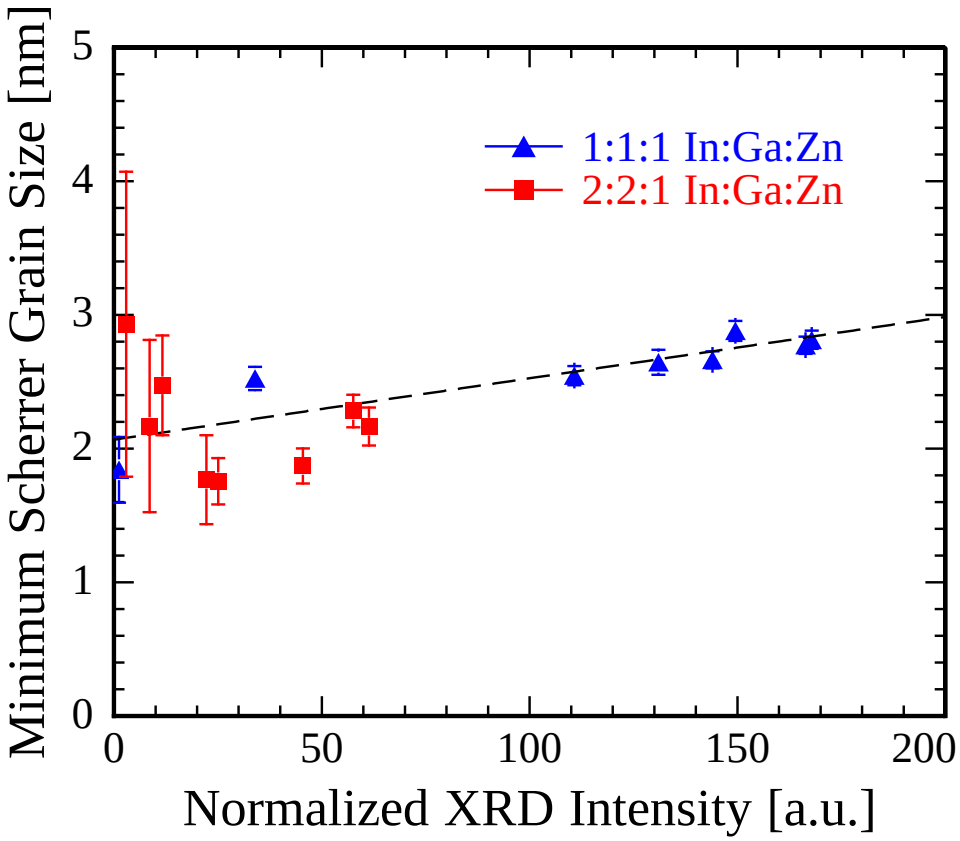

Figure 5.3: Scherrer grain size as a function of the normalized XRD intensity, a measure of crystallinity, for films deposited from Zn-rich (blue) and Zn-deficient (red) targets. The dashed line (a fit to the Zn-rich dataset) is provided as a guide to the eye.

5.3 Discussion

In comparing Fig. 5.4 to Fig. 5.1a and Fig. 5.1b, the initial increase in mobility in annealed films (between room temperature and 195°C) corresponds well with the onset of crystallinity. However, it is unclear whether this is due solely to the crystallization of the films or due to other densification effects. Intermediate temperatures between room temperature and 190°C are not readily accessible reliably on the sputter system used in this study due to temperature fluctuations

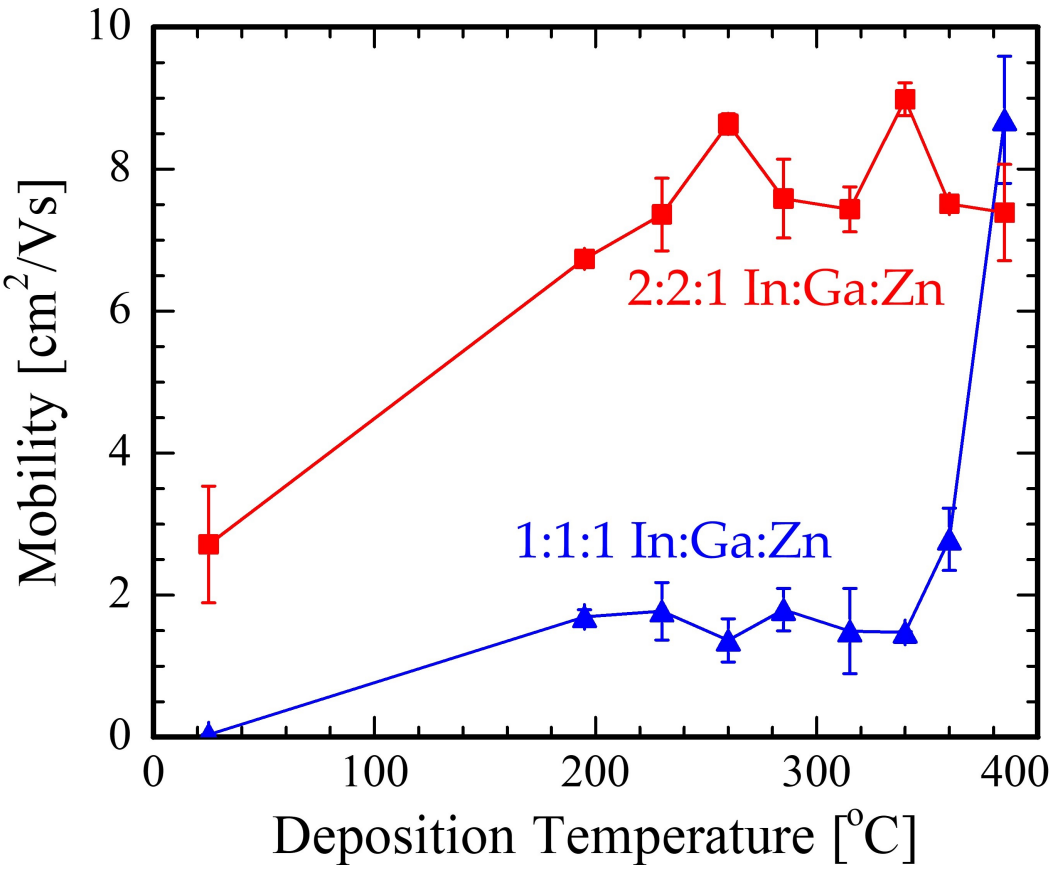

Figure 5.4: IGZO carrier mobility extracted from measured TFT *IV* characteristics for films deposited from Zn-rich (blue) and Zn-deficient (red) targets.

in the temperature controller. Comparison with measured cation fraction values (using EDS) as a function of temperature (Figure 5.5 and Figure 5.6) suggest that this effect is not due to change in composition, instead showing a gradual decrease in Zn fraction over a temperature range where mobility remains essentially constant.

Nevertheless, the mobilities of the low-Zn films are consistent with published values in literature for a-IGZO films of the same composition (near 10 cm^2/Vs). The high-Zn films however, with mobilities <5 cm^2/Vs, more closely resemble a-IGZO devices of similar composition than CAAC IGZO de-

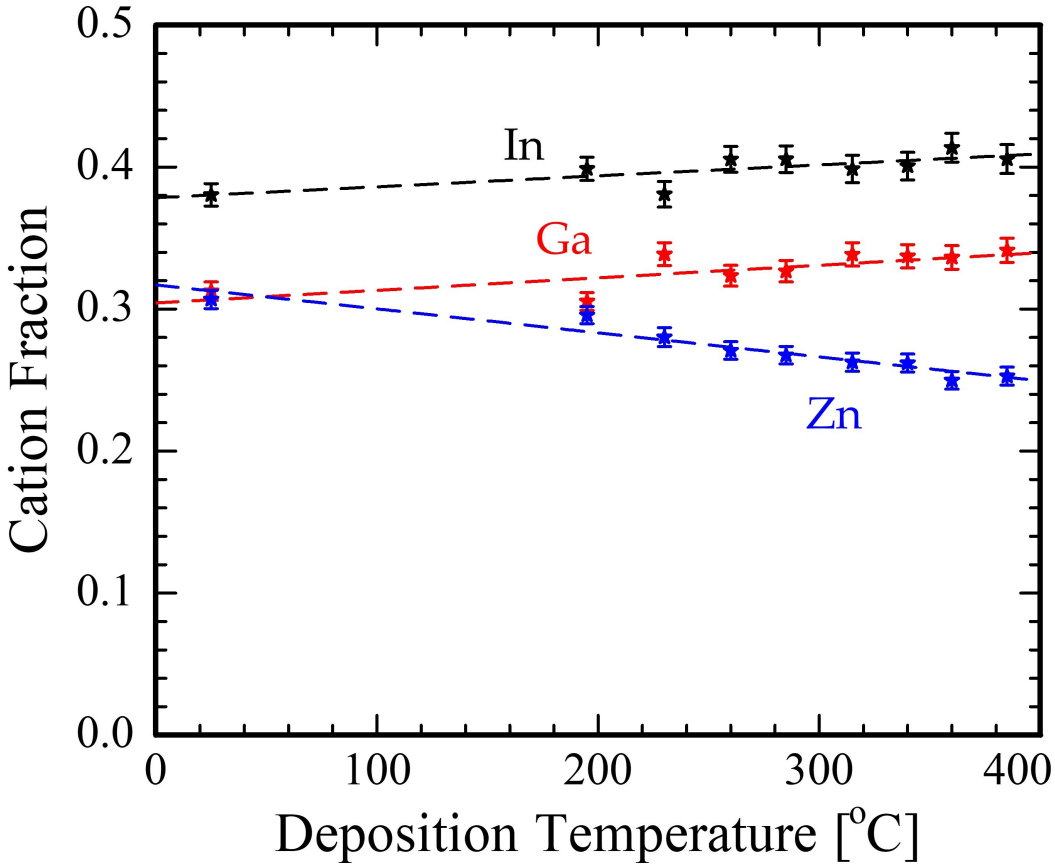

Figure 5.5: Cation fraction in the films deposited using the 1:1:1 In:Ga:Zn IGZO target as a function of temperature. Measurements were taken by calibrated EDS.

vices of similar composition (~10 cm^2/Vs) [16]. It is important to note that the devices measured in this study were constructed as inverted-staggered bottom-gate TFTs, while in other studies top-gate TFTs were used [16, 87, 167]. This is consistent with the hypothesis presented in Chapter 4: the ~5 nm nucleation layer of disordered IGZO at the semiconductor-dielectric interface is expected to exhibit electronic characteristics different than those in the bulk CAAC IGZO film structure. In contrast, top-gate TFTs with a crystalline semiconductor-dielectric interface are expected to exhibit bulk CAAC carrier transport closer to single crystalline values. However, the observed ~10 cm^2/Vs mobilities for

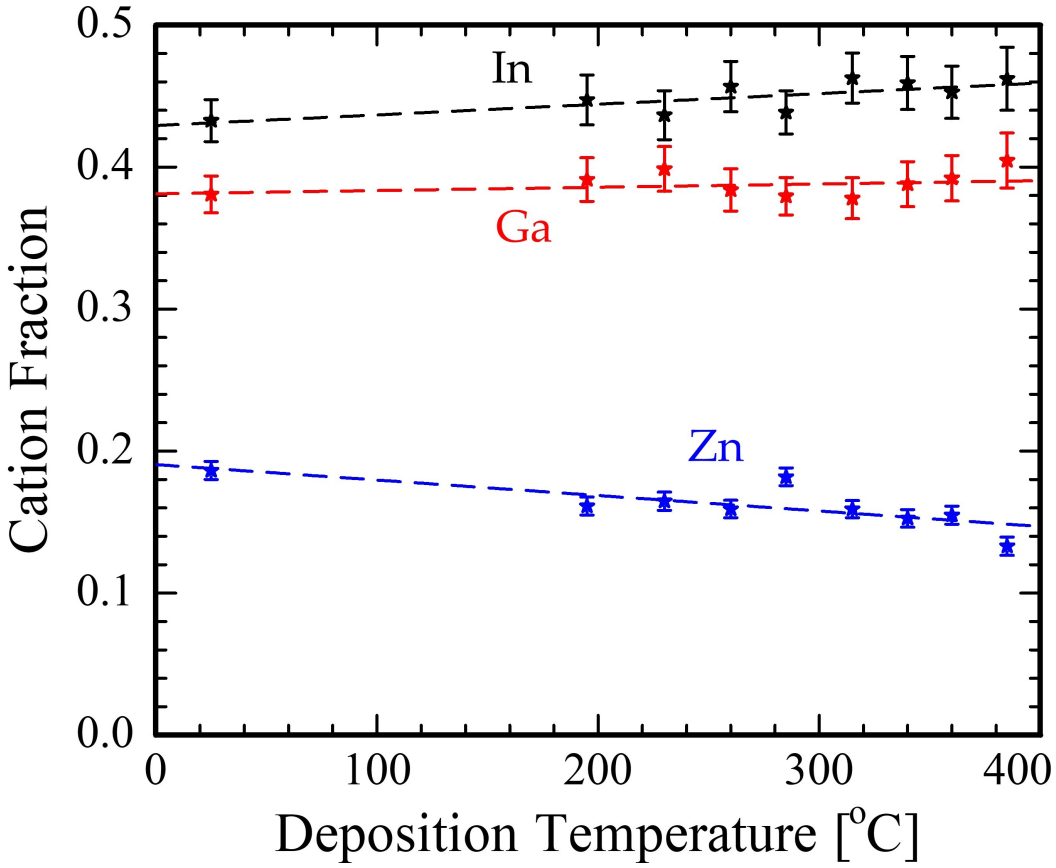

Figure 5.6: Cation fraction in the films deposited using the 2:2:1 In:Ga:Zn IGZO target as a function of temperature. Measurements were taken by calibrated EDS.

CAAC films is still far below the expected 80 cm^2/Vs values for single crystal films.

Interestingly, at high temperatures above 340°C, the mobility of high-Zn films sharply increases, which occurs above the transition from highly ordered CAAC IGZO to polycrystalline IGZO (~310°C in Fig. 5.1a). We believe that the film texture quality does not cause this mobility effect. Instead, this effect is likely linked to the disordered nucleation layer. As the mobility in high-Zn films reach ~10 cm^2/Vs at the highest deposition temperature—the same as expected from top-gate TFT studies—we believe that this may represent a critical temper-

ature where the thickness of the disordered layer is diminished and bottom-gate TFTs approach the behavior of top-gate TFTs.

5.4 Conclusions

In this work, a systematic study of structural and electronic properties is presented as a function of sputter target composition and substrate temperature. It was found that, while high-Zn films readily formed CAAC upon heating during deposition, low-Zn films retain low-crystallinity, small-domain structures even at the highest deposition temperature of 380°C. Carrier mobility in the base films are also seen to depend strongly on the composition, with low-Zn films exhibiting nearly four times the mobility of high-Zn films. At the highest temperature conditions, the mobility of CAAC IGZO (high-Zn) films is observed to rise rapidly, attributed to the reduction of the thickness of the disordered nucleation layer as new crystalline domains can nucleate and grow more readily at these high temperatures.

CHAPTER 6

PHASE FORMATION AND CRYSTALLIZATION KINETICS IN THE $InGaO_3(ZnO)_m$ HOMOLOGOUS SERIES USING LASER SPIKE ANNEALING

6.1 Introduction

Recent structural studies of IGZO are focused primarily on the development of the CAAC microstructure [13, 14, 16, 142, 146, 185]. CAAC is normally formed in the $InGaZnO_4$ composition, which yields highly aligned, near-crystalline films. However, this composition is just one of a series of potential compositions in the ternary phase diagram, and CAAC will form over significant portion of the space near this equimolar composition. We can also view $InGaZnO_4$ as one member of a pseudobinary range of compositions along the $InGaO_3(ZnO)_m$ composition line. The structure of this broader class of homologous compounds is complex; very little is known regarding these compositions, and the kinetics of their formation have not been widely investigated. Even in this portion of the ternary system, work has concentrated on the integer m structures which have well-defined crystal structures, and that data has been obtained primarily by heating powder samples for several days [49–52]. Beyond these near-equilibrium studies, virtually nothing is known regarding the mechanism for structure formation in this pseudobinary system.

Much of the difficulty in discussing the compositions is due, in part, to limitations in thermal processing and structural characterization techniques. Conventional furnace annealing and rapid thermal processing typically occurs on timescales ranging from several seconds to several hours, overlooking the

critical early phases of the structural development. On the extremely short timescales, films have been studied after heating on the order of tens of nanoseconds through pulsed excimer laser annealing [187–189]. These timescales are generally too short to observe solid phase changes and instead require transition to the melt (similar to the limitations for silicon processing). It is likely, however, that thermal processing on millisecond timescales could achieve solid-phase structural development leading to understanding of the phase development kinetics.

Laser spike annealing (LSA), a technique used for over a decade to activate dopants in silicon and other semiconductors [190], is capable of annealing on the millisecond timescale [191] and has been shown to be effective at bridging the thermal processing gap between the nanosecond and the second regimes. LSA has been extended by Bell *et al.* [12] to high-throughput thermal processing studies by exploiting lateral temperature gradients across the annealing beam in a variant termed lateral gradient LSA (lgLSA); this technique has enabled study of material propertes as a function of both annealing time and temperature. As an example, Chung *et al.* [65] used this technique to explore a-IGZO TFTs and demonstrated the fabrication of metastable high-mobility devices.

The lgLSA technique requires use of spatially-resolved characterization techniques to probe properties as a function of the peak annealing temperature across an lgLSA stripe. For understanding phase development, structural characterization by X-ray diffraction (XRD) or electron diffraction using transmission electron microscopy (TEM) are commonly used. While typical lab-scale XRD equipment enables fairly quick characterization turnaround (minutes – hours), these tools are usually limited in spatial resolution to mm or cm scales,

limiting their use with the lgLSA techniuqe. TEM-based electron diffraction has the requisite spatial resolution, but is difficult to use routinely due to time-intensive sample preparation. However, wide angle X-ray scattering (WAXS) measurements using a focused synchrotron source (12 μm lateral dimensions) addresses both the spatial resolution and signal intensity requirements for structural interrogation across the lgLSA thermal profile.

In this work, the lgLSA technique was used to characterize the annealing behavior of IGZO films deposited with a one-dimensional concentration gradient. These composition gradients were generated by co-sputtering from a 2:2:1 In:Ga:Zn IGZO and a ZnO target. Annealing durations were explored over two orders of magnitude in timescale with peak temperatures up to 1200°C. Microbeam focused WAXS measurements were used to determine the structural development as a function of lgLSA position (temperature) across the thermal gradient. These data provide insight into the nature of the as-deposited structure of IGZO films with varying Zn concentration, the development of various phases in the $InGaO_3(ZnO)_m$ homologous compound series, and the local defect chemistry supported in these structures. A model for the formation and growth of IGZO crystalline structures, consistent with these observations and others in the literature, is developed.

6.2 The Equilibrium Crystal Structure of $InGaO_3(ZnO)_m$

In this section, key structural motifs that occur in the crystal structure of $InGaO_3(ZnO)_m$ are discussed. For integer values of m, the $InGaO_3(ZnO)_m$ structure can be understood as a modified ZnO wurtzite structure with the follow-

ing key differences: (1) In atoms segregate to form In_2O_3 sheets, with Zn and Ga adopting a random solution on intervening cation sheets; (2) cation vacancies coalesce within the Zn/Ga layers to form vacant cation planes (relative to the ideal wurtzite structure); and (3) Zn/Ga cations in these sheets align to "distorted" tetrahedral sites (again relative to the ideal tetrahedral sites in the wurtzite structure).

Figure 6.1 shows a space-filling model of the ZnO ($m = \infty$) wurtzite structure, highlighting the hexagonal symmetry and hexagonal close-packed (HCP) anion sublattice arrangement; Zn cations are arranged on tetrahedral sites within the oxygen sublattice (Figure 6.1c). Figure 6.2 shows a simlar space-filling model for the $InGaO_3(ZnO)$ ($m = 1$) phase, highlighting the critical changes from the ZnO structure. In the $m = 1$ phase, indium atoms are arranged into pure In_2O_3 planes adopting octahedral coordination within the anion sublattice (Fig. 6.2b, marked by the magenta lines). These In_2O_3 planes give rise to strong low-angle superlattice peaks in X-ray diffraction due to the relatively high atomic number Z of indium. Between these In_2O_3 planes, remaining Zn and Ga atoms are arranged on two $(Zn, Ga)O_x$ planes spaced evenly between the In_2O_3 planes. This structure changes with m as shown in Figure 6.3; as m increases, the In_2O_3 planes become increasingly separated with the equilibrium structure exhibiting $(m + 1)$ $(Zn, Ga)O_x$ planes between the In_2O_3 planes. Zn and Ga in ideal tetrahedral sites are shown for comparison in Fig. 6.2b; however, in reality, these atoms occupy "distorted" tetrahedral sites.

The distortion of Zn and Ga from ideal tetrahedral positions is a key structural difference from the wurtzite motif. Figure 6.4a shows an enlarged region of the ZnO wurtzite structure, and Figure 6.4b shows the modified wurzite struc-

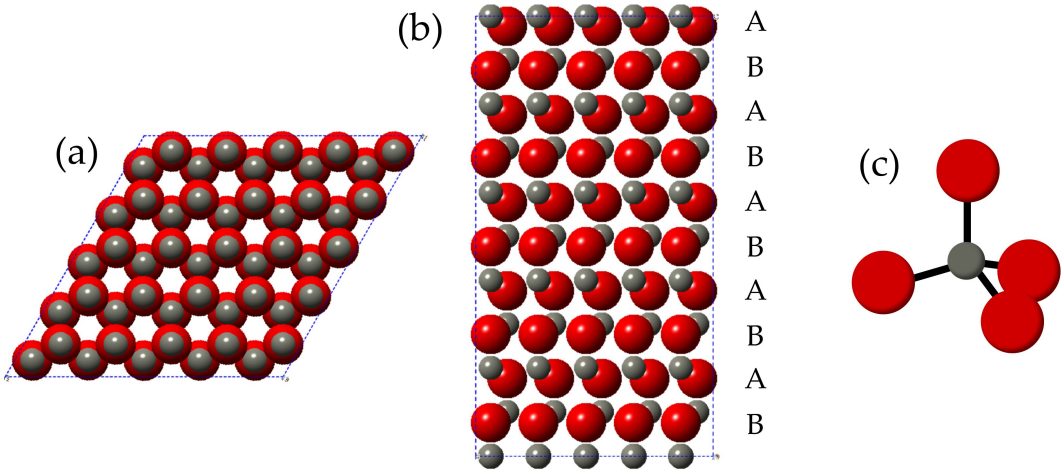

Figure 6.1: Space-filling model of the ZnO wurtzite structure (a) along the (0 0 1) zone axis and (b) along the (1 0 0) zone axis, where the HCP-like stacking of oxygen sublattice planes is labeled. (c) Schematic showing Zn on a tetrahedral site within the oxygen anion sublattice.

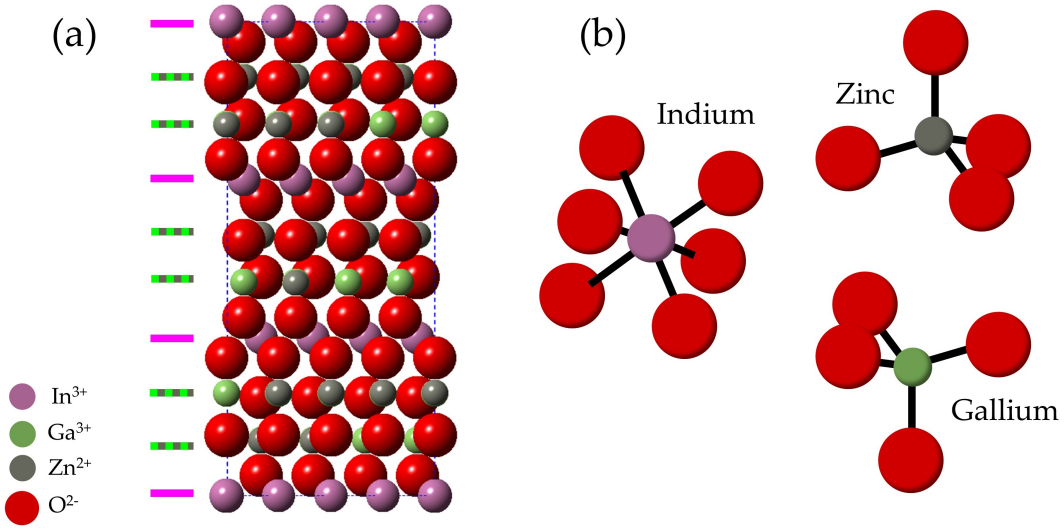

Figure 6.2: (a) Space-filling model of the $InGaO_3(ZnO)$ (m = 1) structure along the (0 0 1) zone axis. Cation planes are indicated by the lines to the left, with magenta representing pure In_2O_3 planes and dotted green/gray representing $(Zn, Ga)O_x$ planes. (b) A schematic showing the position of cations in the structure. Indium adopts 6-fold coordination and is located at octahedral sites in the anion sublattice. Gallium and zinc adopt an arrangment similar to the ideal tetrahedral arrangement shown here, but with distortions that are discussed in the text.

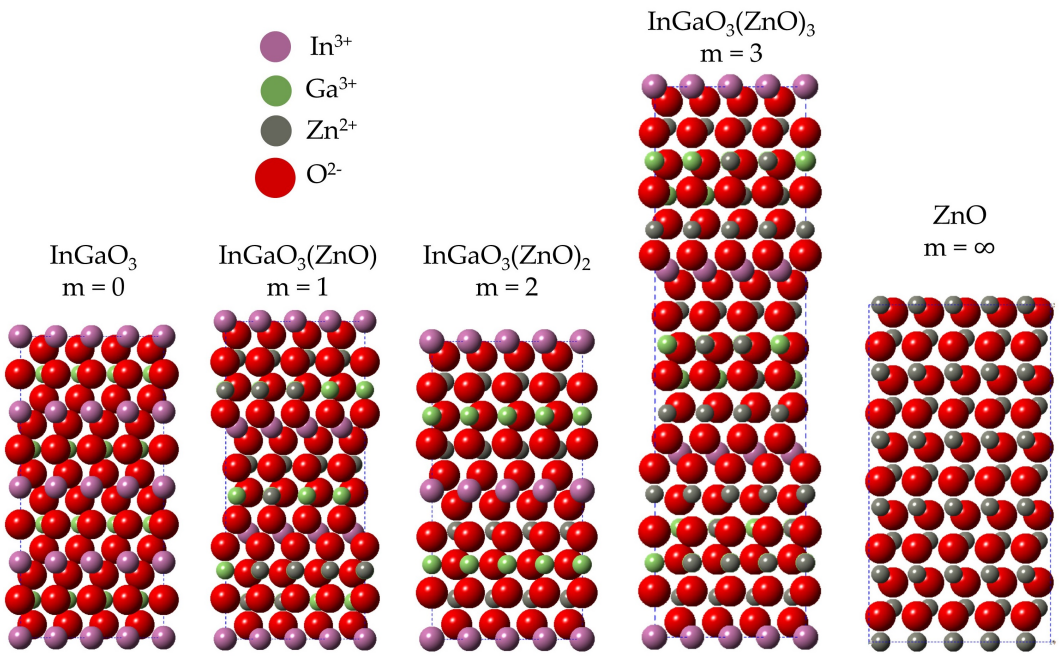

Figure 6.3: Selected structures from the $InGaO_3(ZnO)_m$ homologous structure series: $InGaO_3$ ($m = 0$), $InGaO_3(ZnO)$ ($m = 1$), $InGaO_3(ZnO)_2$ ($m = 2$), $InGaO_3(ZnO)_3$ ($m = 3$), and ZnO ($m = \infty$). Structural data from Refs. [2–4].

ture with In and Ga substitution (for an $m = 1$ composition) and In atoms located on octahedral sites within the oxygen sublattice. This direct substitution of In and Ga into the ZnO crystal structure is not charge balanced as Zn cations are 2+ charged while In and Ga cations are 3+ charged. The higher-valence cations are hence accomodated by cation vacancies, which ultimately coalesce into a complete plane for integer m. When the center $(Zn, Ga)O_x$ plane in Figure 6.4b is removed and the structure is allowed to relax, the remaining $(Zn, Ga)O_x$ planes distort from their ideal tetrahedral sites toward the observed equilibrium positions shown in Figure 6.4c.

To summarize, the equilibrium structure of $InGaO_3(ZnO)_m$ can be considered as a modified wurtzite structure with an alternating stacking pattern of cation planes as labeled in Figure 6.4c. Indium atoms are arranged on octa-

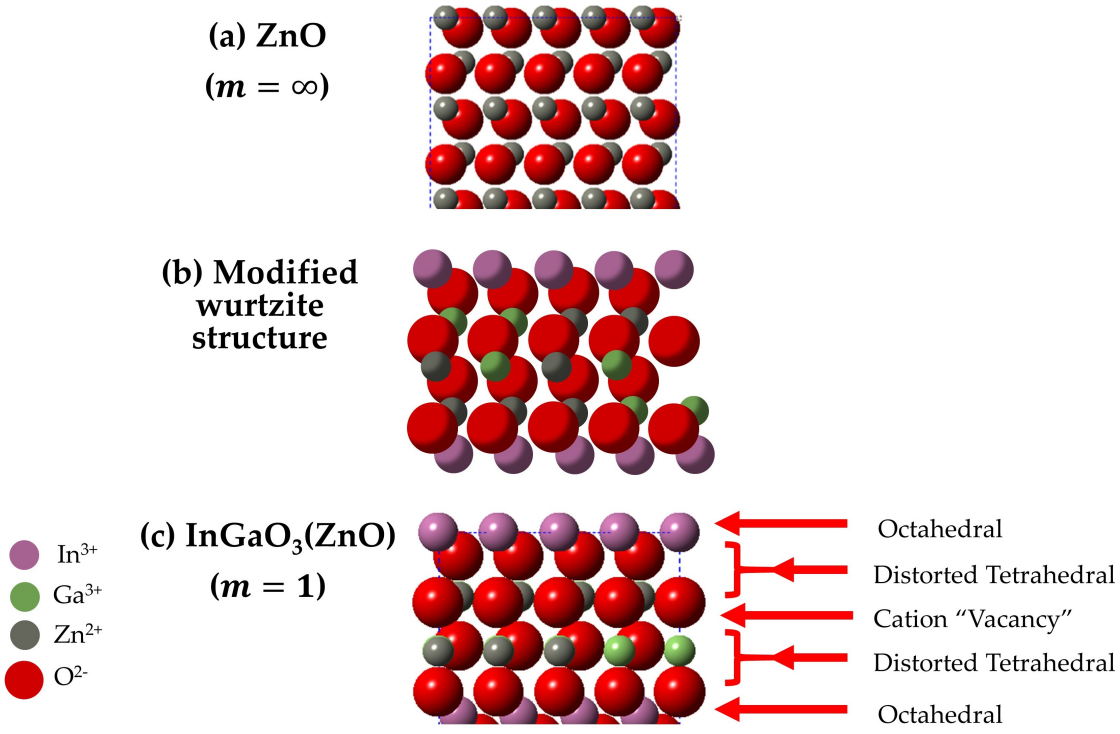

Figure 6.4: Comparison of the (a) ZnO wurtzite structure and (c) $InGaO_3(ZnO)$ structure ($m = 1$). (b) A hypothetical modified wurtzite structure in which In atoms occupy octahedral sites, but with an excess of $(Zn, Ga)O_x$ planes. In (c), the various cation plane types are identified.

hedral planes, while Ga and Zn are arranged on distorted tetrahedral planes. Cation "vacancy" planes, relative to the ZnO wurtzite structure, form to satisfy charge balance. This plane is most clearly seen for the $m = 1$ structure. The In_2O_3 plane superlattice gives rise to low-angle (low-q) peaks, as shown in the calculated diffraction patterns in Figure 6.5.

The driving force for the formation of this layered structure depends upon the balance between entropy (which drives the system toward a random solution) and enthalpic considerations (which drives the ordering). While some studies address particular aspecs of the thermodynamics of phase formation in $InGaO_3(ZnO)_m$ [57], no complete energetic picture exists. However, comparing

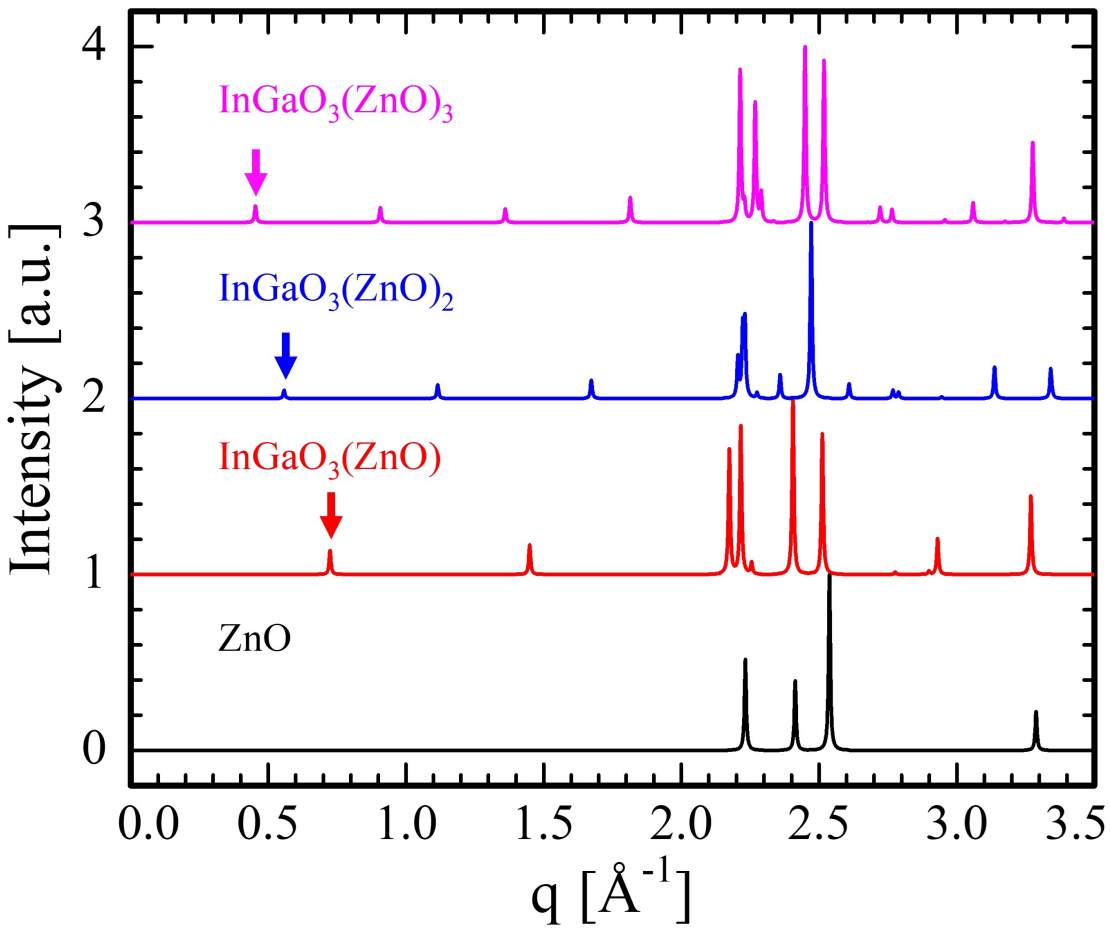

Figure 6.5: Calculated powder diffraction patterns for ZnO and $InGaO_3(ZnO)_m$ ($1 \leq m \leq 3$). Arrows mark the primary scattering peaks that arise from the In_2O_3 planes. Patterns were calculated using CrystalDiffract [15]. Structural data from Refs. [2–4].

$InGaO_3(ZnO)_m$ with other similar compounds provides insight into the defect energetics in these materials.

$InGaO_3(ZnO)_m$ belongs to yet a wider class of isostructural materials with the chemical formula $InMO_3(ZnO)_m$, where M = In, Ga, Al, or Fe [57]. The limiting case where M = In ($In_2O_3(ZnO)_m$), for example, exhibits a structure consisting of In_2O_3 sheets with remaining In and Zn atoms arranged onto $(Zn, In)O_x$ planes spaced evenly between the In_2O_3 planes on "distorted" tetrahedral sites.

This isostructural phenomenon can be attributed to the isovalent states (3+ charge) adopted by In and Ga cations; hence, these structures are expected to have identical electrostatic contributions to enthalpic penalty for solid solution formation (i.e., a random solution vs. a layered In_2O_3 structure). However, the larger size of the In cation would induce greater lattice strain in a solid solution as compared with the Ga cation; therefore we would expect a an overall higher enthalpic penalty for the In/Zn solid solution phases as compared to the Ga/Zn solid solutions in the $InGaO_3(ZnO)_m$ alloys.

As the composition approaches pure ZnO (with increasing m), there must be a threshold value of m where the entropic gain in a complete solid solution overcomes enthalpic forces driving the formation of In_2O_3 planes. In the limit of pure ZnO, Ga and In impurities must be randomly distributed with corresponding vacancies. While this limiting m value is not specifically known for $InMO_3(ZnO)_m$ systems, in the $In_2O_3(ZnO)_m$ system the layered structure has been observed by HRTEM to at least the $m = 20$ phase [60]. In contrast, the $InGaO_3(ZnO)_m$ system has only been characterized up to the $m = 13$ phase with the layered structure still forming as the equilibrium configuration [50]. In systems with higher Zn content ($m > 20$ for $In_2O_3(ZnO)_m$ and $m > 13$ for $InGaO_3(ZnO)_m$), layered In_2O_3 structures have not been observed to form, instead retaining the structure of the parent simple oxides. While these observations from literature support our hypothesis, more detailed energy calculations are needed to fully understand the thermodynamics of $InGaO_3(ZnO)_m$.

This discussion has focused on equilibrium structures for integral values of m. In the case of non-integer values of m, several possibilities exist for equilibrium. The structure may macroscopically phase separate into the two nearest-m

phases ($m = 1$ and $m = 2$ structures for an overall $m = 1.5$ composition) [50]. Alternatively, the energy penalty may be sufficiently small that local spacing between In_2O_3 planes alternate between the closest m values to average the actual composition. Data from [16] suggests the latter hypothesis. In any case, the nature of this phase development has not been extensively studied and is the subject of this work.

6.3 Experimental

6.3.1 Deposition Conditions

Compositional gradient IGZO thin film samples were prepared with varying Zn cation fractions by co-sputtering from targets of 2:2:1 In:Ga:Zn IGZO and ZnO. The relative RF power on each target established the specific composition ranges. These samples constitute a set of $InGaO_3$-ZnO pseudo-binary composition spreads. Three particular composition spreads were investigated extensively in this study: a Zn-deficient range from $0.8 \leq m \leq 3.8$, a Zn-rich range from $3.9 \leq m \leq 23.8$, and an intermediate range from $1.4 \leq m \leq 6.7$. The deposition conditions, resulting composition gradients, and lgLSA dwell times explored are summarized in Table 6.1.

Deposited film composition in this chapter will be referenced in terms of the coefficient m. The value of m is related to the Zn cation fraction f_{Zn} by:

$$f_{Zn} = \frac{m}{m+2} \tag{6.1}$$

The In:Ga ratio was maintained at nominally 1:1 for all samples.

Table 6.1: Summary of $InGaO_3(ZnO)_m$ composition spreads explored in this study. Samples 1, 2, and 3 are referred to as Zn-deficient, Zn-rich, and intermediate respectively in the text.

Sample	IGZO Power (W)	ZnO Power (W)	m Range	Gradient (% Zn/cm)	Dwells
1	200	60	0.8 – 3.8	4.72 ± 0.06	250 μs 2 ms
2	120	180	3.9 – 23.8	3.28 ± 0.02	250 μs 2 ms 10 ms
3	180	120	1.4 – 6.7	4.45 ± 0.05	250 μs 2 ms 10 ms

6.3.2 Annealing Conditions

Samples were laser annealed using the lgLSA technique (discussed in Chapter 3) using three dwell times (250 μs, 2 ms, and 10 ms) up to a maximum peak temperature of T_{peak} = 1200°C (at the center of each stripe). Laser-annealed stripes were separated by 1.5 mm to avoid overlap of thermally modified regions and to ensure film areas between scans remained nominally unannealed. Dwell times were interspersed to provide data for all dwells at each nominal composition. Along the length of the composition gradient, microstructural information was thus obtained as a function of temperature, time, and composition.

6.3.3 Measurement Conditions

Film structures were characterized using the microbeam wide-angle X-ray scattering (μ-WAXS) station at the Cornell High Energy Synchroton Source (CHESS)

G-line (G1) with monochromated 9.93 keV X-rays. Using X-ray focusing optics, the incident X-ray beam was focused to a ~12 μm spot, and measurements were taken every 25 μm across the sample. Using a 2D X-ray detector, the μ-WAXS technique enabled identification of both general structure and texture within the film.

6.4 Compact Visualization of Structural Data

6.4.1 Raw Data: As-Deposited Films

Figure 6.6 shows select 2D diffraction patterns from various film compositions (m) both as-deposited and after annealing to a peak temperature of 1200°C for 2 ms. As-deposited films with $m \leq 2$ exhibit diffuse scattering consistent with amorphous films, and consistent with other IGZO literature [13, 133, 187, 188]. In the $m = 2$ as-deposited film, a faint signal indicating crystallization and film texturing during deposition is observed. For films with $m > 2$, clear crystalline structures with strong texturing (arc-like diffraction patterns) are observed in the as-deposited films.

6.4.2 Raw Data: Annealed Films

For all compositions, a crystalline microstructure does develop after annealing up to 1200°C for the 2 ms dwell (Fig. 6.6). Annealed films near $m = 1$ compositions yield a randomly-oriented polycrystalline pattern with the $InGaO_3(ZnO)$ structure. With increasing Zn fraction to $m = 1.5$, films retain the polycrys-

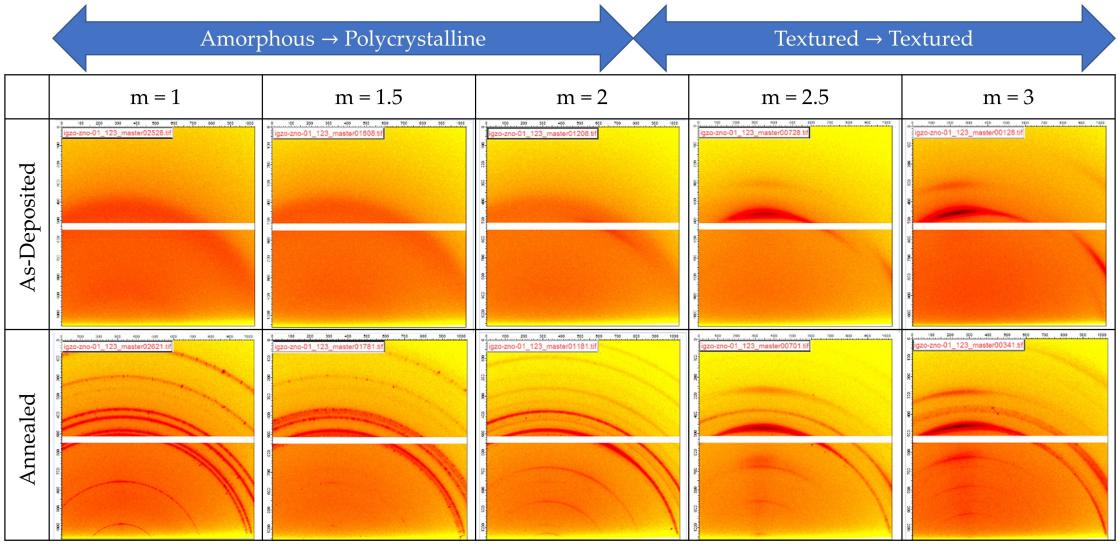

Figure 6.6: Raw 2D diffraction patterns collected using μ-WAXS from selected areas as a function of composition (m coefficient), both before and after LSA (T_{peak} = 1200°C, 2 ms dwell). As-deposited films were amorphous for low m compositions and nanocrystalline for high m, as shown by the arrows above.

talline character but with some peaks showing clearly weaker scattering. The $InGaO_3(ZnO)_2$ structure forms for $m = 2$ films with some small degree of texturing observed. Increasing the Zn fraction further to $m = 2.5$, films continue to exhibit the $InGaO_3(ZnO)_2$ structure, but strong texturing is clearly observed. These patterns also reveal both weak diffuse scattering (smaller crystalline domains) and strong narrow-banded scattering (larger crystalline domains). Films with composition near $m = 3$ maintain similar patterns corresponding to the formation of $InGaO_3(ZnO)_3$.

6.4.3 Raw Data: Conclusions and Challenges

Visual analysis of the diffraction patterns (Fig. 6.6) before and after LSA highlight two clear phase transition regimes. In the low-m regime, annealing of an

amorphous as-deposited film leads to a randomly-oriented polycrystalline microstructure. In the higher-m regime, as-deposited films exhibit an initial textured crystalline microstructure leading to texture-driven templating of crystalline phases during anneals. While Figure 6.6 only shows 10 diffraction patterns across the composition space, the extent of structural data accessible in these patterns is clearly demonstrated. For the three measured samples presented in this study, ~10,000 such diffraction scans were measured. Given the enormous amount of data present, it was impractical to rely on individual inspection of diffraction patterns to search for structural trends as a function of temperature, time, and composition.

6.4.4 Data Compression to 1D Format

For the purposes of crystal phase identification and quick screening of regions of interest, the 2D diffraction data were compressed to a more manageable form as 1D patterns similar to those measured in a more conventional θ-2θ XRD scan. The 2D diffraction patterns contain structural information both radially (related to the momentum transfer vector q and the lattice plane spacing) and azimuthally (related to plane orientation, or texturing). Integrating these diffraction patterns azimuthally converts these data to a 1D diffraction scan, analogous to a θ-2θ XRD scan with q plotted along the x-axis. q is related to the inverse plane spacing d and the scattering angle θ by:

$$q = \frac{2\pi}{d} = \frac{4\pi \sin(2\theta/2)}{\lambda} \tag{6.2}$$

where λ is the wavelength of the incident X-ray beam (1.25 Å for this 9.93 keV synchroton source).

6.4.5 Example 1D Dataset

Figure 6.7 shows resulting 1D plots of integrated X-ray scattering intensity as a function of q for the films annealed to 1200°C (corresponding to Fig. 6.6). Diffraction patterns (for different film compositions) are offset along the y-axis for clarity. Film areas with integer values of m exhibit clear, distinct peaks corresponding to their respective $InGaO_3(ZnO)_m$ phase. In contrast, film areas with off-integer values exhibit increasingly mixed-phase characteristics. For example, $m = 1.5$ films exhibit weak diffraction from both $InGaO_3(ZnO)$ and $InGaO_3(ZnO)_2$ planes, and $m = 2.5$ films exhibit weak diffraction from both $InGaO_3(ZnO)_2$ and $InGaO_3(ZnO)_3$ planes. Given the short annealing time and temperatures well below the melt, we do not believe these mixed patterns are large grain phase separations, but rather some level of local order development.

This data representation retains all of the lattice spacing information, and allows comparison of several diffraction patterns within the same figure. However, all explicit information on film texture is lost due to the azimuthal integration. The only possible remaining manifestation of texturing is the deviation of observed peak intensities from expected literature values for powder samples due to the specific of the orientation of the 2D X-ray detector relative to the sample, and the finite solid angle subtended by the area detector. As can be seen in Fig. 6.6, the detector fails to capture some of the out-of-plane scattering in the [0 0 1] direction due to the pixel dead space (center band of the image), and X-rays scattered in the [1 0 1] and [1 0 0] directions fall outside the detectable range altogether. Nevertheless, the 1D representation of Fig. 6.7 provides an efficient method for indexing and analyzing diffraction peaks.

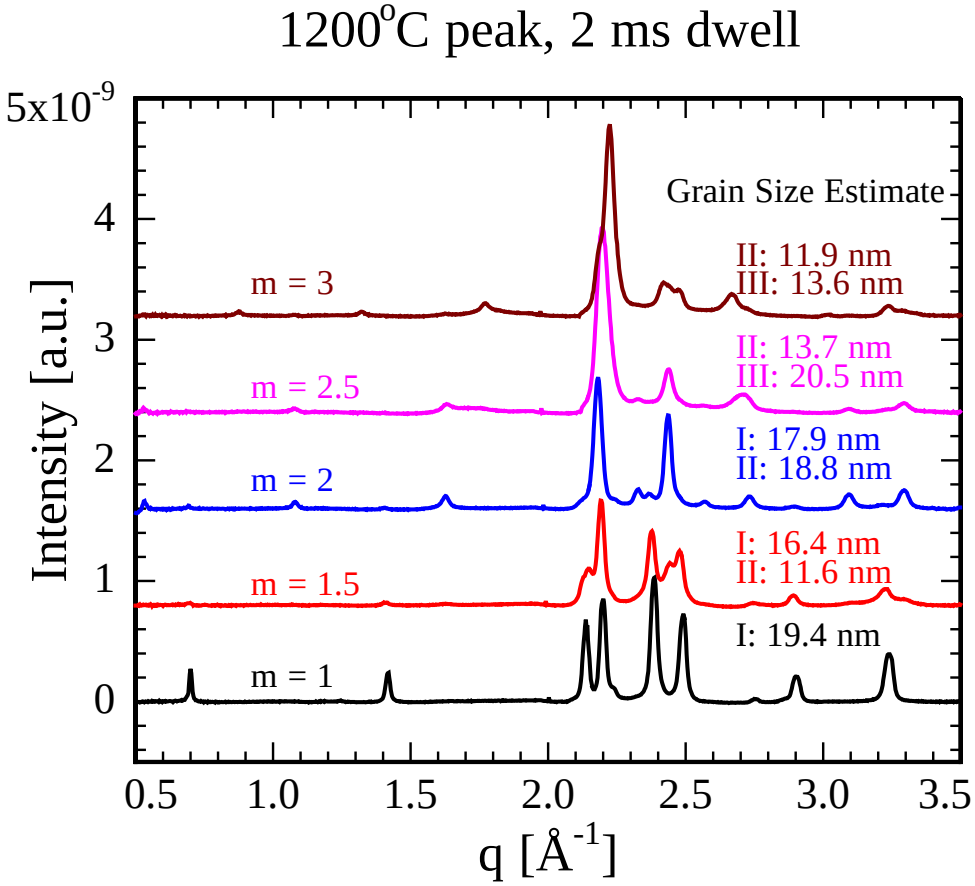

Figure 6.7: Diffraction patterns of selected areas after LSA (T_{peak} = 1200 °C). This 1D representation is formed by integrating the data from Fig. 6.6 azimuthally and is analogous to a θ-2θ XRD scan.

6.4.6 Representation of Diffraction Data Series

This 1D representation of the diffraction data can be used to effectively screen the effects of temperature, time, and composition across the composition gradient. As an example, Figure 6.8 shows diffraction data collected across two laser scans in the Zn-deficient sample near $m = 1.3$. Each diffraction pattern is offset by a small amount in y, and correspond to diffraction measurements every 25 μm. The approximate peak temperature profile across the scans is shown on

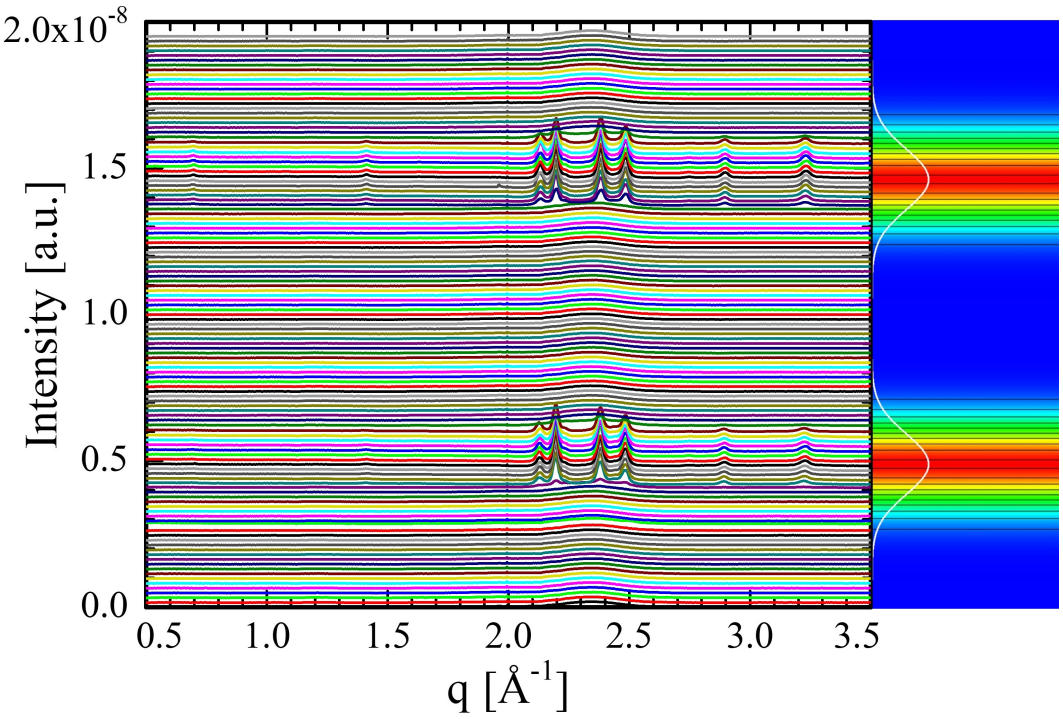

Figure 6.8: A waterfall-type plot of integrated diffraction data collected across a 3 mm length of Sample 1 ($m \approx 1.3$) in 25 μm intervals. The y-axis range corresponds roughly to 3 mm, and adjacent laser-annealed stripes are spatially offset by 1.5 mm. To the right is a schematic of the peak annealing temperature within each laser-annealed region over the 3 mm range from which these diffraction patterns were measured.

the right, with scans between the stripes showing unannealed behavior. This waterfall-type plot is effective at displaying sharply contrasting diffraction patterns in adjacent regions (i.e., amorphous vs. crystalline), and higher-q peaks ($q > 2$ Å^{-1}) are clearly observed. However, it is difficult to view weaker scattering peaks (such as at $q \approx 0.7$ Å^{-1} and $q \approx 1.4$ Å^{-1}) and is impractical for interpreting diffraction measurements across the full composition range of each sample.

6.4.7 Representing lgLSA Data as Color Maps

Figure 6.9 provides a more effective representation of the same sample region as in Fig. 6.8, with intensity shown as a "heatmap" color spectrum from dark blue (low intensity) to orange (high intensity) on a logarithmic scale.[1] The y-axis represents physical distance along the sample, while the scattering vector q is across the x-axis. Each horizontal "stripe" corresponds to a single diffraction measurement taken along the sample, with ~120 individual measurements represented in this image. As in Fig. 6.8, the formation of strong peaks in the range $2.0 < q < 2.5$ Å^{-1} is clearly observed. Also seen is a sharp transition from conditions retaining the as-deposited amorphous structure to a crystallized structure; this indicates a critical crystallization temperature at each dwell, discussed below. Additionally, lower-intensity peaks near $q \approx 0.7$, 1.4, and 2.75 Å^{-1}, not readily apparent in Fig. 6.8, are now clearly observed.

Figures 6.10 and 6.11 plot these data across the entire composition range (length) of each of the three samples. It is important to recall that each "spike" in these figures is actually a collection of scans over the full range of peak temperatures, and that the various dwell times are interspersed along the sample. In Fig. 6.10, the broad peaks in the $2 < q < 2.5$ Å^{-1} range, extending over several mm of sample area (composition range), arise from scattering in the as-deposited film structure. The narrow bands (spaced 1.5 mm apart) indicate laser annealed areas, with additional diffraction peaks forming in the low-m regimes. The boxed region in Fig. 6.10b corresponds to the area shown in Fig. 6.9. These peaks are more clearly shown in Fig. 6.11, plotted on an over-saturated scale

[1] For greater contrast, the logarithm of the intensity $\log(I)$ is plotted rather than the magnitude in intensity I.

to emphasize the lower intensity scatter of the developed structure.[2] This view provides a concise representation of the diffraction data, showing clearly the transition from the amorphous structure between laser-annealed stripes (diffuse scattering) to the crystalline structure with clear diffraction peaks.[3]

6.4.8 Regions of Interest

This heatmap representation provides a clear and succinct method for visually screening diffraction data as a function of peak annealing temperature (within a single laser-annealed stripe), annealing time (adjacent stripes), and composition (across the length of the sample). The remainder of this chapter focuses on three regions of interest to explore phase formation in this system. First, the nature of the as-deposited structure is developed from diffraction data collected between each laser-annealed stripe. Second, the low-Zn regime near $m = 1$ stoichiometry provides insight into the transition from the amorphous as-deposited phase to polycrystalline films and the organization of cations in the IGZO lattice. Last,

[2]Unfortunately, while all regions of interest in Fig. 6.10 can be distinguished on an computer monitor, printed versions of the figure do not provide the same color gamut range. Fig. 6.11 is provided as a supplement.

[3]Several image artifacts should be clearly noted:

- The bright and dark bands near the top and bottom of the images are artifacts from strips of rolled copper tape used to calibrate the sample-to-detector distance.
- The "clipping" near $q = 2.2$ Å^{-1} of the bright band (band extends from $2.2 < q < 2.4$ Å^{-1} approximately) originates from placement of the detector relative to the sample (see Fig. 6.6); clipping occurs when the dead area of the 2D detector (center stripe) overlaps with the textured $(0\,0\,x)$ peak. While it is not optimal to lose signal from this peak, this detector orientation was chosen to maximize resolution of the lower-q peaks while still capturing high-q peaks useful for phase indexing.
- The apparent drift in the peak positions in Fig. 6.10b for $y > 65$ mm (below the bright yellow stripe artifact from the copper tape) is due to an uncalibrated sample-to-detector distance due to an error in stage motion set-up during the scan. All other regions are calibrated.

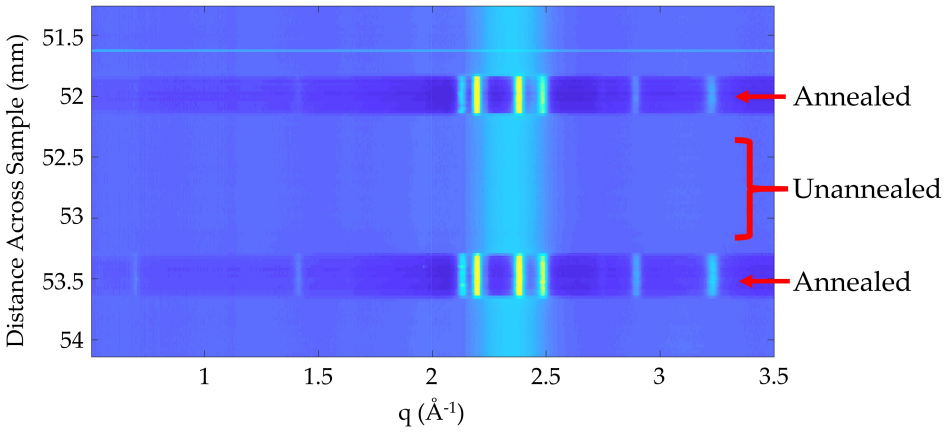

Figure 6.9: Heatmap representation of the diffraction data shown in Fig. 6.8 ($m \approx 1.3$). Intensity is shown as a color spectrum from dark blue (low intensity) to bright yellow (high intensity). The transition from the amorphous as-deposited structure (unannealed) to a crystalline $InGaO_3(ZnO)$ structure (annealed) is readily apparent. Film areas were annealed using a 250 μs dwell (upper stripe) and a 2 ms dwell (lower stripe).

phase transformations from textured crystalline as-deposited films to higher-order structures in an off-stoichiometry regime near $m \approx 2.4$ are explored to develop a model for the structural development of these alloys.

6.5 As-Deposited Film Structure

6.5.1 Observations of As-Deposited Film Structure

Information on the as-deposited structure was obtained from the regions between laser-annealed stripes, where films remain nominally unannealed, as identified in Figure 6.9. In the extended view of Fig. 6.10, these unannealed regions appear as broad yellow bands with slight distortions spaced every 1.5 mm

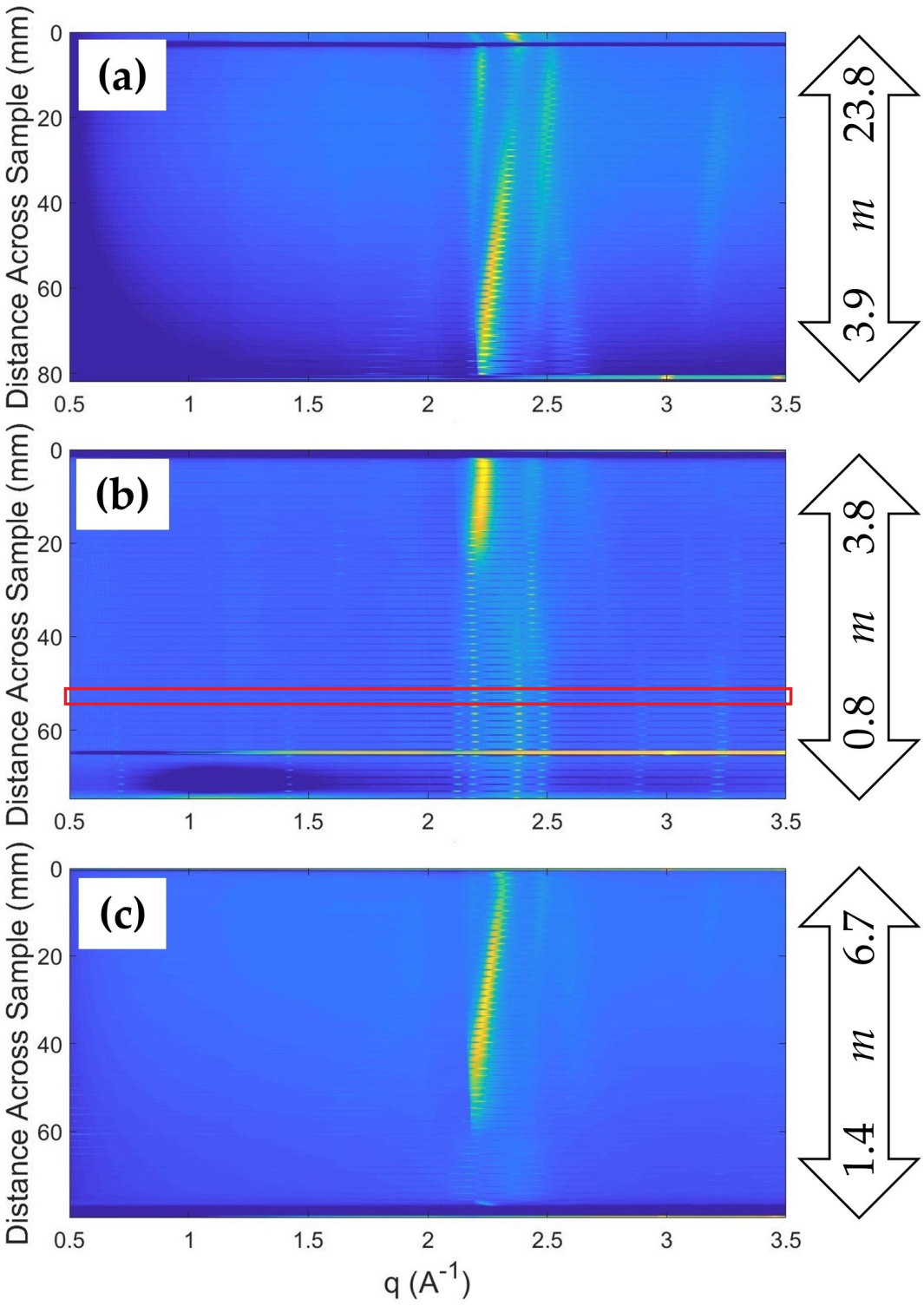

Figure 6.10: Heatmap plots of the combined diffraction data for (a) the Zn-rich sample, (b) the Zn-deficient sample, and (c) the intermediate sample (samples 2, 1, and 3 respectively). (a) and (b) together demonstrate the full range of composition space investigated in this study, while (c) covers composition ranges spanning the boundary between the two. The boxed region marked in red in (b) are the scans shown in Fig. 6.9.

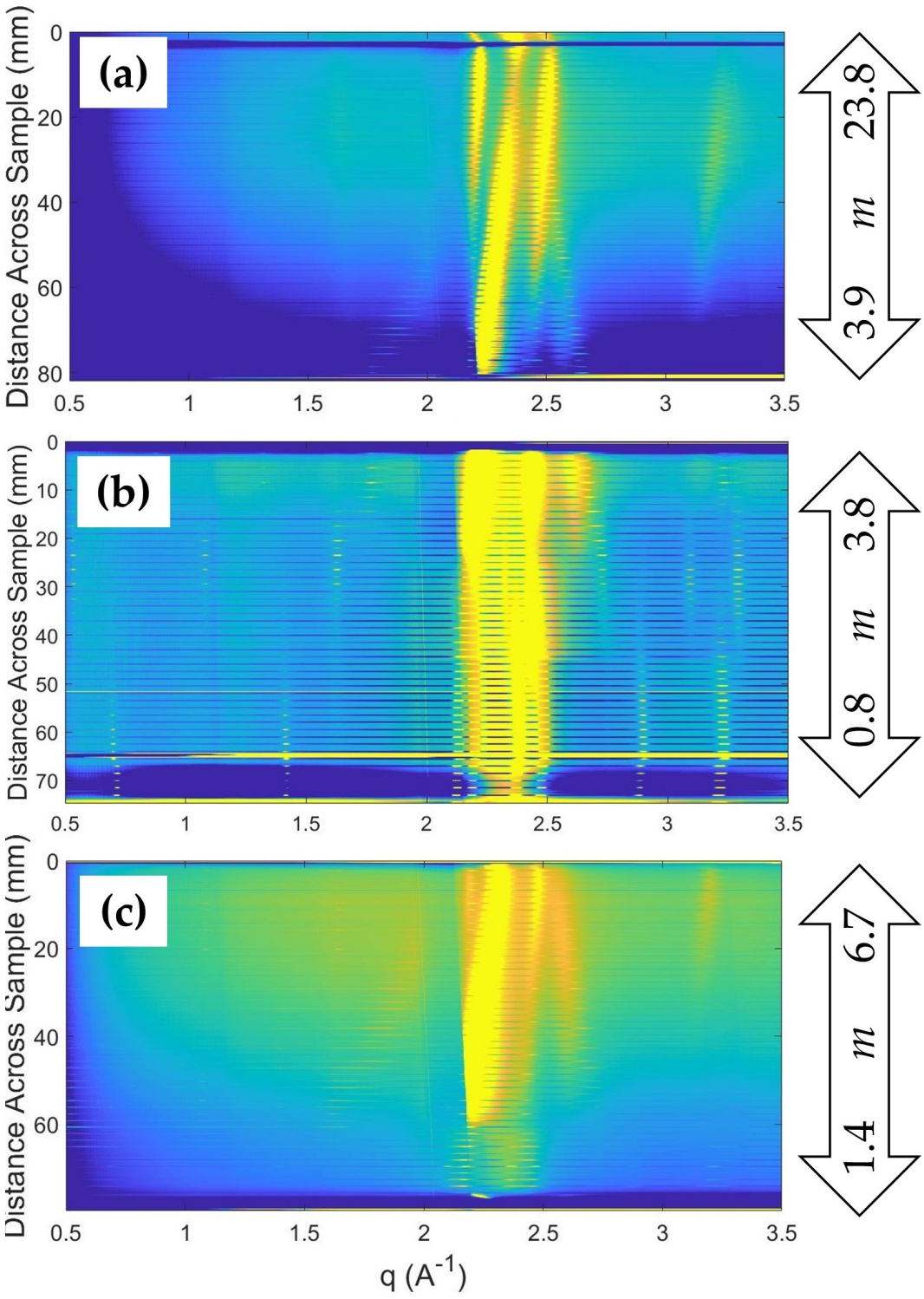

Figure 6.11: Over-saturated heatmap plots of the same data shown in Fig. 6.10, highlighting the lower-intensity peaks.

corresponding to each laser-annealed band.

In low-Zn (low-m) films, the as-deposited structure (room temperature) exhibits only diffuse scattering near $q = 2.3$ Å^{-1}, consistent with an amorphous structure; this structure is clearly seen in the unnanealed regions of Fig. 6.9. This agrees well with films reported in IGZO literature sputtered from targets with compositions near $m = 1$ (1:1:1 In:Ga:Zn) to achieve amorphous films suitable for display applications. Crystalline films in this composition range only form when deposited on substrates heated above ~200°C [13]. With increasing Zn fraction, as-deposited films begin to develop a crystalline microstructure near $q = 2.2$ Å^{-1}. This transition is seen clearly in Fig. 6.10b with the development of a strong peak at ~20 mm from the Zn-rich edge of the sample (from the top of the image) corresponding to $m \approx 2$.

6.5.2 Classification of As-Deposited Structure

Fig. 6.10a and 6.11a shows this $q = 2.2$ Å^{-1} crystalline peak persisting to higher-m compositions. With increasing m, the peak shifts to higher q indicating a decreasing lattice spacing d with increasing Zn fraction. At a Zn fraction near $m \approx 6$, three additional diffraction peaks develop, which again shift toward higher-q (lower d spacing) with increasing Zn concentration. The position of these peaks can be extrapolated to $m \to \infty$, as shown schematically in Figure 6.12. The estimated q values of 2.23, 2.41, 2.54, and 3.29 Å^{-1} correspond well to the (0 1 0), (0 0 2), (0 1 1), and (0 1 2) diffraction peaks of the pure ZnO wurtzite structure.

The lattice constant shift with decreasing Zn constant is consistent with sub-

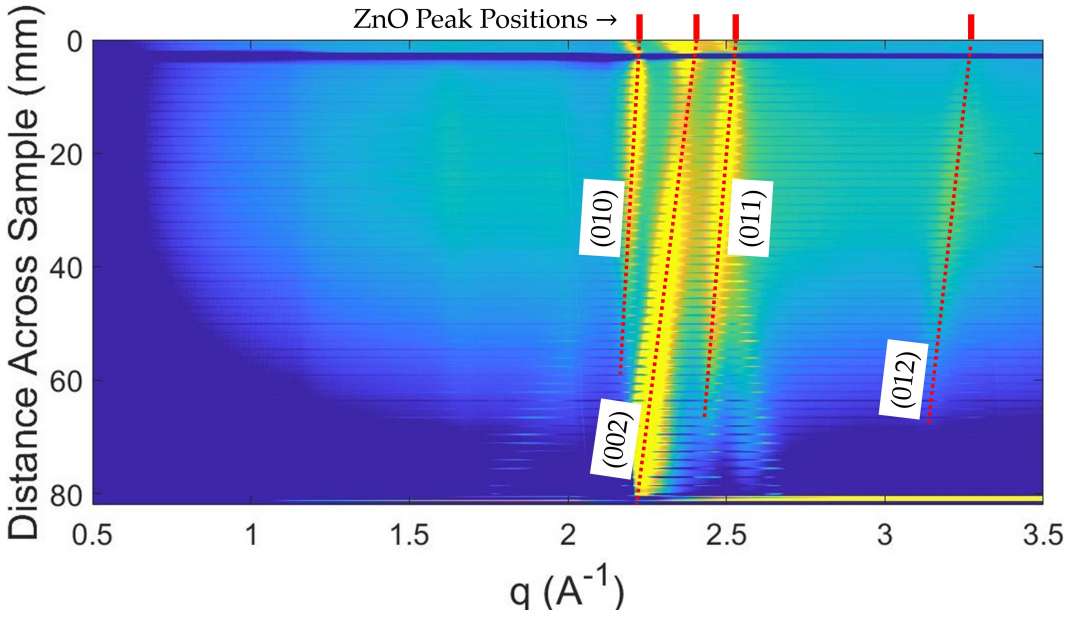

Figure 6.12: Saturated heatmap of Zn-rich film sample from Fig. 6.11a with dotted lines indicating approximate peak position. These lines are extrapolated to $m \rightarrow \infty$ (pure ZnO), indicating good agreement with the positions expected for a ZnO wurtzite structure.

stitutional alloying. The addition of larger In^{3+} and Ga^{3+} cations increases the average lattice plane spacing and shifts all observed diffraction peaks to lower-q. As no new peaks corresponding to other symmetries are observed, this data is consistent with the formation of a simple solid solution between ZnO and $InGaO_3$ in a distorted ZnO-like wurtzite structure.

In addition to the shift of peaks with m, the (0 1 0), (0 1 1), and (0 1 2) peaks appear to disappear near $m \approx 6$. While the origin of this effect is not clearly evident from the heatmap representation, the raw 2D diffraction patterns (Figure 6.13) provide additional insight. Fig. 6.13a shows diffraction from an $m \approx 8$ film, exhibiting a nearly random polycrystalline (only weak texturing) microstructure. The (0 1 0), (0 0 2), and (0 1 1) peaks are seen as broad arcs near the center of the image, and the (0 1 2) peak is seen faintly near the top of the image. In contrast,

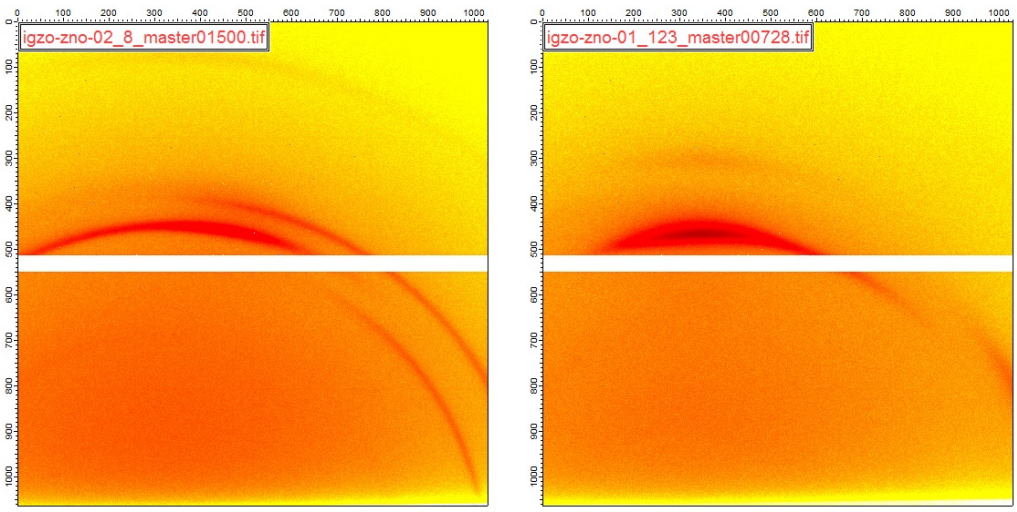

(a) $m = 8$ (b) $m = 2.5$

Figure 6.13: Unannealed diffraction patterns for (a) an $m = 8$ region exhibiting polycrystalline-like morphology and (b) an $m = 2.5$ region, showing strong texturing.

an $m = 2.5$ film (Fig. 6.13b) exhibits strong texturing; the (0 0 2) peak scatters primarily out-of-plane, and the remaining wurtzite peaks are scattered outside the detector range. This texturing leads to a loss in peak intensity in the integrated 1D representation.

While the diffraction data clearly shows a continuous transition between pure ZnO and a distorted wurtzite $InGaO_3(ZnO)_m$ structure, the question of cation charge balance remains. Zn adopts a 2+ valence state in an ionic solid, while Ga and In both adopt a 3+ state. Substitution of Zn cations with In or Ga cations requires a compensating crystalline defect for charge balance. One potential compensation mechanism is the creation of cation vacancies as described below in equation 6.3 and shown schematically in Figure 6.14.

$$In^{\times} + Ga^{\times} + 3\left(Zn^{2+}_{Zn^{2+}}\right)^{\times} \rightarrow \left(V^{0}_{Zn^{2+}}\right)^{2-} + \left(In^{3+}_{Zn^{2+}}\right)^{+} + \left(Ga^{3+}_{Zn^{2+}}\right)^{+} + 3\,Zn^{\times} \tag{6.3}$$

To maintain the 1:1 In:Ga stoichiometry, In^{3+} and Ga^{3+} must be added in pairs, replacing three Zn^{2+} cations. With increasing substitution and deviation from

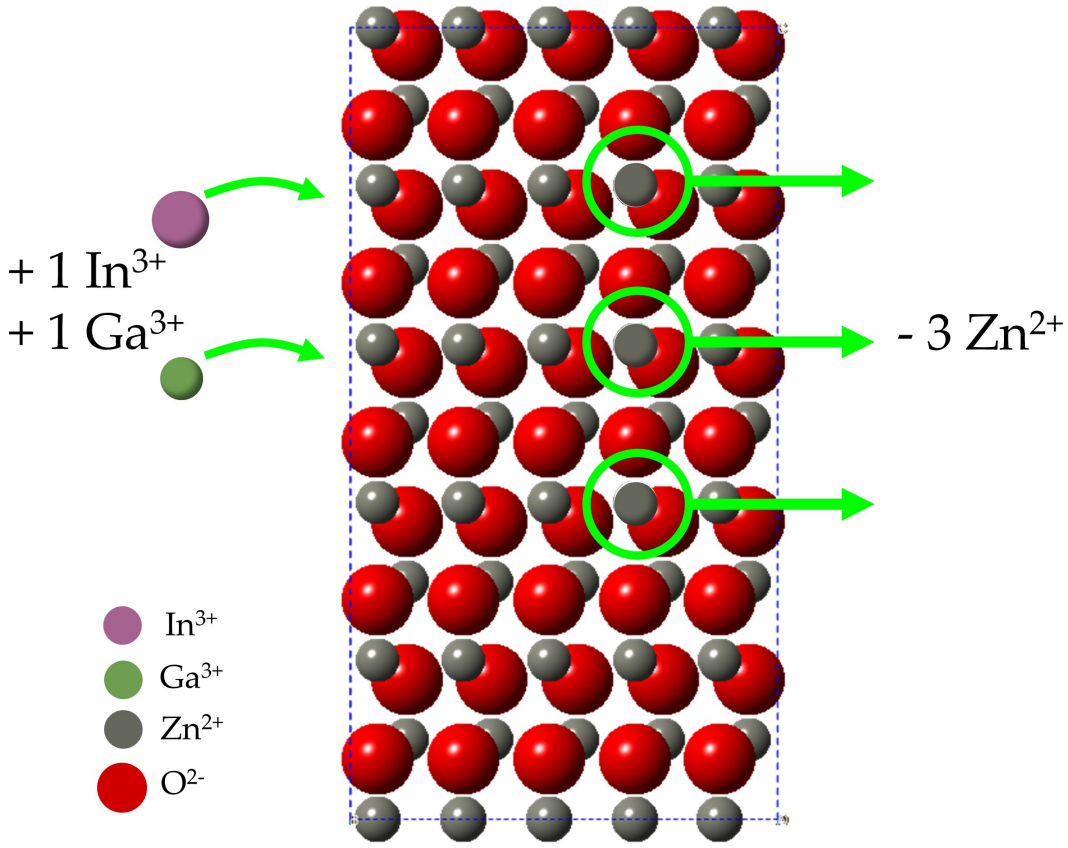

Figure 6.14: Schematic showing a potential charge balance mechanism for the substitution of a In^{3+} and a Ga^{3+} cation into the ZnO lattice by the removal of three Zn^{2+} cations and the formation of a cation vacancy.

pure ZnO, the as-deposited structure accumulates an increasing number of these cation vacancies. In addition to the segregation of In atoms onto In_2O_3 planes with annealing, these vacancies also coalesce to form the cation vacancy planes shown in Figure 6.4c. This vacancy mechanism forms the basis of our model of $InGaO_3(ZnO)_m$ phase development, discussed subsequently.

6.6 Structural Development from Amorphous As-Deposited IGZO Films

6.6.1 Amorphous to Crystalline Transformations

Figure 6.9 demonstrates an amorphous-to-crystalline phase transformation under two laser dwell conditions (250 μs and 2 ms) in the composition range near $m = 1.3$. Each laser-annealed stripe was annealed with a Gaussian thermal profile, with the center of each horizontal stripe reaching a peak temperature of 1200 °C. Both laser-annealed areas in this figure exhibit a relatively sharp amorphous to crystalline transition, suggesting a well-defined phase transformation temperature. This transformation is more clearly shown in Figure 6.15 with individual diffraction scans at varying peak temperatures. For both laser dwells, the transition from amorphous to crystalline occurs between 600 and 750 °C.

6.6.2 Quantification of the Onset of Crystallinity

The onset temperature of crystallization was quantified by tracking the scattering intensity of a characteristic peak of the $InGaO_3(ZnO)$ phase. Figure 6.16 details one diffraction pattern of the $m = 1.3$ film, showing characteristic peaks of the $InGaO_3(ZnO)$ phase. The (0 0 6) peak at $q = 1.41$ Å^{-1} was fit with a Lorentizan function (shown in the figure inset), and the area under the fit curve (peak intensity) was determined as a function of annealing temperature for each dwell time.[4]

[4]For this analysis, the (0 0 6) peak was chosen primarily because most of the $InGaO_3(ZnO)$ peaks become convoluted with $InGaO_3(ZnO)_2$ peaks that form for higher values of m. The (0 0 3)

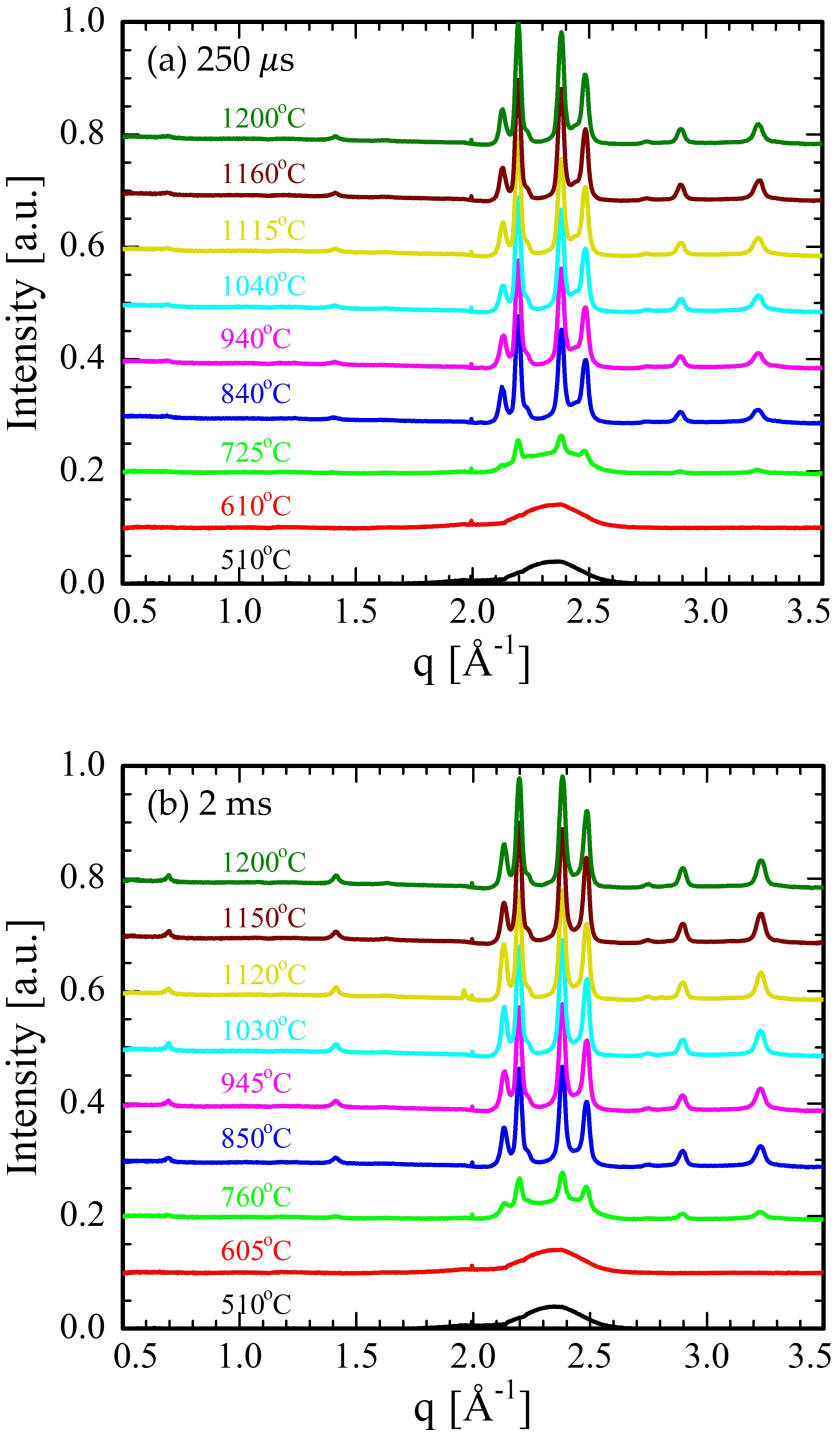

Figure 6.15: Integrated diffraction measurements of $m = 1.3$ film regions laser annealed at select temperatures for (a) 250 μs and (b) 2 ms dwells. In both cases, the crystallization threshold is between 600 and 750°C.

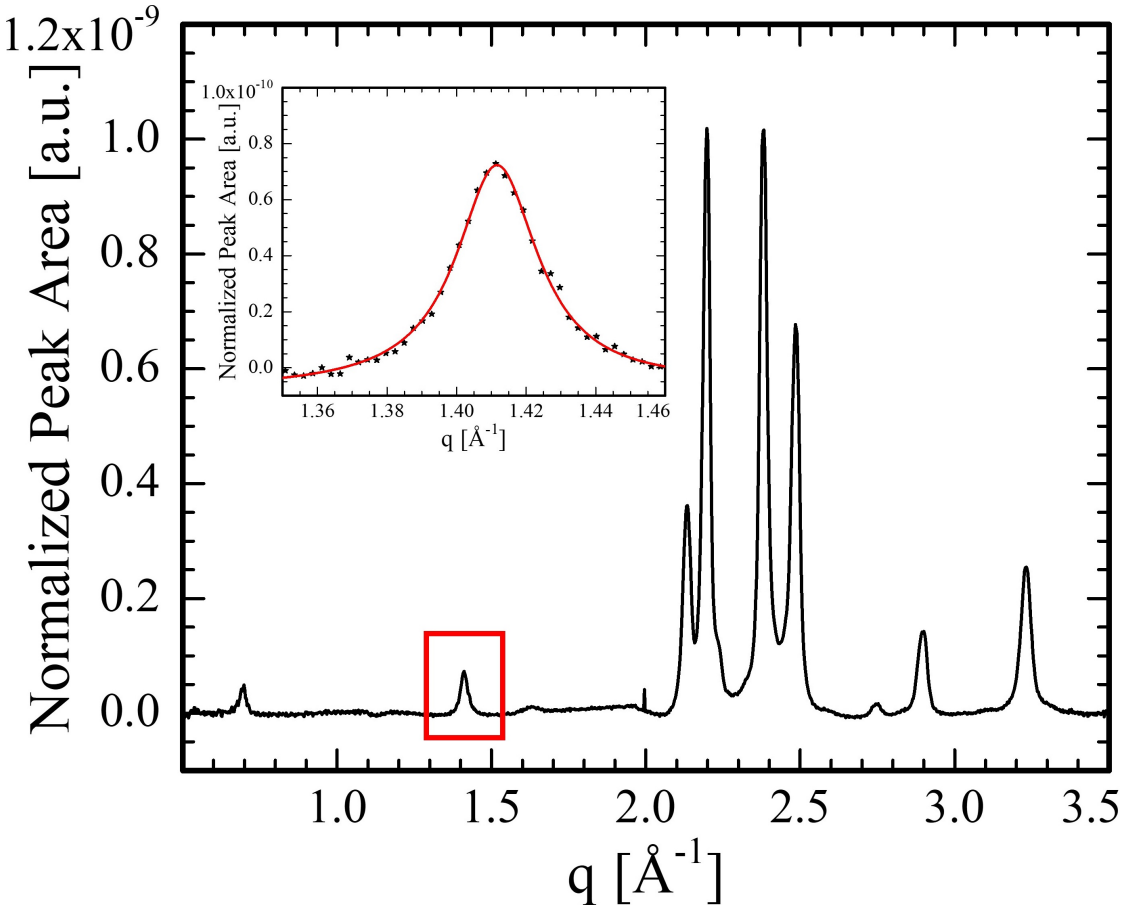

Figure 6.16: Example spectrum used to determine the crystallization onset temperature. The characteristic (0 0 6) peak was selected as it does not overlap with any other expected peaks. This peak was fit with a Lorentzian function (inset), and the total peak intensity (integrated area) was tracked as a function of temperature, composition, and time.

These results are shown in Figure 6.17 for all film samples exhibiting signal from the $InGaO_3(ZnO)$ phase. For all film compositions, and for both dwell times investigated, the crystallization onset temperature is observed near ~650°C. This is consistent with optical microsopy images (Fig. 6.18) showing the extent of the visible effects of film crystallization in film regions annealed ≥650°C. To understand the film morphology, Figure 6.19 shows raw 2D μ-WAXS diffraction patterns from an $m = 1.3$ film annealed for 2 ms. Films annealed

peak could also be used, but typically the integrated signal is lower than the (0 0 6) peak.

at low temperatures exhibited the amorphous microstructure, while increasing the temperature above 650 °C results in a randomly-oriented polycrystalline morphology. This crystallization onset temperature is independent of dwell (within the resolution of these experiments). This would be expected for pure phase transformations, and the amorphous-to-polycrystalline phase transformation temperature of ~650 °C is consistent with furnace annealing studies of IGZO [192].

6.6.3 Determination of Film Crystallinity Fraction

In the integrated (0 0 6) intensity plots (Figure 6.17), the maximum signal intensity decreases with increasing m (Zn content). This behavior may be associated with a change in the overall film crystallinity. Comparison of the (0 0 6) signal to the amorphous diffuse peak can be used as a quantitative measure of the crystallinity. Figure 6.20 shows the normalized signal intensity of the amorphous peak and the (0 0 6) peak for selected compositions for 2 ms anneals. The amorphous signal intensity remains constant for all samples, indicating a stable film thickness. As the amorphous signal decreases for temperatures above 650 °C, the (0 0 6) signal begins to rise. This signal increases sharply between 650 °C and 900 °C before either saturating (in the case near $m = 1$ stoichiometry) or increasing at a lower rate (in the off-stoichiometry $m > 1$ case).

These observations suggest that the reduced (0 0 6) signal intensity with increasing m is not due to a decrease in total film crystallinity. Instead, each of the films shown in Fig. 6.17 appear fully crystalline above ~900 °C, adopting the $InGaO_3(ZnO)$ ($m = 1$) structure. However, the overall composition of these

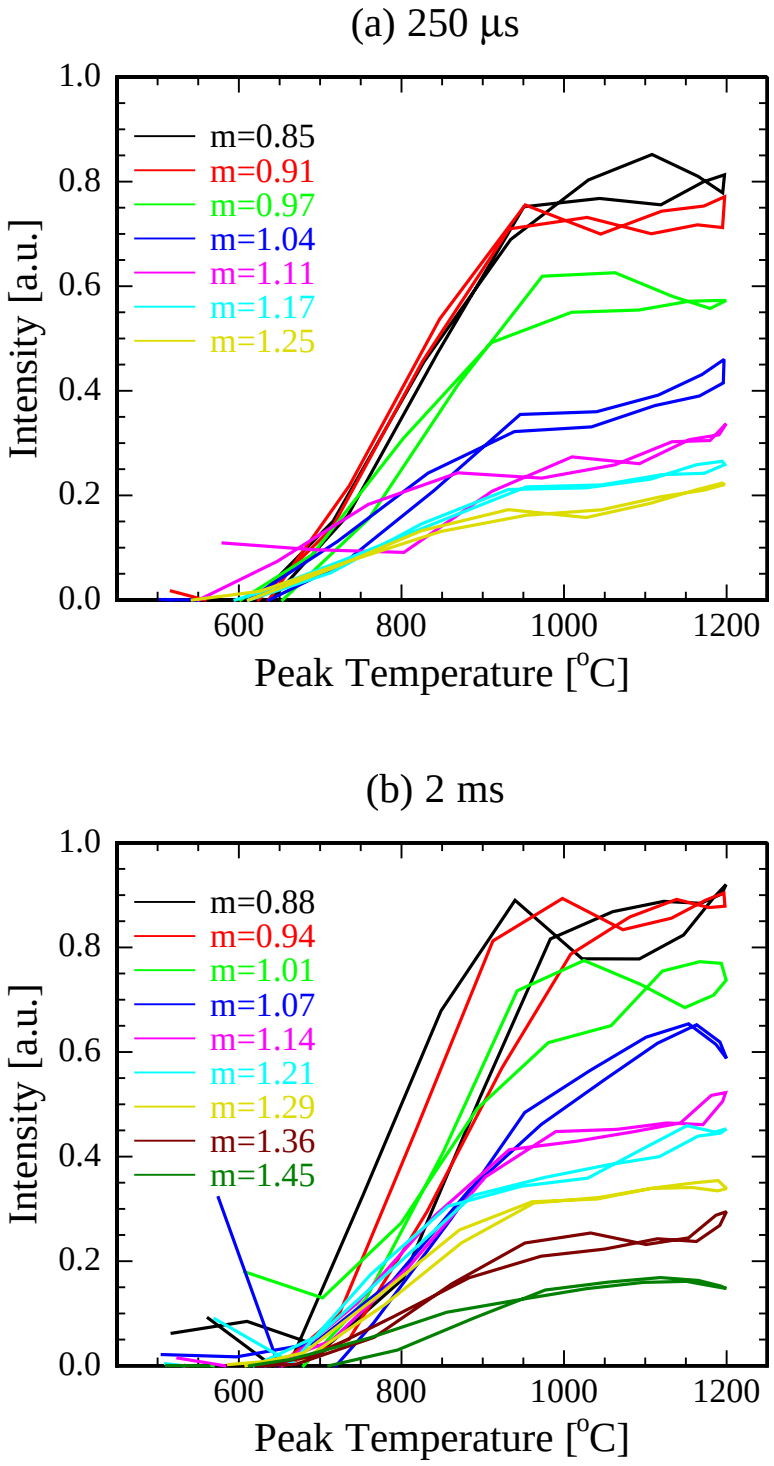

Figure 6.17: Integrated (0 0 6) peak intensity as a function of peak annealing temperature for compositions between $m = 0.85$ and $m = 1.45$, and annealing time: (a) 250 μs dwell and (b) 2 ms.

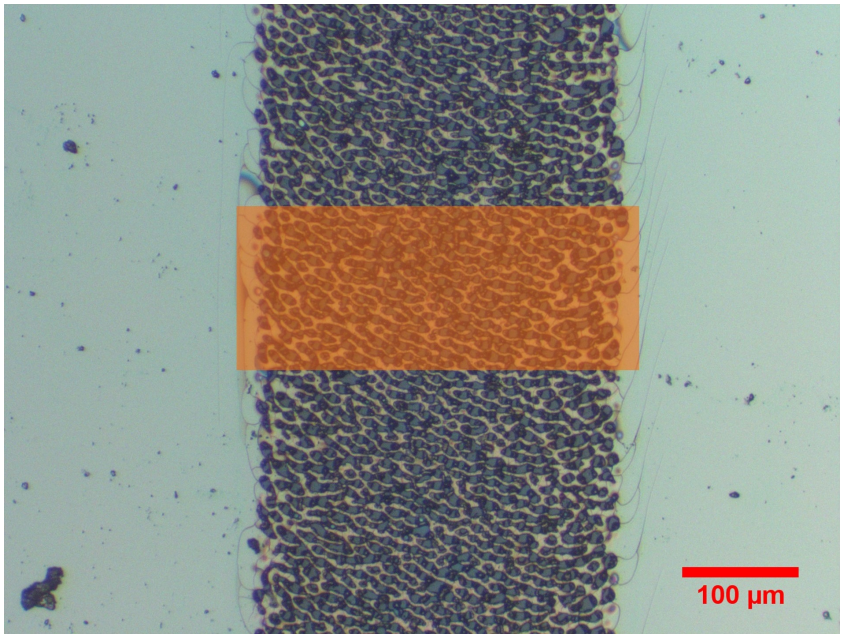

(a) 250 μs dwell time.

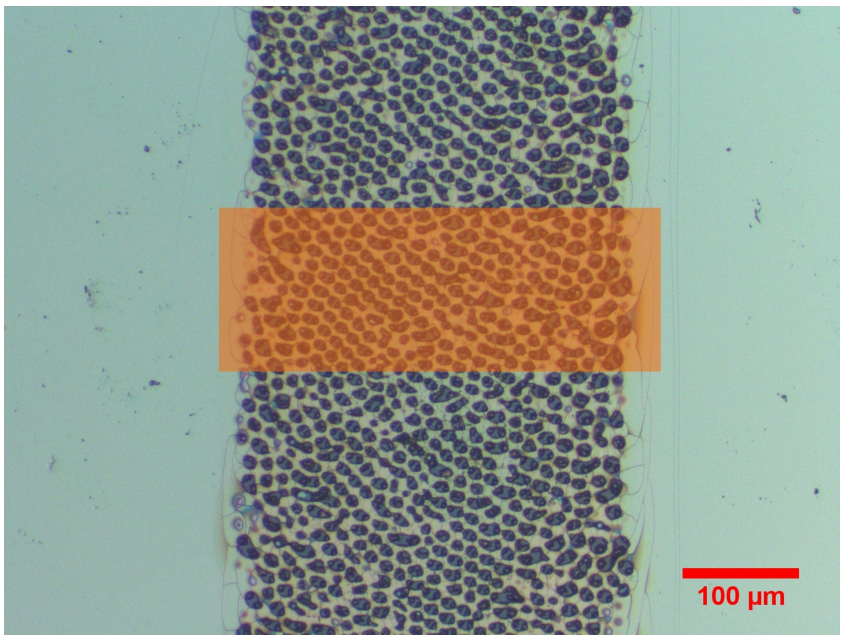

(b) 2 ms dwell time.

Figure 6.18: Optical microscope images of laser annealed stripe regions (m = 1.3) annealed at (a) 250 μs and (b) 2 ms. The width of the orange box shows the lateral extent of film regions annealed ≥650 °C (360 μm range for a 250 μs dwell and 420 μm range for a 2 ms dwell), the nominal crystallization temperature. Dramatic morphology changes are clearly observed with this crystallization.

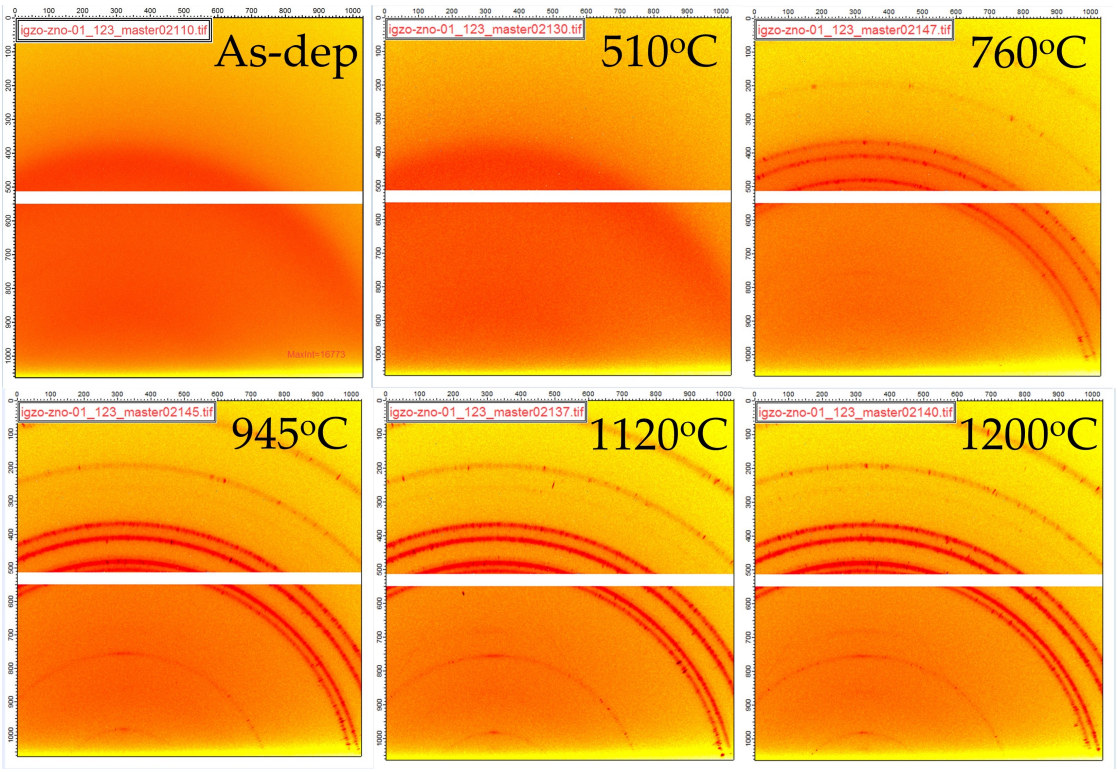

Figure 6.19: 2D μ-WAXS diffraction patterns for an m = 1.3 region annealed with a 2 ms dwell time at a series of temperatures along the lgLSA thermal profile, identifying polycrystalline $InGaO_3(ZnO)$.

films with $m > 1$ contain excess amounts of Zn relative to the ideal $InGaO_3(ZnO)$ structure. This off-stoichiometry would be expected in equilibrium to induce phase segregation to form $InGaO_3(ZnO)_2$. However signal from this phase is seen only minimally in films regions with $m >$ ~1.3. The accomodation of this off-stoichiometry can be better understood by considering the creation of cation substitution point defects.

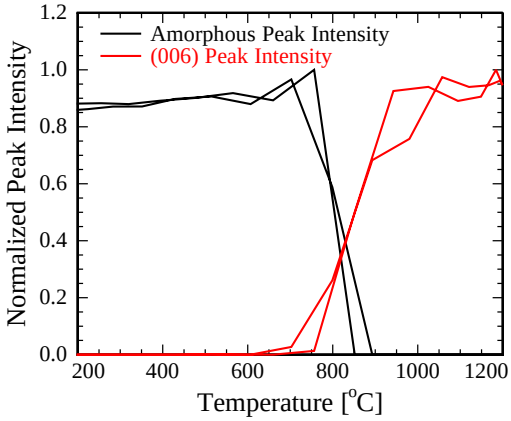

(a) m = 0.94

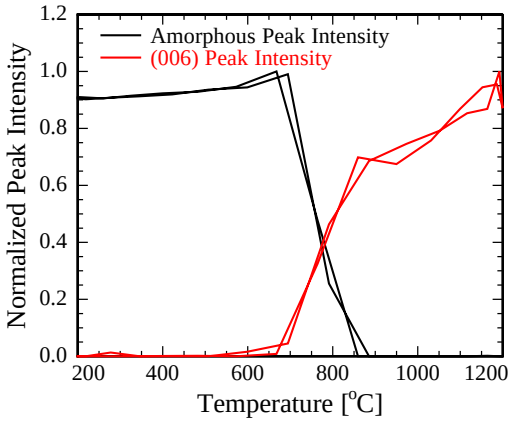

(b) m = 1.21

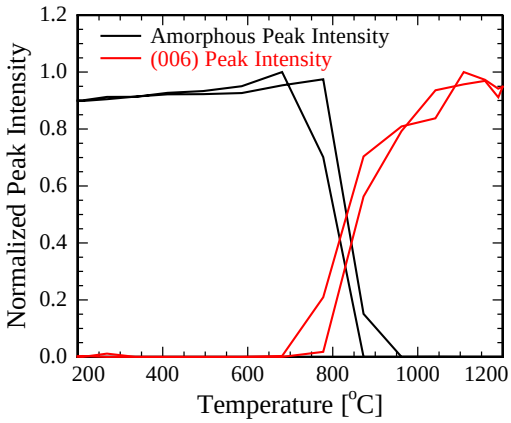

(c) m = 1.45

Figure 6.20: Comparison of the amorphous and (0 0 6) integrated peak intensities as a function of peak temperature in films annealed for 2 ms for selected compositions. The absence of any amorphous signal above ~900 °C in all cases suggests full crystallization of all films.

6.6.4 Cationic Disorder in IGZO

Model of Cationic Disorder

The effect of adding Zn to the equilibrium integer *m* structures can be understood from the valence and local coordination states of each atom. Figure 2.4a shows the equilibrium structure of $InGaO_3(ZnO)$ composed of In_2O_3 sheets separated by two $(Zn,Ga)O_{1.5}$ sheets in which the In, Ga, and Zn adopt 3+, 3+, and 2+ valence states respectively.

With increasing *m*, Zn atoms replace an In atom and a Ga atom in the structure. The vacant 6-fold-coordinated In site can either be filled by a Zn^{2+} or a Ga^{3+} ion to form an antisite defect. However, since Zn^{2+} adopts 4-fold coordination in the pure ZnO (wurtzite) structure, and because of the known solubility between isovalent In^{3+} and Ga^{3+}, it is more likely that Ga substitutes for In, giving the $Ga^{3+}_{In^{3+}}$ antisite defect. This implies that all additional Zn^{2+} atoms occupy sites in the $(Zn, Ga)_x$ sheet.

Effects of Cationic Disorder in Diffraction Patterns

The effect of these antisite defects can be readily observed in the diffraction patterns. $InGaO_3(ZnO)$ (0 0 3) and (0 0 6) peaks are formed by reflections from the superlattice-forming In_2O_3 layers. Antisite defects on the In lattice sites will reduce the scattering intensity since the the atomic scattering factor scales with atomic number *Z* (i.e., electron density). Random substitution effects on particular cation sites can be directly estimated by simulating diffraction patterns. Figure 6.21 demonstrates this effect, comparing ideal $InGaO_3(ZnO)$ (Fig. 6.21a)

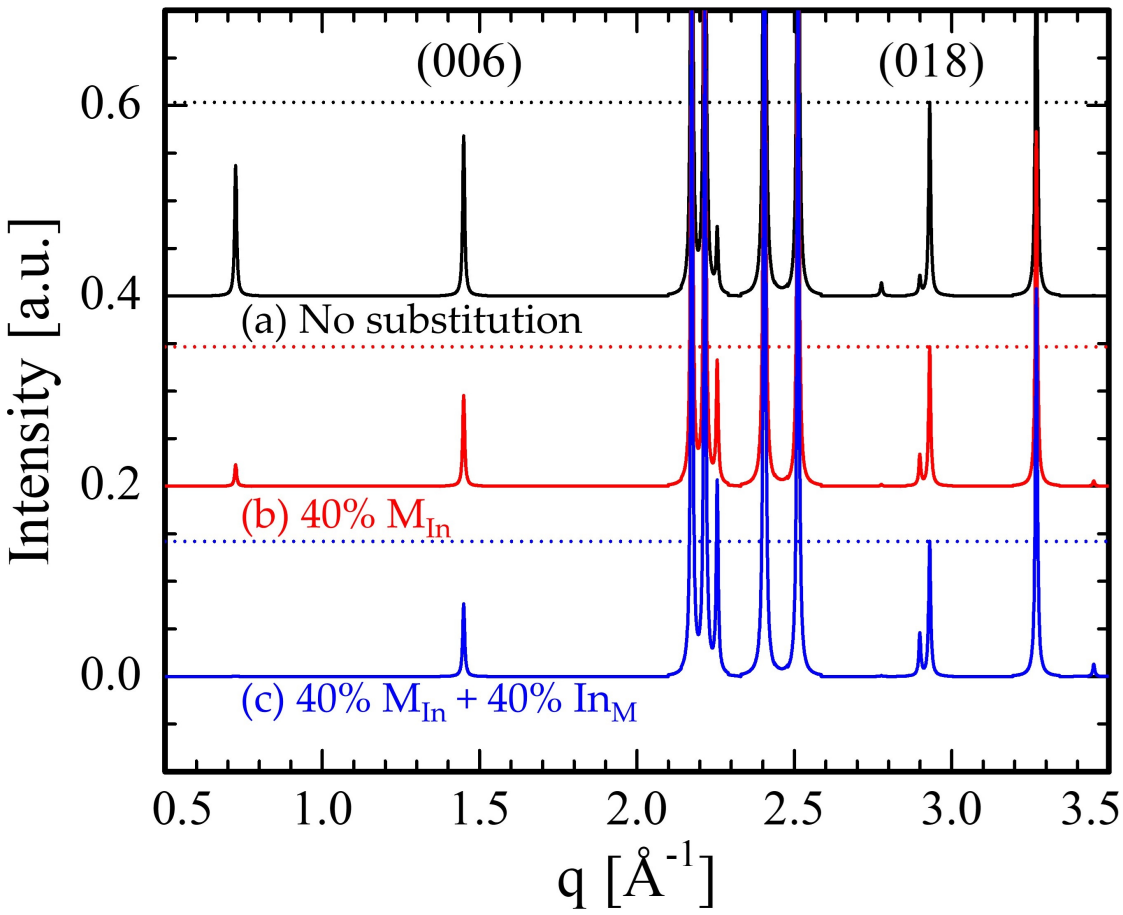

Figure 6.21: Simulated powder diffraction patterns for $InGaO_3(ZnO)_m$ (a) without cation substitution, (b) with 40% *M* (*M* = Zn or Ga) substitution on In lattice sites, and (c) with 40% *M* substitution on In lattice sites and 40% In substitution on *M* lattice sites. Effect of substitution is quantitatively determined by comparing the ratio of the (0 1 8) peak (peak amplitude indicated by dotted line) and the (0 0 6) peak. Data from Ref. [3] with spectra generated using CrystalDiffract [15].

with vary degrees of cation substitution. Fig. 6.21b shows the calculated pattern for $InGaO_3(ZnO)$, with 40% of the In cation sites replaced at random with lower-*Z* cation *M* (while *M* is modeled as Ga, it is left general here as Zn and Ga are not really distinguishable in X-ray diffraction). These data clearly show not only the reduction in superlattice peak scattering intensities, but also changes in the scattering intensities of other peaks. Measured data (Figure 6.22) show a similar trend with increasing *m*.

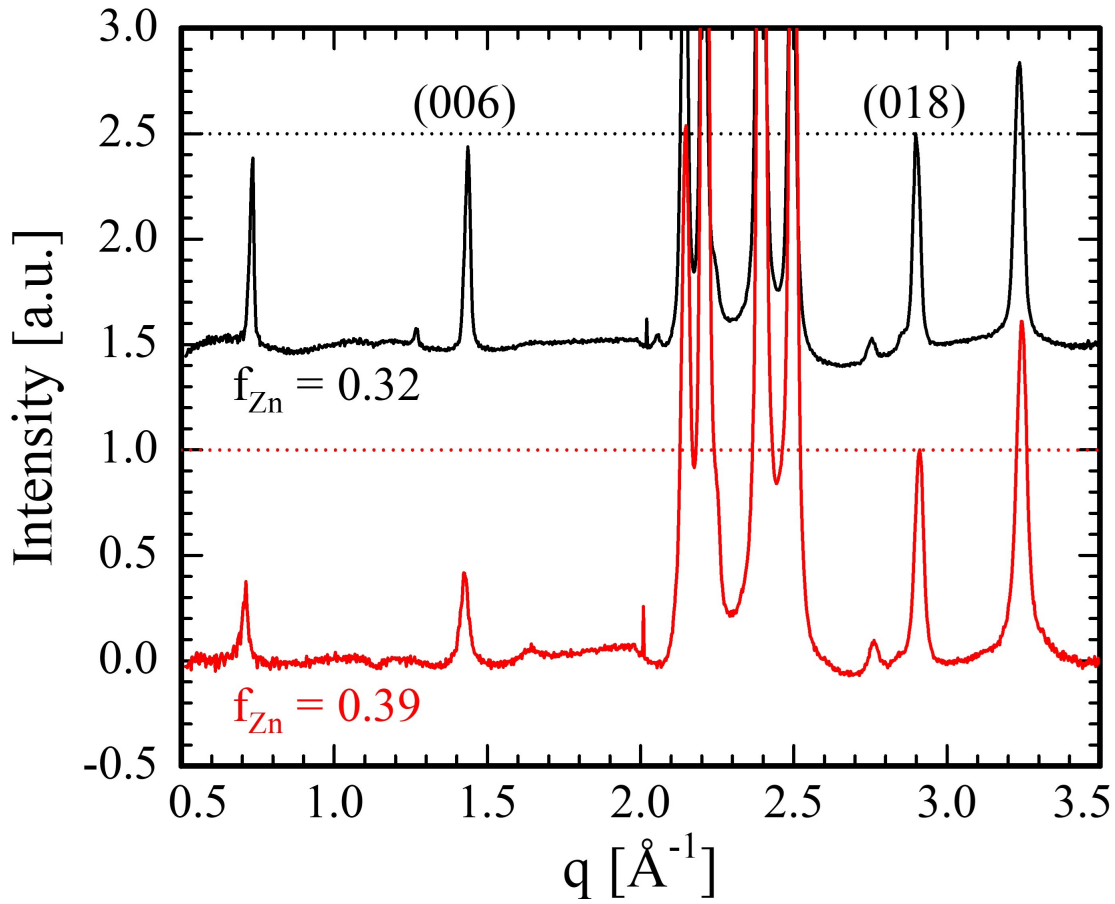

Figure 6.22: Measured diffraction patterns for $InGaO_3(ZnO)_m$ films near $m = 1$ stoichiometry ($f_{Zn} = 0.32$) and Zn-rich with $m > 1$ ($f_{Zn} = 0.39$).

These calculated patterns were semiquantitatively analyzed by comparing the scattering intensity of the (0 0 6) peak to another characteristic peak, the (0 1 8) peak (Fig. 6.21).[5] The ratio of the (0 1 8) peak intensity to the (0 0 6) peak intensity increases as a function of the fraction of substituted In sites, (Figure 6.23), indicating an expected trend in relative scattering intensities with increasing m (Zn fraction). This suggests that, while cationic substitution on In sites may contribute to this effect reducing the relative (0 1 8) peak intensity, other factors must be considered to fully explain the data. To compare with the experimen-

[5]Here, the (0 1 8) peak is chosen because it avoids potential overlap with diffraction peaks of the $InGaO_3(ZnO)_2$ phase and avoids dead areas of the 2D X-ray detector.

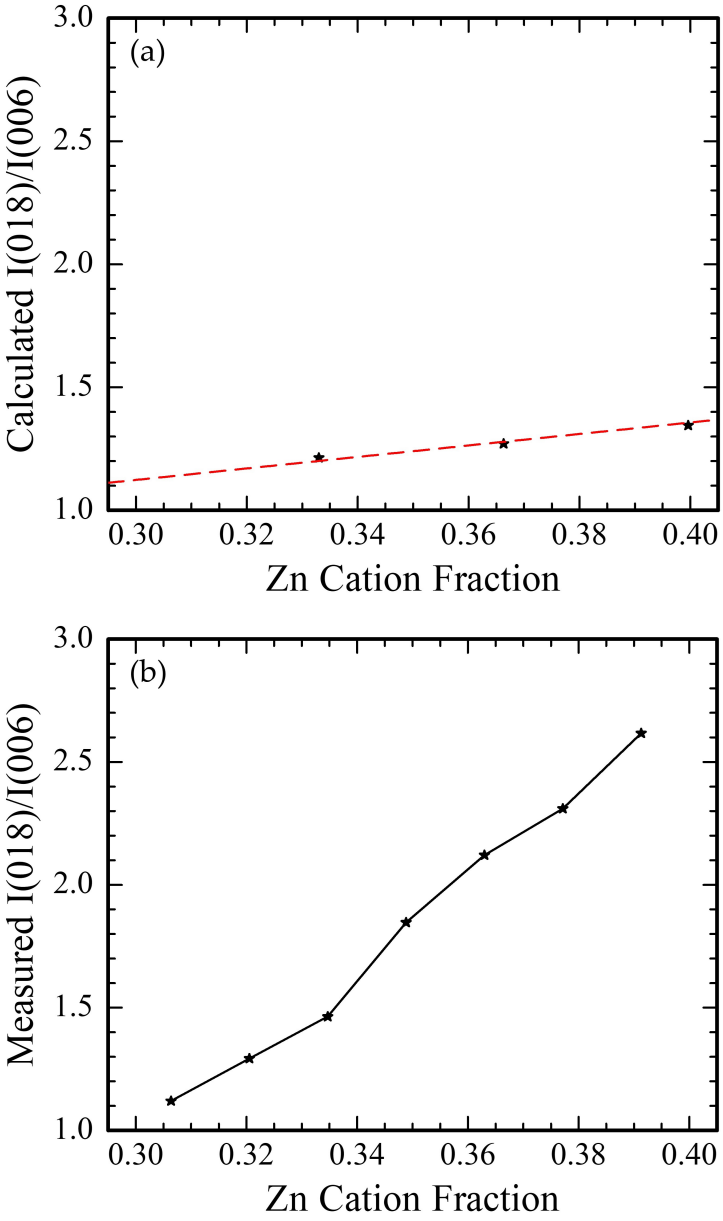

Figure 6.23: Comparison of peak intensity ratio of the (0 1 8) peak to the (0 0 6) peak. (a) Calculated ratio as a function of Zn substitution on In sites and (b) observed ratio as a function of film Zn fraction. The substitution fraction is converted to an equivalent *m* value for comparison.

tal data, the subsitution fraction has been converted to an effective *m* value in Fig. 6.23a.

The calculated intensity ratios range from 1.1 to 1.4, while the measured

range is much larger (1.1 – 2.6) over this composition range, as shown in Fig. 6.23. While laser annealing on millisecond timescales is sufficient to form a crystalline lattice, it may not provide atoms sufficient time and mobility to move to their equilibrium sites, and additional cationic disorder on the (Zn,Ga)O_x lattice sites could also contribute to this scattering intensity effect. Fig. 6.21c shows the combined effect of both 40% substitution on In sites and 40% substitution on M sites (i.e., indium within the (Ga,Zn)O_x layers). This combined substitution results in a further decrease in the relative (0 0 6) intensity (and therefore further increase in the (0 0 6) to (0 1 8) intensity ratio), and nearly complete disappearance of the (0 0 3) peak. This suggests cationic disorder results from not only composition effects, but also from the short timescales used during LSA. This leads to a structure with antisite defects both dictated by stoichiometry and frozen in during transient thermal processing. Overall, however, we believe that the $InGaO_3(ZnO)$ structure accomodates off stoichiometry ($m > 1$) by substitutional cationic disorder.

6.6.5 Link to CAAC

To conclude this section on the formation of the $InGaO_3(ZnO)$ structure, one final observation is made. CAAC IGZO, discussed extensively in Chapter 4, is textured nanocrystalline $InGaO_3(ZnO)$ formed by substrate heating during deposition (in a process that would otherwise yield amorphous films at room temperature) rather than by post-deposition thermal processing. However, the formation mechanism of CAAC IGZO is likely to be similar to that of forming $InGaO_3(ZnO)$ from amorphous IGZO by thermal annealing, but with potentially a few critical differences.

Behavior reported in existing CAAC literature support this cationic disorder model. Figure 6.24 shows a comparison between single-crystal $InGaO_3(ZnO)$ and CAAC IGZO using high-angle annular dark-field scanning transmission electron microscopy (HAADF-STEM), in which higher-Z elements exhibit greater contrast due to enhanced electronic scattering. The In planes are clearly discernable from the Zn/Ga planes in Fig. 6.24a. This contrasts starkly with the image of CAAC IGZO in Fig. 6.24b. While some of the CAAC IGZO atomic planes show greater contrast (i.e., appear In-rich), uniformly spaced In-rich planes are not observed. While some regions of Fig. 6.24b (near the center) hint at In-rich plane formation, the absense of high-contrast In-rich sheets strongly suggests a large degree of cationic disorder between cation planes. The increase in measurement noise (manifesting as "fuzziness" in the image) could originate from several sources. Careful sample preparation and consistent image acquisition settings rule out experimental differences between the samples shown [193]. However, the increased noise could arise from local lattice distortions due to cation substitution. Da Silva *et al.* [57] found computationally that the inclusion of M^{3+} (where M = In or Ga) in the $(Zn, Ga)O_x$ layers can lead to local lattice distortions as the M^{3+} ions attempt to maximize oxygen-coordination. They predicted distortion-field effects that have been directly observed in HRTEM of $InGaO_3(ZnO)_m$ and other isostructural systems [58–62]. This degree of distortion may explain in part the images observed in literature, linking the structural formation here to the growth mechanism of CAAC IGZO.

This observation perhaps also adds additional clarity to the origin of the electronic properties of CAAC IGZO. In particular, TFTs fabricated from CAAC IGZO exhibit electron mobilities up to only 10 cm^2/Vs [16], roughly the same as reported for TFTs fabricated from a-IGZO of similar composition [194]. How-

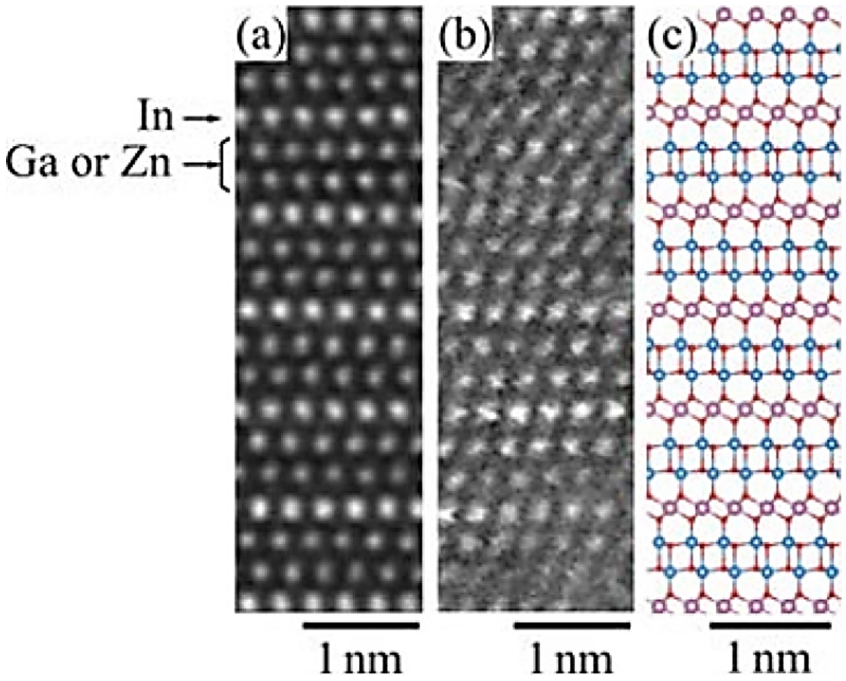

Figure 6.24: Literature-reported cross-section HAADF-STEM image of (a) single-crystal $InGaO_3(ZnO)$ and (b) CAAC IGZO. An atomic model of the $InGaZnO_4$ structure is shown in (c), identifying expected cation placement. Reprinted with permission from [16]. Copyright 2017 John Wiley and Sons.

ever, single crystal IGZO TFTs demonstrated by Nomura *et al.* [63, 195] exhibit much higher mobilities near 80 cm^2/Vs. This discrepancy between the behavior of nanocrystalline CAAC and single crystalline IGZO may be better understood in the context of this cationic disorder model. It has been hypothesized that the overlap of the metal cation *s*-orbitals strongly contribute to the character of the conduction band minimum and electron transport path. Indium, with its larger ionic radius, therefore contributes more to the mobility than the Ga and Zn ions. Single crystal IGZO, with its fully formed In_2O_3 sheets, provides a well-defined, well-ordered conduction path and hence a high mobility. CAAC IGZO, which does not exhibit the clear formation of In_2O_3 planes, is more disordered leading to mobility characteristics similar to amorphous films.

6.7 Structural Development from Crystalline As-Deposited IGZO Films

6.7.1 Observation of Crystal-to-Crystal Phase Transformation

Other phase transformations evident in the diffraction data (Fig. 6.10 and 6.11) give additional clues to the nature of the structural evolution of $InGaO_3(ZnO)_m$. Figure 6.25 shows an enlarged subset of data from the intermediate composition sample (Fig. 6.10c and Fig. 6.11c) from a film region where m = 2.4 and annealed at three dwell times: 250 μs, 2 ms, and 10 ms (from top to bottom). The transition from the as-deposited wurtzite structure to the high temperature annealed structure is clearly seen for all dwell times. Diffuse bands centered near 0.75, 1.4, and 1.8 $Å^{-1}$ are observed, corresponding to small-grain $InGaO_3(ZnO)_3$ structures. For higher temperature anneals, a clear pattern corresponding to $InGaO_3(ZnO)_2$ also develops. Further, annealing near the peak temperature (1200°C) for 10 ms leads to the development of the $InGaO_3(ZnO)$ structure.

With increasing annealing temperature, the diffuse peak formed near q = 1.8 $Å^{-1}$ shifts to lower q, reaching ~1.6 $Å^{-1}$ at 1200°C. This shift, evident in Fig. 6.25, is more clearly observed in the raw 2D μ-WAXS data shown in Figure 6.26 for regions annealed at select temperatures for 10 ms. At moderate temperatures (750°C), diffuse higher-order superlattice peaks begin to form. The white arrow in Fig. 6.26 points to the center of the (0 0 12) superlattice peak. With increasing temperature up to 1090°C, this superlattice peak shifts to slightly lower q. Diffraction patterns at 1200°C demonstrate this offset with the development of sharp $InGaO_3(ZnO)_2$ and $InGaO_3(ZnO)$ peaks.

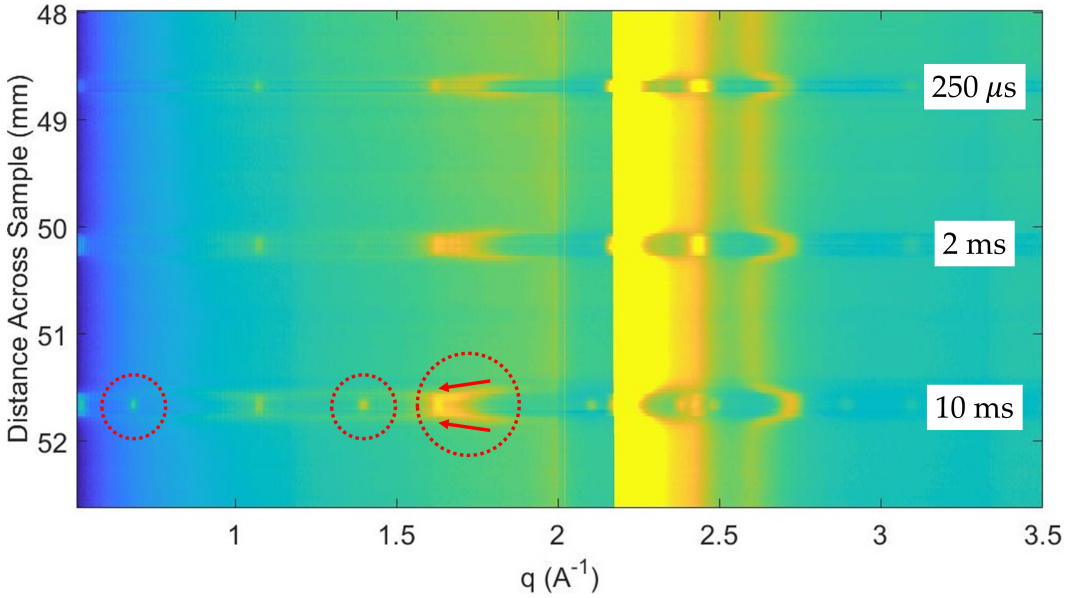

Figure 6.25: Saturated heatmap plot of diffraction data in a $m = 2.4$ region annealed at $T_{\text{peak}} = 1200\,^{\circ}\text{C}$ for 250 μs (top), 2 ms (middle), and 10 ms (bottom). All dwells show the transition from a crystalline as-deposited structure (between scans) to various $InGaO_3(ZnO)_m$ structures. The 10 ms dwell scans clearly show the formation of diffuse low-q peaks at intermediate annealing temperatures. The diffuse peaks at 0.75, 1.4, and 1.8 Å^{-1} mentioned in the text are indicated in the 10 ms dwell data.

Figure 6.27 shows a waterfall plot of integrated diffraction patterns from the same film. The formation of the diffuse $InGaO_3(ZnO)_3$ (0 0 12) peak at $q \approx 1.8$ Å^{-1} is observed first near 750 °C. With increasing temperature, the peak shifts until reaching $q \approx 1.65$ Å^{-1}, which would be expected for the $InGaO_3(ZnO)_2$ (0 0 6) peak. The observed diffuse peak in the intermediate range is interpreted as a shift in the average lattice spacing from ~3.5 Å ($q = 1.8$ Å^{-1}) to ~3.8 Å ($q = 1.65$ Å^{-1}), suggesting a continuous transition from a $InGaO_3(ZnO)_3$ structure to a $InGaO_3(ZnO)_2$ structure. At temperatures above 1090 °C, sharp peaks at $q = 1.4$ Å^{-1} and $q = 1.65$ Å^{-1} form corresponding to the $InGaO_3(ZnO)$ (0 0 6) and the $InGaO_3(ZnO)_2$ (0 0 6) peaks respectively.

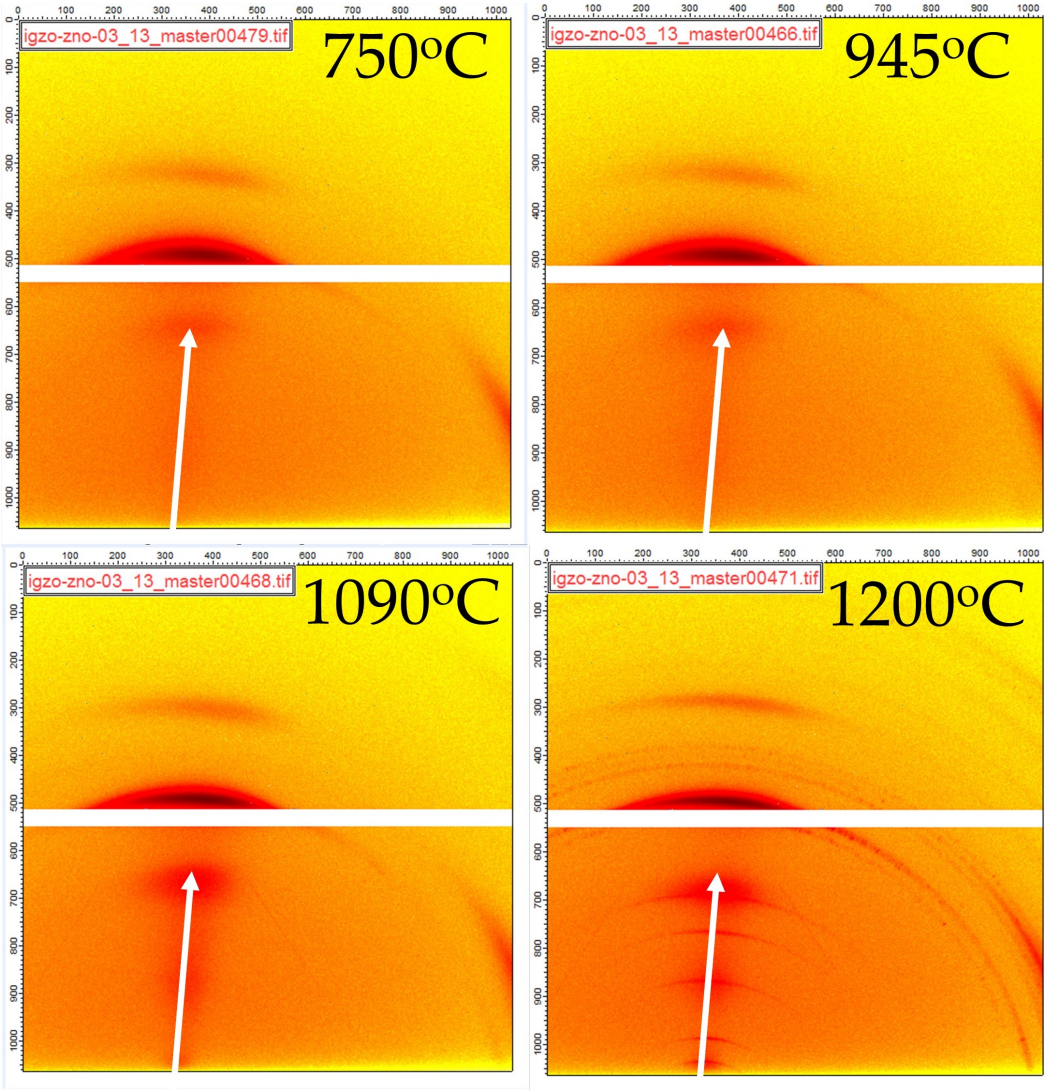

Figure 6.26: 2D μ-WAXS diffraction patterns for an $m = 2.4$ region annealed with a 10 ms dwell time at a series of temperatures, showing the formation of higher-order peaks with increasing annealing temperature. The overlaid white arrow points to the center of the diffuse peak observed at 750 °C, which we identify as the (0 0 12) peak of the $InGaO_3(ZnO)_3$ structure. In all four patterns, the arrow is a constant q value showing the shift to lower q at higher temperatures. At 1200 °C, sharp peaks corresponding to the nucleation of $InGaO_3(ZnO)_2$ and $InGaO_3(ZnO)$ are observed.

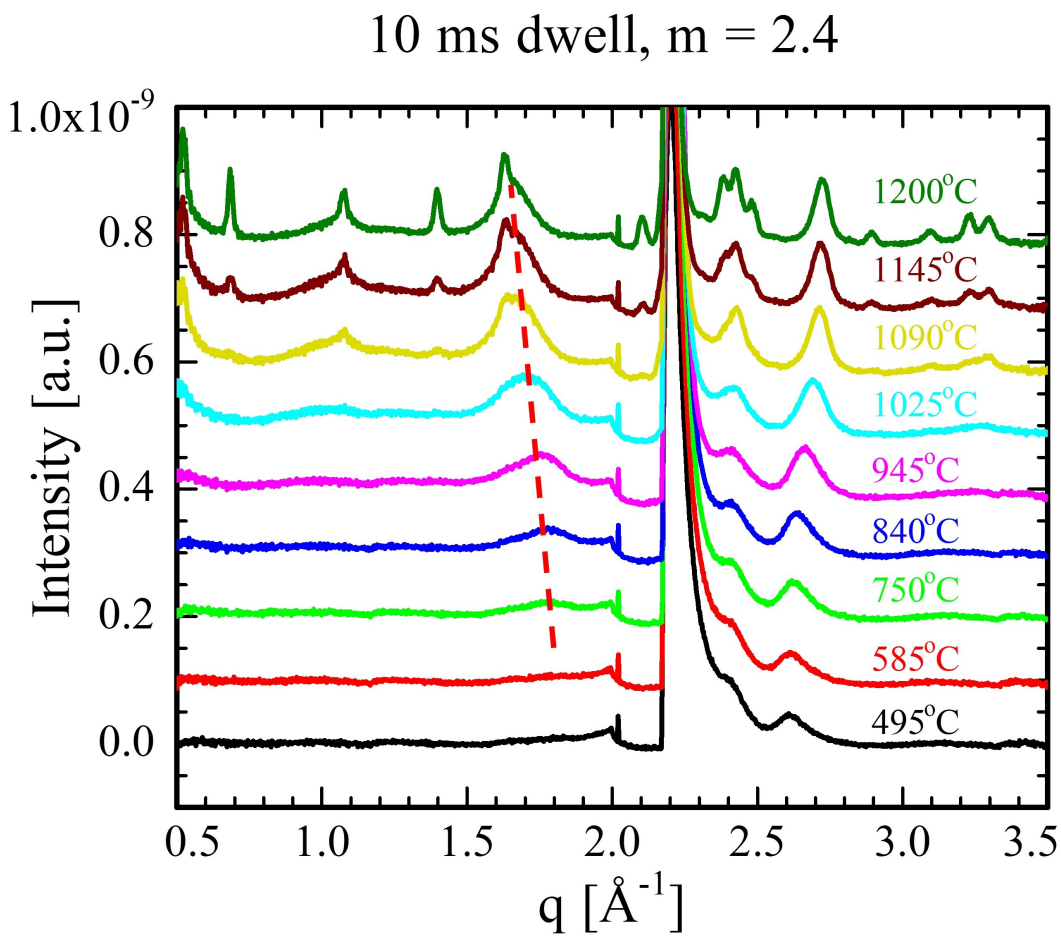

Figure 6.27: Waterfall-type plot of integrated diffraction measurements of m = 2.4 film regions laser annealed at select temperatures for 10 ms. The formation of a diffuse peak consistent with the (0 0 12) peak (q = 1.8 Å^{-1}) is observed at ~750°C. This peak appears to shift toward lower-q values with increasing peak annealing temperature, as shown schematically by the dashed line.

6.7.2 Quantification of Phase Development

Integrated diffraction scans, such as Fig. 6.27, can be used to quantitatively track peak intensity to determine the onset temperature of each phase. Figure 6.28a shows an enlarged subset of these integrated scans as an example: one from a region annealed at 675°C showing only weak $InGaO_3(ZnO)_3$ signal and one from a region annealed at 1175°C exhibiting both strong scat-

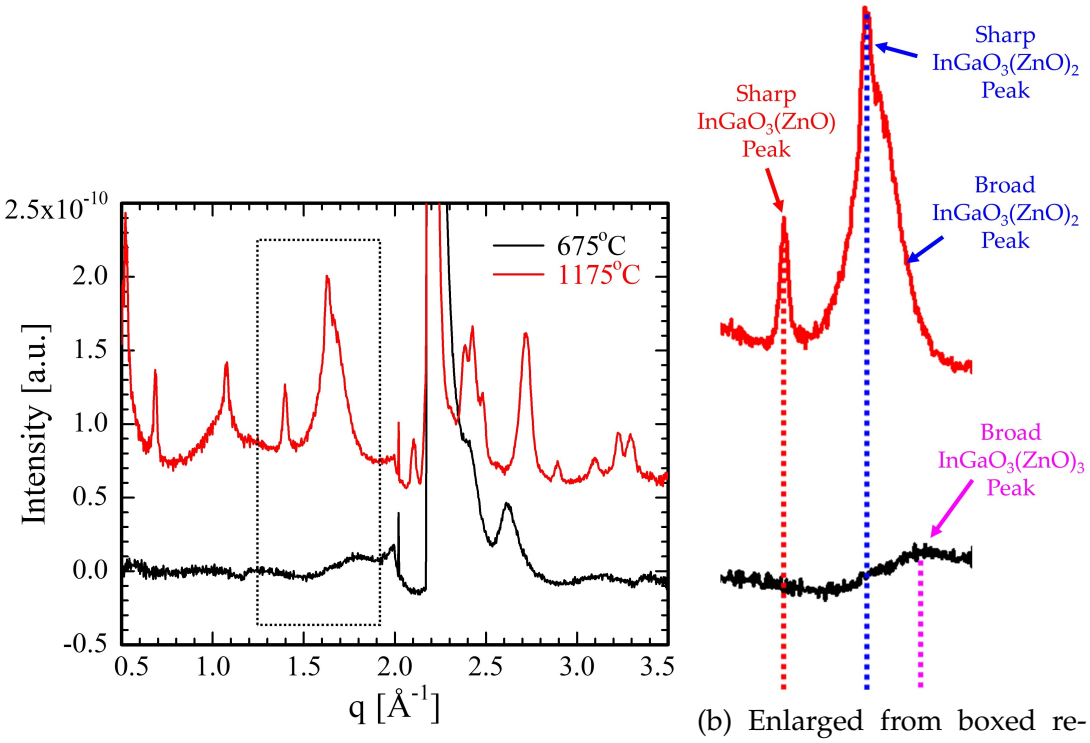

(a) Example diffraction patterns

(b) Enlarged from boxed region in (a)

Figure 6.28: (a) Example diffraction scans for $m = 2.4$ annealed for 10 ms at 675 °C and 1175 °C, indicating the wurtzite as-deposited structure and a complex annealed structure respectively. (b) An enlarged view of the boxed region in (a) marking the different structures observed.

tering from large $InGaO_3(ZnO)$ and $InGaO_3(ZnO)_2$ grains and weak scattering from smaller $InGaO_3(ZnO)_2$ domains. While only one diffuse peak is observed for the $InGaO_3(ZnO)_3$ phase at lower temperatures, the logarithmic heatmap in Fig. 6.25 provides some evidence for the formation of all expected $InGaO_3(ZnO)_3$ peaks. The relative intensity of these peaks is also expected to vary in this non-integer m composition regime due to cationic disorder. Figure 6.29 compares the calculated powder diffraction patterns for an ideal $InGaO_3(ZnO)_3$ crystal and one with cationic disorder. In both cases, the (0 0 12) superlattice peak is the dominant feature.

To simplify data processing, a smaller subset of this data was used in the

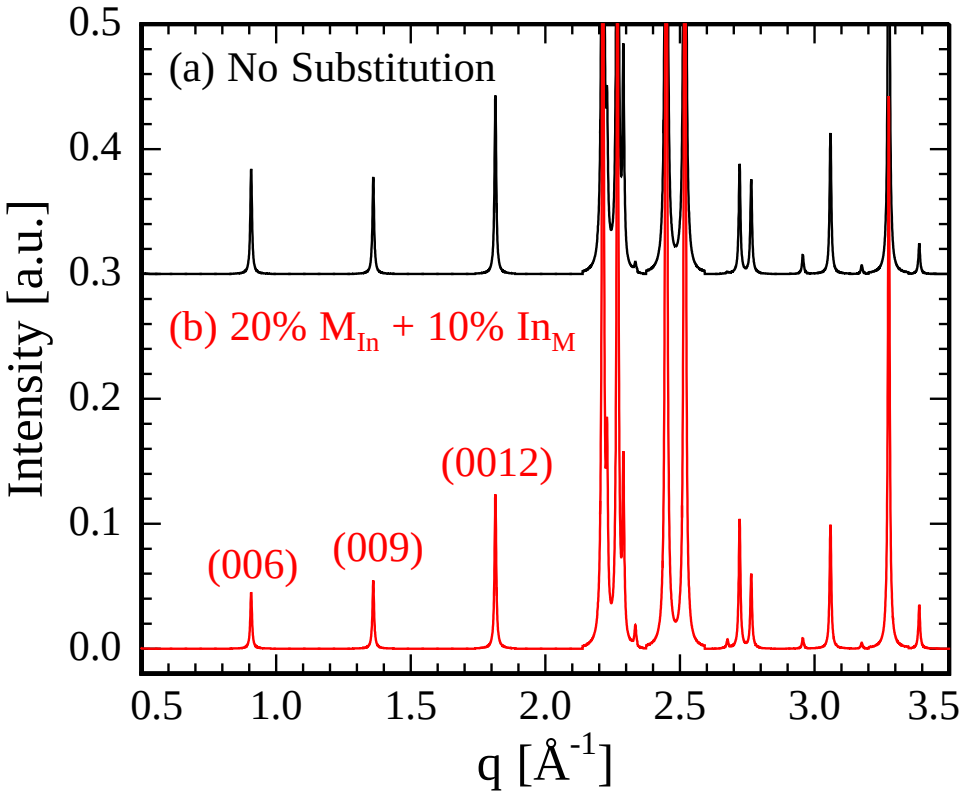

Figure 6.29: Simulated powder diffraction patterns for $InGaO_3(ZnO)_3$ (a) without cation substitution and (b) with 20% M (M = Zn or Ga) substitution on In lattice sites and 10% In substitution on M lattice sites. The scale was chosen to highlight the (0 0 6), (0 0 9), and (0 0 12) superlattice peaks. Data from Ref. [3], and generated using CrystalDiffract [15].

$1.3 < q < 1.9$ Å^{-1} range (Fig. 6.28b). Similar to the amorphous-to-crystalline phase transformation analysis discussed previously, the integrated intensity of each of the observed peaks was calculated and plotted as a function of temperature for each dwell. Each diffraction pattern was fit with 4 independent superimposed Lorentzian curves: a sharp $InGaO_3(ZnO)$ peak, a sharp $InGaO_3(ZnO)_2$ peak, a diffuse $InGaO_3(ZnO)_2$ peak, and a diffuse $InGaO_3(ZnO)_3$ peak. The results of this analysis are shown in Figure 6.30. For all dwells, the diffuse $InGaO_3(ZnO)_3$ peak is first observed to emerge, followed by a dif-

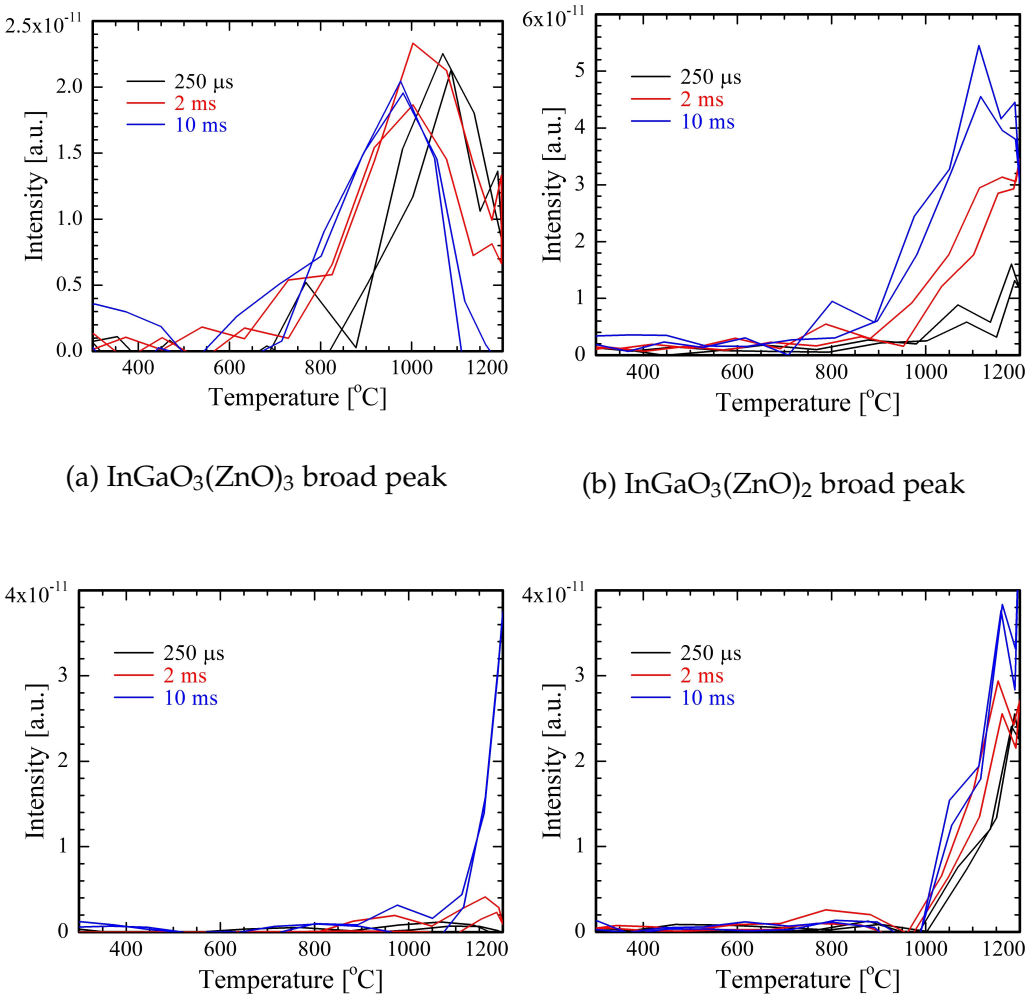

(a) $InGaO_3(ZnO)_3$ broad peak

(b) $InGaO_3(ZnO)_2$ broad peak

(c) $InGaO_3(ZnO)$ sharp peak

(d) $InGaO_3(ZnO)_2$ sharp peak

Figure 6.30: Integrated intensity of peaks observed in Fig. 6.28 as a function of temperature and dwell time for (a) the $InGaO_3(ZnO)_3$ broad peak, (b) $InGaO_3(ZnO)_2$ broad peak, (c) $InGaO_3(ZnO)$ sharp peak, and (d) $InGaO_3(ZnO)_2$ sharp peak.

fuse $InGaO_3(ZnO)_2$ peak at higher temperatures. At a critical temperature near 990°C, the sharp $InGaO_3(ZnO)_2$ signal is observed in all films. For 2 ms and 10 ms dwells at temperatures above 1090°C, a sharp $InGaO_3(ZnO)$ signal ultimately appears.

While the onset temperature of the sharp crystalline peaks occurred at approximately the same temperature independent of dwell (Fig. 6.30c and d), the onset of the diffuse peaks are clearly dwell-dependent (Fig. 6.30a and b). This onset temperature T_x, which can be defined for a particular peak as the temperature where the observed scattered signal is greater than the noise threshold, can be used to estimate an activation enthalpy for formation. T_x can be viewed as the peak temperature required to form a crystalline phase at a particular dwell time t_{dwell}, equivalent to crystalline nuclei developing at a characteristic rate of t_{dwell}^{-1}. This allows construction of a rate vs. inverse temperature Arrhenius type plot from these data, as shown in Figure 6.31.

The onset of the peaks were fit to constant activation enthalpy lines in Fig. 6.31. For both $InGaO_3(ZnO)_2$ and $InGaO_3(ZnO)_3$ phases, the onset follows an Arrhenius behavior with activation enthalpies of ~1.6 eV and ~1.4 eV respectively (and potentially equal within experimental error). These values are roughly consistent with literature values for activation energies for metal diffusion in ZnO (structurally very similar to IGZO). Nakagawa *et al.* reported values of 1.17 eV for In [196] and 1.47 eV for Ga [197], suggesting that the formation mechanism for these structures are limited by atomic motion in the lattice. In contrast, the sharp crystalline signals occur at specific temperatures that are nearly invariant with processing time (990 °C for $InGaO_3(ZnO)_2$ and 1090 °C for $InGaO_3(ZnO)$). This suggests a critical energy barrier for the development of the extended planar structure of larger grains.

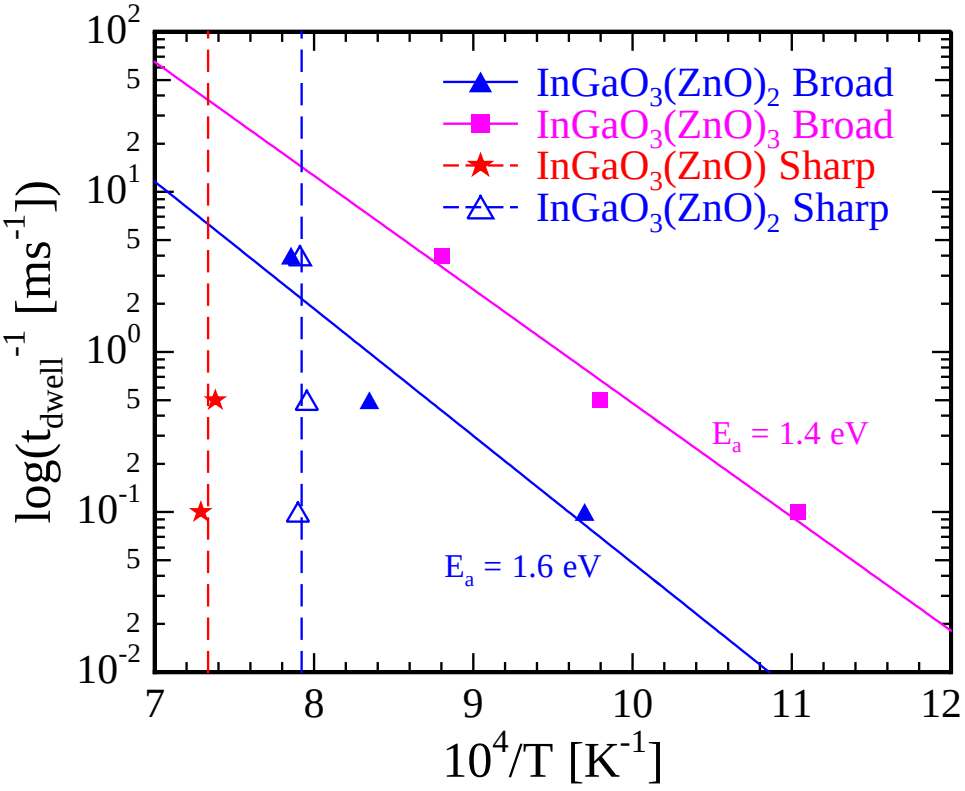

Figure 6.31: Inverse dwell time (t_{dwell}^{-1}) as a function of inverse onset temperature of crystallization ($10^4/T_x$). Formation of the broad $InGaO_3(ZnO)_2$ and $InGaO_3(ZnO)_3$ peaks exhibit Arrhenius behavior with activation ethalpies of ~1.6 eV and ~1.4 eV respectively. In contrast, formation of the sharp $InGaO_3(ZnO)$ and $InGaO_3(ZnO)_2$ peaks are abrupt near 1090°C and 990°C respectively.

6.7.3 Growth Model From Wurtzite Films

The formation of broad $InGaO_3(ZnO)_m$ peaks at lower annealing temperatures (<990°C) is consistent with intragranular cation diffusion and the formation of In_2O_3 superlattice planes within the pre-existing as-deposited wurtzite structure. The broad peaks observed correspond to a grain size of ~10 nm, approximately the same as the estimated grain size of the as-deposited wurtzite structure.

From these data, a tentative model for the formation and growth of the IGZO structure is propsed. As evident in Figure 6.1 and Figure 6.2, the IGZO crystal structure bears great resemblance to the ZnO wurtzite structure. Both structures are composed of a hexagonally-ordered oxygen anion sublattice with cation planes spaced throughout the structure. Whereas the anion sublattice is stacked in an *ABABAB* arrangement in ZnO, the planes in $InGaO_3(ZnO)$ are stacked in an *ABABCACABCBC* arrangement, but maintining the overall hexagonal packing. We believe the as-deposited structure of $InGaO_3(ZnO)_m$ is a disordered wurtzite structure similar to the equilibrium structure of ZnO, but with random substitution of In and Ga onto Zn cation sites with compensating cation vacancies for charge balance.

With annealing, cations diffuse to coalesce into In_2O_3 and cation vacancy planes. For a film with an integer value of m, the structure is driven toward the equilibrium arrangement of $InGaO_3(ZnO)_m$ with periodic In_2O_3 planes and $(m + 1)$ $(Zn, Ga)O_x$ planes, as shown in Figure 6.32 for the case where $m = 2$. Slight deviations in stoichiometry are readily accomodated by antisite point defects. However, beyond a critical threshold, large composition devations require unsupportable cationic disorder and become energetically unfavorable. These larger devations must then be accomodated by more complex layered structures or complete phase separation into Zn-rich and Zn-deficient phases (relative to the average).

However, no nucleation-like events were observed for low temperature anneals. Consequently, we believe the resulting structure must develop continuously from the as-deposited structure. This suggests a phase segregation mechanism that is not classical nucleation and growth. One possibility is shown

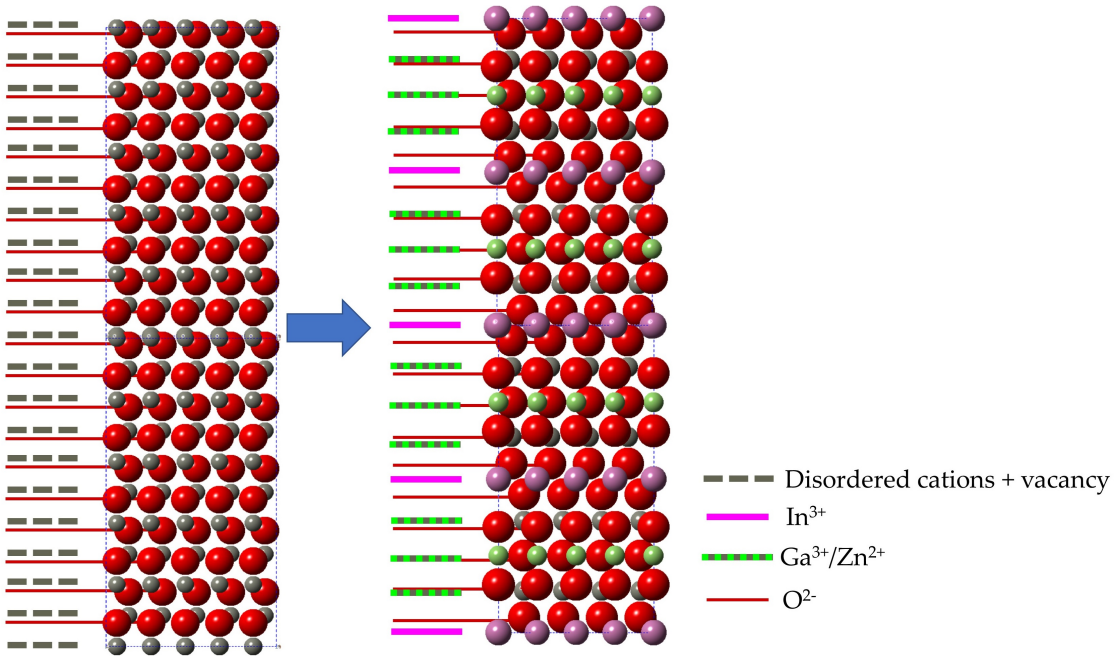

Figure 6.32: Model for structural formation from the as-deposited wurtzite structure when m = integer (m = 2).

schematically in Figure 6.33 for the non-integer m case where m = 2.5. Ultimately the structure must segregate into macroscopic m = 2 and m = 3 regions (as determined by the number of $(Zn, Ga)O_x$ planes between In_2O_3 sheets), but a metastable low-energy configuration with no cationic defects can also form with varying numbers of $(Zn, Ga)O_x$ planes between In_2O_3 sheets.

In this metastable state, the structure can be viewed as alternating sheets of m = 2 and m = 3 structures, accomodating the non-integer m composition. This superstructure has no additional energetic penalties from grain boundaries (or, alternatively, viewed as very low energy coherent grain boundaries along the (0 0 1) face). This model is consistent with literature reports showing HAADF STEM images of off-stoichiometry IGZO films; Figure 6.34 shows the equilibrium structure of an m = 1.5 film with clear alternating m = 1 and m = 2 lay-

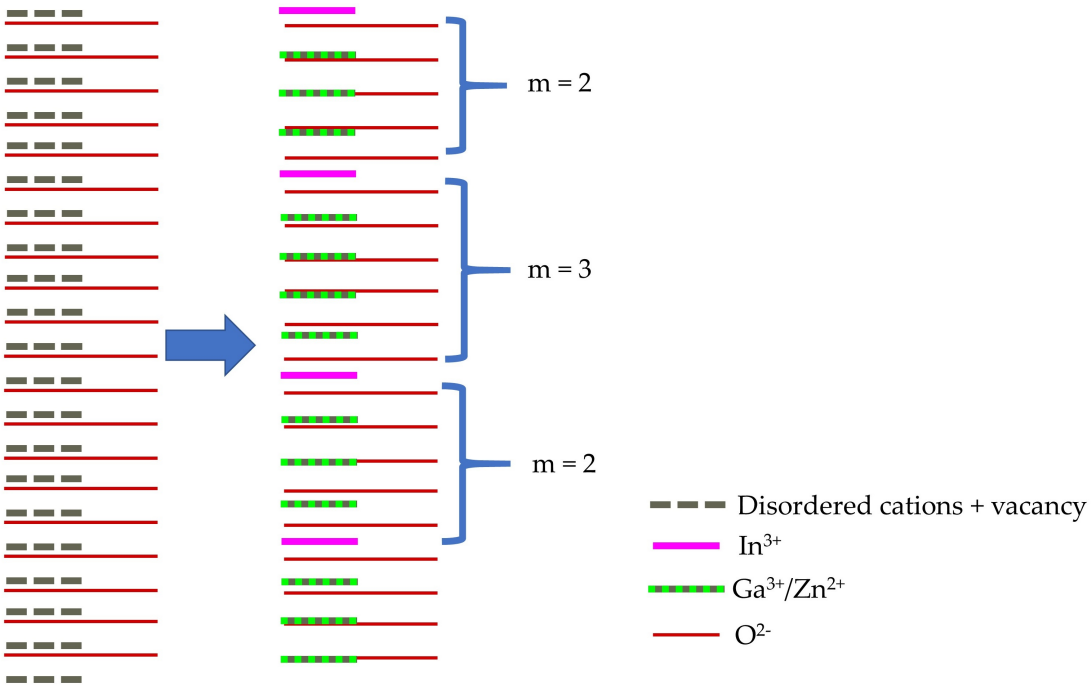

Figure 6.33: Model for structural formation from the as-deposited wurtzite structure to a set of alternating m structures for films with non-integer m (m = 2.5 here).

ers [16].[6]

At the highest annealing temperatures, sharp peaks are formed which indicate formation of larger grains. Below these temperatures, only gradual evolution in crystal structure are observed with no clear changes in grain size. However, the existence of a critical transformation temperature that is invarient with thermal processing time suggests nucleation and growth of these larger grains at high temperatures. At present, these large crystalline domains are poorly understood, and the formation suggests a transformation linked to the energet-

[6]This is included here primarily as an illustration of the alternating m structure. Unfortunately, there are no comparable structures in this study to the literature m = 1.5 structure. As-deposited films with compostion m = 1.5 are amorphous as-deposited and millisecond timescale annealing yields polycrystalline films in this composition regime which were not characterized by HRTEM.

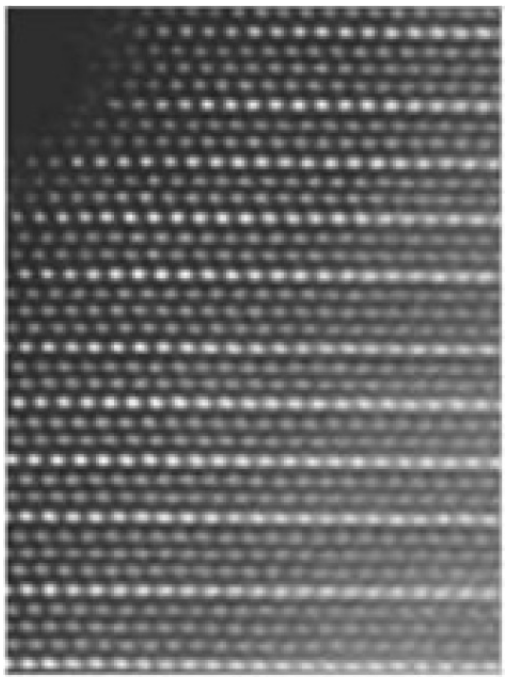

Figure 6.34: Literature-reported cross-section HAADF-STEM image of an IGZO film with $m = 1.5$ composition showing alternating $InGaO_3(ZnO)$ and $InGaO_3(ZnO)_2$ layering. Reprinted with permission from [16]. Copyright 2017 John Wiley and Sons.

ics of the point defects associated with cationic disorder. In a film with composition $m = 2.5$ (where one would expect $InGaO_3(ZnO)_2$ and $InGaO_3(ZnO)_3$ phases at equilibrium), the initial formation of $InGaO_3(ZnO)$ and $InGaO_3(ZnO)_2$ would require a large density of antisite defects on the 6-fold coordinated In-rich planes. Much more work is needed to fully understand this transformation.

6.8 Conclusions

This work explored the fundamental mechanisms of the formation and growth of crystalline IGZO, within the homologous $InGaO_3(ZnO)_m$ compounds. A high-throughput combinatorial approach was used incorporating co-sputter de-

position, millisecond-timescale laser annealing with a built-in temperature gradient, and spatially-resolved structural characterization using microbeam wide-angle X-ray scattering. These techniques enabled the probing of structural evolution as a function of temperature, time, and composition. This deeper understanding of the nature of crystalline IGZO may help to elucidate the structure of CAAC IGZO and enable its successful implementation for high-performance display applications.

As-deposited films are amorphous in the $InGaO_3$-rich composition range, with increasing the Zn fraction (increasing m) leading to textured crystalline films with a wurtzite structure for $m \geq 2$. At the highest Zn fractions investigated, films became increasingly polycrystalline ZnO-like as-deposited. The position of the characteristic (0 0 2) wurtzite peak varies continuously as a function of Zn fraction, indicating a continuous shift in the lattice plane spacing with composition and forming a basis for the formation model used in this work.

Under millisecond heating, films evolved toward equilibrium $InGaO_3(ZnO)_m$ layered structures. Amorphous IGZO films with compositions near $m = 1$ crystallized into a random polycrystalline structure under laser irradiation with deviations in film stoichiometry ($m > 1$) hypothesized to being accomodated by cationic disorder. This model accounts for both the variation in diffraction pattern intensities as a function of composition in this work, and apparent disorder in CAAC IGZO seen in literature reports.

Crystal-to-crystal transformations for Zn-rich compositions were discussed within the context of a new growth model for these homologous structures. Under millisecond heating, we hypothesize that indium atoms within the as-deposited wurtzite structure begin to order into octahedrally-coordinated

planes, resulting in diffuse X-ray scattering peaks. In non-integer *m* regions, this leads to a complex layered structure, with alternating regions of the closest *m* structures. The proposed model is also consistent with structures seen in literature.

CHAPTER 7

CONCLUSIONS AND FUTURE WORK

The advent of IGZO as an active semiconductor material in display transistors has enabled the development of high-performance displays due to a ten-fold higher electron mobility relative to a-Si while maintaining uniformity and low production costs. However, the long-term stability issues caused by material defects jeapordize large-scale implementation of IGZO. CAAC IGZO provides tremendous promise in addressing these issues owing to its textured crystalline morphology. Devices fabricated from CAAC exhibit drastically improved threshold stability and reduced leakage current while maintaining the benefits of a-IGZO. However, until this work, virtually nothing was known regarding the development of the CAAC structure or the phase formation and crystallization kinetics of the general ternary IGZO system.

The growth regimes of RF sputtered highly aligned CAAC IGZO films were identified in this work. The CAAC microstructure readily forms during heated deposition of IGZO films with compositions near the 1:1:1 In:Ga:Zn cation ratio in a reactive oxygen environment. Optimally-textured CAAC IGZO films were found to form near 310°C and in 10% O_2 (balance Ar) under the conditions investigated. With higher substrate temperatures or in higher O_2 partial pressures, the c-axis alignment is lost and films adopt a more random microstructure due to continuous nucleation.

A high-throughput approach was used to probe the fundamental mechanism for the formation and growth of crystalline $InGaO_3(ZnO)_m$. Experiments combined co-sputter deposition, millisecond timescale lgLSA, and spatially-resolved characterization using μ-WAXS. As-deposited films exhibited

a wurtzite crystal structure similar to ZnO, strongly suggesting a solid solution between ZnO and $InGaO_3$. Under millisecond heating, films evolved toward equilibrium layered structures consisting of nearly pure In_2O_3 layers with $(Ga, Zn)O_x$ interlayers. Accomodation of off-stoichiometry (in films regions with non-integer m) was attributed to cationic disorder and the formation of antisite defects. Observed crystal-to-crystal transformations in non-integer m composition regions suggest a new model for the formation of these structures in which interdiffusion leads to the gradual formation of the In_2O_3 superlattice with varying numbers of $(Zn, Ga)O_x$ layers, consistent with observations from literature.

Considering the CAAC structure within the context of these new models, there are several key implications that have yet to be explored. While CAAC devices exhibit improved threshold stability characteristics, the crystalline morpholgy does not improve carrier mobility—in stark contrast with LTPS vs. a-Si:H. This difference has been attributed to cationic disorder in this complex ternary oxide. However, millisecond heating has been shown to be sufficient to allow cationic ordering in IGZO films, driving structures toward the equilibrium $In_2O_3/(Ga, Zn)O_x$ layered structure. This suggests that LSA of CAAC IGZO may open a pathway toward increasing the mobility of CAAC films beyond what has been previously reported.

Further, other possible methods of CAAC production have been revealed. Large-scale implementation of CAAC IGZO has been hampered by the current limitations of industrial processing equipment. CAAC structure, formed by substrate heating during deposition, would require large-area (~2 m × 2 m) substrate temperature control not readily achieved in deposition tools cur-

rently equipped for the room temperature deposition of a-IGZO. Manufacturers considering CAAC IGZO are faced with either accepting the resulting non-uniformities or captial investment in new equipment. However, this work has demonstrated the formation of $InGaO_3(ZnO)_m$ from as-deposited textured wurtzite during millisecond timescale laser-annealing—without alteration of the textured microstructure. Replacing *in situ* heating during deposition with post-deposition millisecond heating is a promising pathway toward successful CAAC implementation.

Lastly, the combinatorial approach used in this work can be extended to fundamental materials research. The short annealing timescales coupled with the extremely fast quench rates inherent in LSA enable exploration of new metastable material systems. This work—even across only a single pseudo-binary ($InGaO_3$–ZnO)—has demonstrated the vastness of structural information that has been previously impractical or impossible to access. Other high-throughput characterization methods can also be coupled with these combinatorial techniques to effectively screen structures formed by transient thermal processing (i.e., micro-cell or micro-Hall measurements for electrochemical or device applications, respectively). This combined approach presents an exciting avenue for future work in materials discovery and high-throughput screening for advanced material applications.

APPENDIX A

TRANSISTOR OPERATION AND KEY PERFORMANCE METRICS

TFT operation bears great similarity with the operation of a metal-oxide-semiconductor field effect transistor (MOSFET). Both devices incorporate a conductor-insulator-semiconductor stack and are governed by the same transport behavior, and therefore they both exhibit similar current-voltage (IV) characteristics. For this reason, analysis of TFT behavior is typically done using MOSFET characterization techniques. The basic operation of a MOSFET device can be understood by consideration of the band structure at the metal-oxide-semiconductor (MOS) interface.

A.1 IV Characteristics

In the on-state of the MOSFET transistor, when an inversion channel is formed, the drain-source current is

$$I_{DS}(y) = -q\,W\,n_s(y)\,v_n(y) \tag{A.1}$$

where y is the direction of current flow in the channel, W is the channel width, $n_s(y)$ electron density per unit area at a given position y, and $v(y)$ is the drift velocity of charge carriers (with electrons moving opposite the direction of current flow).

For small electric fields in the y-direction, the drift velocity is given by

$$v_n(y) = -\mu_n E_y = \mu_n \left(\frac{\partial V(y)}{\partial y} \right)_x \tag{A.2}$$

Assuming that μ_n and V_T are both constant and taking the gradual-channel approximation (bulk charge controlled by vertical x-direction field only), then the potential drop at any y coordinate in the channel is $V_{GS} - V_T - V(y)$, and the inversion charge in the channel is

$$Q_n(y) = -q\, n_s(y) = -C_{ox}\left[V_{GS} - V_T - V(y)\right] \tag{A.3}$$

Substituting the above expressions into equation A.1 gives

$$I_{DS}(y) = \mu_n\, C_{ox}\, W\left[V_{GS} - V_T - V(y)\right]\frac{dV(y)}{dy} \tag{A.4}$$

Integrating $I_{DS}(y)$ across the channel length from the source ($y = 0$ and $V(0) = V_S = 0$ as a reference) and the drain ($y = L$ and $V(L) = V_{DS}$) gives the classical MOSFET equation:

$$I_{DS} = \mu_n\, C_{ox}\frac{W}{L}\left[(V_{GS} - V_T)\; V_{DS} - \frac{1}{2}V_{DS}^2\right] \tag{A.5}$$

The MOSFET equation describes the IV characteristics of a transistor below pinch-off, at which current saturation occurs. As can be seen from equation A.5, the current through the transistor is a function of both the gate voltage V_{GS} and drain voltage V_{DS}. Transistors are typically charcterized by two types of IV curves: the transfer characteristics (I_{DS} vs. V_{GS} at fixed V_{DS}), showing the switching behavior of the transistor, and the output characterstics (I_{DS} vs. V_{DS} at fixed V_{GS}), showing the different operating regimes of the transistor. Examples of these curves are shown in Figure A.1 and Figure A.2.

While equation A.5 is derived based on the assumptions of an inversion channel, this equation is frequently used to interpret TFT data and extract device parameters even in the accumulation mode. Three quantitatve parameters

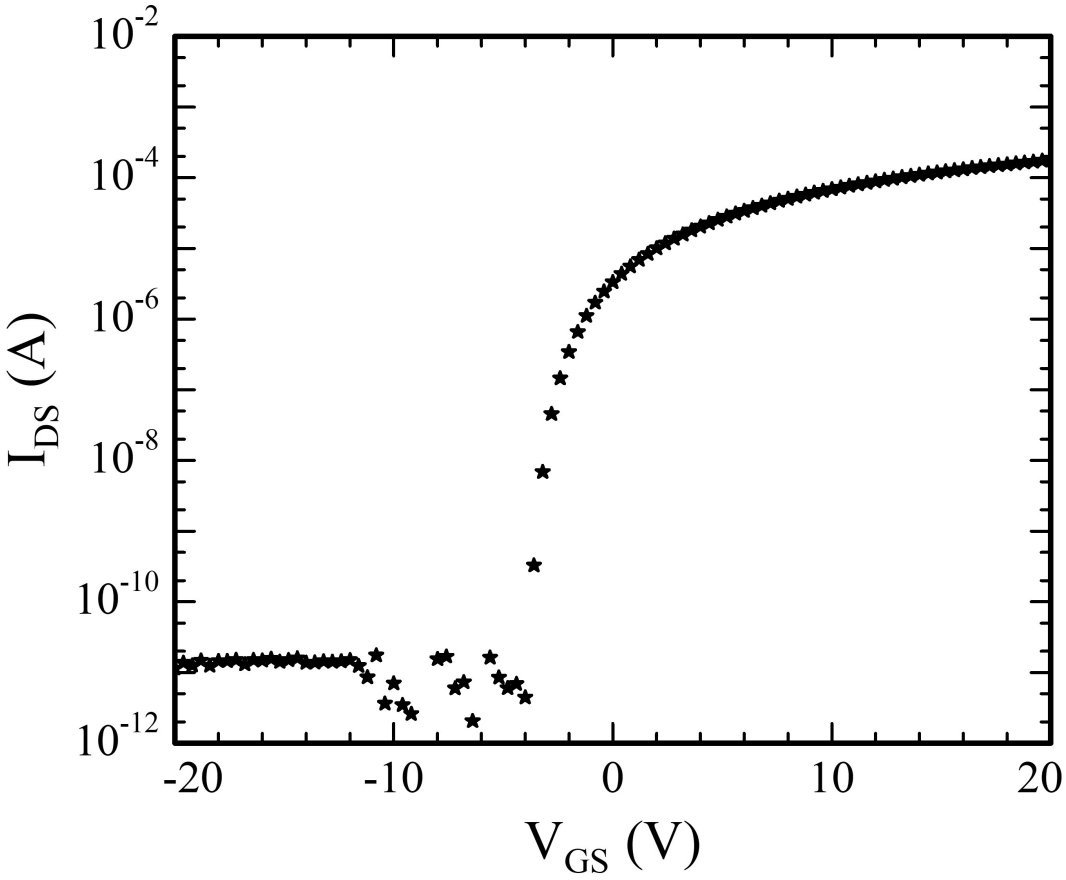

Figure A.1: Transfer characteristics of a TFT.

can be extracted from these *IV* characteristics: the carrier mobility (of the carrier composing the channel), the threshold voltage, and the subthreshold slope. In the preceeding plots, the carrier mobility μ is reflected in the scaling of current with increased gate voltage, and the threshold voltage V_T determines the gate voltage at which the transistor switches from a state of negligible current into the on-state. Figure A.1 (transfer characteristics), plotted on a logarithmic *y*-axis scale, shows the sharp change in current as the transistor is switched from subthreshold to above-threshold. This region is characterized by the subthreshold slope and is related to carrier traps located at the dielectric-semiconductor interface.

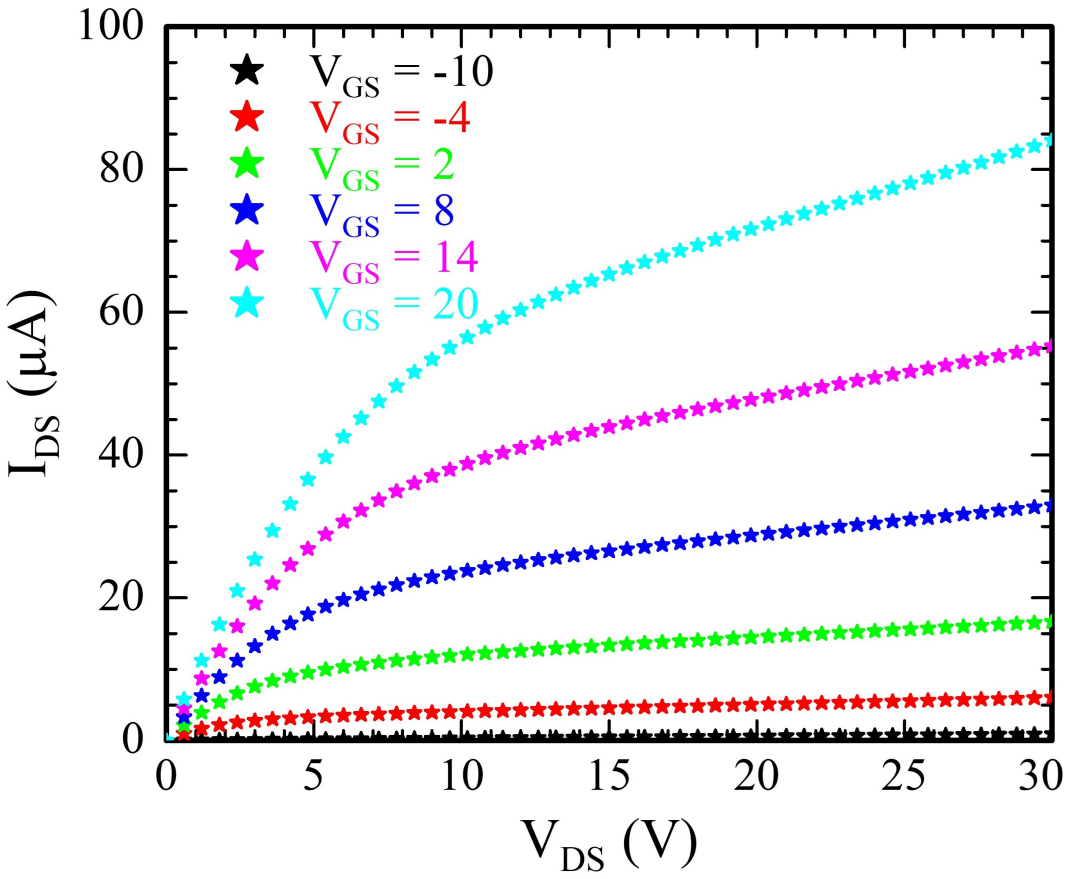

Figure A.2: Output characteristics of a TFT.

A.2 Parameter Extraction

Throughout TFT literature, a vast number of parameter extraction methods are used to extract carrier mobility μ and threshold voltage V_T. This section will summarize the methods used in this work. The methods presented here provide a good "average" over a wide range of applied gate voltages.

In this work, both carrier mobility μ and threshold voltage V_T (or, more appropriately, the on-voltage V_{on}, as accumulation-mode TFTs do not exploit carrier inversion) are both extracted from the linear small-signal regime of the output characteristics. The linear regime can be seen in Figure A.2 at low V_{DS} values

where the transistor acts as a gate-modulated resistor with an IV slope equal to the conductance g_d, defined as:

$$g_d \equiv \left(\frac{\partial I_{DS}}{\partial V_{DS}}\right)_{V_{GS}} \tag{A.6}$$

The IV characteristics of this region are equivalent to taking the small-signal limit of equation A.5 as $V_{DS} \to 0$, eliminating the V_{DS}^2 term:

$$I_{DS}|_{V_{DS}\to 0} = \mu_n C_{ox} \frac{W}{L} (V_{GS} - V_T) V_{DS} \tag{A.7}$$

Differentiating equation A.7 with respect to V_{DS} gives the small-signal conductance

$$g_d|_{V_{DS}\to 0} \equiv \left(\frac{\partial I_{DS}}{\partial V_{DS}}\right)_{V_{GS}}\Bigg|_{V_{DS}\to 0} = \mu_n C_{ox} \frac{W}{L} (V_{GS} - V_T) \tag{A.8}$$

which is a linear function of V_{GS} valid for any $V_{GS} > V_T$. Indeed, plotting the small-signal conductance extracted from the output IV characteristics as a function of V_{GS} exhibits linear characteristics above a certain threshold in voltage values. Fitting a line to values where g_d is non-neglible allows direct extraction of μ_n and V_T – assuming the remaining physical dimensions are known (channel width W, channel length L, and gate insulator capacitance C_{ox}).

The subthreshold slope is extracted from the transfer characteristics. Figure A.1 is plotted on a logarithmic y-axis scale, highlighting the abrupt change in I_{DS} with increasing V_{GS} near the threshold voltage V_T. The inverse of the slope linear portion (on the semilogarithmic scale) is defined as the subthreshold slope S

$$S \equiv \left(\frac{\partial V_{GS}}{\partial \log I_{DS}}\right)_{V_{DS}} \tag{A.9}$$

which has units of V/decade (decade of current, since I_{DS} is plotted on a logarithmic scale).

It can be shown [18] that S is related to the capacitances of the gate insulator (C_{ox}) and the depletion layer in the channel (C_d) and to any trapped interface charge at the semiconductor-oxide interface (qN_{it}). Hence, it can be shown that the subthreshold slope is related to the density of interface traps by

$$S \equiv \left(\frac{\partial V_{GS}}{\partial \log I_{DS}} \right)_{V_{DS}} \approx \frac{kT}{q} \left(1 + \frac{C_d + qN_{it}}{C_{ox}} \right) \ln 10 \tag{A.10}$$

In the limiting case where there are no trapped interface charges and the gate insulator capacitance is dominant ($C_{ox} \gg C_d$), S reaches a minimum value of 59.5 mV/decade.

As a final note on the subthreshold slope: it is fairly common in TFT literature for some authors to present values of S as a metric for defect state density. Indeed, while S is a function of the interface trap state density, the reader is urged to exercise caution with this interpretation. The transfer characteristics from which S is extracted are usually measured on timescales on the order of a few seconds. By necessity, S only contains information on trap states that carriers can escape from on timescales of ~1 second. While it may be a valid to assume this nature for all traps in MOSFETs fabricated from high-quality crystalline semiconductors, this is a poor assumption for TFTs—often fabricated from relatively high-defect materials. As such, S provides only limited information on trap states with long characteristic relaxation times or on metastable defects.

A.3 Deviations from MOSFET behavior in TFTs

Three main distinctions between TFTs and MOSFETs can be drawn. First, the channel layer in a TFT has a finite thickness, making the device much more susceptible to surface states at the backchannel. Second, while conduction in a MOSFET is determined by the existence of shallow dopant states in the semiconductor bandgap, TFT operation is determined by a distribution of defect states in the semiconductor. This limits the use of the full-depletion approximation (assumption of abrupt depletion zone edges) frequently invoked for a MOSFET. Last, and in large part due to the above points, a TFT is typically operated as a majority carrier accumulation-mode device rather than a minority carrier inversion-mode device.

APPENDIX B

AMORPHOUS SEMICONDUCTOR THEORY

One shouldn't work on semiconductors, that is a filthy mess; who knows whether any semiconductor exists.

—Wolfgang Pauli in a letter to Rudolf Peierls, 1931 [198]

A basic understanding of amorphous semiconductor theory is paramount to understanding the current state of the art of, and the challenges remaining in, the IGZO research field and the display semiconductor industry as a whole. Nearly every undergraduate student in a reputable materials science progam is exposed at some level to band theory as it is developed from the Schrödinger equation with a periodic potential provided by a crystalline lattice. Crystalline semiconductor theory, and the argument of a perfectly periodic potential, fails in the disordered structure of an amorphous solid. However, amorphous semiconductors are often a forgotten facet of traditional semiconductor education. To the best of the author's knowledge, most IGZO literature assumes this amorphous semiconductor knowledge that has been developed since the 1950s to explain the electronic behavior of the chalcogenide glasses and amorphous silicon. This section provides a brief summary of the key elements of semiconductor theory. The basics of amorphous semiconductor theory and the electronic repercussions of the amorphous structure are discussed as they pertain to the retention of the band gap and the formation of localized states not present in a crystalline material.

B.1 Impact of Amorphization on the Electronic Structure

Modern semiconductor theory is primarily based on the model of a free electron experiencing the periodic atomic potentials of a perfect crystal. It should then follow that, without perfect atomic arrangement, amorphous solids could not exhibit semiconductor behavior. Indeed, the concept of an amorphous semiconductor initially sparked debate when they were first discovered [198]. However, while the well-accepted model did not support amorphous semiconductors, the astute observer would realize the validity of a bandgap in an amorphous material as many amorphous glass systems are transparent in the visible or infrared range [199].

Indeed, much of the current understanding of the electronic structure of IGZO is based on considering the implication of defects within the amorphous structure. This section develops the concepts and terminology common to the field of amorphous semiconductors. Special attention is given to the doping mechanism in a-Si as a model system to draw general conclusions regarding doping in amorphous semiconductors. Lastly, the role of hydrogen in a-Si is explored both as a defect passivator and in terms of local structural relaxation.

B.1.1 Retention of the Bandgap

Weaire and Thorpe [200–203] showed that the band gap of a material most strongly depends on the short-range ordering rather than the long-range ordering previously thought necessary for band splitting. With the loss of a perfectly periodic potential however, the solutions to the Schrodinger equations that are

valid for a crystalline system are no longer valid for an amorphous system. A wavefunction with a well-defined momentum vector k in a crystalline lattice is perturbed by the disorder in the structure, resulting in a poorly-defined k that is now no longer conserved in electronic transitions and a loss of wavefunction phase coherence over only a few atomic distances due to scattering. Indeed, this scattering is the primary origin of the reduced carrier mobility in an amorphous semiconductor as compared to its crystalline analogue [204].

The loss of electron momentum conservation in an amorphous semiconductor then changes our basic description of these materials. Therefore, E-k dispersion relationships are not strictly valid, and the distinction between a direct and an indirect band gap transition loses fundamental meaning. For this reason, carriers in amorphous semiconductors are typically discussed in terms of their spatial position and the density of states rather than in terms of electron momentum [204].

B.1.2 The Electron Wavefunction and the Mobility Edge

Due to the structural disorder in terms of bond lengths and angles, characteristic electronic binding energies are replaced with a distribution of binding energies. In the schematic density of states distribution shown in Figure B.1, the abrupt band edges (E_C for the conduction band minimum and E_V for the valence band maximum) are then replaced with "tails" extending into the bandgap. Other structural defects, such as the dangling bond in a-Si, exhibit energy levels within the bandgap.

Anderson in 1958 [205] derived one of the most important implications of

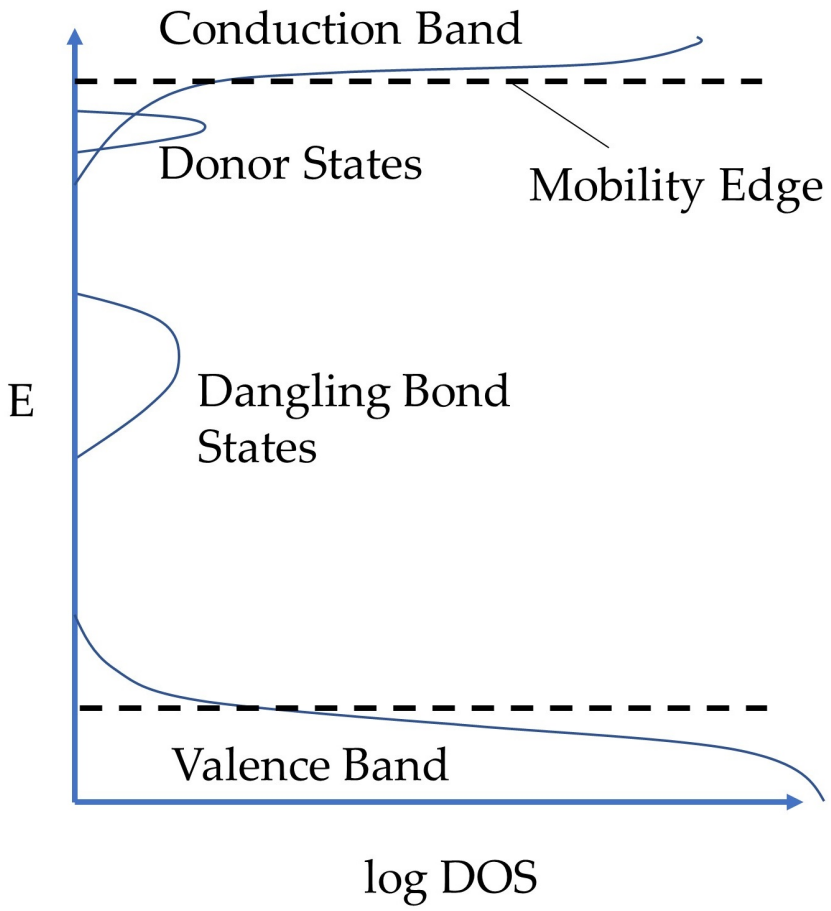

Figure B.1: Schematic density of states in the band gap of amorphous silicon.

these local wavefunction distortions caused by structural disorder. If it is assumed that the result of the disordered structure is a distribution of atomic potentials (rather than a well-defined potential in a crystalline material), the electron wavefunction can form one of two types of states: (1) higher-energy extended states, which resemble a heavily-scattered crystalline wavefunction that allows electronic transport and (2) lower-energy localized states, in which the electron is spatially confined to within a few atomic spacings.

From Anderson's theory of localization, there exists an energy threshold between extended and localized states known as the mobility edge, defined as E_C

for the conduction band mobility edge (and analogously E_V for the valence band mobility edge). The mobility edge derives its name from the zero-temperature limit, at which only electrons with energies above E_C can contribute to conduction. At finite temperatures, conduction can occur by thermal excitation of carriers to E_C or by thermally-controlled carrier hopping between localized states. The concept of a mobility edge replaces that of a crystalline band edge in amorphous semiconductor theory [199, 206–208]. However, it should be noted that this is merely an extrapolation of the density of states concept; the mobility gap (defined by the difference between the conduction band and valence band mobility edges) is generally much larger than the analogous crystalline bandgap [204]. For example, a-Si exhibits an optical bandgap of 1.7 eV compared with 1.1 eV in crystalline Si [209, 210].

B.1.3 Doping in Amorphous Semiconductors

The structure of an amorphous semiconductor further complicates the picture when it comes to the doping mechanism. In crystalline silicon for instance, substitutional impurity atoms (ex: phosphorus or boron) are topologically constrained, and hence all substitutional dopants are forced into 4-fold coordination and contribute a weakly-bound electron or hole to the silicon lattice.

Elementary structural considerations of amorphous solids are based on the Mott 8-N rule [206], which suggest that all elements in a random amorphous network can be expected to bond with optimal valency. Thus, while Si in a-Si would optimally form four bonds, B and P would both tend toward 3-fold coordination, and early theoretical predictions concluded that doping an amorphous

semiconductor was impossible [211]. Experimental work has since clearly disproven this prediction, as impurity-containing precursors included in the a-Si deposition environment are clearly linked to increased conductivity. However, doping in amorphous silicon is exceedingly complex as compared to crystalline silicon.

The mechanism of donor state formation from dopant atoms can be explained by amending the Mott 8-N rule to allow incorporation of charged impurities into the amorphous network. For example, while a P atom would preferentially form 3 bonds, a singly-ionized P^+ would preferentially form a 4-fold coordinated structure in the a-Si network. The donor states are added below the conduction band mobility edge E_C, effectively adding to the tail states as shown in Fig. B.1. Due to the larger formation energy of the 4-fold coordinated P^+, only a small fraction of phosphorus atoms are 4-fold coordinated. To maintain charge balance however, another defect—a dangling bond—must also be created. The dangling bond defect state then acts as a compensating defect, and captures nearly all the electrons provided by the donor phosphorus [212, 213].

Three very important conclusions must be drawn with regard to doping in an amorphous semiconductor. First, the doping efficiency is normally very low. Depending on growth conditions, the doping efficiency of a-Si ranges from 10% to as low as 0.1% [213]. Second, carriers provided by dopants are not "free" for conduction as they are in a crystalline semiconductor, but instead add electron states to the localized band tail states. Last, and most importantly, the introduction of dopant states frequently introduces a second compensating defect. None of these conclusions are directly addressed in the IGZO literature, but are paramount for true understanding of the electronic structure of IGZO.

B.1.4 Hydrogen and Metastability

Hydrogen is typically incorporated into the a-Si network to passivate dangling bonds and eliminate the associated trap states in the middle of the band gap (Fig. B.1). Hydrogenated a-Si (a-Si:H) typically contains a large enough fraction of hydrogen to be considered an alloy. In device-grade a-Si:H, hydrogen atomic fractions used are ~10% to reduce the dangling bond defect density to ~10^{16} cm^{-3} [18]. However, the incorporation of hydrogen in the a-Si network has some unforeseen consequences.

As a material consisting of a frozen "liquid-like" disordered structure far from an equilibrium crystal state, it is unsurprising that amorphous semiconductors exhibit metastable structural and electronic characteristics. The defect density of such a material is frozen-in during formation, and over time the structure can relax to lower energy configurations.

There are several examples in literature of such a relaxation in a-Si, as measured by the increase of conductivity with annealing [64], the decrease of band tail density with annealing [214], or observation of a thermal history-dependent dangling bond defect density [215]. These effects can be understood by the disordered arrangement of Si-Si bonds, in which there is a distribution of bond energies cause by various bond lengths and angles in the network. Rearrangement of these bonds is assisted by hydrogen diffusion throughout the network: (1) hydrogen from one dangling bond diffuses and breaks a weak bond, (2) the broken bond enables local structural relaxation, (3) hydrogen diffuses to another weak bond, leaving a stronger bond in its place.

As a metastable material consisting of weakly-bound Si-Si bonds, a-Si ex-

hibits transient defect behavior not seen in its crystalline form. Staebler and Wronski [216] observed that external stimuli, such as optical illumination, can induce localized gap state defects, and relaxation to quasi-equilibrium (as an amorphous solid is never in true equilibrium) has been attributed again to the diffusion of H to re-establish bond equilibrium [217]. While there has been debate to whether these induced states are "created" by illumination (bond breaking) or originate from a shift in defect state occupancy (de-trapping of carriers), it is clear that such transient behavior can negatively impact the a-Si device performance. This is one of several mechanisms by which a-Si TFTs manifest threshold instability.

While the passivating characteristics of incorporated hydrogen may be more specific to group IV semiconductors, hydrogen nevertheless can play a role in other systems. It should be noted that the existence of metastable electronic properties does not require hydrogen-incorporating states in the amorphous semiconductor; hydrogen merely provides a potential mechanism for relaxation. Indeed, IGZO-based devices are known to exhibit such behavior by other mechanisms.

B.2 Electronic Consequences of the Amorphous Structure and Effects on Device Performance

The amorphous structure of a semiconductor material has very profound impacts on the electronic properties. They can be summarized in the following categories [204]:

B.2.1 Bonding Disorder

The variation of bond lengths and angles, or so-called weak bonds, gives rise to localized tail states. These extend the conduction and valence bands of the crystalline state into the band gap through tail-like states. Characteristic of these states is the localization of the electron wavefunction to within a few atomic spacings, leading to a loss of wavefunction percolation throughout the material and the introduction of scattering centers and a reduction in carrier mobility.

B.2.2 Structural Defects

Dangling bonds and dopants both give rise to electronic states in the band gap. Due to the disordered nature of the host structure, these states have a distribution of energies rather than a discrete energy (as in a crystal). These states give rise to charge carrier trapping during device operation, and provide a leakage current mechanism by hopping among defect states—even when the device is switched "off."

B.2.3 Alternative Bonding Configurations

Because of the weakly bonded nature of the disordered network, local structural relaxation through external stimuli can result in the rearrangement of network bonds, leading to metastable electronic properties and transient device behavior manifested as long-term instabilities.

APPENDIX C

SILICON NITRIDE DEPOSITED BY PECVD

The following section was written as part of a report for a collaborator working on the silicon nitride SiN_x plasma-enchanced chemical vapor deposition (PECVD) process. While all of the proprietary information has been omitted, the included deposition theory notes are useful for any researcher involved in work with this material for device fabrication.

C.1 PECVD SiN_x Deposition Theory

Silicon nitride films are typically deposited by a reaction of SiH_4, NH_3, and N_2 gaseous precursors. Deposited films are characteristically off-stoichiometry silicon nitride SiN_x and include a high atomic fraction of H (5-30 at% – hence why these films are often referred to as an SiN_x:H alloy). Claassen *et al.* [17] proposed a multi-step reaction mechanism describing precursor dissociation, intermediate condensation, and elimination of hydrogen from the resultant SiN_x film.

C.1.1 Gas Phase Dissociation Reactions

Within a PECVD chamber, the deposition plasma consists of electrons, stable molecules, and active species formed by electronic collisions: excited molecules, ionized species, and free radicals. It is the dissociation of the precursors into ions and free radicals that contributes to the growth of the SiN_x film. These dissociation reactions produce free hydrogen and a wide spectrum of intermediate active species: (1) ions SiH_x^+, NH_x^+, and N_2^+; and (2) free radicals SiH_x, NH_x,

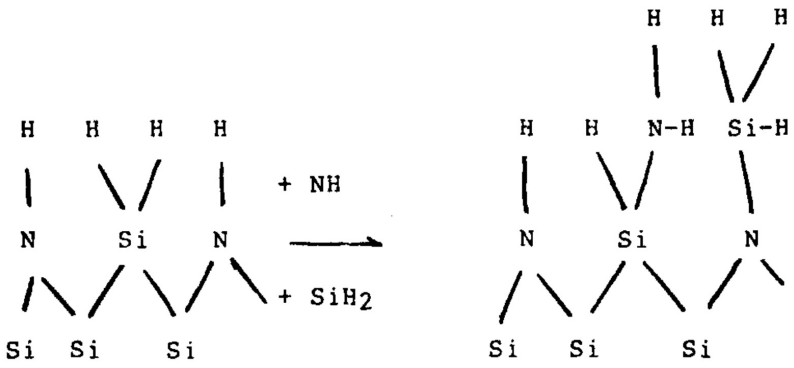

Figure C.1: Schematic diagram of the condensation reaction of intermediate species in the gas phase to form the SiN_x film network [17].

and N.

It is thought that the free radical species dominate the growth process, as free radical concentrations are typically several orders of magnitude higher than ion concentrations in the plasma [218]. It has also been shown [219, 220] that SiH_2 and NH are the most prevalent intermediates for consideration in subsequent reactions.

It is important to note that the kinetics of these dissociation reactions are largely temperature-independent. The average thermal energy of an electron involved in a dissociation reaction is much higher than that of the gas, and is governed by the degree of ionization in a plasma (and therefore dependent upon only the RF parameters, such as power and frequency).

C.1.2 Condensation Reactions

Direct condensation of these intermediate species, as shown schematically in Figure C.1, is the main growth pathway during deposition.

However at higher deposition pressures where gas phase collisions are more probable, homogeneous nucleation reactions within the gas can also occur, for example:

$$SiH_2 + SiH_4 \rightarrow Si_2H_6 \tag{C.1}$$

$$NH + SiH_2 \rightarrow SiNH_3 \tag{C.2}$$

The coalescence of these larger species in the growing film give rise to increased free volume, hydrogen content, and ultimately increased tensile stresses (discussed in greater detail below). These condensation reactions are only weakly temperature-dependent due to the low activation energy of reactions involving radicals. Therefore, due to the weak temperature dependence of the dissociation and condensation reactions, deposition rate is expected to be a weak function of temperature.

C.1.3 Hydrogen Elimination

Another reaction with major implications for SiN_x film stress, both as-deposited and annealed, is shown in Figure C.2. N-H and Si-H groups within the deposited film can react to form a cross-linked structure (e.g. N-Si and Si-Si bonds) and H_2. This cross-linking contributes to local densification and a state of film tension.

This reaction is thermally-activated, and therefore depends strongly on substrate temperature. While this reaction is presented in the context of film deposition, it is extremely important to note that this reaction also provides the mechanism for changes in film stress due to post-deposition annealing.

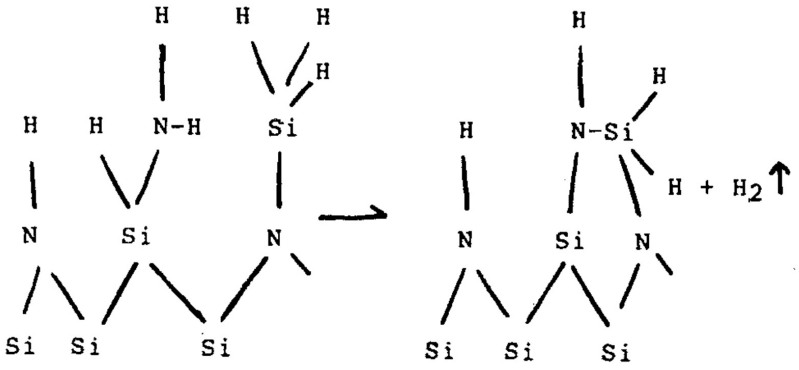

Figure C.2: Schematic diagram of the hydrogen elimination reaction leading to hydrogen evolution, local densification due to cross-linking, and the primary origin of tensile stresses in SiN_x.

C.1.4 Ion Bombardment

In addition to these chemical reactions, films can also be subjected to ion bombardment during deposition. At low RF frequencies, ions can be accelerated by the alternating electric field into the growing film. These ions can become implanted or break bonds in the film, leading to local expansion and a state of compression.

However at high RF frequencies (>4 MHz), ions are unable to follow the alternating field (not enough time for acceleration across substantial distances) [221]. This reduces ion flux to the film surface, resulting in a film with increased tensile (or reduced compressive) stress. All films in this study were deposited in this regime using an RF frequency of 13.56 MHz, and the effects of ion bombardment is nominally negligible.

C.2 Process Tuning

These theoretical considerations can be applied to tune the process to achieve target film properties. The following describe arbitrary targets to illustrate the point:

1. Target bandgap: 5 eV (UV-transparent); the bandgap serves as a rough, indirect measure of composition, and a bandgap of 5 eV corresponds to a relatively N-rich film
2. Target tensile film stress: 800 MPa; positive stress values refer to tensile stress
3. Target thickness uniformity: <1% deviation; calculated as (standard deviation)/(average) of film thickness

Table C.1 shows the measured film properties for films deposited under various conditions. All films were deposited at a substrate temperature of 400°C with an RF power of 200 W. Sample 1 was deposited using an arbitrarily defined "default" recipe. Each subsequent run represents the effects of changing a single process parameter.

The deposition pressure for run 2 (and all subsequent runs) was set to 5 Torr to reach target metrics. Increasing pressure substantially increased film stress and improves film thickness uniformity. These changes are attributed to the increased rate of reaction in the gas phase discussed previously. The coalescence of larger species with more bonded hydrogen atoms results in higher stress films (hydrogen elimination reaction), and the increased scattering in the gas phase gives rise to the improved uniformity.

Table C.1: Resulting bandgap, tensile film stress, and thickness uniformity (U) achieved by tuning the pressure and setpoint inlet gas flow rates. Run 4B designates the base process used for all subsequent experiments. Films in this table were deposited at 400°C with 200 W RF power.

Run	Pressure (Torr)	SiH_4 Flow (sccm)	NH_3 Flow (sccm)	N_2 Flow (sccm)	Process Implication	Bandgap (eV)	Stress (MPa)	U (%)
1	1.9	20	30	1425	(Default)	3.5	290	1.4
2	5	20	30	1425	Pressure ↑	3.6	640	0.5
3A	5	20	40	1415	NH_3:SiH_4 ↑	3.8	660	0.6
4A	5	20	60	1395	NH_3:SiH_4 ↑↑	3.8	700	0.6
3B	5	15	22.5	1069	Total Flow ↓	3.9	740	0.6
4B	5	10	15	712.5	Total Flow ↓↓	4.8	860	0.4

Runs 3A and 4A show the effect of changing NH_3:SiH_4 ratio in the inlet gas flow, which is generally a control of film stoichiometry. This was achieved by varying the flow rate of NH_3 while maintaining a constant SiH_4 rate and total flow rate (i.e. N_2 flow was varied to balance). A limited effect on stoichiometry was observed: bandgap increased slightly from run 2 to 3A, but was unchanged between 3A and 4A. This suggests a deposition regime controlled by SiH_4 flow. However no effect on bandgap (stoichiometry) was observed. This suggests that the observed deposition reaction is in a regime limited by SiH_4 flow.

Runs 3B and 4B show the effect of changing the total flow rate of the inlet gases and maintaining a constant NH_3:SiH_4 ratio. This is achieved by scaling all gas flow rates (by a factor of 0.75 in Run 3B and 0.5 in Run 4B). Because the reaction occurs in a SiH_4-limited regime, varying total flow rate can also be considered analogous to varying SiH_4 flow rate. This has the observed effect of increasing the bandgap (more N-rich film), and this stoichiometry shift by varying total gas flow further supports the hypothesis of a deposition regime in which SiH_4 is the limiting reactant. For the purposes of this study, a bandgap of 4.8 eV is considered on-target (~5 eV).

It is also noted that, while pressure played the largest role in increasing film tensile stress under the conditions observed, increasing the ratio of NH_3:SiH_4 and decreasing the total gas flow both had the effect of slightly increasing film stress. This effect is also observed in the literature [222–224] and originates from the nature of hydrogen bonding structure within the film and the effect of these bonds on the hydrogen elimination reaction.

Hydrogen in PECVD silicon nitride can be bound to either a silicon atom (Si-H bond) or a nitrogen atom (N-H bond). It has been shown that the fraction of H atoms bonded to either Si or N can be modulated by varying the NH_3:SiH_4 gas flow ratio [222] or SiH_4 flow rate [223]. Parsons *et al.* [223] linked this effect to the sensitivity of gas phase reaction products measured by mass spectroscopy to small changes in silane flow rate. A SiH_4 flow rate reduction leads to an excess of excited nitrogen in the gas phase, which is reflected as increased N-H bonding in the film. Therefore, in general, films deposited with a higher NH_3:SiH_4 ratio or lower SiH_4 flow rate are expected to have a higher fraction of N-H bonds relative to Si-H bonds.

Paduscheck *et al.* [224] have presented evidence correlating the mechanical stress in SiN_x films following thermal treatment to the relative fraction of N-H bonds in the films. As the number of N-H bonds is reduced by the hydrogen elimination reaction, films exhibit a large increase in tensile stress. However, no such correlation with Si-H bond reduction was observed. This was supported in work by Stein *et al.* [222] which showed that, in films of similar composition, N-H bonds are eliminated above 300 °C thermal treatments while Si-H bond elimination required temperatures above ~600 °C. At the temperatures investigated in this study, we can conclude from this evidence that the removal of N-H bonds

dominates the hydrogen elimination reaction. Therefore films with increased N content, either by increasing the NH_3:SiH_4 ratio or reducing the SiH_4 flow rate, can be expected to exhibit increased tensile stress in as-deposited films.

APPENDIX D

ETCH RATES

The following is a compilation of etch recipes and associated etch rates accumulated and used (or at least explored) during the extent of this work. All data is specific to the equipment in the Cornell Nanoscale Science and Technology Facility (CNF) from August 2012 to August 2017.

Table D.1: Etch rates of various materials characterized for the processing equipment in CNF. Abbreviations: T = thermally grown film, P = PECVD film, * indicates that the etch rate was too non-uniform to be reasonably measured, and ** indicates the films etched too quickly for accurate measurement.

Tool	Etchant	Etched Film	Etch Rate (nm/min)	Mask	Selectivity	Date
Oxford 81	CF_4	S1813	105	-	-	03/29/13
Oxford 81	CF_4	S1827	100	-	-	08/12/14
Oxford 81	CF_4	P SiO_2	38	S1827	0.4	08/12/14
Oxford 81	CF_4	P SiN_x	80	S1827	0.8	08/12/14
Oxford 81	CF_4/O_2	S1813	147	-	-	02/03/17
Oxford 81	CF_4/O_2	T SiO_2	14.8	S1813	0.1	02/03/17
Oxford 81	CF_4/O_2	P SiN_x	228	S1813	1.6	02/03/17
Oxford 81	CHF_3/O_2	S1813	30.2	-	-	02/03/17
Oxford 81	CHF_3/O_2	T SiO_2	48.4	S1813	1.6	02/03/17
Oxford 81	CHF_3/O_2	P SiN_x	103.8	S1813	3.4	02/03/17
Oxford 81	SF_6/O_2	S1813	82	-	-	02/03/17
Oxford 81	SF_6/O_2	T SiO_2	10.7	S1813	0.1	02/03/17
Oxford 81	SF_6/O_2	P SiN_x	*	S1813	1.6	02/03/17
Oxford 81	SF_6/CF_4	S1827	95			09/21/13
Oxford 81	SF_6/CF_4	P Mo/Ti	> 50?			06/10/13
Oxford 81	O_2	S1813	234	-	-	03/29/13
PT 720	CF_4/O_2	S1813	43	-	-	03/08/17
PT 720	CF_4/O_2	T SiO_2	19	S1813	0.43	03/08/17
PT 720	CF_4/O_2	P SiN_x	118	S1813	2.7	03/08/17
PT 770	"moh" recipe	S1813	225	-	-	02/08/17
PT 770	"moh" recipe	InGaAs	124	S1813	0.6	02/08/17
PT 770	"moh" recipe	T SiO_2	> 19**	S1813	-	02/08/17
PT 770	"moh" recipe	P SiN_x	> 51**	S1813	-	02/08/17
PT 770	"bsong1" recipe	P SiO_2	30	-	-	From Jena-Xing group
PT 770	"bsong1" recipe	GaN	80-100	P SiO_2	2.7-3.3	From Jena-Xing group
Wet Hood	HCl/HNO_3 (70°)	ITO	50	-	-	11/07/12
Wet Hood	HCl/HNO_3 (R.T.)	ITO	5	-	-	07/31/13
Wet Hood	HCl (R.T.)	ITO	2	-	-	07/31/13
Wet Hood	HCl/H_2O_2 (R.T.)	Cu	1700	-	-	09/27/13

Table D.2: Summary of dry etch recipe parameters specific to CNF processing equipment. Etch rates reported in Table D.1 were measured using these etch recipes.

Tool	Etchant/ Recipe	P (mTorr)	RF Power (W)	Gas	Flow (sccm)
Oxford 81	CHF_3/O_2 CHF3/O2 OXIDE	50	200	CHF_3 O_2	50 2
Oxford 81	SF_6/O_2 SF6/O2 SI ETCH	125	100	SF_6 O_2	45 15
Oxford 81	CF_4 CF4 ETCH	40	150	CF_4	30
Oxford 81	CF_4/O_2 CF4 ETCH (mod)	40	150	CF_4 O_2	30 5
Oxford 81	SF_6/CF_4 CF4 ETCH (mod)	40	100	SF_6 CF_4	20 20
Oxford 81	O_2 OXYGEN CLEAN	60	150	O_2	50
PT 720	CF_4/O_2 CF4O2	40	150	CF_4 O_2	30 2
PT 770	$Ar/BCl_3/Cl_2$ moh (InGaAs etch)	15	50 (RIE) 850 (ICP)	Ar BCl_3 Cl_2	10 16 6
PT 770	$Ar/BCl_3/Cl_2$ bsong1 (GaN etch)	6	23 (RIE) 250 (ICP)	Ar BCl_3 Cl_2	10 10 20

Table D.3: Summary of wet etch recipe parameters. Etch rates reported in Table D.1 were measured using these etch recipes.

Etched Material	Etchant	Chemicals	Ratio	Temp. (°C)
ITO	HCl/HNO_3 (70°)	$H_2O/HCl/HNO_3$	50:45:5	70
ITO	HCl/HNO_3 (R.T.)	$H_2O/HCl/HNO_3$	100:100:5	Room T
ITO	HCl (R.T.)	H_2O/HCl	3:1	Room T
Cu	HCl/H_2O_2 (R.T.) Use fresh solution!	$H_2O/HCl/H_2O_2$	18:1:1	Room T

BIBLIOGRAPHY

[1] J. Hoogboom, T. Rasing, A. E. Rowan, and R. J. M. Nolte. LCD alignment layers. Controlling nematic domain properties. *Journal of Materials Chemistry*, 16(14):1305–1314, 2006.

[2] R. D. Shannon and C. T. Prewitt. Synthesis and structure of phases in the In_2O_3-Ga_2O_3 system. *Journal of Inorganic and Nuclear Chemistry*, 30(6):1389–1398, 1968.

[3] S. B. Narendranath, A. K. Yadav, T. G. Ajithkumar, D. Bhattacharyya, S. N. Jha, K. K. Dey, T. Raja, and R. N. Devi. Investigations into variations in local cationic environment in layered oxide series $InGaO_3(ZnO)_m$ (m = 1–4). *Dalton Transactions*, 43:2120–2126, 2013.

[4] S. C. Abrahams and J. L. Bernstein. Remeasurement of the structure of hexagonal ZnO. *Acta Crystallographica Section B: Structural Science, Crystal Engineering, and Materials*, 25(7):1233–1236, 1969.

[5] T. Kamiya, K. Nomura, and H. Hosono. Origins of high mobility and low operation voltage of amorphous oxide TFTs: Electronic structure, electron transport, defects and doping. *Journal of Display Technology*, 5(7):273–288, 2009.

[6] H. Omura, H. Kumomi, K. Nomura, T. Kamiya, M. Hirano, and H. Hosono. First-principles study of native point defects in crystalline indium gallium zinc oxide. *Journal of Applied Physics*, 105(9):093712, 2009.

[7] K. Nomura, H. Ohta, A. Takagi, T. Kamiya, M. Hirano, and H. Hosono. Room-temperature fabrication of transparent flexible thin-film transistors using amorphous oxide semiconductors. *Nature*, 432(7016):488–492, 2004.

[8] T. Kamiya and H. Hosono. Material characteristics and applications of transparent amorphous oxide semiconductors. *NPG Asia Materials*, 2(1):15–22, 2010.

[9] J. K. Jeong. Photo-bias instability of metal oxide thin film transistors for advanced active matrix displays. *Journal of Materials Research*, 28(16):2071–2084, 2013.

[10] Y. Kurokawa, Y. Okamoto, T. Nakagawa, T. Aoki, M. Ikeda, M. Kozuma, T. Osada, T. Ikeda, N. Yamade, Y. Okazaki, H. Miyairi, M. Fujita, J. Koyama, and S. Yamazaki. Applications of crystalline indium-gallium-zinc-oxide technology to LSI: Memory, processor, image sensor, and field programmable gate array. In *5th Asia Symposium on Quality Electronic Design (ASQED)*, Penang, Indonesia, 2013.

[11] M. Tsubuku, R. Watanabe, N. Ishihara, H. Kishida, M. Takahashi, S. Yamazaki, Y. Kanzaki, H. Matsukizono, S. Mori, and T. Matsuo. Negative-bias photodegradation mechanism in InGaZnO TFT. *Digest of Technical Papers - SID International Symposium*, 44(1):166–169, 2013.

[12] R. T. Bell, A. G. Jacobs, V. C. Sorg, B. Jung, M. O. Hill, B. E. Treml, and M. O. Thompson. Lateral temperature-gradient method for high-throughput characterization of material processing by millisecond laser annealing. *ACS Combinatorial Science*, 18(9):548–558, 2016.

[13] D. M. Lynch, B. Zhu, B. D. A. Levin, D. A. Muller, D. G. Ast, R. G. Greene, and M. O. Thompson. Characterization of reactively sputtered c-axis aligned nanocrystalline $InGaZnO_4$. *Applied Physics Letters*, 105(26):262103, 2014.

[14] D. M. Lynch, B. Zhu, B. D. A. Levin, D. A. Muller, D. G. Ast, R. G. Greene, and M. O. Thompson. Deposition conditions and HRTEM characterization of CAAC IGZO. *SID Symposium Digest of Technical Papers*, pages 308–311, 2015.

[15] CrystalMaker Software Ltd. CrystalDiffract, 2017.

[16] N. Kimizuka and S. Yamazaki. *Physics and Technology of Crystalline Oxide Semiconductor CAAC-IGZO: Fundamentals*. Wiley, West Sussex, UK, 2017.

[17] W. A. P. Claassen, W. G. J. N. Walkenburg, M. F. C. Willemsen, and W. M. v. d. Wijgert. Influence of deposition temperature, gas pressure, gas phase composition and RF frequency on composition and mechanical stress of plasma silicon nitride layers. *Journal of the Electrochemical Society: Solid-State Science and Technology*, 132(4):893–898, 1985.

[18] S. D. Brotherton. *Introduction to Thin Film Transistors: Physics and Technology of TFTs*. Springer, Cham, Switzerland, 2013.

[19] IMARC Group. Global TFT LCD panel market expected to reach USD 210 billion in 2022, driven by the increasing demand for TFT LCD products. URL: http://www.imarcgroup.com/global-tft-lcd-market-worth-us-120-billion, 2017.

[20] M. Nag, A. Bhoolokam, S. Steudel, A. Chasin, K. Myny, J. Maas, G. Groeseneken, and P. Heremans. Back-channel-etch amorphous indium-gallium-zinc oxide thin-film transistors: The impact of source/drain metal etch and final passivation. *Japanese Journal of Applied Physics*, 53(11):111401, 2014.

[21] P. Bocko. From Novelty to Ubiquity: Challenges & Strategies of Scaling the LCD Platform. In *ARPA-E Workshop on Micro-PV*, 2014.

[22] Corning Incorporated. Eagle XG® Slim Glass Product Information Sheet, 2013.

[23] S. Wagner, H. Gleskova, I.-C. Cheng, and M. Wu. Silicon for thin-film transistors. *Thin Solid Films*, 430(1-2):15–19, 2003.

[24] D. G. Ast. Materials limitations of amorphous-Si:H transistors. *IEEE Transactions on Electron Devices*, ED-30(5):532–539, 1983.

[25] V. O. Gupta. A survey on stunning IGZO technology. *International Journal of Applied Information Systems*, 2249(0868), 2013.

[26] J. Robertson. Silicon versus the rest. *Canadian Journal of Physics*, 92(7/8):553–560, 2014.

[27] J. Y. W. Seto. The electrical properties of polycrystalline silicon films. *Journal of Applied Physics*, 46(12):5247–5254, 1975.

[28] T. Kamiya, K. Nomura, and H. Hosono. Present status of amorphous In-Ga-Zn-O thin-film transistors. *Science and Technology of Advanced Materials*, 11(4):044305, 2010.

[29] T. Kamiya, K. Nomura, and H. Hosono. Electronic structures above mobility edges in crystalline and amorphous In-Ga-Zn-O: Percolation conduction examined by analytical model. *Journal of Display Technology*, 5(12):462–467, 2009.

[30] J. S. Park, W. Maeng, H. Kim, J. S. Park, J. Seok, W. Maeng, H. Kim, J. S. Park, W. Maeng, H. Kim, and J. S. Park. Review of recent developments in

amorphous oxide semiconductor thin-film transistor devices. *Thin Solid Films*, 520(6):1679–1693, 2012.

[31] A. Suresh, P. Wellenius, A. Dhawan, and J. Muth. Room temperature pulsed laser deposited indium gallium zinc oxide channel based transparent thin film transistors. *Applied Physics Letters*, 90(12):123512, 2007.

[32] F. C. M. van de Pol, F. R. Blom, and T. J. A. Popma. R.F. planar magnetron sputtered ZnO films I: Structural properties. *Thin Solid Films*, 204(2):349–364, 1991.

[33] S. Limpijumnong, P. Reunchan, A. Janotti, and C. G. Van De Walle. Hydrogen doping in indium oxide: An *ab initio* study. *Physical Review B - Condensed Matter and Materials Physics*, 80(19):1–4, 2009.

[34] S. Lee, B. Bierig, and D. C. Paine. Amorphous structure and electrical performance of low-temperature annealed amorphous indium zinc oxide transparent thin film transistors. *Thin Solid Films*, 520(10):3764–3768, 2012.

[35] J. F. Wager. Transparent electronics—display applications? *Journal of the SID*, 38(1):1824–1825, 2007.

[36] J. Kohanoff and N. I. Gidopoulos. Density functional theory: Basics, new trends and applications. In S. Wilson, editor, *Handbook of Molecular Physics and Quantum Chemistry*, volume 2, pages 532–568. John Wiley & Sons, Chichester, 2003.

[37] K. Burke. *The ABC of DFT*. Irvine, CA, 2007.

[38] W. Körner, D. F. Urban, and C. Elsässer. Origin of subgap states in amorphous In-Ga-Zn-O. *Journal of Applied Physics*, 114(16):163704, 2013.

[39] T. Kamiya, K. Nomura, M. Hirano, and H. Hosono. Electronic structure of oxygen deficient amorphous oxide semiconductor a-$InGaZnO_{4-x}$: Optical analyses and first-principle calculations. *Physica Status Solidi C*, 5(9):3098–3100, 2008.

[40] T. Kamiya, K. Nomura, and H. Hosono. Electronic structure of the amorphous oxide semiconductor a-$InGaZnO_{4-x}$: Tauc-Lorentz optical model and origins of subgap states. *Physica Status Solidi A*, 206(5):860–867, 2009.

[41] T. Kamiya, K. Nomura, and H. Hosono. Subgap states, doping and defect formation energies in amorphous oxide semiconductor a-$InGaZnO_4$ studied by density functional theory. *Physica Status Solidi (A) Applications and Materials Science*, 207(7):1698–1703, 2010.

[42] T. Moriga, D. R. Kammler, T. O. Mason, G. B. Palmer, and K. R. Poeppelmeier. Electrical and optical properties of conducting homologous compounds in the indium-gallium-zinc oxide system. *Journal of the American Ceramic Society*, 82(10):2705–2710, 1999.

[43] K. Nomura, T. Kamiya, H. Yanagi, E. Ikenaga, K. Yang, K. Kobayashi, M. Hirano, and H. Hosono. Subgap states in transparent amorphous oxide semiconductor, In-Ga-Zn-O, observed by bulk sensitive x-ray photoelectron spectroscopy. *Applied Physics Letters*, 92(20):202117, 2008.

[44] H. Tang, K. Ishikawa, K. Ide, H. Hiramatsu, S. Ueda, N. Ohashi, H. Kumomi, H. Hosono, and T. Kamiya. Effects of residual hydrogen in sputtering atmosphere on structures and properties of amorphous In-Ga-Zn-O thin films. *Journal of Applied Physics*, 118(20):0–6, 2015.

[45] H. Tang, K. Ide, H. Hiramatsu, S. Ueda, N. Ohashi, H. Kumomi,

H. Hosono, and T. Kamiya. Effects of thermal annealing on elimination of deep defects in amorphous In-Ga-Zn-O thin-film transistors. *Thin Solid Films*, 614(B):73–78, 2016.

[46] E. K.-H. Yu, S. Jun, D. H. Kim, and J. Kanicki. Density of states of amorphous In-Ga-Zn-O from electrical and optical characterization. *Journal of Applied Physics*, 116(15):154505, 2014.

[47] C. Chen, K. Abe, H. Kumomi, and J. Kanicki. Density of states of a-InGaZnO from temperature-dependent field-effect studies. *IEEE Transactions on Electron Devices*, 56(6):1177–1183, 2009.

[48] Y. G. Chang, H. S. Lee, K. Choi, and S. Im. Capacitance-voltage measurement with photon probe to quantify the trap density of states in amorphous thin-film transistors. *IEEE Electron Device Letters*, 33(7):1015–1017, 2012.

[49] N. Kimizuka and T. Mohri. Spinel, $YbFe_2O_4$, and $Yb_2Fe_3O_7$ types of structures for compounds in the In_2O_3 and Sc_2O_3-A_2O_3-BO systems [A: Fe, Ga, or Al; B: Mg, Mn, Fe, Ni, Cu, or Zn] at Temperatures over 1000°C. *Journal of Solid State Chemistry*, 60(3):382–384, 1985.

[50] M. Nakamura, T. Mohri, and N. Kimizuka. The phase relations in the In_2O_3-Ga_2ZnO_4-ZnO system at 1350°C. *Journal of Solid State Chemistry*, 93(2):298–315, 1991.

[51] N. Kimizuka and T. Mohri. Structural classification of $RAO_3(MO)_n$ compounds (R = Sc, In, Y, or lanthanides; A = Fe(III), Ga, Cr, or Al; M = divalent cation; n = 1–11). *Journal of Solid State Chemistry*, 78(1):98–107, 1989.

[52] N. Kimizuka, M. Isobe, and M. Nakamura. Syntheses and single crystal data of homologous compounds, $In_2O_3(ZnO)_m$ (m = 3, 4, and 5), $InGaO_3(ZnO)_3$, and $Ga_2O_3(ZnO)_m$ (m = 7, 8, 9, and 16) in the In_2O_3-$ZnGa_2O_4$-ZnO System. *Journal of Solid State Chemistry*, 116(1):170–178, 1995.

[53] M. Isobe, N. Kimizuka, M. Nakamura, and T. Mohri. Structures of $LuFeO_3(ZnO)_m$ (m =1, 4, 5 and 6). *Acta Crystallographica Section C: Crystal Structure Communications*, 50(3):332–336, 1994.

[54] K. Nomura, T. Kamiya, H. Ohta, K. Ueda, M. Hirano, and H. Hosono. Carrier transport in transparent oxide semiconductor with intrinsic structural randomness probed using single-crystalline $InGaO_3(ZnO)_5$ films. *Applied Physics Letters*, 85(11):1993–1995, 2004.

[55] M. Orita, H. Tanji, M. Mizuno, H. Adachi, and I. Tanaka. Mechanism of electrical conductivity of transparent $InGaZnO_4$. *Physical Review B*, 61(3):1811–1816, 2000.

[56] K. Nomura, H. Ohta, K. Ueda, T. Kamiya, M. Hirano, and H. Hosono. Carrier transport of extended and localized states in $InGaO_3(ZnO)_5$. *Materials Research Society Symposium Proceedings*, 811:E2.9.1–E2.9.6, 2004.

[57] J. L. F. Da Silva, Y. Yan, and S.-H. Wei. Rules of structure formation for the homologous $InMO_3(ZnO)_n$ compounds. *Physical Review Letters*, 100(25):25–28, 2008.

[58] S. C. Andrews, M. A. Fardy, M.C. Moore, S. Aloni, M. Zhang, V. Radmilovic, and P. Yang. Atomic-level control of the thermoelectric properties in polytypoid nanowires. *Chemical Science*, 2(4):706–714, 2011.

[59] N. Uchida and Y. Bando. High-resolution electron microscopy of homologous compounds $InFeO_3(ZnO)_m$. *Journal of Electron Microscopy*, 43(3):146–150, 1994.

[60] C. Li, Y. Bando, M. Nakamura, and N. Kimizuka. A modulated structure of $In_2O_3(ZnO)_m$ as revealed by high-resolution electron microscopy. *Journal of Electron Microscopy*, 46(2):119–127, 1997.

[61] C. Li, Y. Bando, M. Nakamura, M. Onoda, and N. Kimizuka. Modulated structures of homologous compounds $InMO_3(ZnO)_m$ (M = In, Ga; m = integer) described by four-dimensional superspace group. *Journal of Solid State Chemistry*, 139(2):347–355, 1998.

[62] F. Wolf, B. H. Freitag, and W. Mader. Inversion domain boundaries in ZnO with additions of Fe_2O_3 studied by high-resolution ADF imaging. *Micron*, 38(5):549–552, 2007.

[63] K. Nomura, H. Ohta, K. Ueda, T. Kamiya, M. Hirano, and H. Hosono. Thin-film transistor fabricated in single-crystalline transparent oxide semiconductor. *Science*, 300(5623):1269–1272, 2003.

[64] R. A. Street, J. Kakalios, and M. Hack. Electron drift mobility in doped amorphous silicon. *Physical Review B*, 38(8):5603–5609, 1988.

[65] C. Chung, B. Zhu, D. G. Ast, R. G. Greene, and M. O. Thompson. High mobility amorphous $InGaZnO_4$ thin film transistors formed by CO_2 laser spike annealing. *Applied Physics Letters*, 106(12):123506, 2015.

[66] R. M. Hill. Variable-range hopping. *Physica Status Solidi (a)*, 34(2):601–613, 1976.

[67] F. A. Kröger and H. J. Vink. Relations between the concentrations of imperfections in crystalline solids. In F. Seitz and D. Turnbull, editors, *Solid State Physics: Advances in Research and Applications, Volume 3*, pages 307–435. Academic Press, New York, 1956.

[68] T. C. Chen, T. C. Chang, T. Y. Hsieh, C. T. Tsai, S. C. Chen, C. S. Lin, F. Y. Jian, and M. Y. Tsai. Investigation of the gate-bias induced instability for InGaZnO TFTs under dark and light illumination. *Thin Solid Films*, 520(5):1422–1426, 2011.

[69] A. Janotti and C. G. Van De Walle. Oxygen vacancies in ZnO. *Applied Physics Letters*, 87(12):1–3, 2005.

[70] J. B. Varley, J. R. Weber, A. Janotti, and C. G. van De Walle. Oxygen vacancies and donor impurities in β-Ga_2O_3. *Applied Physics Letters*, 97(14):97–100, 2010.

[71] I.-L. Kang and C.-H. Park. First-principles study of microscopic properties of O vacancies in single-crystalline $InGaZnO_4$. *Journal of the Korean Physical Society*, 56(1):480–484, 2010.

[72] P. Agoston, K. Albe, R. M. Nieminen, and M. J. Puska. Intrinsic n-type behavior in transparent conducting oxides: A comparative hybrid-functional study of In_2O_3, SnO_2, and ZnO. *Physical Review Letters*, 103(24):1–4, 2009.

[73] S. Kwon, J. H. Noh, J. Noh, and P. D. Rack. Quantitative Calculation of Oxygen Incorporation in Sputtered IGZO Films and the Impact on Transistor Properties. *Journal of The Electrochemical Society*, 158(3):H289, 2011.

[74] T. T. T. Nguyen, O. Renault, B. Aventurier, G. Rodriguez, J. P. Barnes, and F. Templier. Analysis of IGZO thin-film transistors by XPS and relation with electrical characteristics. *IEEE/OSA Journal of Display Technology*, 9(9):770–774, 2013.

[75] T. Mudgal, N. Walsh, R. G. Manley, and K. D. Hirschman. Impact of Annealing on Contact Formation and Stability of IGZO TFTs. *ECS Journal of Solid State Science and Technology*, 3(9):Q3032–Q3034, 2014.

[76] A. K. Singh, A. Janotti, M. Scheffler, and C. G. Van De Walle. Sources of electrical conductivity in SnO_2. *Physical Review Letters*, 101(5):1–4, 2008.

[77] M. D. McCluskey, M. C. Tarun, and S. T. Teklemichael. Hydrogen in oxide semiconductors. *Journal of Materials Research*, 27(17):2190–2198, 2012.

[78] J. B. Varley, J. R. Weber, A. Janotti, and C. G. Van De Walle. Oxygen vacancies and donor impurities in β-Ga_2O_3. *Applied Physics Letters*, 97(14):10–13, 2010.

[79] C. G. Van De Walle. Hydrogen as a cause of doping in zinc oxide. *Physical Review Letters*, 85(5):1012–1015, 2000.

[80] C. G. Van De Walle. Defect analysis and engineering in ZnO. *Physica B: Condensed Matter*, 308-310:899–903, 2001.

[81] T. Kamiya and H. Hosono. Roles of Hydrogen in Amorphous Oxide Semiconductor. *ECS Transactions*, 54(1):103–113, 2013.

[82] T. Kamiya, K. Nomura, and H. Hosono. Electronic structure, carrier transport, defects and impurities in amorphous oxide semiconductor. *SID Symposium Digest of Technical Papers*, 44(1):11–13, jun 2013.

[83] S. I. Oh, G. Choi, H. Hwang, W. Lu, and J. H. Jang. Hydrogenated IGZO thin-film transistors using high-pressure hydrogen annealing. *IEEE Transactions on Electron Devices*, 60(8):2537–2541, 2013.

[84] K. Nomura, T. Kamiya, and H. Hosono. Effects of Diffusion of Hydrogen and Oxygen on Electrical Properties of Amorphous Oxide Semiconductor, In-Ga-Zn-O. *ECS Journal of Solid State Science and Technology*, 2(1):P5–P8, 2013.

[85] Pfeiffer Vacuum. Working with turbopumps. 2003.

[86] T. Miyase, K. Watanabe, I. Sakaguchi, N. Ohashi, K. Domen, K. Nomura, H. Hiramatsu, H. Kumomi, H. Hosono, and T. Kamiya. Roles of Hydrogen in Amorphous Oxide Semiconductor In-Ga-Zn-O: Comparison of Conventional and Ultra-High-Vacuum Sputtering. *ECS Journal of Solid State Science and Technology*, 3(9):Q3085–Q3090, 2014.

[87] K. Kato, Y. Shionoiri, Y. Sekine, K. Furutani, T. Hatano, T. Aoki, M. Sasaki, H. Tomatsu, J. Koyama, and S. Yamazaki. Evaluation of off-state current characteristics of transistor using oxide semiconductor material, indium-gallium-zinc oxide. *Japanese Journal of Applied Physics*, 51(2R):021201, 2012.

[88] Y. Hanyu, K. Domen, K. Nomura, H. Hiramatsu, H. Kumomi, H. Hosono, and T. Kamiya. Hydrogen passivation of electron trap in amorphous In-Ga-Zn-O thin-film transistors. *Applied Physics Letters*, 103(20):2011–2014, 2013.

[89] H. K. Noh, J. S. Park, and K. J. Chang. Effect of hydrogen incorporation on the negative bias illumination stress instability in amorphous In-Ga-Zn-O thin-film-transistors. *Journal of Applied Physics*, 113(6), 2013.

[90] Jihoon Kim, Seokhwan Bang, Seungjun Lee, Seokyoon Shin, Joohyun Park, Hyungtak Seo, and Hyeongtag Jeon. A study on H_2 plasma treatment effect on a-IGZO thin film transistor. *Journal of Materials Research*, 27(17):2318–2325, 2012.

[91] S. W. Tsao, T. C. Chang, S. Y. Huang, M. C. Chen, S. C. Chen, C. T. Tsai, Y. J. Kuo, Y. C. Chen, and W. C. Wu. Hydrogen-induced improvements in electrical characteristics of a-IGZO thin-film transistors. *Solid-State Electronics*, 54(12):1497–1499, 2010.

[92] K. M. Yu, J. T. Yuh, S. H. K. Park, M. K. Ryu, E. J. Yun, and B. S. Bae. Trap states of the oxide thin film transistor. *Japanese Journal of Applied Physics*, 52(10S):10MA12, 2013.

[93] T. Kim, Y. Nam, J.-H. Hur, S.-H. K. Park, and S. Jeon. Effect of hydrogen on dynamic charge transport in amorphous oxide thin film transistors. *Nanotechnology*, 27(32):325203, 2016.

[94] H. J. Kim, S. Y. Park, H. Y. Jung, B. G. Son, C.-K. Lee, C.-K. Lee, J. H. Jeong, Y.-G. Mo, K. S. Son, M. K. Ryu, S. Lee, and J. K. Jeong. Role of incorporated hydrogen on performance and photo-bias instability of indium gallium zinc oxide thin film transistors. *Journal of Physics D: Applied Physics*, 46(5):55104, 2013.

[95] K. Domen, T. Miyase, K. Abe, H. Hosono, and T. Kamiya. Positive gate bias instability induced by diffusion of neutral hydrogen in amorphous in-Ga-Zn-O thin-film transistor. *IEEE Electron Device Letters*, 35(8):832–834, 2014.

[96] Tsang Long Chen, Kuan Chang Huang, Hsuan Yi Lin, C. H. Chou, H. H.

Lin, and C. W. Liu. Enhanced current drive of double-gate α-IGZO thin-film transistors. *IEEE Electron Device Letters*, 34(3):417–419, 2013.

[97] Y.-C. Chen, T.-C. Chang, H.-W. Li, W.-F. Chung, S.-C. Chen, C.-P. Wu, Y.-H. Chen, Y.-H. Tai, T.-Y. Tseng, and F.-S. Yeh. Characterization of environment-dependent hysteresis in indium gallium zinc oxide thin film transistors. *Surface and Coatings Technology*, 231:531–534, 2013.

[98] A. Hino, Y. Takanashi, H. Tao, S. Morita, M. Ochi, H. Goto, K. Hayashi, and T. Kugimiya. Effects of thermal annealing on variations of electron traps in the channel region of amorphous In-Ga-Zn-O thin film transistor. *Journal of Vacuum Science and Technology B: Microelectronics and Nanometer Structures*, 32(3):031210, 2014.

[99] J. M. Kwon, J. Jung, Y. S. Rim, D. L. Kim, and H. J. Kim. Improvement in negative bias stress stability of solution-processed amorphous In-Ga-Zn-O thin-film transistors using hydrogen peroxide. *ACS Applied Materials and Interfaces*, 6(5):3371–3377, 2014.

[100] S. Sallis, K.T. Butler, N.F. Quackenbush, D.S. Williams, M. Junda, D. A. Fischer, J.C. Woicik, N.J. Podraza, B.E. White, A. Walsh, and L.F.J. Piper. Origin of deep subgap states in amorphous indium gallium zinc oxide: Chemically disordered coordination of oxygen. *Applied Physics Letters*, 104(23):232108, 2014.

[101] W. H. Han and K. J. Chang. Subgap States near the Conduction-Band Edge Due to Undercoordinated Cations in Amorphous In-Ga-Zn-O and Zn-Sn-O Semiconductors. *Physical Review Applied*, 6(4):1–9, 2016.

[102] W. H. Han, Young Jun Oh, K. J. Chang, and Ji Sang Park. Electronic Struc-

ture of Oxygen Interstitial Defects in Amorphous In-Ga-Zn-O Semiconductors and Implications for Device Behavior. *Physical Review Applied*, 3(4):1–8, 2015.

[103] A. Hino, T. Kishi, H. Tao, S. Morita, K. Hayashi, and T. Kugimiya. Study of Electronic Structure and Film Composition at the Back Channel Surface of Amorphous In-Ga-Zn-O Thin Films. *ECS Journal of Solid State Science and Technology*, 2(4):P156–P159, 2013.

[104] H. K. Noh, K. J. Chang, B. Ryu, and W. J. Lee. Electronic structure of oxygen-vacancy defects in amorphous In-Ga-Zn-O semiconductors. *Physical Review B - Condensed Matter and Materials Physics*, 84(11):1–8, 2011.

[105] Y. W. Lee, S.-J. Kim, S.-Y. Lee, W.-G. Lee, K.-S. Yoon, J.-W. Park, and M.-K. Han. An Investigation of the different charge trapping mechanisms for SiN_x and SiO_2 gate insulator in a-IGZO TFTs. *Electrochemical and Solid-State Letters*, 15(4):H84–H87, 2012.

[106] A. Suresh and J. F. Muth. Bias stress stability of indium gallium zinc oxide channel based transparent thin film transistors. *Applied Physics Letters*, 92(3):033502, 2008.

[107] M. J. Powell. Charge trapping instabilities in amorphous silicon-silicon nitride thin-film transistors. *Applied Physics Letters*, 43(6):597–599, 1983.

[108] M. J. Powell, C. van Berkel, and J. R. Hughes. Time and temperature dependence of instability mechanisms in amorphous silicon thin-film transistors. *Applied Physics Letters*, 54(14):1323–1325, 1989.

[109] F. R. Libsch and J. Kanicki. Bias-stress-induced stretched-exponential time

dependence of charge injection and trapping in amorphous thin-film transistors. *Applied Physics Letters*, 62(11):1286–1288, 1993.

[110] B. Kim, E. Chong, D. Hyung Kim, Y. Woo Jeon, D. Hwan Kim, and S. Yeol Lee. Origin of threshold voltage shift by interfacial trap density in amorphous InGaZnO thin film transistor under temperature induced stress. *Applied Physics Letters*, 99(6):6–8, 2011.

[111] S. Y. Lee, D. H. Kim, E. Chong, Y. W. Jeon, and D. H. Kim. Effect of channel thickness on density of states in amorphous InGaZnO thin film transistor. *Applied Physics Letters*, 98(12):3–5, 2011.

[112] M. E. Lopes, H. L. Gomes, M. C R Medeiros, P. Barquinha, L. Pereira, E. Fortunato, R. Martins, and I. Ferreira. Gate-bias stress in amorphous oxide semiconductors thin-film transistors. *Applied Physics Letters*, 95(6):1–3, 2009.

[113] T.-Y. Hsieh, T.-C. Chang, T.-C. Chen, and M.-Y. Tsai. Review of Present Reliability Challenges in Amorphous In-Ga-Zn-O Thin Film Transistors. *ECS Journal of Solid State Science and Technology*, 3(9):Q3058–Q3070, 2014.

[114] S. Park, E. N. Cho, and I. Yun. Instability of light illumination stress on amorphous In-Ga-Zn-O thin-film transistors. *Journal of the Society for Information Display*, 21(8):333–338, 2013.

[115] T. C. Chen, T. C. Chang, T. Y. Hsieh, M. Y. Tsai, C. T. Tsai, S. C. Chen, C. S. Lin, and F. Y. Jian. Analyzing the effects of ambient dependence for InGaZnO TFTs under illuminated bias stress. *Surface and Coatings Technology*, 231(2012):465–470, 2013.

[116] T. Kojiri, T. Matsuda, and M. Kimura. Thermally enhanced threshold voltage shifts in amorphous In-Ga-Zn-O thin-film transistor. *Japanese Journal of Applied Physics*, 53(12):125802, 2014.

[117] K.-H. Lee, J. S. Jung, K. S. Son, J. S. Park, T. S. Kim, R. Choi, J. K. Jeong, J.-Y. Kwon, B. Koo, and S. Lee. The effect of moisture on the photon-enhanced negative bias thermal instability in Ga-In-Zn-O thin film transistors. *Applied Physics Letters*, 95(23):232106, 2009.

[118] H. Oh, S. M. Yoon, M. K. Ryu, C. S. Hwang, S. Yang, and S. H. K. Park. Transition of dominant instability mechanism depending on negative gate bias under illumination in amorphous In-Ga-Zn-O thin film transistor. *Applied Physics Letters*, 98(3):033504, 2011.

[119] K. Nomura, T. Kamiya, and H. Hosono. Stability and high-frequency operation of amorphous In-Ga-Zn-O thin-film transistors with various passivation layers. *Thin Solid Films*, 520(10):3778–3782, 2012.

[120] Y. J. Chung, U. K. Kim, E. S. Hwang, and C. S. Hwang. Indium tin oxide/InGaZnO bilayer stacks for enhanced mobility and optical stability in amorphous oxide thin film transistors. *Applied Physics Letters*, 105(1):013508, 2014.

[121] B. Ryu, H. K. Noh, E. A. Choi, and K. J. Chang. O-vacancy as the origin of negative bias illumination stress instability in amorphous In-Ga-Zn-O thin film transistors. *Applied Physics Letters*, 97(2):2–4, 2010.

[122] K. H. Ji, J. I. Kim, H. Y. Jung, S. Y. Park, R. Choi, Y. G. Mo, and J. K. Jeong. Comprehensive studies of the degradation mechanism in amor-

phous InGaZnO transistors by the negative bias illumination stress. *Microelectronic Engineering*, 88(7):1412–1416, 2011.

[123] S. Yang, K. H. Ji, U. K. Kim, C. S. Hwang, S.-H. K. Park, C.-S. Hwang, J. Jang, and J. K. Jeong. Suppression in the negative bias illumination instability of Zn-Sn-O transistor using oxygen plasma treatment. *Applied Physics Letters*, 99(10):10–12, 2011.

[124] J. K. Jeong, H. W. Yang, J. H. Jeong, Y.-G. Mo, and H. D. Kim. Origin of threshold voltage instability in indium-gallium-zinc oxide thin film transistors. *Applied Physics Letters*, 93(12):3–5, 2008.

[125] Y.-C. Chen, T.-C. Chang, H.-W. Li, S.-C. Chen, W.-F. Chung, Y.-H. Chen, Y.-H. Tai, T.-Y. Tseng, and F.-S. Yeh. Surface states related the bias stability of amorphous In-Ga-Zn-O thin film transistors under different ambient gasses. *Thin Solid Films*, 520(5):1432–1436, 2011.

[126] S. H. Choi and M. K. Han. Highly reliable multiple-channel IGZO thin-film transistors employing asymmetric spacing and channel width. *IEEE Electron Device Letters*, 34(6):771–773, 2013.

[127] H. Y. Jung, Y. Kang, A. Y. Hwang, C. K. Lee, S. Han, D.-H. Kim, J.-U. Bae, W.-S. Sin, and J. K. Jeong. Origin of the improved mobility and photo-bias stability in a double-channel metal oxide transistor. *Scientific Reports*, 4(19):3765, 2014.

[128] H.-M. Chen, T.-C. Chang, Y.-H. Tai, K.-F. Chen, H.-C. Chiang, K.-H. Liu, C.-K. Lee, W.-T. Lin, C.-C. Cheng, C.-H. Tu, and C.-Y. Liu. Improvements in the reliability of a-InGaZnO thin-film transistors with triple

stacked gate insulator in flexible electronics applications. *Thin Solid Films*, 595:176–180, 2015.

[129] S. Oh, J.-H. Baeck, D. Lee, T. Park, H. S. Shin, J. U. Bae, K.-S. Park, and I. Kang. Improvment of PBTS stability in self-aligned coplanar a-IGZO TFTs. *SID 2015 Digest*, pages 1143–1146, 2015.

[130] J. Raja, K. Jang, S. Q. Hussain, N. Balaji, S. Chatterjee, S. Velumani, and J. Yi. Boosting the mobility and bias stability of oxide-based thin-film transistors with ultra-thin nanocrystalline InSnO:Zr layer. *Applied Physics Letters*, 106(3), 2015.

[131] Y.-G. Kim, S. Yoon, S. Hong, J. S. Choi, and H. J. Kim. Enhancement in positive bias stress stability of In-Ga-Zn-O thin-film transistors with vertically graded-oxygen-vacancy active layer. *SID 2015 Digest*, pages 1209–1212, 2015.

[132] M. Nag, A. Chasin, M. Rockele, S. Steudel, K. Myny, A. Bhoolokam, A. Tripathi, B. van der Putten, A. Kumar, J.-L. van der Steen, J. Genoe, F. Li, J. Maas, E. van Veenedaal, G. Gelinck, and P. Heremans. Single-source dual-layer amorphous IGZO thin-film transistors for display and circuit applications. *Journal of the Society for Information Display*, 21(3):129–136, 2013.

[133] C. Y. Chung, B. Zhu, R. G. Greene, M. O. Thompson, and D. G. Ast. High mobility, dual layer, c-axis aligned crystalline/amorphous IGZO thin film transistor. *Applied Physics Letters*, 107(18), 2015.

[134] M. Furuta, J. Jiang, G. Tatsuoka, and D. Wang. (Invited) Doping and De-

fect Passivation in In-Ga-Zn-O by Fluorine. *ECS Transactions*, 67(1):41–49, 2015.

[135] B.-Y. Su, S.-Y. Chu, Y.-D. Juang, and S.-Y. Liu. Effects of Mg doping on the gate bias and thermal stability of solution-processed InGaZnO thin-film transistors. *Journal of Alloys and Compounds*, 580:10–14, 2013.

[136] J. Raja, K. Jang, N. Balaji, W. Choi, T. T. Trinh, and J. Yi. Negative gate-bias temperature stability of N-doped InGaZnO active-layer thin-film transistors. *Applied Physics Letters*, 102(8), 2013.

[137] C. T. Lee, Y. H. Lin, and J. H. Lin. High stability mechanisms of quinary indium gallium zinc aluminum oxide multicomponent oxide films and thin film transistors. *Journal of Applied Physics*, 117(4):045309, 2015.

[138] H. S. Shin, B. D. Ahn, Y. S. Rim, and H. J. Kim. Annealing temperature dependence on the positive bias stability of IGZO thin-film transistors. *Journal of Information Display*, 12(4):209–212, 2011.

[139] Jayapal Raja, Kyungsoo Jang, Hong Hanh Nguyen, Thanh Thuy Trinh, Woojin Choi, and Junsin Yi. Enhancement of electrical stability of a-IGZO TFTs by improving the surface morphology and packing density of active channel. *Current Applied Physics*, 13(1):246–251, 2013.

[140] K. Park, H.-W. Park, H. S. Shin, J. Bae, K.-S. Park, I. Kang, K.-B. Chung, and J.-Y. Kwon. Reliability of crystalline indium-gallium-zinc-oxide thin-film transistors under bias stress with light illumination. *IEEE Transactions on Electron Devices*, 62(9):2900–2905, 2015.

[141] S. Yamazaki and T. Matsuo. Future possibilities of crystalline oxide semi-

conductor, especially c-axis-aligned crystalline IGZO. *SID 2015 Digest*, pages 673–676, 2015.

[142] S. Yamazaki. New crystalline structure yields reliable thin-film transistors. *SPIE Newsroom*, 2012.

[143] J. Zhang, X. Wen, L. Hu, W. Xu, D. L. Zhu, P.J. Cao, W. J. Liu, S. Han, X. Liu, F. Jia, Y. X. Zeng, and Y. Lu. C-axis Oriented Crystalline IGZO Thin-Film Transistors by Magnetron Sputtering. *Journal of Materials Chemistry C*, 5:2388–2396, 2017.

[144] J. G. E. Gardeniers, Z. M. Rittersma, and G. J. Burger. Preferred orientation and piezoelectricity in sputtered ZnO films. *Journal of Applied Physics*, 83(12):7844–7854, 1998.

[145] K. Ellmer. Magnetron sputtering of transparent conductive zinc oxide: relation between the sputtering parameters and the electronic properties. *Journal of Physics D: Applied Physics*, 33(4):R17–R32, 2000.

[146] S. Yamazaki, H. Suzawa, K. Inoue, K. Kato, T. Hirohashi, K. Okazaki, and N. Kimizuka. Properties of crystalline In-Ga-Zn-oxide semiconductor and its transistor characteristics. *Japanese Journal of Applied Physics*, 53(4S):04ED18, 2014.

[147] S. Yamazaki. Private communication, 2015.

[148] D. G. Ast. IGZO and a-Si:H: A topological constraint theory view. *ECS Transactions*, 79(1):59–68, 2017.

[149] J. A. Thornton. The microstructure of sputter-deposited coatings. *Journal of Vacuum Science & Technology A: Vacuum, Surfaces, and Films*, 4(6):3059–3065, 1986.

[150] B. Zhu, K. E. Roach, D. M. Lynch, C.-Y. Chung, D. G. Ast, R. G. Greene, and M. O. Thompson. Effects of RF sputtering parameters on c-axis aligned crystalline (CAAC) $InGaZnO_4$ films using design of experiment (DOE) approach. *ECS Journal of Solid State Science and Technology*, 5(6):P368–P375, 2016.

[151] B. Zhu, D. M Lynch, C.-Y. Chung, D. G. Ast, R. G. Greene, and M. O. Thompson. Effects of RF sputtering parameters and film composition on c-axis aligned crystalline (CAAC) IGZO films. *SID Symposium Digest of Technical Papers*, pages 677–680, 2015.

[152] B. Zhu, D. M. Lynch, Chung C., D. G. Ast, R. G. Greene, M. O. Thompson, C.-Y. Chung, D. G. Ast, R. G. Greene, and M. O. Thompson. Chemical etch rate and X-ray structure of reactive sputtered c-axis aligned crystalline $In_xGa_yZn_zO_4$ films. *ECS Journal of Solid State Science and Technology*, 4(5):Q43–Q45, 2015.

[153] P. Sigmund. Theory of sputtering. I. Sputtering yield of amorphous and polycrystalline targets. *Physical Review*, 184(2):383–416, 1969.

[154] *The Basics of Sputtering*. Materials Research Corporation, Orangeburg, NY, 3rd edition, 1980.

[155] H. Gnaser and W. O. Hofer. The emission of neutral clusters in sputtering. *Applied Physics A Solids and Surfaces*, 48(3):261–271, 1989.

[156] T. Abe and T. Yamashina. The deposition rate of metallic thin films in the reactive sputtering process. *Thin Solid Films*, 30(1):19–27, 1975.

[157] R. E. Jones, H. F. Winters, and L. I. Maissel. Effect of oxygen on the rf-

sputtering rate of SiO_2. *Journal of Vacuum Science and Technology*, 5(3):84–87, 1968.

[158] J. A. Bearden. X-ray wavelengths. *Reviews of Modern Physics*, 39(1):78–124, 1967.

[159] N. C. Barbi. *Electron Probe Microanalysis Using Energy Dispersive X-ray Spectroscopy*. Princeton Gamma-Tech, Princeton, NJ, 1980.

[160] L. C. Feldman and J. W. Mayer. *Fundamentals of Surface and Thin Film Analysis*. North-Holland, New York, 1986.

[161] J. Goldstein, D. Newbury, D. Joy, C. Lyman, P. Echlin, E. Lifshin, L. Sawyer, and J. Michael. *Scanning Electron Microscopy and X-ray Microanalysis*. Springer, New York, 3rd edition, 2003.

[162] J. J. Friel. *X-ray and Image Analysis in Electron Microscopy*. Princeton Gamma-Tech, Princeton, NJ, 2nd edition, 2003.

[163] W. Kern. The evolution of silicon wafer cleaning technology. *Journal of the Electrochemical Society*, 137(6):1887–1892, 1990.

[164] B. D. Cullity. *Elements of X-ray Diffraction*. Addison-Wesley, Reading, MA, 2nd edition, 1978.

[165] J. I. Langford and A. J. C. Wilson. Scherrer after sixty years: A survey and some new results in the determination of crystallite size. *Journal of Applied Crystallography*, 11(2):102–113, 1978.

[166] U. Holzwarth and N. Gibson. The Scherrer equation versus the 'Debye-Scherrer equation'. *Nature Nanotechnology*, 6(9):534, 2011.

[167] D. Matsubayashi, Y. Kobayashi, S. Matsuda, T. Obanai, N. Ishihara, T. Tanaka, S. Tezuka, H. Suzawa, and S. Yamazaki. Low turn-on voltage due to conduction band lowering effect in crystalline indium gallium zinc oxide transistors. *Japanese Journal of Applied Physics*, 53(4S):04EF02, 2014.

[168] W. Assenmacher, G. Schnakenburg, Y. Michiue, Y. Kanke, N. Kimizuka, and W. Mader. Synthesis and crystal structure characterization of $InGaZnO_4$ with a new defect structure. *Journal of Solid State Chemistry*, 215:176–183, 2014.

[169] M. Nespolo, A. Sato, T. Osawa, and H. Ohashi. Synthesis, crystal structure and charge distribution of $InGaZnO_4$. X-ray diffraction study of 20kb single crystal and 50kb twin by reticular merohedry. *Crystal Research and Technology*, 35(2):151–165, 2000.

[170] P. Sharma, K. Sreenivas, L. M. Belova, and K. V. Rao. Imaging of piezoelectric activity in laser-ablated c-axis-oriented $LiNbO_3$/ZnO thin film multilayer on glass using atomic force microscopy. *Journal of Materials Research*, 18(9):2025–2028, 2003.

[171] V. Gupta and K. Sreenivas. Pulsed laser deposition of zinc oxide (ZnO). In C. Jagadish and S. J. Pearton, editors, *Zinc Oxide Bulk, Thin Films and Nanostructures*, pages 85–174. Elsevier, Amsterdam, 2006.

[172] T. Maruyama and T. Morishita. Copper nitride thin films prepared by radio-frequency reactive sputtering. *Journal of Applied Physics*, 78(6):4104–4107, 1995.

[173] Y. Shigesato and D. C. Paine. A microstructural study of low resistivity

tin-doped indium oxide prepared by d.c. magnetron sputtering. *Thin Solid Films*, 238(1):44–50, 1994.

[174] D. Zhong, J. J. Moore, T. R. Ohno, J. Disam, S. Thiel, and I. Dahan. Deposition and characterization of NiAl and Ni-Al-N thin film from a NiAl compound target. *Surface and Coatings Technology*, 130(1):33–38, 2000.

[175] N. Puychevrier and M. Menoret. Synthesis of III-V semiconductor nitrides by reactive cathodic sputtering. *Thin Solid Films*, 36(1):141–145, 1976.

[176] Y. Yoshino, K. Inoue, M. Takeuchi, and K. Ohwada. Effects of interface micro structure in crystallization of ZnO thin films prepared by radio frequency sputtering. *Vacuum*, 51(4):601–607, 1998.

[177] H. S. Shin, B. D. Ahn, Y. S. Rim, and H. J. Kim. Annealing temperature dependence on the positive bias stability of IGZO thin-film transistors. *Journal of Information Display*, 12(4):209–212, 2011.

[178] H. Yabuta, N. Kaji, M. Shimada, T. Aiba, K. Takada, H. Omura, T. Mukaide, I. Hirosawa, T. Koganezawa, and H. Kumomi. Microscopic structure and electrical transport property of sputter-deposited amorphous indium-gallium-zinc oxide semiconductor films. *Journal of Physics: Conference Series*, 518(1):12001, 2014.

[179] T. I. Selinder, G. Larsson, U. Helmersson, and S. Rudner. Resputtering effects on the stoichiometry of $YBa_2Cu_3O_x$ thin films. *Journal of Applied Physics*, 69(1):390–395, 1991.

[180] T. Kawata, M. Oota, N. Ishihara, M. Nakashima, T. Takasu, Y. Kurosawa, K. Kairiki, M. Tsubuku, and S. Yamazaki. Morphological and electrical

difference in c-axis aligned crystalline IGZO films based on the sputtering method. *SID 2016 Digest*, pages 1330–1332, 2016.

[181] H. Werner. Quantitative analysis of films by ion microbeam methods. II: SIMS. *Mikrochimica Acta*, 114(1):107–127, 1994.

[182] M. Morita, T. Ohmi, E. Hasegawa, M. Kawakami, and M. Ohwada. Growth of native oxide on a silicon surface. *Journal of Applied Physics*, 68(3):1272–1281, 1990.

[183] J. C. Phillips. Private communication, 2015.

[184] J. C. Mauro. Topological constraint theory of glass. *American Ceramic Society Bulletin*, 90(4):31–37, 2011.

[185] S. Yamazaki. The behavior of c-axis-aligned a-b-plane-anchored crystal (CAA crystal). *ECS Transactions*, 67(1):29–40, 2015.

[186] I. Katakuse, T. Ichihara, Y. Fujita, T. Matsuo, T. Sakurai, and H. Matsuda. Mass distributions of copper, silver and gold clusters and electronic shell structure. *International Journal of Mass Spectrometry and Ion Processes*, 67(2):229–236, 1985.

[187] Mitsuru Nakata, Kazushige Takechi, Shinya Yamaguchi, Eisuke Tokumitsu, Hirotaka Yamaguchi, and Setsuo Kaneko. Effects of excimer laser annealing on InGaZnO4 thin-film transistors having different active-layer thicknesses compared with those on polycrystalline silicon. *Japanese Journal of Applied Physics*, 48(11):1–6, 2009.

[188] A. Shimomura, M. Koyama, Y. Ishiyama, M. Ohta, M. Tsubuku, E. Kikuchi, T. Hirohashi, M. Takahashi, and S. Yamazaki. Crystallogra-

phy of excimer laser-crystallized In-Ga-Zn-O film. In *Active-Matrix Flat-panel Displays and Devices (AM-FPD) 2013*, pages 155–158, Kyoto, Japan, 2013.

[189] T. Chen, M. Y. Wu, R. Ishihara, K. Nomura, T. Kamiya, H. Hosono, and C. I. M. Beenakker. Excimer laser crystallization of $InGaZnO_4$ on SiO_2 substrate. *Journal of Materials Science: Materials in Electronics*, 22(11):1694–1696, 2011.

[190] S. Talwar, M. O. Thompson, and D. A. Markle. Laser scanning apparatus and methods for thermal processing, 2004.

[191] K. A. Iyengar, P. Clancy, and M. Thompson. A 3D model for simulating temperature and stress profiles during sub-millisecond Laser Spike Annealing (T. In *18th IEEE Conference on Advanced Thermal Processing of Semiconductors (RTP)*, Gainesville, FL, 2010.

[192] A. Suko, J. Jia, S. Nakamura, E. Kawashima, F. Utsuno, K. Yano, and Y. Shigesato. Crystallization behavior of amorphous indium-gallium-zinc-oxide films and its effects on thin-film transistor performance. *Japanese Journal of Applied Physics*, 55(3):035504, 2016.

[193] B. D. A. Levin. Private communication, 2017.

[194] M. R. Moon, S. Na, H. Jeon, C.-H. An, K. Park, D. Jung, H. Kim, Y.-B. Lee, and H.-J. Lee. Effects of substrate heating on the amorphous structure of InGaZnO films and the electrical properties of their thin film transistors. *Applied Physics Express*, 3(11):3–5, 2010.

[195] K. Nomura, T. Kamiya, H. Ohta, K. Ueda, M. Hirano, and H. Hosono. Carrier transport in transparent oxide semiconductor with intrinsic structural

randomness probed using single-crystalline $InGaO_3(ZnO)_5$ films. *Applied Physics Letters*, 85(11):1993–1995, 2004.

[196] T. Nakagawa, K. Matsumoto, I. Sakaguchi, M. Uematsu, H. Haneda, and N. Ohashi. Analysis of indium diffusion profiles based on the Fermi-level effect in single-crystal zinc oxide. *Japanese Journal of Applied Physics*, 47(10R):7848–7850, 2008.

[197] T. Nakagawa, I. Sakaguchi, M. Uematsu, Y. Sato, N. Ohashi, H. Haneda, and Y. Ikuhara. Diffusion model of gallium in single-crystal ZnO proposed from analysis of concentration-dependent profiles based on the Fermi-level effect. *Japanese Journal of Applied Physics, Part 1*, 46(7A):4099–4101, 2007.

[198] L. Hoddeson, G. Baym, and M. Eckert. The development of the quantum mechanical electron theory of metals, 1926-1933. In L. Hoddenson, E. Braun, J. Teichmann, and S. Weart, editors, *Out of the Crystal Maze: Chapters from the History of Solid-State Physics*, pages 88–181. Oxford University Press, New York, 1992.

[199] N. F. Mott and E. A. Davis. *Electronic Processes in Non-Crystalline Materials*. Oxford University Press, Oxford, UK, 2nd edition, 1979.

[200] D. Weaire. Existence of a gap in the electronic density of states of a tetrahedrally bonded solid of arbitrary structure. *Physical Review Letters*, 26(25):1541–1543, 1971.

[201] M. F. Thorpe and D. Weaire. Electronic density of states of amorphous Si and Ge. *Physical Review Letters*, 27(23):1581–1584, 1971.

[202] D. Weaire and M. F. Thorpe. Electronic properties of an amorphous solid. I. A simple tight-binding theory. *Physical Review B*, 4(8):2508–2520, 1971.

[203] M. F. Thorpe and D. Weaire. Electronic properties of an amorphous solid. II. Further aspects of the theory. *Physical Review B*, 4(10):3518–3527, 1971.

[204] R. A. Street. *Hydrogenated Amorphous Silicon*. Cambridge University Press, Cambridge, UK, 1991.

[205] P. W. Anderson. Absence of diffusion in certain random lattices. *Physical Review*, 109(5):1492–1505, 1958.

[206] N. F. Mott. Electrons in disordered structures. *Advances in Physics*, 16(61):49–144, 1967.

[207] N. F. Mott. Conduction in non-crystalline materials III. Localized states in a pseudogap and near extremities of conduction and valence bands. *Philosophical Magazine*, 19(160):835–852, 1969.

[208] M. H. Cohen. Review of the theory of amorphous semiconductors. *Journal of Non-Crystalline Solids*, 4:391–409, 1970.

[209] G. D. Cody, T. Tiedje, B. Abeles, B. Brooks, and Y. Goldstein. Disorder and the optical-absorption edge of hydrogenated amorphous silicon. *Physical Review Letters*, 47(20):1480–1483, 1981.

[210] G. D. Cody. Urbach edge of crystalline and amorphous silicon: a personal review. *Journal of Non-Crystalline Solids*, 141:3–15, 1992.

[211] J. Robertson. Electronic structure of amorphous semiconductors. *Advances in Physics*, 32(3):361–452, 1983.

[212] R. A. Street. Localized states in doped amorphous silicon. *Journal of Non-Crystalline Solids*, 77-78(1):1–16, 1985.

[213] R. A. Street. The density of states in hydrogenated amorphous silicon. *Proceedings of SPIE*, 673:10–16, 1987.

[214] R. A. Street, M. Hack, and W. B. Jackson. Mechanisms of thermal equilibration in doped amorphous silicon. *Physical Review B*, 37(8):4209–4224, 1988.

[215] R. A. Street and K. Winer. Defect equilibria in undoped a-Si:H. *Physical Review B*, 40(9):6236–6249, 1989.

[216] D. L. Staebler and C. R. Wronski. Reversible conductivity changes in discharge-produced amorphous Si. *Applied Physics Letters*, 31(4):292–294, 1977.

[217] W. B. Jackson and J. Kakalios. Evidence for hydrogen motion in annealing of light-induced metastable defects in hydrogenated amorphous silicon. *Physical Review B*, 37(2):1020–1023, 1988.

[218] B. Drevillon, J. Huc, A. Lloret, J. Perrin, G. de Rosny, and J. P. M. Schmitt. Silane dissociation mechanisms and thin film formation in a low pressure multipole dc discharge. *Applied Physics Letters*, 37(7):646–648, 1980.

[219] G. Turban, Y. Catherine, and B. Grolleau. Mass spectroscopy of a silane glow discharge during plasma deposition of a-Si:H films. *Thin Solid Films*, 67(2):309–320, 1980.

[220] S. Yokoyama, M. Hirose, and Y. Osaka. Electron spin resonance in discharge-produced silicon nitride. *Japanese Journal of Applied Physics*, 20(1):L35–L37, 1981.

[221] R. H. Bruce. Ion response to plasma excitation frequency. *Journal of Applied Physics*, 52(12):7064–7066, 1981.

[222] H. J. Stein, V. A. Wells, and R. E. Hampy. Properties of plasma-deposited silicon nitride. *Journal of The Electrochemical Society*, 126(10):1750–1754, 1979.

[223] G. N. Parsons, J. H. Souk, and J. Batey. Low hydrogen content stoichiometric silicon nitride films deposited by plasma-enhanced chemical vapor deposition. *Journal of Applied Physics*, 70(3):1553–1560, 1991.

[224] P. Paduschek, Ch. Hopfl, and H. Mitlehner. Hydrogen-related mechanical stress in amorphous silicon and plasma-deposited silicon nitride. *Thin Solid Films*, 110(4):291–304, 1983.